Blazar Jets Imaged with Very Long Baseline Interferometry (VLBI) - Kinematics of Helical Trajectories in 3C273 and 3C345

David Gareth Jon Porter
School of Physics and Astronomy, Cardiff University

Thesis Presented for the Degree of Doctor of Philosophy
(Physics and Astronomy)

February 18, 2010

UMI Number: U585329

All rights reserved

INFORMATION TO ALL USERS
The quality of this reproduction is dependent upon the quality of the copy submitted.

In the unlikely event that the author did not send a complete manuscript
and there are missing pages, these will be noted. Also, if material had to be removed,
a note will indicate the deletion.

UMI U585329
Published by ProQuest LLC 2013. Copyright in the Dissertation held by the Author.
Microform Edition © ProQuest LLC.
All rights reserved. This work is protected against
unauthorized copying under Title 17, United States Code.

ProQuest LLC
789 East Eisenhower Parkway
P.O. Box 1346
Ann Arbor, MI 48106-1346

Abstract

In this work a large collection of VLBI (Very Long Baseline Interferometry) maps are presented based upon data from the VLBA (Very Long Baseline Array) for 29 sources. The maps are the result of three epochs of imaging. A kinematic study was undertaken with a view to understanding some interesting structure seen in the quasars 3C273 and 3C345. Fortunately, these two sources present a large number of components and it was possible to perform model fitting to pinpoint their positions. In addition, model fitting was performed upon all of the sources that were successfully imaged. The aim of this was to eventually derive component velocities for as many blazars studied as possible. The outcomes of the work are presented in tables in the main thesis. In order to further understand the 3C273 and 3C345 jet structures seen a physical model was developed with A. Papageorgiou. With this kinematic model it was possible to trace out a variety of helical jet structures. The free parameters are the injection velocity for new components, the period of jet precession, the viewing angle and the jet half angle. Using the Levenberg-Marquardt algorithm (references given below) it was possible to fit jet trajectories to my model fitted component data. The algorithm produced quantitative output for some of the free parameters in my physical model. Therefore I report average jet half angles for 3C273 and 3C345 of 2.968 ± 0.153 degrees and 2.519 ± 0.573 degrees respectively. In addition, I find the precessional periods of 3C273 and 3C345 to be 71.161 ± 19.066 years and 48.478 ± 3.385 years respectively.

Acknowledgments

...you know that when your faith succeeds in facing such trials, the result is the ability to endure.
(James 1:3)

I would like to begin by thanking those closest to me for their constant love and support. I would like to acknowledge my parents for always being at the other end of the phone to lend their encouragement and understanding. Diolch yn fawr iawn to Llinos for suffering my many research frustrations. You are such a positive person with the brightest of personalities. (I can't wait for the 23rd of July!) Your love and belief in me has kept me going to reach this place. All three of you were such an important and real component of what I have achieved and I dedicate this thesis to you.

Thanks to my family and friends who have not been mentioned so far. I do appreciate their trying to understand what my PhD was all about!

A huge thank you to my future best man Dave Cunnah. Those lunch time breaks really helped to maintain my sanity at times! Also your advice and input with regard to my curve fitting work was a huge help and I would have been struggling without it. Thank you for your time and effort. I really do value and enjoy our friendship.

I must say a huge thank you to Andreas Papageorgiou for playing a massive role in what I have managed to do. His guidance on the dark and forbidding world of VLBI map making was invaluable to me. I would also like to thank him for his contribution to the helical jet model that we developed together. His ability to point me in the right direction was a key element in deriving an interesting model to use in my work. Finally, I would

like to say thank you to Andreas for his patience and time. I can remember feeling rather guilty at times over how many questions I had to ask you!

I would like to thank Piers Horner for his kind help and advice. It was a pleasure to work with him and his knowledge of IDL was most valuable to me. I really do appreciate the time that he gave over to our discussions.

Finally, I would like to give my thanks to Walter Gear for his input and for giving me the opportunity to pursue a research project on AGN.

Contents

1 Introduction 7

1.1 The Main Features of an AGN 7

1.2 Context 9

1.3 Blazar Jets: A General Description 9

1.4 Blazar Jets: Physical Mechanisms 10

1.4.1 The Nature of Components in Extragalactic Jets 10

1.4.2 Shock Acceleration 11

1.4.3 The Three Stages of the Shock-in-Jet Model 11

1.4.4 Doppler Beaming 12

1.4.5 Superluminal Motion 13

1.5 Thesis Summary 16

2 Observational Techniques 17

2.1 Interferometry Basics 17

2.2 uv Coverage, Visibilities and Source Brightness Distribution 18

2.3 Cleaning and Self-Calibration 20

2.4 Hybrid Mapping 21

2.5 The Very Long Baseline Array (VLBA) 21

2.6 Stokes Parameters, D-terms and the Instrumental Polarisation 21

2.7 Calibration for Imaging 23

2.7.1 Initial Calibration 23

2.7.2 EVPA Calibration 24

2.7.3 Instrumental Polarisation 24

3 Results 27

3.1 Source List 27

3.2 Observational Details 27

3.2.1 August 2007 Epoch 27

3.2.2 November 2007 Epoch 36

3.2.3 January 2008 Epoch 44

3.3 VLBI Maps 52

3.4 Component Positions and Kinematics 139

3.5 Jet Model Fitting Results 139

3.6 Kinematic Plots 186

4 Development of a Physical Model 253

4.1 The Component Injection Angle 253

4.2 Component Injection Velocity 256

4.3 Component Displacements 257

4.4 Plotting Component Displacements 258

4.5 Vector Transformation from Three Dimensions to Two 258

4.6 Obtaining 2D map or sky coordinates 262

5 Application of the Physical Model to Results 267

5.1 3C273 Plots 269

5.2 3C345 Plots 272

6 Principle Results of Kinematic Study 275

6.1 Jet Velocities 275

6.2 Application of a Physical Model to Model Fitting Results 279

7 Discussion, Conclusions and Further Work 281

7.1 Component Velocities 281

7.2 Fitting the Physical Model 282

Chapter 1

Introduction

The work herein has focused on relativistic Blazar jets imaged on pc-scales. Astrophysical jets were discovered by Heber Curtis in 1917, who described M87's jet as a straight ray connected with the nucleus (McKinney and Blandford, 2009). Specifically, the source 3C273 was observed as a jet-like feature at radio wavelengths in 1963 (Kembhavi and Narlikar, 1999). Therefore, there has been much time to study blazar jets and VLBI has allowed high resolution (mas) imaging of such sources. Our limit is now the core, where the jets become optically thick and we can see no further. Unfortunately, this also limits our ability to understand what is occurring physically in the innermost parts of AGN systems. Indeed, one of the most interesting questions on blazar jets is how they are launched in the first place. It may be possible that the inner torus provides a funnel that collimates the jets in the first instance. Also, it may be the case that magnetic field lines that become twisted in the plasma present in the accretion disc become present in the jets as well. The wound up lines of magnetic field could accelerate and collimate the flow.

As a group, Blazars are composed of Quasars and BL Lac objects. Both of these subgroups can be described via the Unified Model of AGN. This model is best considered using a diagram. The conception of AGN unification in Figure 1.1 is an excellent visual picture, taken from http://crab0.astr.nthu.edu.tw/ hchang/ga2/f2703-unifiedmodel.JPG.

The sketches in Figure 1.2 also give an impression of the importance of viewing angle in the context of AGN unification.

The unified model provides a convenient conceptual picture of the principle workings of an AGN. But how have AGN been classified into different groups? There are two important divisions:

1. The division between objects with or without strong broad emission lines.
2. The division between sources which do or do not have strong radio emission and jets. This is the radio loud/ radio quiet division.

1.1 The Main Features of an AGN

Diagrams of the Unified Model such as Figure 1.1 help in showing broadly how the *main* features of AGN are situated. At the centre of the AGN lies a supermassive black hole (10^6

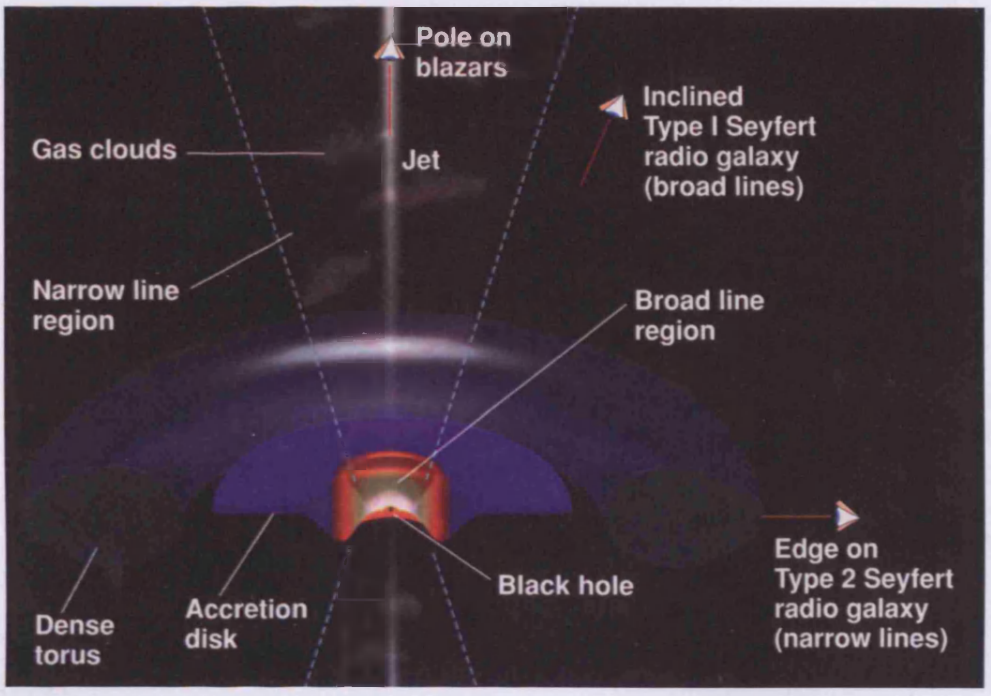

Figure 1.1: A diagram of the Unified Model of AGN.

up to 10^9 solar masses). This is sometimes thought of as the central engine of the AGN. An accretion disc surrounds the black hole and remains in place due to the immense gravity of the central engine. This accretion disc provides a 'fuel supply' for the AGN and jets, where plasma infalls towards the black hole. There is a torus of dusty material that exists around the accretion disc and black hole. The material therein has gravitational potential energy. To infall onto the accretion disc such matter must lose angular momentum. As it does so it is accelerated and heated to very high temperatures forming a plasma. This is the plasma that was previously mentioned with respect to the accretion disc. The accretion disc thus becomes very bright, contributing to the huge luminosity of the AGN.

It should be noted that material infalling towards the black hole is unlikely to be of uniform density. More dense regions of material will boost the luminosity of the accretion disc and less dense regions will lower it, although only temporarily (Freedman and Kaufmann III, 2002). This introduces the variability property of AGN.

One of the most prominent features of AGN is their variability. In some cases this can be quite rapid. For example, quasars can exhibit optical variability over timescales as long as years and as short as 15 minutes. It is known that optical variables show significant behaviour of this kind at radio wavelengths as well (Zeilik and Gregory, 1998).

It is thought that jets in blazars are launched by magnetic processes in plasma that is accreting onto black holes (Meier and Nakamura, 2006). Magnetic field structures are thought to exist in the accretion discs of AGN (due to the presence of plasma). It is thought that these structures become twisted near the black hole as the AGN system rotates around its centre of mass. It is thought that helical magnetic field lines then emerge perpendicular to the plane of the accretion disc. These are some of the most notable structures close to the site of jet launching.

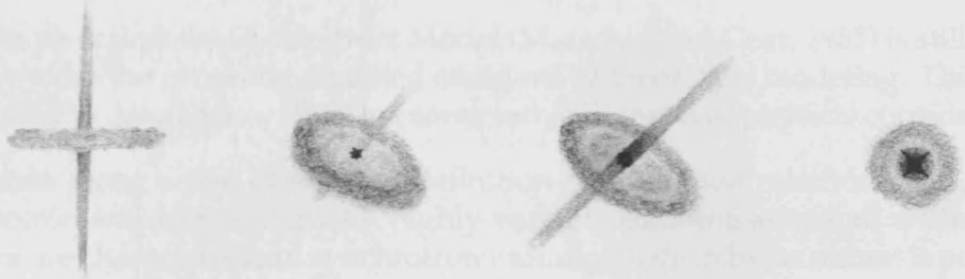

Figure 1.2: Sketches of the main AGN types (sketches by the author, based on material in Cosmos by Giles Sparrow (Sparrow, 2006)).

1.2 Context

It is suitable at this early stage to ask where we might find Blazars in the Universe, both in terms of scale and distance.

Radio loud AGN are associated with elliptical galaxies whereas radio quiet AGN are found mostly in disks (Krolik, 1999). With VLBI, the cores of AGN may be resolved in pc-scale images of the jets. The accretion disc that surrounds the central black hole has a typical size of order $10^{-3}pc$. As an indication of their extent, the jets can be studied on kpc-scales.

In the sample of 29 sources that were analysed for this work, redshifts ranged from very much less than unity, up to around two.

1.3 Blazar Jets: A General Description

Of the various objects that the Standard Model of Active Galactic Nuclei (AGN) suggests, Blazars are the most powerful. Some of the brightest Blazars can reach fluxes of around $20Jy$. This scales down to roughly $100mJy$ for the weakest observed sources. As a class of AGN, Blazars encompass Bl Lac objects and Highly Polarised Quasars (HPQs) and as such, are radio-loud as well as being compact. Rapid variability is observed over all wavelengths in timescales as short as days. In terms of the spectra of such sources, radio emission is seen to have a very flat profile. This then breaks into a steep spectrum in the millimetre through to the infrared range. The continuum emission from Blazars is significantly polarised.

1.4 Blazar Jets: Physical Mechanisms

At present (on pc-scales) the Shock-in-Jet Model (Marscher and Gear, 1985) is still considered by many to be the generally accepted standard of theoretical modeling. This model will be discussed in detail below. But first some rather more basic physical considerations.

Viewing Blazars along a line of sight by definition close to their relativistic jets, we observe synchrotron emission along with highly variable emission across all wavelengths. Blazar spectra are characteristic of synchrotron radiation, which by its nature is polarised. Synchrotron radiation can be defined in terms of a power law energy spectrum as follows:

$$N(E)dE \propto E^{-s}dE \tag{1.1}$$

Where $N(E)dE$ is the number of electrons per unit volume at an energy E and s is the spectral index for the electron distribution.

In terms of a frequency spectrum for relativistic electrons, I shall take the convention that α (frequency spectral index) is positive, but implies a negative power law frequency spectrum (that is, $I(\nu) \propto \nu^{-\alpha}$) for AGN.

Electrons emitting synchrotron radiation lose energy at a rate given in the following expression:

$$-\frac{dE}{dt} = \frac{4}{3}\sigma_T c \left(\frac{E}{m_e c^2}\right)^2 \frac{B^2}{2\mu_o} \propto E^2 B^2 \tag{1.2}$$

Where $\sigma_T = \frac{e^4}{6\pi\epsilon_o^2 c^4 m^2}$ is the Thompson cross-section, the effective surface area of an electron with respect to a nearby photon.

A compact radio core is observed in the one-sided jets of Blazars (usually at their ends). When imaging with VLBI this is commonly referred to as the VLBI core. It is usually unresolved even by high frequency VLBI. In addition, radio components called knots are also observed. They are thought to be associated with periods of high activity within the central engine of the AGN. Knots are often seen to propagate down the jets at superluminal speeds, although some can be observed to be stationary. It is common to observe relativistic jets having bends in their structure, which could be associated with such knots in the jet flow.

1.4.1 The Nature of Components in Extragalactic Jets

Intense regions of emission that stand out in images of jets are a familiar phenomenon. As well as imaging of components with the VLBA for example, it is known that jet components' synchrotron self-absorbed spectra superpose to give an apparently flat overall spectrum in the radio to millimetre regimes. The spectrum falls off at infrared frequencies. Figure 1.3 shows how the overall spectrum would look. The arrow indicates spectra for individual components tending towards lower frequencies with time. This occurs as the components proceed down a jet flow.

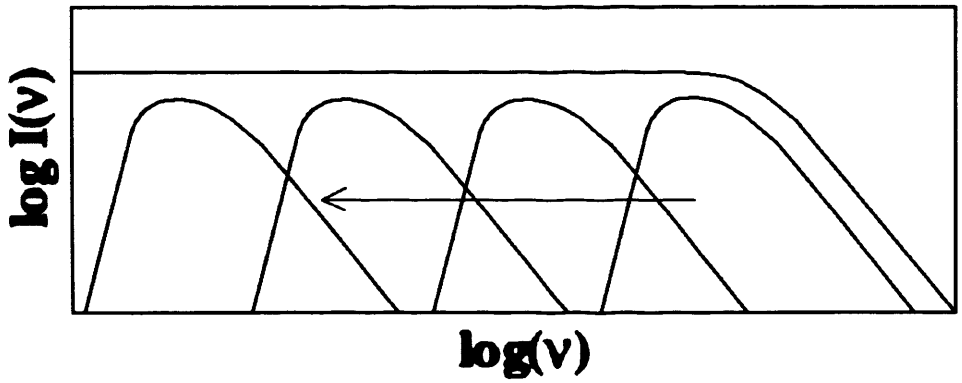

Figure 1.3: Frequency Spectrum of Jet Components

The actual nature of components is still debatable. The components could be shocks. This means that components are the means by which electrons in the jets are reaccelerated. Alternatively, components could be intense regions of plasma injected into the jet flow from the core.

1.4.2 Shock Acceleration

Energetic particles may gain further energy by elastically scattering off magnetic structures within extragalactic jets (Rieger et al., 2007). Shocks will cause magnetic field lines to become more prominent along a direction perpendicular to the jet axis.[1] Therefore magnetic structures that are predominantly perpendicular to the jet axis can be considered as originating from jet components.

Shock acceleration favours particles whose mean free paths are a) longer than the width of the shock and b) shorter than the length of fluid either side of the shock (Krolik, 1999). In this case, each time a particle crosses the shock it will be reflected back and will gain energy steadily.

The creation of shocks could be a result of an atypically large injection of relativistic electrons into a jet (Garcia, 1995).

1.4.3 The Three Stages of the Shock-in-Jet Model

There is an apparent paradox raised by the lengths of Blazar jets when the rate of energy loss by synchrotron radiation is considered. Without some form of additional acceleration of the electrons it is difficult to answer this paradox.

A possible solution is shocks. They are likely to exist in extremely fast flows (Reynolds, 2002) and they could propagate down the jet providing electron acceleration. This would prolong the lifetime of the electrons.

[1] If R is taken to be a measure of distance along a jet's axis, then it may be shown that $B_{\perp} \propto R^{-1}$ whereas $B_{||} \propto R^{-2}$. Here $B_{\perp}$ and $B_{||}$ are components of the magnetic field lines that are perpendicular and parallel to the jet axis respectively.

The shock-in-jet model allows us to concisely summarize the evolution of a typical flaring jet component into three epochs. Following the breakdown of this model given by Marscher and Gear (1985) a newly injected jet component will initially have the effect of boosting the flux density observed in the millimetre to infrared regimes. However this process is short-lived and the first phase of the shock-in-jet model begins almost instantaneously. In this phase, referred to by Marscher and Gear (1985) as the Compton stage, the initial flux density boost caused by the new component has the effect of increasing the photon energy density, u_{ph} in the jet as described below:

$$u_{ph} \propto K(B^{3s+7}R^{s+5})^{\frac{1}{8}} \propto R^{-\frac{(13s+17)+3a(3s+7)}{24}} \tag{1.3}$$

Here $K = K_0(\frac{R_0}{R})^{\frac{2(s+2)}{3}}$ and is a parameter of the electron energy distribution, R is the distance from the vertex of the jet that is modelled as a cone, a is the exponent of radial variation in magnetic field strength[2] such that $B \propto R^{-a}$ and s is as defined earlier. This leads to Inverse Compton processes dominating, imposing large energy losses on the electron distribution in the region. These losses are observed as a 'bump' of x-ray emission in the Blazar frequency spectrum. This boost in x-ray emission leads to an increase in flux density due to synchrotron losses as the jet component propagates down the jet. (Often, the resulting sequence of boosted emission in x-rays and then in the millimetre to infrared range is the first sign to extragalactic astronomers that a Blazar is in the process of flaring. Also, the x-ray flare will lag slightly behind the initial flare in flux density in the millimetre to infrared regimes that initiates the Compton stage.) This is thus termed the Synchrotron stage; the second of the three epochs in the shock-in-jet model. Beginning in the millimetre to infrared wavebands, this boost in synchrotron emission will shift down into lower frequencies (towards the radio waveband) with a fairly constant peak flux density, S_m as the component evolves:

$$S_m \propto \upsilon_m^{\frac{(2s-5)(2+3a)}{4(s+2)+3a(s-1)}} \propto R^{\frac{-8(s-1)-3a(4s-9)}{6(s+4)}} \upsilon^{\frac{-5}{2(s+4)}} \tag{1.4}$$

υ_m above is the turnover frequency of synchrotron emission. In the final epoch, the adiabatic stage, the shock is seen to expand and decay such that its flux density, S_υ is modelled via the following equation:

$$S_\upsilon \propto R^{\frac{-7(s-1)}{6}} \upsilon^{\frac{-(s-1)}{2}} \tag{1.5}$$

The energy of the shock decreases as the reciprocal of its separation from the core, until it is no longer resolved. Radiative processes appear to be no longer important during this final phase.

1.4.4 Doppler Beaming

The emission from Blazars is highly Doppler beamed due to the relativistic nature of the jets. This is best seen graphically, once some definitions have been made:

If we define the Lorentz factor, Γ in the usual way:

[2] $a = 1$ for a magnetic field perpendicular to the jet axis whereas $a = 2$ for parallel magnetic fields.

$$\Gamma = \frac{1}{\sqrt{1-(\frac{v}{c})^2}} \tag{1.6}$$

Then we can define the Doppler boosting factor, δ as:

$$\delta = \frac{1}{\Gamma(1-\frac{v}{c}\cos\theta)} \tag{1.7}$$

Where v is the velocity of the source. Now if we imagine a polar coordinate space with an AGN source at the centre and a line of sight joining it to an observer on the earth, he/she will see Doppler boosted emission as they look down the forward jet from the AGN. As the the polar plot in Figure 1.4 demonstrates, emission from the source is highly beamed close to the line of sight at $0°$. In this plot, theta is the viewing angle of observation (varying from 0 up to 2π radians) and delta is the Doppler boosting factor defined above.

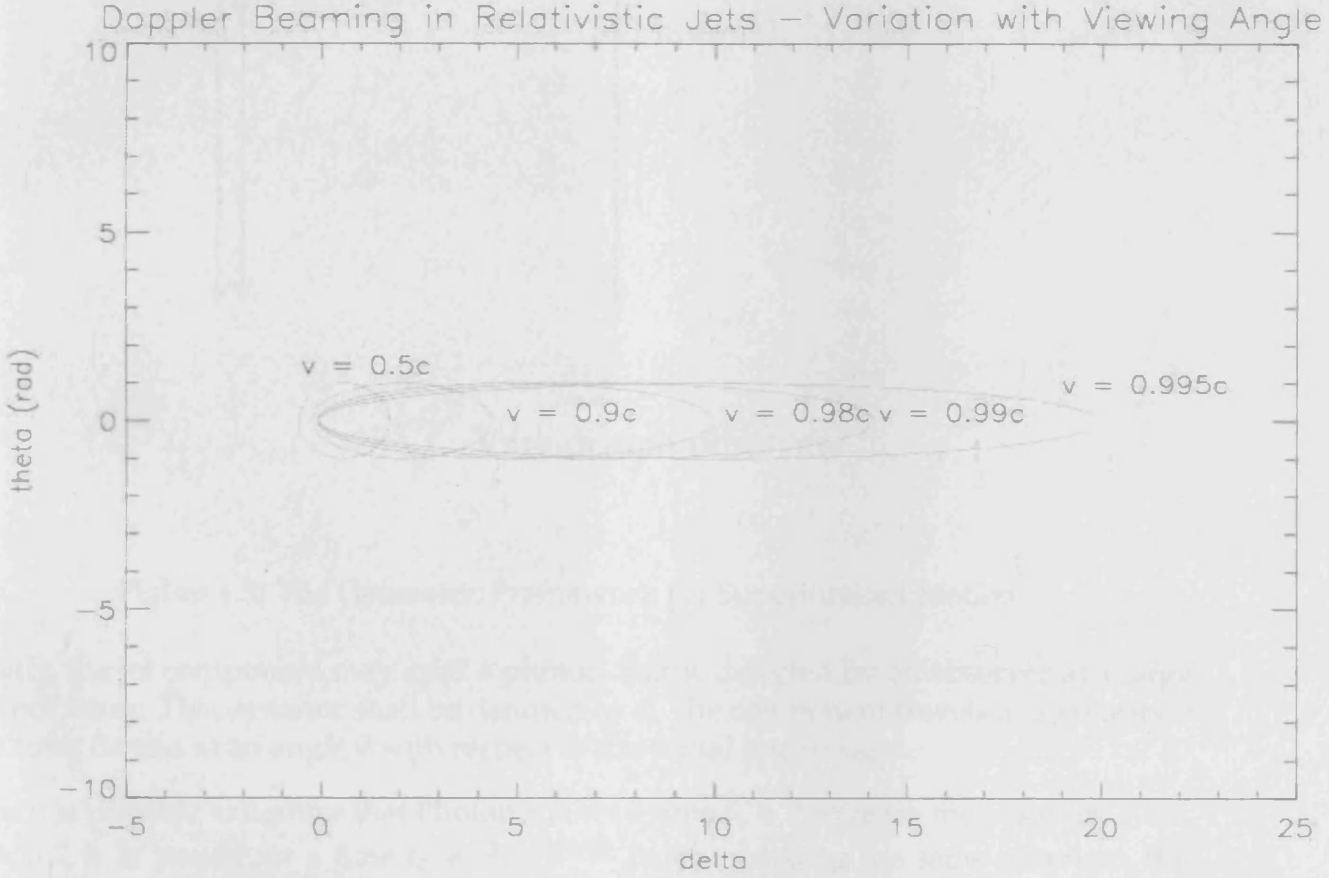

Figure 1.4: Doppler Beaming in Relativistic Jets

1.4.5 Superluminal Motion

Firstly, it is important to be clear on what is meant by a knot or jet component. These are bright and compact features that can be distinguished in VLBI images of relativistic jets. There is a possibility that components might be hydrodynamical features such as internal shocks (Hardcastle, 2007).

Components that are visible along relativistic jets can exhibit a phenomenon called superluminal motion. This is a geometric effect that can lead to apparent component velocities greater than that of light according to the observer. The effect is most significant for small angles between the relativistic jet and the line of sight.

Consider the following case, with a relativistic jet component moving from one observed position to another:

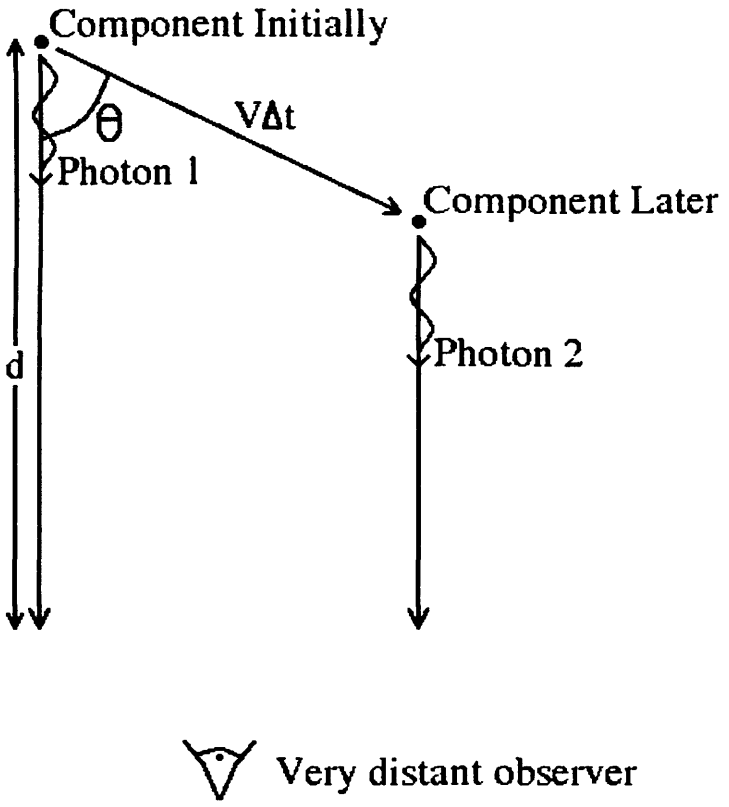

Figure 1.5: The Geometric Framework for Superluminal Motion

Initially, the jet component may emit a photon that is detected by an observer at a large distance away. This distance shall be denoted as d. The component travels at a velocity v for a time Δt and at an angle θ with respect to the initial line of sight.

Thus, it is possible to deduce that Photon 1 takes a time $t_1 = \frac{d}{c}$ to reach the observer. Also, Photon 2 is in transit for a time $t_2 = \frac{d - v\Delta t cos(\theta)}{c}$ before reaching the same observer. But Photon 2 was emitted a time Δt after Photon 1. Therefore Photon 2 actually reaches the observer after a time $t_2 = \Delta t + \frac{d - v\Delta t cos(\theta)}{c}$.

In the time Δt between the two photon emissions, the component traveled a transverse (from the observer's point of view) distance $v\Delta t sin(\theta)$. Hence the apparent transverse velocity as seen by the observer is $v_{app} = \frac{v\Delta t sin(\theta)}{t_2 - t_1}$. With substitution and canceling of terms the following final expression can be obtained for the apparent transverse velocity, v_{app}:

$$v_{app} = \frac{v \sin(\theta)}{1 - \frac{v \cos(\theta)}{c}} \tag{1.8}$$

It can be noticed that as $vcos(\theta)$ tends towards c, v_{app} tends to infinity.

v_{app} can be plotted to see its angular dependence, as has been implemented in Figure 1.6. Here, theta is the angle that was previously defined, shown now in radians. It ranges from 0 up to π on the graph.

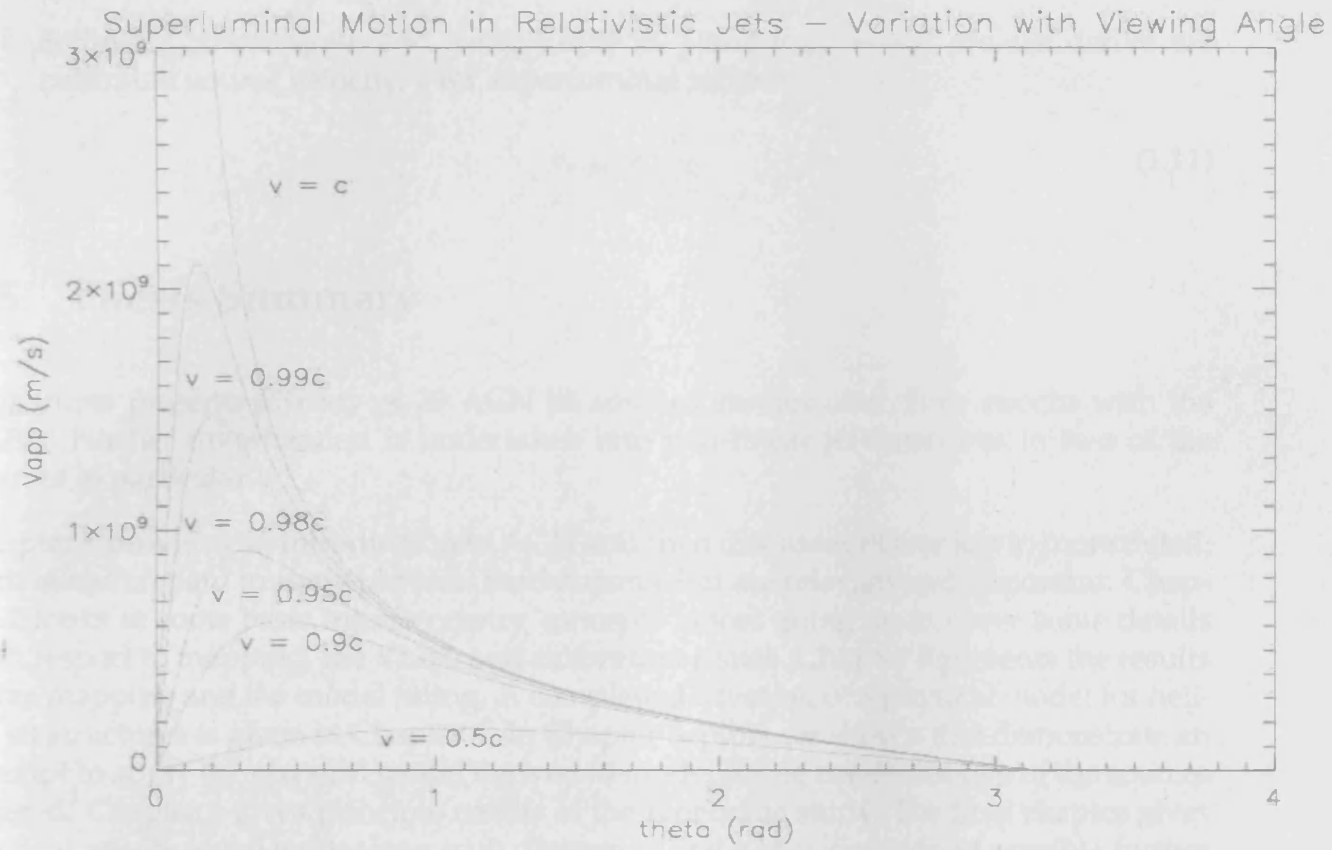

Figure 1.6: Angular Dependence of Superluminal Motion in Relativistic Jets

The graph shows that superluminal motion is most significant at smaller angles between the relativistic jet and the line of sight. No superluminal motion is observed at 0 radians since along the line of sight there will be no transverse motion observed. There is a singularity when $v = c$ that can be seen on the graph.

By maximising V_{app} in (1.8) with respect to θ in the usual way we obtain $\cos(\theta) = \frac{v}{c}$ and by manipulating this, $\sin(\theta) = \frac{1}{\Gamma}$. Via a small angle approximation for θ (given that the line of sight is close to the jet axis) one can show that the optimal viewing angle for superluminal motion is:

$$\theta \sim \frac{1}{\Gamma} \tag{1.9}$$

This is the same as the width of a Doppler beamed cone of synchrotron emission. One can perform a number of other different exercises to derive similarly useful expressions within this context:

1. By substitution of $\cos(\theta) = \frac{v}{c}$ and $\sin(\theta) = \frac{1}{\Gamma}$ above into (1.8) we can derive an

expression for the maximum value of V_{app}:

$$V_{app}^{max} = v\Gamma \tag{1.10}$$

Note that this expression depends only upon v. Taking $v = 0.999c$ for a numerical result we obtain $V_{app}^{max} = 22.34c$.

2. Setting $V_{app} = c$ again and using $\cos(\theta) = \frac{v}{c}$ and $\theta_{max} = 45^\circ$ we can derive the minimum source velocity, v for superluminal motion:

$$v_{min} = \frac{c}{\sqrt{2}} \tag{1.11}$$

1.5 Thesis Summary

This thesis presents a study of 29 AGN jet sources studies over three epochs with the VLBA. Further investigation is undertaken into non-linear jet structures in two of the sources in particular.

Chapter 1 provides an introduction to AGN and then discusses Blazar jets in more detail, with attention paid to some physical mechanisms that are relevant and important. Chapter 2 looks at some basic interferometry concepts before going on to cover some details with respect to mapping, the VLBA and calibration issues. Chapter 3 presents the results of the mapping and the model fitting. A complete derivation of a physical model for helical jet structures is given in Chapter 4. In Chapter 5, plots are shown that demonstrate an attempt to apply the physical model derived to model fitting results for two of the sources imaged. Chapter 6 gives principle results of the kinematic study. The final chapter gives the final results of the work along with discussion and a consideration of possible further study.

Chapter 2

Observational Techniques

In this chapter I describe the VLBA as an array of interferometers and give an account of the underlying principles that allow it to image sources such as Blazars.

2.1 Interferometry Basics

The principle benefit of interferometry in terms of imaging is resolution. With a single radio dish the resolution is approximately the wavelength of the signal divided by the dish diameter. However, for an interferometer the resolution is approximately the wavelength of the signal divided by the baseline length (the distance between the two dishes in the interferometer). Therefore interferometry will yield improved resolution.

Let us take the simple example of a two element interferometer as shown in Figure 2.1. The two antennas shall be labeled with the numbers 1 and 2 and are separated by the baseline length, s. There is a path difference between the two signals, P. This varies throughout an observing day due to the change in direction of the received signal.

Kitchin (2003) discusses two causes of the path difference P. Firstly, there will be delays in the electronics and cables connecting the antennae to the central processing unit. Secondly, the angle of inclination of the source to the line joining the two antennae. The former is usually small and can be ignored or corrected for. The latter will change as the rotation of the earth alters the inclination angle. The rate of change of P varies throughout an observing day due to interference in the source signal.

The path difference also varies because the effective separation of the antennae, d (the apparent separation of the antennae as seen from the direction of the source) varies in time.

The change in d causes the resolution of the interferometer to change and this will alter the uv coverage with the interferometer's tracks moving either outward or inward depending on a positive or negative rate of change of d. uv coverage shall be covered in more detail in the next section.

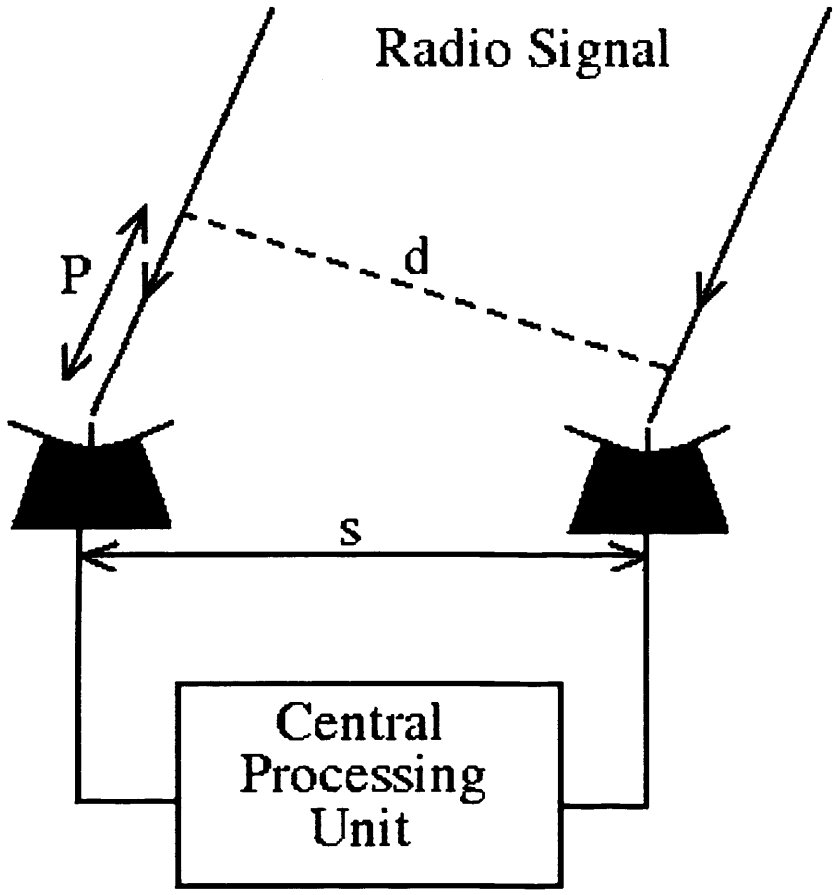

Figure 2.1: A basic interferometer arrangement (Kitchin, 2003)

2.2 uv Coverage, Visibilities and Source Brightness Distribution

Two antennae arranged upon an east-west line will follow a circular track perpendicular to the earth's rotational axis. Therefore for convenience, the uv plane is taken to be perpendicular to the earth's axis. As mentioned in the previous section, a range of tracks will be traced out upon the uv plane depending on the geometry of the interferometer as it is with respect to the source.

The VLBA's constituent antennae observe a source simultaneously and at discrete points in time in order to build up a picture of the brightness distribution of a source. The discrete samples are called visibilities. It is these that are measured by the VLBA. The Fourier transform of a function is always symmetrical. Therefore when an interferometer makes an observation of a source, two visibilities are plotted about the centre of the uv plane (that is, with the centre of the uv plane in between the two points). As the earth rotates the antennae comprising each interferometer trace out curves in the Fourier or uv plane. It is in this plane that the VLBA's interferometers operate. The array tracks are formed as follows. Consider a single baseline array (two dishes). Due to the earth's

rotation they trace out curves in the uv plane on the sky as shown in Figure 2.2.

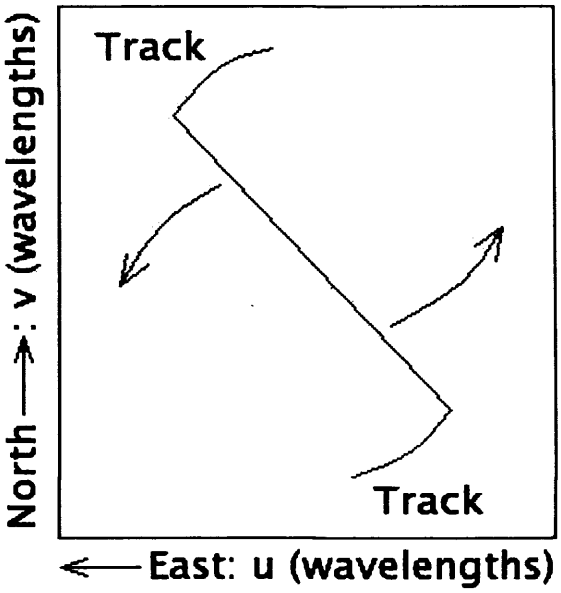

Figure 2.2: uv Coverage

Here, u and v are effectively coordinates on the sky. The centre of the plot represents the (0,0) position in terms of u and v. Coordinates are always set up such that East points to the left and North upwards. Scales are in mas.

The technique of aperture synthesis in the case of the VLBA allows constituent interferometers to contribute their own visibilities (Fourier components) to the uv plane for a source. Longer baselines contribute higher angular frequency and therefore higher resolution information about a source and vice versa for shorter baselines. With a network of antennae, good uv plane sampling allows a good image of the source without sidelobe features contaminating the beam (hence the term dirty beam in such a case). These result from gaps in the uv coverage. A single twelve hour observation by a two-element interferometer samples components of the Fourier transform of the field of view covered in the uv plane. In reality, a series of twelve hour observations are made using all of the available baseline lengths. The uv plane is then sampled out to the maximum baseline length, which gives the highest resolution information.

The distribution of visibilities V(u,v) and the brightness distribution of the source on the sky B(x,y) form a Fourier pair such that the following equations can be written (Reynolds, 2002):

$$V(u,v) = \int_{-\infty}^{\infty}\int_{-\infty}^{\infty} B(x,y)e^{2i\pi(ux+vy)dxdy} \tag{2.1}$$

$$B(x,y) = \int_{-\infty}^{\infty}\int_{-\infty}^{\infty} V(u,v)e^{-2i\pi(ux+vy)dudv} \tag{2.2}$$

Therefore, given that the distribution of visibilities are measured by the interferometer, an image of the brightness distribution of a source can be found by taking the Fourier transform.

2.3 Cleaning and Self-Calibration

The making of VLBI maps is a loop process in terms of cleaning and self-calibration. Figure 2.3 indicates the extent of this. Cleaning VLBI maps deconvolves the dirty map. It brings together a number of steps which are outlined below (Högbom, 1974):

1. Calculate the dirty beam by taking the Fourier transform of the uv coverage sampling. In addition, find the dirty map by taking the Fourier transform of the visibility data.
2. At the point where the dirty map reaches its maximum intensity, subtract off the dirty beam to leave a residual map. The dirty beam should be normalised to a factor between zero and unity (the loop gain), multiplied by the maximum of the dirty map.
3. Repeat the subtractions with the dirty beam, each time taking the residual map from the previous iteration as the dirty map. Stop when the maximum intensity of the dirty map is no longer significant with respect to the general noise level.
4. Take the final residual map, and return to it all of the subtracted (clean) components with their respective positions and amplitudes.

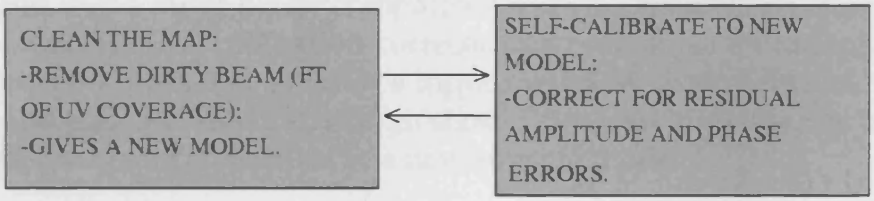

Figure 2.3: A simple diagram of the cleaning process undertaken during VLBI map making

For instruments such as the VLBA, closure phase is utilised. The atmospheric conditions cause phase delays that may be canceled out via the closure phase of three antennae.

Following Kitchin (2003), we can consider a simple three element interferometer. We indicate that the phases for the three baselines independent of atmospheric effects are ϕ_{12}, ϕ_{23} and ϕ_{31}. Finally, we show the atmospheric phase delays as a_1, a_2 and a_3. The observed phases are then:

$$\phi_{12} + a_1 - a_2 \tag{2.3}$$

$$\phi_{23} + a_2 - a_3 \tag{2.4}$$

$$\phi_{31} + a_3 - a_1 \tag{2.5}$$

The closure phase is then given by the phase sum around the baselines and it can be seen that the atmospheric phase delays will cancel completely to leave:

$$\phi_{123} = \phi_{12} + \phi_{23} + \phi_{31} \tag{2.6}$$

Thus the closure phase is independent of the effects of atmosphere and this reduces the number of unknowns in the imaging procedure.

There are drawbacks that come with the use of closure phase. In a triangle of antennas, one must be taken as a reference antenna, such that the phases of the other two are measured relative to it. The problem here is that no measure of absolute phase is possible. The main disadvantage of closure phase is that it removes atmospheric phase delays at the expense of source position (Jennison, 1958).

2.4 Hybrid Mapping

Hybrid mapping as a procedure involves iterative self-calibration with a view to estimating unknown phase and/ or amplitude errors at each antenna. The errors in question do not affect closure phases and amplitudes.

It may be possible to use three programs for hybrid mapping. The first should correct the visibilities in the input file by comparison with the predictions of an input model. It should also estimate the calibration corrections to minimise the disagreement between the corrected visibilities and the user's input model. A second program should make a dirty map and then a CLEAN algorithm should clean the dirty map to produce an array of delta functions that can be used as a new starting model.

2.5 The Very Long Baseline Array (VLBA)

The VLBA is a network of amplitude interferometers situated across America. It can achieve resolutions of mas or even micro-arcseconds thanks to the large distances between antennas (see Figure 2.4). In the case of the VLBA, signals are recorded onto tapes at each station. There is a separate correlation centre that processes all of the data (tapes) from the constituent antennas.

Data from the VLBA was utilised in order to produce high resolution maps of close to thirty relativistic jet sources. Figure 2.4 shows how the antennas making up the VLBA are distributed across the United States.

2.6 Stokes Parameters, D-terms and the Instrumental Polarisation

For frequency bands above 1GHz, Cassegrain feeds are located on a circle at the top of a feed cone. The outputs of the feeds are circular waveguide apertures. From these the

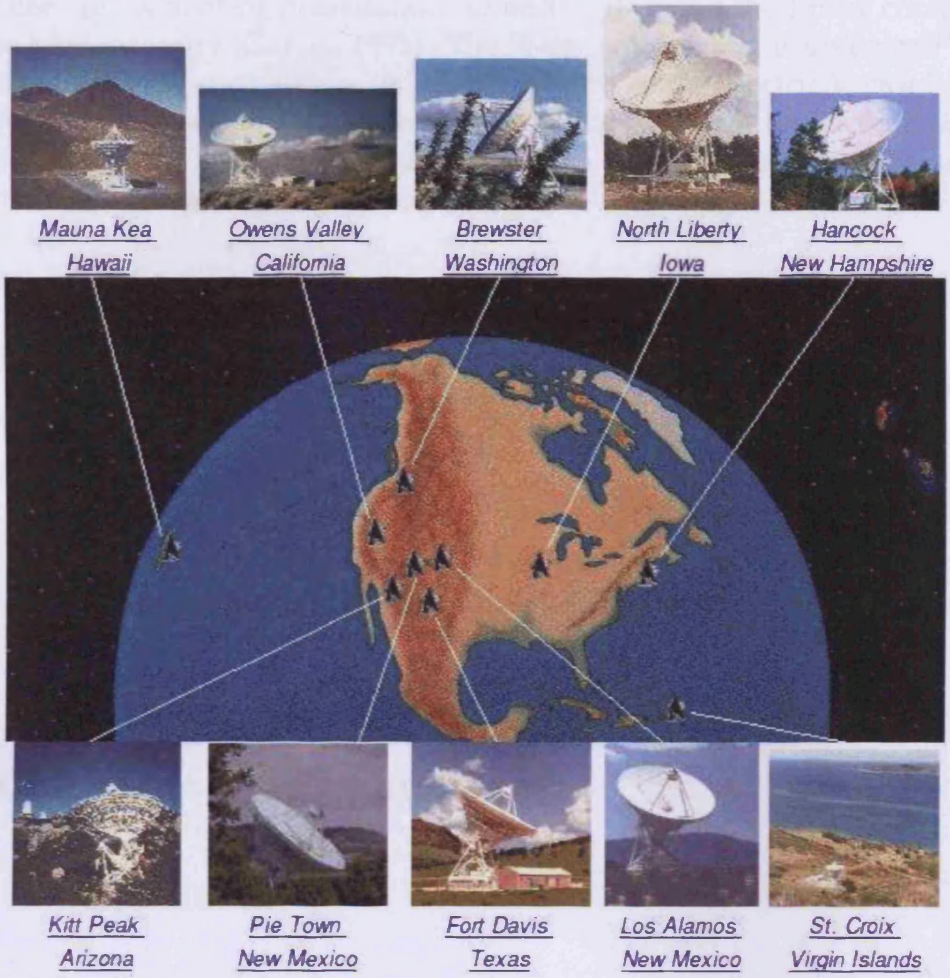

Figure 2.4: The constituent antennas of the VLBA (image taken from www.vlba.nrao.edu/sites).

signals pass to the polarisers (waveguide devices) that produce outputs corresponding to opposite circularly polarised components (Thompson, 1995). Circular feed correlators can produce four cross correlations. The time averaged expressions are shown below (Burke and Graham-Smith, 2002) in terms of the Stokes parameters.

$$\langle RR^* \rangle = I + V \tag{2.7}$$

$$\langle RL^* \rangle = Q + iU \tag{2.8}$$

$$\langle LR^* \rangle = Q - iU \tag{2.9}$$

$$\langle LL^* \rangle = I - V \tag{2.10}$$

With these equations laid out, it is appropriate to explain the significance of each of Stokes parameters. These are used to describe polarised radiation. V essentially demonstrates

the circular component of polarisation, Q and U describe the linear component and I gives the total intensity (Garcia, 1995). The linear polarisation is given as $P = Q + iU = mIe^{2i\chi}$ where m is the percentage polarisation and χ is the Electric Vector Position Angle or EVPA. For polarised radiation, this is the plane in which the electric field lies. It is perpendicular to the plane of the magnetic field. The polarised flux density, p and the EVPA are therefore given as follows:

$$p = mI = \sqrt{Q^2 + U^2} \tag{2.11}$$

$$\chi = \frac{1}{2} tan^{-1} \frac{U}{Q} \tag{2.12}$$

The RR and LL cross-correlations provide information on the total intensity for a source, I. Polarisation information (in the form of data for Stokes parameters Q and U) for each source is provided by RL and LR cross-correlations.

2.7 Calibration for Imaging

2.7.1 Initial Calibration

Initial Amplitude Calibration:

It is necessary to perform an initial amplitude calibration since the measured correlation coefficients are in arbitrary units. To convert to a unit such as Jy the following expression may be utilised for the correlated flux density on baseline i-j, S_{cij} (Walker, 2004):

$$S_{cij} = \rho \frac{A}{\eta_s} \sqrt{\frac{T_{si} T_{sj}}{K_i K_j e^{-\tau_i} e^{-\tau_j}}} \tag{2.13}$$

The measured coefficients from the correlators are given as ρ here. A is a correlator specific scaling factor. η_s represents the system efficiency. T_s represents the system temperature at an antenna. K is the gain in units of degrees Kelvin per Jansky. This incorporates the antenna gain curve, which gives the distortion of the antenna due to gravity as a function of elevation. $e^{-\tau_j}$ indicates absorption in the atmosphere.

Fringe Fitting:

Instrumental frequency phase offsets can create slopes in phase within each of the IFs (intermediate frequencies).[1] This can present a problem when it comes to averaging. To avoid cancellation of phases during frequency and time averaging it is necessary to remove slopes in phase with a fringe fit.

[1] Intermediate frequencies allow the interferometers to observe a range of frequencies. For the observations in this work there were four IFs in operation at and just above 43GHz. IFs are utilised in VLBI in order to increase the bandwidth of observation. This in turn yields greater sensitivity.

After the first fringe fit, phases can be flat within the IFs but disjointed between them due to atmospheric effects. Before averaging, this must also be corrected for with another fringe fit.

2.7.2 EVPA Calibration

The EVPA is calculated from Stokes Q and U parameters as follows:

$$EVPA, \chi = \frac{1}{2} arctan \frac{U}{Q} \tag{2.14}$$

A final step in the imaging of VLBI sources is a correction for an rotation in the EVPAs that applies to all images made. Prior to this step, all EVPAs will be correct relative to each other, but will be rotated by a fixed amount that must be calculated and corrected for (assuming the correction is not zero).

The EVPA rotation arises due to a difference in phase at the reference antenna. This phase difference is between the right and left hand gains and can be denoted as θ. The EVPA rotation is then equal to $\theta/2$.

There are a number of ways to tackle this calibration issue:

1. Integrated polarisation position angle comparison with the Very Large Array (VLA). The integrated EVPA along a source should be the same as the EVPA as measured by the VLA, a lower resolution instrument. Observation times need to be as consistent as possible in this comparison. The EVPAs of many Blazars can be variable on timescales as short as (or shorter than) days.

2. The EVPA of fairly stable components in sources. This is a comparison with the source observed in other epochs. Some sources contain components with EVPAs that are more or less stable of multiple epochs of observation. At the time of imaging, 0954+658 and 1730-130 were examples of sources that contained such components.

3. Core-dominated polarisation sources. For sources where the polarisation is sufficiently compact, it is possible to make a direct EVPA comparison with the VLA to check for a correction. Again, the same considerations on observation times are necessary. Examples at the time of imaging were 0420-014 and OJ287.

Analyses of the EVPA correction required for the August and November 2007, as well as the January 2008 epochs were undertaken. It was decided that no correction to EVPAs was necessary for any of the three epochs after this analysis.

2.7.3 Instrumental Polarisation

The VLBA utilises circularly polarised feeds. There will be some degree of leakage between the feeds. This means that right circular polarisation (RCP) can contaminate the

left circular polarisation (LCP) feed and vice versa. Polarisation leakage will corrupt any polarisation maps that are made unless it is dealt with.There will be an effect upon the total intensity image, but this will not be as significant.

It is possible to deal with the instrumental polarisation by consideration of D-terms. The voltages at the RCP and LCP feeds can be expressed as follows:

$$V_R = G_R(E_R e^{-i\phi} + D_R E_L e^{i\phi}) \tag{2.15}$$

$$V_L = G_L(E_L e^{i\phi} + D_L E_R e^{-i\phi}) \tag{2.16}$$

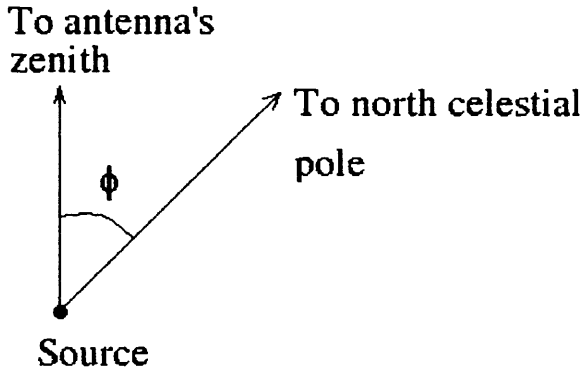

Figure 2.5: Geometric demonstration of the parallactic angle.

The G terms are gains for the RCP and LCP feeds, which may be determined by self-calibration. ϕ indicates the parallactic angles. These describe the rotation of the feeds of an altitude-azimuth telescope relative to a source that is tracked across the sky. A geometrical appreciation of the parallactic angle is given in Figure 2.5.

The RL and LR correlations complete with D-terms can be shown as:

$$R_i L_j^* = G_{Ri} G_{Lj}^* [P + I(D_{Lj}^* e^{2i\phi_j} + D_{Ri} e^{2i\phi_i})] \tag{2.17}$$

$$L_i R_j^* = G_{Li} G_{Rj}^* [P + I(D_{Rj}^* e^{-2i\phi_j} + D_{Li} e^{-2i\phi_i})] \tag{2.18}$$

The above expressions are valid for small D-term values of a few percent or less. Given a good range of parallactic angles it is possible to determine the D-terms. Clean components analysis can be performed whereby jet components are identified within a defined perimeter. In these regions it is assumed that the polarisation is constant. This is a fairly safe assumption to make across a jet component. In implementing this procedure, equations containing the D-terms can be constrained. This allows calculation of the D-terms themselves.

Chapter 3

Results

3.1 Source List

The source list given was part of a long term blazar monitoring scheme undertaken by the Boston University Blazar Group. Long term observation is important for Blazar study in order to investigate their typical behaviours (Hovatta et al., 2008).

Data was analysed for the following sources: 0235+164, 0336-019, 0420-014, 0528+134, 0716+714, 0735+178, 0827+243, 0829+046, 0836+710, 0954+658, 1127-145, 1156+295, 1219+285, 1222+216, 1406-076, 1510-089, 1611+343, 1622-297, 1633+382, 1730-130, 3C111, 3C273, 3C279, 3C345, 3C446, 3C454.3, BL Lac, CTA102 and OJ287.

3.2 Observational Details

For the 43GHz observations on the 6th August 2007, the 1st November 2007 and the 17th January 2008 I include a log of the observational scans of the sources studied. The log gives time ranges for the scans of each source along with other information.

3.2.1 August 2007 Epoch

Scan summary listing

Scan	Source	Qual	Calcode	Sub	Timerange	FrqID	START
1	0235+164	: 0000	V	1	0/10:14:25 - 0/10:19:08	1	1
2	3C446	: 0000	V	1	0/10:19:12 - 0/10:24:08	1	7215
3	CTA102	: 0000	V	1	0/10:24:12 - 0/10:29:06	1	15025
4	3C454.3	: 0000	V	1	0/10:29:10 - 0/10:34:05	1	22780
5	0235+164	: 0000	V	1	0/10:34:10 - 0/10:39:07	1	30588
6	0336-019	: 0000	V	1	0/10:39:10 - 0/10:44:03	1	38391
7	0420-014	: 0000	V	1	0/10:44:07 - 0/10:49:03	1	44737
8	3C111	: 0000		1	0/10:49:07 - 0/10:54:01	1	51127
9	BLLAC	: 0000	V	1	0/10:54:05 - 0/10:59:01	1	58782
10	3C446	: 0000	V	1	0/10:59:05 - 0/11:04:01	1	66592
11	CTA102	: 0000	V	1	0/11:04:05 - 0/11:09:01	1	74142
12	3C454.3	: 0000	V	1	0/11:09:05 - 0/11:13:58	1	81802
13	0235+164	: 0000	V	1	0/11:14:03 - 0/11:18:58	1	89557
14	0336-019	: 0000	V	1	0/11:19:02 - 0/11:23:56	1	97367
15	3C111	: 0000		1	0/11:24:00 - 0/11:28:58	1	105122
16	0420-014	: 0000	V	1	0/11:29:00 - 0/11:34:00	1	112931
17	BLLAC	: 0000	V	1	0/11:35:05 - 0/11:39:57	1	119359
18	3C446	: 0000	V	1	0/11:39:59 - 0/11:44:54	1	126578
19	CTA102	: 0000	V	1	0/11:44:59 - 0/11:49:52	1	132735
20	3C454.3	: 0000	V	1	0/11:49:56 - 0/11:54:52	1	140390
21	0235+164	: 0000	V	1	0/11:54:56 - 0/11:59:52	1	148200
22	0336-019	: 0000	V	1	0/11:59:56 - 0/12:04:52	1	156000
23	3C111	: 0000		1	0/12:04:56 - 0/12:09:50	1	163810
24	0420-014	: 0000	V	1	0/12:10:13 - 0/12:14:52	1	171552
25	0528+134	: 0000	V	1	0/12:14:54 - 0/12:19:49	1	178698
26	BLLAC	: 0000	V	1	0/12:19:51 - 0/12:24:49	1	185041
27	3C446	: 0000	V	1	0/12:24:51 - 0/12:29:47	1	191353
28	CTA102	: 0000	V	1	0/12:29:51 - 0/12:34:47	1	196466
29	3C454.3	: 0000	V	1	0/12:34:51 - 0/12:39:45	1	202784
30	0235+164	: 0000	V	1	0/12:39:49 - 0/12:44:45	1	209129
31	0336-019	: 0000	V	1	0/12:44:49 - 0/12:49:42	1	216839
32	3C111	: 0000		1	0/12:49:47 - 0/12:54:42	1	224594
33	0420-014	: 0000	V	1	0/12:54:47 - 0/12:59:42	1	232404
34	0528+134	: 0000	V	1	0/12:59:46 - 0/13:04:40	1	240214

Figure 3.1: Log of the August 2007 observation details.

Scan	Source	Qual	Calcode	Sub	Timerange	FrqID	START
35	0716+714	: 0000	V	1	0/13:04:44 - 0/13:09:42	1	247969
36	0735+178	: 0000	V	1	0/13:09:44 - 0/13:14:40	1	255773
37	0827+243	: 0000	V	1	0/13:14:44 - 0/13:19:40	1	262163
38	0829+046	: 0000	V	1	0/13:19:42 - 0/13:24:37	1	268505
39	0235+164	: 0000	V	1	0/13:24:42 - 0/13:29:37	1	272539
40	0336-019	: 0000	V	1	0/13:29:42 - 0/13:34:35	1	279790
41	3C111	: 0000		1	0/13:34:39 - 0/13:39:35	1	287540
42	0420-014	: 0000	V	1	0/13:39:39 - 0/13:44:33	1	295350
43	0528+134	: 0000	V	1	0/13:44:37 - 0/13:49:33	1	303105
44	0716+714	: 0000	V	1	0/13:49:37 - 0/13:54:35	1	310915
45	BLLAC	: 0000	V	1	0/13:54:37 - 0/13:59:35	1	318720
46	3C454.3	: 0000	V	1	0/13:59:37 - 0/14:04:30	1	325105
47	0235+164	: 0000	V	1	0/14:04:35 - 0/14:09:30	1	330181
48	0336-019	: 0000	V	1	0/14:10:00 - 0/14:14:28	1	337767
49	3C111	: 0000		1	0/14:14:32 - 0/14:19:28	1	344860
50	0420-014	: 0000	V	1	0/14:19:32 - 0/14:24:28	1	352670
51	0528+134	: 0000	V	1	0/14:24:32 - 0/14:29:30	1	360480
52	0735+178	: 0000	V	1	0/14:29:32 - 0/14:34:26	1	368282
53	0827+243	: 0000	V	1	0/14:34:30 - 0/14:39:25	1	374627
54	0829+046	: 0000	V	1	0/14:39:30 - 0/14:44:23	1	381017
55	0954+658	: 0000	V	1	0/14:44:27 - 0/14:49:27	1	387360
56	0235+164	: 0000	V	1	0/14:50:32 - 0/14:55:24	1	395160
57	0336-019	: 0000	V	1	0/14:55:28 - 0/15:00:22	1	402427
58	3C111	: 0000		1	0/15:00:26 - 0/15:05:21	1	410182
59	0420-014	: 0000	V	1	0/15:05:26 - 0/15:10:19	1	417992
60	0528+134	: 0000	V	1	0/15:10:23 - 0/15:15:19	1	425747
61	0716+714	: 0000	V	1	0/15:15:23 - 0/15:20:19	1	433557
62	0735+178	: 0000	V	1	0/15:20:23 - 0/15:25:19	1	441367
63	0829+046	: 0000	V	1	0/15:25:21 - 0/15:30:17	1	449121
64	0827+243	: 0000	V	1	0/15:30:21 - 0/15:35:17	1	455512
65	0836+710	: 0000	V	1	0/15:35:21 - 0/15:40:14	1	463222
66	0954+658	: 0000	V	1	0/15:40:19 - 0/15:45:16	1	470977
67	OJ287	: 0000	V	1	0/15:45:19 - 0/15:50:14	1	478780
68	0235+164	: 0000	V	1	0/15:50:18 - 0/15:55:12	1	485171
69	0336-019	: 0000	V	1	0/15:55:16 - 0/16:00:12	1	492816
70	3C111	: 0000		1	0/16:00:16 - 0/16:05:12	1	500626
71	0420-014	: 0000	V	1	0/16:05:16 - 0/16:10:10	1	508436

Figure 3.2: Log of the August 2007 observation details.

Scan	Source	Qual	Calcode	Sub	Timerange		FrqID	START
72	0528+134	: 0000	V	1	0/16:10:39 -	0/16:15:09	1	516178
73	0716+714	: 0000	V	1	0/16:15:14 -	0/16:20:09	1	523258
74	0735+178	: 0000	V	1	0/16:20:14 -	0/16:25:07	1	531068
75	0829+046	: 0000	V	1	0/16:25:11 -	0/16:30:07	1	538823
76	0827+243	: 0000	V	1	0/16:30:11 -	0/16:35:05	1	546633
77	0836+710	: 0000	V	1	0/16:35:09 -	0/16:40:05	1	554388
78	0954+658	: 0000	V	1	0/16:40:09 -	0/16:45:05	1	562198
79	OJ287	: 0000	V	1	0/16:45:09 -	0/16:50:07	1	570008
80	1156+295	: 0000	V	1	0/16:50:09 -	0/16:55:02	1	577810
81	1219+285	: 0000	V	1	0/16:55:07 -	0/17:00:02	1	584155
82	1222+216	: 0000	V	1	0/17:00:06 -	0/17:05:04	1	590545
83	3C111	: 0000		1	0/17:06:11 -	0/17:11:01	1	596971
84	0528+134	: 0000	V	1	0/17:11:05 -	0/17:16:01	1	604224
85	0716+714	: 0000	V	1	0/17:16:05 -	0/17:20:58	1	612034
86	0735+178	: 0000	V	1	0/17:21:03 -	0/17:25:58	1	619786
87	0829+046	: 0000	V	1	0/17:26:03 -	0/17:30:56	1	627596
88	0827+243	: 0000	V	1	0/17:31:00 -	0/17:35:56	1	635351
89	0836+710	: 0000	V	1	0/17:36:00 -	0/17:40:56	1	643161
90	0954+658	: 0000	V	1	0/17:41:00 -	0/17:45:56	1	650962
91	OJ287	: 0000	V	1	0/17:46:00 -	0/17:50:54	1	658772
92	3C111	: 0000		1	0/17:50:58 -	0/17:55:53	1	666527
93	0528+134	: 0000	V	1	0/17:55:58 -	0/18:00:51	1	674337
94	0716+714	: 0000	V	1	0/18:00:55 -	0/18:05:51	1	682092
95	0735+178	: 0000	V	1	0/18:05:55 -	0/18:10:51	1	689902
96	0829+046	: 0000	V	1	0/18:11:20 -	0/18:15:49	1	697685
97	0827+243	: 0000	V	1	0/18:15:53 -	0/18:20:49	1	704770
98	0836+710	: 0000	V	1	0/18:20:53 -	0/18:25:51	1	712580
99	1127-145	: 0000	V	1	0/18:25:53 -	0/18:30:46	1	720382
100	3C273	: 0000	V	1	0/18:30:51 -	0/18:35:46	1	726727
101	OJ287	: 0000	V	1	0/18:35:51 -	0/18:40:46	1	733117
102	0716+714	: 0000	V	1	0/18:40:50 -	0/18:45:44	1	740827
103	0954+658	: 0000	V	1	0/18:45:48 -	0/18:50:46	1	748582
104	1127-145	: 0000	V	1	0/18:50:48 -	0/18:55:44	1	756383
105	1156+295	: 0000	V	1	0/18:55:48 -	0/19:00:44	1	762774
106	1219+285	: 0000	V	1	0/19:00:46 -	0/19:05:42	1	770445
107	1222+216	: 0000	V	1	0/19:05:46 -	0/19:10:41	1	776836
108	3C273	: 0000	V	1	0/19:10:46 -	0/19:15:39	1	783226

Figure 3.3: Log of the August 2007 observation details.

Scan	Source	Qual	Calcode	Sub	Timerange	FrqID	START
109	3C279	: 0000	V	1	0/19:15:43 - 0/19:19:40	1	789571
110	1406-076	: 0000	V	1	0/19:19:42 - 0/19:24:38	1	794656
111	1127-145	: 0000	V	1	0/19:24:42 - 0/19:29:42	1	798635
112	3C111	: 0000		1	0/19:30:47 - 0/19:35:37	1	806216
113	0528+134	: 0000	V	1	0/19:35:41 - 0/19:40:37	1	812126
114	0735+178	: 0000	V	1	0/19:40:41 - 0/19:45:34	1	818516
115	0829+046	: 0000	V	1	0/19:45:39 - 0/19:50:34	1	826171
116	0827+243	: 0000	V	1	0/19:50:38 - 0/19:55:32	1	833981
117	OJ287	: 0000	V	1	0/19:55:36 - 0/20:00:32	1	841736
118	0836+710	: 0000	V	1	0/20:00:36 - 0/20:05:32	1	849546
119	0716+714	: 0000	V	1	0/20:05:36 - 0/20:10:32	1	857356
120	0735+178	: 0000	V	1	0/20:10:59 - 0/20:15:30	1	865118
121	0829+046	: 0000	V	1	0/20:15:34 - 0/20:20:29	1	872235
122	0827+243	: 0000	V	1	0/20:20:34 - 0/20:25:27	1	878625
123	OJ287	: 0000	V	1	0/20:25:31 - 0/20:30:27	1	884966
124	0836+710	: 0000	V	1	0/20:30:31 - 0/20:35:27	1	891354
125	0954+658	: 0000	V	1	0/20:35:31 - 0/20:40:27	1	897744
126	1127-145	: 0000	V	1	0/20:40:31 - 0/20:45:25	1	904134
127	1156+295	: 0000	V	1	0/20:45:29 - 0/20:50:25	1	910479
128	1219+285	: 0000	V	1	0/20:50:29 - 0/20:55:24	1	916869
129	1222+216	: 0000	V	1	0/20:55:29 - 0/21:00:22	1	923259
130	3C273	: 0000	V	1	0/21:00:26 - 0/21:05:22	1	929604
131	3C279	: 0000	V	1	0/21:05:26 - 0/21:10:22	1	935994
132	1406-076	: 0000	V	1	0/21:10:24 - 0/21:15:20	1	942338
133	0716+714	: 0000	V	1	0/21:15:24 - 0/21:20:22	1	947451
134	0735+178	: 0000	V	1	0/21:20:24 - 0/21:25:20	1	953735
135	0829+046	: 0000	V	1	0/21:25:24 - 0/21:30:17	1	958847
136	0827+243	: 0000	V	1	0/21:30:22 - 0/21:35:17	1	965102
137	OJ287	: 0000	V	1	0/21:35:22 - 0/21:40:15	1	971492
138	0836+710	: 0000	V	1	0/21:40:19 - 0/21:45:15	1	977837
139	0954+658	: 0000	V	1	0/21:45:19 - 0/21:50:15	1	984215
140	1127-145	: 0000	V	1	0/21:50:19 - 0/21:55:15	1	990605
141	1156+295	: 0000	V	1	0/21:55:19 - 0/22:00:13	1	996995
142	1219+285	: 0000	V	1	0/22:00:17 - 0/22:05:12	1	1003340
143	1222+216	: 0000	V	1	0/22:05:17 - 0/22:10:10	1	1009730
144	3C273	: 0000	V	1	0/22:10:40 - 0/22:15:10	1	1016070
145	3C279	: 0000	V	1	0/22:15:14 - 0/22:20:10	1	1021890

Figure 3.4: Log of the August 2007 observation details.

Scan	Source	Qual	Calcode	Sub	Timerange	FrqID	START
146	1406-076	: 0000	V	1	0/22:20:14 - 0/22:25:12	1	1028280
147	OJ287	: 0000	V	1	0/22:26:19 - 0/22:31:09	1	1034715
148	0836+710	: 0000	V	1	0/22:31:13 - 0/22:36:06	1	1040378
149	0954+658	: 0000	V	1	0/22:36:11 - 0/22:41:06	1	1046723
150	1127-145	: 0000	V	1	0/22:41:10 - 0/22:46:04	1	1053113
151	1156+295	: 0000	V	1	0/22:46:08 - 0/22:51:04	1	1059458
152	1219+285	: 0000	V	1	0/22:51:08 - 0/22:56:04	1	1065848
153	1222+216	: 0000	V	1	0/22:56:08 - 0/23:01:04	1	1072238
154	3C273	: 0000	V	1	0/23:01:08 - 0/23:06:02	1	1078628
155	3C279	: 0000	V	1	0/23:06:06 - 0/23:11:01	1	1085451
156	1406-076	: 0000	V	1	0/23:11:06 - 0/23:15:59	1	1093241
157	1510-089	: 0000	V	1	0/23:16:03 - 0/23:20:59	1	1100996
158	1611+343	: 0000	V	1	0/23:21:03 - 0/23:25:59	1	1108806
159	1633+382	: 0000	V	1	0/23:26:03 - 0/23:30:59	1	1116616
160	3C345	: 0000	V	1	0/23:31:03 - 0/23:35:59	1	1124426
161	OJ287	: 0000	V	1	0/23:36:01 - 0/23:40:57	1	1132176
162	0836+710	: 0000	V	1	0/23:41:01 - 0/23:45:54	1	1138566
163	0954+658	: 0000	V	1	0/23:45:59 - 0/23:50:54	1	1146211
164	1127-145	: 0000	V	1	0/23:50:58 - 0/23:55:54	1	1154021
165	1156+295	: 0000	V	1	0/23:55:58 - 1/00:00:53	1	1161831
166	1219+285	: 0000	V	1	1/00:01:23 - 1/00:05:51	1	1168770
167	1222+216	: 0000	V	1	1/00:06:12 - 1/00:10:51	1	1175777
168	3C273	: 0000	V	1	1/00:10:55 - 1/00:15:51	1	1182933
169	3C279	: 0000	V	1	1/00:15:55 - 1/00:20:51	1	1190743
170	1406-076	: 0000	V	1	1/00:20:55 - 1/00:25:49	1	1198553
171	1510-089	: 0000	V	1	1/00:25:53 - 1/00:30:49	1	1206308
172	1611+343	: 0000	V	1	1/00:30:53 - 1/00:35:46	1	1214118
173	1633+382	: 0000	V	1	1/00:35:51 - 1/00:40:46	1	1221873
174	3C345	: 0000	V	1	1/00:40:51 - 1/00:45:46	1	1229683
175	1622-297	: 0000	V	1	1/00:45:50 - 1/00:50:48	1	1237493
176	1127-145	: 0000	V	1	1/00:51:55 - 1/00:56:45	1	1245288
177	1156+295	: 0000	V	1	1/00:56:49 - 1/01:01:43	1	1250080
178	1219+285	: 0000	V	1	1/01:01:47 - 1/01:06:42	1	1257654
179	1222+216	: 0000	V	1	1/01:06:47 - 1/01:11:40	1	1265464
180	3C273	: 0000	V	1	1/01:11:44 - 1/01:16:40	1	1273219
181	3C279	: 0000	V	1	1/01:16:44 - 1/01:21:40	1	1281029
182	1406-076	: 0000	V	1	1/01:21:44 - 1/01:26:40	1	1288839

Figure 3.5: Log of the August 2007 observation details.

Scan	Source	Qual	Calcode	Sub	Timerange			FrqID	START
183	1510-089	: 0000	V	1	1/01:26:44	-	1/01:31:38	1	1296649
184	1611+343	: 0000	V	1	1/01:31:42	-	1/01:36:38	1	1304404
185	1633+382	: 0000	V	1	1/01:36:42	-	1/01:41:35	1	1312214
186	3C345	: 0000	V	1	1/01:41:40	-	1/01:46:35	1	1319969
187	1622-297	: 0000	V	1	1/01:46:39	-	1/01:51:35	1	1327779
188	1730-130	: 0000	V	1	1/01:51:39	-	1/01:56:35	1	1335589
189	1156+295	: 0000	V	1	1/01:56:37	-	1/02:01:33	1	1343342
190	1219+285	: 0000	V	1	1/02:01:37	-	1/02:06:33	1	1349733
191	1222+216	: 0000	V	1	1/02:07:00	-	1/02:11:33	1	1357385
192	3C273	: 0000	V	1	1/02:11:37	-	1/02:16:30	1	1363250
193	3C279	: 0000	V	1	1/02:16:35	-	1/02:21:30	1	1368326
194	1406-076	: 0000	V	1	1/02:21:35	-	1/02:26:28	1	1373438
195	1510-089	: 0000	V	1	1/02:26:32	-	1/02:31:28	1	1380991
196	1611+343	: 0000	V	1	1/02:31:32	-	1/02:36:28	1	1388801
197	1633+382	: 0000	V	1	1/02:36:32	-	1/02:41:28	1	1396611
198	3C345	: 0000	V	1	1/02:41:32	-	1/02:46:26	1	1404421
199	1622-297	: 0000	V	1	1/02:46:30	-	1/02:51:25	1	1411186
200	1730-130	: 0000	V	1	1/02:51:30	-	1/02:56:27	1	1417570
201	3C279	: 0000	V	1	1/02:57:35	-	1/03:02:22	1	1423996
202	1406-076	: 0000	V	1	1/03:02:26	-	1/03:07:22	1	1428698
203	1510-089	: 0000	V	1	1/03:07:26	-	1/03:12:22	1	1434998
204	1611+343	: 0000	V	1	1/03:12:26	-	1/03:17:22	1	1441388
205	1633+382	: 0000	V	1	1/03:17:26	-	1/03:22:19	1	1447778
206	3C345	: 0000	V	1	1/03:22:24	-	1/03:27:19	1	1454121
207	1622-297	: 0000	V	1	1/03:27:49	-	1/03:32:17	1	1460484
208	1730-130	: 0000	V	1	1/03:32:21	-	1/03:37:17	1	1465840
209	3C279	: 0000	V	1	1/03:37:21	-	1/03:42:17	1	1472224
210	1406-076	: 0000	V	1	1/03:42:44	-	1/03:47:17	1	1476191
211	1510-089	: 0000	V	1	1/03:47:21	-	1/03:52:15	1	1480702
212	1611+343	: 0000	V	1	1/03:52:19	-	1/03:57:14	1	1486948
213	1633+382	: 0000	V	1	1/03:57:19	-	1/04:02:12	1	1493338
214	3C345	: 0000	V	1	1/04:02:16	-	1/04:07:14	1	1499683
215	1622-297	: 0000	V	1	1/04:07:16	-	1/04:12:12	1	1506072
216	1730-130	: 0000	V	1	1/04:12:16	-	1/04:17:14	1	1511185
217	BLLAC	: 0000	V	1	1/04:18:21	-	1/04:23:13	1	1517530
218	1510-089	: 0000	V	1	1/04:23:15	-	1/04:28:08	1	1523099
219	1611+343	: 0000	V	1	1/04:28:12	-	1/04:33:08	1	1528175

Figure 3.6: Log of the August 2007 observation details.

Scan	Source	Qual	Calcode	Sub	Timerange			FrqID	START
220	1633+382	: 0000	V	1	1/04:33:12	-	1/04:38:06	1	1534466
221	3C345	: 0000	V	1	1/04:38:35	-	1/04:43:08	1	1548790
222	1622-297	: 0000	V	1	1/04:43:10	-	1/04:48:06	1	1545760
223	1730-130	: 0000	V	1	1/04:48:10	-	1/04:53:06	1	1550873
224	BLLAC	: 0000	V	1	1/04:53:10	-	1/04:58:06	1	1557164
225	1510-089	: 0000	V	1	1/04:58:08	-	1/05:03:03	1	1563510
226	1611+343	: 0000	V	1	1/05:03:08	-	1/05:08:03	1	1568623
227	1633+382	: 0000	V	1	1/05:08:07	-	1/05:13:01	1	1574905
228	3C345	: 0000	V	1	1/05:13:28	-	1/05:18:05	1	1581229
229	1622-297	: 0000	V	1	1/05:18:07	-	1/05:23:01	1	1586475
230	1730-130	: 0000	V	1	1/05:23:05	-	1/05:27:59	1	1590423
231	BLLAC	: 0000	V	1	1/05:28:03	-	1/05:33:01	1	1596598
232	1510-089	: 0000	V	1	1/05:33:03	-	1/05:37:58	1	1602981
233	1611+343	: 0000	V	1	1/05:38:03	-	1/05:42:56	1	1606957
234	1633+382	: 0000	V	1	1/05:43:00	-	1/05:47:56	1	1613115
235	3C345	: 0000	V	1	1/05:48:00	-	1/05:52:58	1	1619505
236	1622-297	: 0000	V	1	1/05:53:00	-	1/05:57:54	1	1625884
237	1730-130	: 0000	V	1	1/05:57:58	-	1/06:02:54	1	1629832
238	BLLAC	: 0000	V	1	1/06:02:58	-	1/06:07:54	1	1636034
239	3C446	: 0000	V	1	1/06:09:17	-	1/06:13:52	1	1642391
240	CTA102	: 0000	V	1	1/06:13:56	-	1/06:18:50	1	1647328
241	3C454.3	: 0000	V	1	1/06:18:54	-	1/06:23:50	1	1653673
242	1611+343	: 0000	V	1	1/06:23:54	-	1/06:28:50	1	1660063
243	1633+382	: 0000	V	1	1/06:28:54	-	1/06:33:48	1	1666444
244	3C345	: 0000	V	1	1/06:33:52	-	1/06:38:50	1	1672789
245	1730-130	: 0000	V	1	1/06:38:52	-	1/06:43:47	1	1679180
246	BLLAC	: 0000	V	1	1/06:43:52	-	1/06:48:45	1	1684293
247	3C446	: 0000	V	1	1/06:48:49	-	1/06:53:45	1	1690620
248	CTA102	: 0000	V	1	1/06:53:49	-	1/06:58:45	1	1697010
249	3C454.3	: 0000	V	1	1/06:58:49	-	1/07:03:45	1	1703400
250	1611+343	: 0000	V	1	1/07:03:49	-	1/07:08:43	1	1709790
251	1633+382	: 0000	V	1	1/07:08:47	-	1/07:13:42	1	1716135
252	3C345	: 0000	V	1	1/07:13:47	-	1/07:18:42	1	1722525
253	1730-130	: 0000	V	1	1/07:18:45	-	1/07:23:40	1	1728871
254	BLLAC	: 0000	V	1	1/07:23:44	-	1/07:28:38	1	1733984
255	3C446	: 0000	V	1	1/07:28:42	-	1/07:33:38	1	1740230
256	CTA102	: 0000	V	1	1/07:33:42	-	1/07:38:38	1	1746620

Figure 3.7: Log of the August 2007 observation details.

Scan	Source	Qual	Calcode	Sub	Timerange			FrqID	START
257	3C454.3	: 0000	V	1	1/07:38:42	-	1/07:43:38	1	1753010
258	1611+343	: 0000	V	1	1/07:43:42	-	1/07:48:35	1	1759400
259	1633+382	: 0000	V	1	1/07:48:40	-	1/07:53:40	1	1765745
260	3C345	: 0000	V	1	1/07:54:59	-	1/07:59:36	1	1772183
261	1730-130	: 0000	V	1	1/07:59:38	-	1/08:04:34	1	1778069
262	BLLAC	: 0000	V	1	1/08:04:38	-	1/08:09:34	1	1782045
263	3C446	: 0000	V	1	1/08:10:01	-	1/08:14:32	1	1788345
264	CTA102	: 0000	V	1	1/08:14:36	-	1/08:19:31	1	1794160
265	3C454.3	: 0000	V	1	1/08:19:36	-	1/08:24:31	1	1800550
266	0235+164	: 0000	V	1	1/08:24:33	-	1/08:29:29	1	1806893
267	3C345	: 0000	V	1	1/08:29:33	-	1/08:34:29	1	1812006
268	BLLAC	: 0000	V	1	1/08:34:33	-	1/08:39:29	1	1818306
269	3C446	: 0000	V	1	1/08:39:33	-	1/08:44:27	1	1824696
270	CTA102	: 0000	V	1	1/08:44:31	-	1/08:49:27	1	1831041
271	3C454.3	: 0000	V	1	1/08:49:31	-	1/08:54:26	1	1837431
272	0235+164	: 0000	V	1	1/08:54:29	-	1/08:59:28	1	1843773
273	BLLAC	: 0000	V	1	1/09:00:33	-	1/09:05:23	1	1848958
274	3C446	: 0000	V	1	1/09:05:27	-	1/09:10:23	1	1854961
275	CTA102	: 0000	V	1	1/09:10:27	-	1/09:15:23	1	1861351
276	3C454.3	: 0000	V	1	1/09:15:27	-	1/09:20:23	1	1867741
277	0235+164	: 0000	V	1	1/09:20:25	-	1/09:25:20	1	1874083
278	3C446	: 0000	V	1	1/09:25:25	-	1/09:30:18	1	1879195
279	CTA102	: 0000	V	1	1/09:30:22	-	1/09:35:18	1	1885450
280	3C454.3	: 0000	V	1	1/09:35:22	-	1/09:39:49	1	1891840
281	0235+164	: 0000	V	1	1/09:39:53	-	1/09:44:46	1	1897600
282	0336-019	: 0000	V	1	1/09:44:51	-	1/09:49:46	1	1902675
283	0420-014	: 0000	V	1	1/09:49:50	-	1/09:54:44	1	1907787
284	BLLAC	: 0000	V	1	1/09:54:48	-	1/09:59:44	1	1912863
285	3C446	: 0000	V	1	1/09:59:48	-	1/10:04:44	1	1919146
286	CTA102	: 0000	V	1	1/10:04:48	-	1/10:09:44	1	1925368
287	3C454.3	: 0000	V	1	1/10:09:48	-	1/10:14:12	1	1931758

Figure 3.8: Log of the August 2007 observation details.

3.2.2 November 2007 Epoch

Scan summary listing

Scan	Source	Qual	Calcode	Sub	Timerange	FrqID	START
1	0235+164	: 0000	V	1	0/04:32:20 - 0/04:37:03	1	1
2	3C446	: 0000	V	1	0/04:37:07 - 0/04:42:03	1	5840
3	CTA102	: 0000	V	1	0/04:42:07 - 0/04:47:03	1	12221
4	3C454.3	: 0000	V	1	0/04:47:07 - 0/04:52:01	1	18611
5	0235+164	: 0000	V	1	0/04:52:05 - 0/04:57:03	1	24956
6	0336-019	: 0000	V	1	0/04:57:05 - 0/05:02:00	1	31347
7	0420-014	: 0000	V	1	0/05:02:05 - 0/05:06:58	1	36460
8	3C111	: 0000		1	0/05:07:02 - 0/05:11:58	1	41536
9	BLLAC	: 0000	V	1	0/05:12:02 - 0/05:16:56	1	47674
10	3C446	: 0000	V	1	0/05:17:00 - 0/05:21:58	1	54019
11	CTA102	: 0000	V	1	0/05:22:02 - 0/05:26:56	1	60454
12	3C454.3	: 0000	V	1	0/05:27:00 - 0/05:31:56	1	66799
13	0235+164	: 0000	V	1	0/05:32:00 - 0/05:36:53	1	73189
14	0336-019	: 0000	V	1	0/05:36:58 - 0/05:41:53	1	79528
15	3C111	: 0000		1	0/05:41:57 - 0/05:46:53	1	85918
16	0420-014	: 0000	V	1	0/05:46:55 - 0/05:51:55	1	92264
17	BLLAC	: 0000	V	1	0/05:53:02 - 0/05:57:52	1	97426
18	3C446	: 0000	V	1	0/05:57:56 - 0/06:02:49	1	103373
19	CTA102	: 0000	V	1	0/06:02:54 - 0/06:07:49	1	109502
20	3C454.3	: 0000	V	1	0/06:07:54 - 0/06:12:47	1	115892
21	0235+164	: 0000	V	1	0/06:12:51 - 0/06:17:47	1	122237
22	0336-019	: 0000	V	1	0/06:17:51 - 0/06:22:47	1	128627
23	3C111	: 0000		1	0/06:22:51 - 0/06:27:47	1	135017
24	0420-014	: 0000	V	1	0/06:28:16 - 0/06:32:47	1	141368
25	0528+134	: 0000	V	1	0/06:32:49 - 0/06:37:45	1	147130
26	BLLAC	: 0000	V	1	0/06:37:49 - 0/06:42:44	1	152131
27	3C446	: 0000	V	1	0/06:42:47 - 0/06:47:42	1	158450
28	CTA102	: 0000	V	1	0/06:47:46 - 0/06:52:42	1	163559
29	3C454.3	: 0000	V	1	0/06:52:46 - 0/06:57:40	1	169859
30	0235+164	: 0000	V	1	0/06:57:44 - 0/07:02:40	1	176204
31	0336-019	: 0000	V	1	0/07:02:44 - 0/07:07:40	1	182594
32	3C111	: 0000		1	0/07:07:44 - 0/07:12:38	1	188984
33	0420-014	: 0000	V	1	0/07:12:42 - 0/07:17:37	1	195329
34	0528+134	: 0000	V	1	0/07:17:42 - 0/07:22:37	1	201719

Figure 3.9: Log of the November 2007 observation details.

Scan	Source	Qual	Calcode	Sub	Timerange	FrqID	START
35	0716+714	: 0000	V	1	0/07:22:41 - 0/07:27:37	1	208109
36	0735+178	: 0000	V	1	0/07:27:39 - 0/07:32:35	1	214455
37	0827+243	: 0000	V	1	0/07:32:39 - 0/07:37:37	1	219568
38	0829+046	: 0000	V	1	0/07:37:39 - 0/07:42:33	1	224674
39	0235+164	: 0000	V	1	0/07:42:37 - 0/07:47:33	1	227747
40	0336-019	: 0000	V	1	0/07:47:37 - 0/07:52:32	1	234006
41	3C111	: 0000		1	0/07:52:37 - 0/07:57:30	1	240378
42	0420-014	: 0000	V	1	0/07:57:34 - 0/08:02:30	1	246723
43	0528+134	: 0000	V	1	0/08:02:34 - 0/08:07:28	1	253113
44	0716+714	: 0000	V	1	0/08:07:32 - 0/08:12:30	1	259458
45	BLLAC	: 0000	V	1	0/08:12:34 - 0/08:17:30	1	265857
46	3C454.3	: 0000	V	1	0/08:17:32 - 0/08:22:28	1	272198
47	0235+164	: 0000	V	1	0/08:22:32 - 0/08:27:25	1	277311
48	0336-019	: 0000	V	1	0/08:27:55 - 0/08:32:25	1	283565
49	3C111	: 0000		1	0/08:32:29 - 0/08:37:23	1	289275
50	0420-014	: 0000	V	1	0/08:37:27 - 0/08:42:23	1	295620
51	0528+134	: 0000	V	1	0/08:42:27 - 0/08:47:25	1	302010
52	0735+178	: 0000	V	1	0/08:47:27 - 0/08:52:23	1	308401
53	0827+243	: 0000	V	1	0/08:52:27 - 0/08:57:21	1	313514
54	0829+046	: 0000	V	1	0/08:57:25 - 0/09:02:20	1	318590
55	0954+658	: 0000	V	1	0/09:02:25 - 0/09:07:25	1	323702
56	0235+164	: 0000	V	1	0/09:08:27 - 0/09:13:19	1	330012
57	0336-019	: 0000	V	1	0/09:13:23 - 0/09:18:19	1	335971
58	3C111	: 0000		1	0/09:18:23 - 0/09:23:17	1	342361
59	0420-014	: 0000	V	1	0/09:23:21 - 0/09:28:17	1	348706
60	0528+134	: 0000	V	1	0/09:28:21 - 0/09:33:14	1	355096
61	0716+714	: 0000	V	1	0/09:33:42 - 0/09:38:14	1	361414
62	0735+178	: 0000	V	1	0/09:38:18 - 0/09:43:16	1	366455
63	0829+046	: 0000	V	1	0/09:43:18 - 0/09:48:12	1	372846
64	0827+243	: 0000	V	1	0/09:48:16 - 0/09:53:12	1	377922
65	0836+710	: 0000	V	1	0/09:53:16 - 0/09:58:12	1	384222
66	0954+658	: 0000	V	1	0/09:58:16 - 0/10:03:12	1	390612
67	OJ287	: 0000	V	1	0/10:03:14 - 0/10:08:09	1	396958
68	0235+164	: 0000	V	1	0/10:08:14 - 0/10:13:09	1	402071
69	0336-019	: 0000	V	1	0/10:13:13 - 0/10:18:07	1	408353
70	3C111	: 0000		1	0/10:18:11 - 0/10:23:07	1	414698
71	0420-014	: 0000	V	1	0/10:23:11 - 0/10:28:07	1	421088

Figure 3.10: Log of the November 2007 observation details.

Scan	Source	Qual	Calcode	Sub	Timerange	FrqID	START
72	0528+134	: 0000	V	1	0/10:28:11 - 0/10:33:05	1	427478
73	0716+714	: 0000	V	1	0/10:33:09 - 0/10:38:05	1	433823
74	0735+178	: 0000	V	1	0/10:38:09 - 0/10:43:04	1	440213
75	0829+046	: 0000	V	1	0/10:43:09 - 0/10:48:02	1	446603
76	0827+243	: 0000	V	1	0/10:48:06 - 0/10:53:02	1	452948
77	0836+710	: 0000	V	1	0/10:53:06 - 0/10:58:00	1	459338
78	0954+658	: 0000	V	1	0/10:58:04 - 0/11:03:02	1	465683
79	OJ287	: 0000	V	1	0/11:03:06 - 0/11:08:02	1	472118
80	1156+295	: 0000	V	1	0/11:08:04 - 0/11:13:00	1	478464
81	1219+285	: 0000	V	1	0/11:13:04 - 0/11:17:57	1	483577
82	1222+216	: 0000	V	1	0/11:18:02 - 0/11:23:01	1	488653
83	3C111	: 0000		1	0/11:24:09 - 0/11:28:56	1	493804
84	0528+134	: 0000	V	1	0/11:29:00 - 0/11:33:56	1	499699
85	0716+714	: 0000	V	1	0/11:34:25 - 0/11:38:56	1	506050
86	0735+178	: 0000	V	1	0/11:39:00 - 0/11:43:53	1	511900
87	0829+046	: 0000	V	1	0/11:43:58 - 0/11:48:53	1	518245
88	0827+243	: 0000	V	1	0/11:48:58 - 0/11:53:51	1	524635
89	0836+710	: 0000	V	1	0/11:53:55 - 0/11:58:51	1	530980
90	0954+658	: 0000	V	1	0/11:58:55 - 0/12:03:51	1	537370
91	OJ287	: 0000	V	1	0/12:03:55 - 0/12:08:51	1	543760
92	3C111	: 0000		1	0/12:08:55 - 0/12:13:49	1	550150
93	0528+134	: 0000	V	1	0/12:13:53 - 0/12:18:49	1	556495
94	0716+714	: 0000	V	1	0/12:18:53 - 0/12:23:46	1	562885
95	0735+178	: 0000	V	1	0/12:23:51 - 0/12:28:46	1	569230
96	0829+046	: 0000	V	1	0/12:28:50 - 0/12:33:46	1	575620
97	0827+243	: 0000	V	1	0/12:33:50 - 0/12:38:44	1	582010
98	0836+710	: 0000	V	1	0/12:38:48 - 0/12:43:46	1	588355
99	1127-145	: 0000	V	1	0/12:43:48 - 0/12:48:44	1	594746
100	3C273	: 0000	V	1	0/12:48:48 - 0/12:53:42	1	599858
101	OJ287	: 0000	V	1	0/12:53:46 - 0/12:58:41	1	604934
102	0716+714	: 0000	V	1	0/12:58:46 - 0/13:03:41	1	611234
103	0954+658	: 0000	V	1	0/13:03:45 - 0/13:08:41	1	617624
104	1127-145	: 0000	V	1	0/13:08:43 - 0/13:13:39	1	623970
105	1156+295	: 0000	V	1	0/13:13:43 - 0/13:18:39	1	629083
106	1219+285	: 0000	V	1	0/13:19:06 - 0/13:23:37	1	635353
107	1222+216	: 0000	V	1	0/13:23:41 - 0/13:28:37	1	640033
108	3C273	: 0000	V	1	0/13:28:41 - 0/13:33:36	1	645145

Figure 3.11: Log of the November 2007 observation details.

Scan	Source	Qual	Calcode	Sub	Timerange	FrqID	START
109	3C279	: 0000	V	1	0/13:33:41 - 0/13:37:38	1	650257
110	1406-076	: 0000	V	1	0/13:37:40 - 0/13:42:33	1	654317
111	1127-145	: 0000	V	1	0/13:42:38 - 0/13:47:37	1	657279
112	3C111	: 0000		1	0/13:48:42 - 0/13:53:32	1	663463
113	0528+134	: 0000	V	1	0/13:53:36 - 0/13:58:32	1	669393
114	0735+178	: 0000	V	1	0/13:58:36 - 0/14:03:32	1	675783
115	0829+046	: 0000	V	1	0/14:03:36 - 0/14:08:29	1	682173
116	0827+243	: 0000	V	1	0/14:08:34 - 0/14:13:29	1	688518
117	OJ287	: 0000	V	1	0/14:13:33 - 0/14:18:27	1	694872
118	0836+710	: 0000	V	1	0/14:18:31 - 0/14:23:27	1	701217
119	0716+714	: 0000	V	1	0/14:23:31 - 0/14:28:27	1	707607
120	0735+178	: 0000	V	1	0/14:28:31 - 0/14:33:27	1	713997
121	0829+046	: 0000	V	1	0/14:33:31 - 0/14:38:25	1	720387
122	0827+243	: 0000	V	1	0/14:38:29 - 0/14:43:24	1	726732
123	OJ287	: 0000	V	1	0/14:43:29 - 0/14:48:22	1	733122
124	0836+710	: 0000	V	1	0/14:48:26 - 0/14:53:22	1	739467
125	0954+658	: 0000	V	1	0/14:53:26 - 0/14:58:22	1	745857
126	1127-145	: 0000	V	1	0/14:58:26 - 0/15:03:22	1	752247
127	1156+295	: 0000	V	1	0/15:03:26 - 0/15:08:20	1	758637
128	1219+285	: 0000	V	1	0/15:08:24 - 0/15:13:20	1	764982
129	1222+216	: 0000	V	1	0/15:13:24 - 0/15:18:20	1	771372
130	3C273	: 0000	V	1	0/15:18:49 - 0/15:23:17	1	777729
131	3C279	: 0000	V	1	0/15:23:22 - 0/15:28:19	1	783418
132	1406-076	: 0000	V	1	0/15:28:21 - 0/15:33:15	1	789804
133	0716+714	: 0000	V	1	0/15:33:19 - 0/15:38:15	1	794880
134	0735+178	: 0000	V	1	0/15:38:19 - 0/15:43:15	1	801171
135	0829+046	: 0000	V	1	0/15:43:19 - 0/15:48:15	1	807561
136	0827+243	: 0000	V	1	0/15:48:19 - 0/15:53:12	1	813951
137	OJ287	: 0000	V	1	0/15:53:17 - 0/15:58:12	1	820296
138	0836+710	: 0000	V	1	0/15:58:17 - 0/16:03:10	1	826686
139	0954+658	: 0000	V	1	0/16:03:14 - 0/16:08:10	1	833031
140	1127-145	: 0000	V	1	0/16:08:14 - 0/16:13:10	1	839421
141	1156+295	: 0000	V	1	0/16:13:14 - 0/16:18:10	1	845811
142	1219+285	: 0000	V	1	0/16:18:14 - 0/16:23:08	1	852201
143	1222+216	: 0000	V	1	0/16:23:12 - 0/16:28:08	1	858546
144	3C273	: 0000	V	1	0/16:28:12 - 0/16:33:05	1	864936
145	3C279	: 0000	V	1	0/16:33:10 - 0/16:38:05	1	871281

Figure 3.12: Log of the November 2007 observation details.

Scan	Source	Qual	Calcode	Sub	Timerange		FrqID	START
146	1406-076	: 0000	V	1	0/16:38:09 -	0/16:43:09	1	877669
147	OJ287	: 0000	V	1	0/16:44:14 -	0/16:49:04	1	884096
148	0836+710	: 0000	V	1	0/16:49:08 -	0/16:54:04	1	890039
149	0954+658	: 0000	V	1	0/16:54:08 -	0/16:59:01	1	896429
150	1127-145	: 0000	V	1	0/16:59:06 -	0/17:04:01	1	902774
151	1156+295	: 0000	V	1	0/17:04:06 -	0/17:08:59	1	909164
152	1219+285	: 0000	V	1	0/17:09:03 -	0/17:13:59	1	915509
153	1222+216	: 0000	V	1	0/17:14:03 -	0/17:18:59	1	921899
154	3C273	: 0000	V	1	0/17:19:18 -	0/17:23:59	1	928274
155	3C279	: 0000	V	1	0/17:24:03 -	0/17:28:57	1	934114
156	1406-076	: 0000	V	1	0/17:29:01 -	0/17:33:56	1	940459
157	1510-089	: 0000	V	1	0/17:34:01 -	0/17:38:54	1	946849
158	1611+343	: 0000	V	1	0/17:38:58 -	0/17:43:54	1	953194
159	1633+382	: 0000	V	1	0/17:43:58 -	0/17:48:54	1	959584
160	3C345	: 0000	V	1	0/17:48:58 -	0/17:53:54	1	965974
161	OJ287	: 0000	V	1	0/17:53:58 -	0/17:58:52	1	972364
162	0836+710	: 0000	V	1	0/17:58:56 -	0/18:03:52	1	978709
163	0954+658	: 0000	V	1	0/18:03:56 -	0/18:08:52	1	985099
164	1127-145	: 0000	V	1	0/18:08:56 -	0/18:13:49	1	991489
165	1156+295	: 0000	V	1	0/18:13:54 -	0/18:18:49	1	997834
166	1219+285	: 0000	V	1	0/18:18:53 -	0/18:23:47	1	1004224
167	1222+216	: 0000	V	1	0/18:23:51 -	0/18:28:47	1	1010569
168	3C273	: 0000	V	1	0/18:28:51 -	0/18:33:47	1	1016959
169	3C279	: 0000	V	1	0/18:33:51 -	0/18:38:47	1	1023349
170	1406-076	: 0000	V	1	0/18:38:51 -	0/18:43:44	1	1029739
171	1510-089	: 0000	V	1	0/18:43:49 -	0/18:48:44	1	1036084
172	1611+343	: 0000	V	1	0/18:48:49 -	0/18:53:42	1	1042474
173	1633+382	: 0000	V	1	0/18:53:46 -	0/18:58:42	1	1048819
174	3C345	: 0000	V	1	0/18:58:46 -	0/19:03:42	1	1055209
175	1622-297	: 0000	V	1	0/19:03:46 -	0/19:08:44	1	1061599
176	1127-145	: 0000	V	1	0/19:09:51 -	0/19:14:40	1	1067458
177	1156+295	: 0000	V	1	0/19:14:45 -	0/19:19:38	1	1072196
178	1219+285	: 0000	V	1	0/19:19:59 -	0/19:24:38	1	1078446
179	1222+216	: 0000	V	1	0/19:24:42 -	0/19:29:36	1	1084292
180	3C273	: 0000	V	1	0/19:29:40 -	0/19:34:36	1	1090637
181	3C279	: 0000	V	1	0/19:34:40 -	0/19:39:36	1	1097027
182	1406-076	: 0000	V	1	0/19:39:40 -	0/19:44:36	1	1103417

Figure 3.13: Log of the November 2007 observation details.

Scan	Source	Qual	Calcode	Sub	Timerange		FrqID	START
183	1510-089	: 0000	V	1	0/19:44:40 -	0/19:49:33	1	1109807
184	1611+343	: 0000	V	1	0/19:49:38 -	0/19:54:33	1	1116152
185	1633+382	: 0000	V	1	0/19:54:38 -	0/19:59:31	1	1122542
186	3C345	: 0000	V	1	0/19:59:35 -	0/20:04:31	1	1128869
187	1622-297	: 0000	V	1	0/20:04:35 -	0/20:09:31	1	1135259
188	1730-130	: 0000	V	1	0/20:09:35 -	0/20:14:31	1	1141649
189	1156+295	: 0000	V	1	0/20:14:35 -	0/20:19:29	1	1148039
190	1219+285	: 0000	V	1	0/20:19:33 -	0/20:24:28	1	1154384
191	1222+216	: 0000	V	1	0/20:24:33 -	0/20:29:26	1	1160756
192	3C273	: 0000	V	1	0/20:29:30 -	0/20:34:26	1	1167101
193	3C279	: 0000	V	1	0/20:34:30 -	0/20:39:26	1	1172348
194	1406-076	: 0000	V	1	0/20:39:30 -	0/20:44:26	1	1177460
195	1510-089	: 0000	V	1	0/20:44:30 -	0/20:49:24	1	1183751
196	1611+343	: 0000	V	1	0/20:49:28 -	0/20:54:24	1	1190088
197	1633+382	: 0000	V	1	0/20:54:28 -	0/20:59:24	1	1196478
198	3C345	: 0000	V	1	0/20:59:28 -	0/21:04:21	1	1202868
199	1622-297	: 0000	V	1	0/21:04:26 -	0/21:09:21	1	1209213
200	1730-130	: 0000	V	1	0/21:09:53 -	0/21:14:23	1	1215576
201	3C279	: 0000	V	1	0/21:15:45 -	0/21:20:20	1	1221330
202	1406-076	: 0000	V	1	0/21:20:24 -	0/21:25:18	1	1226041
203	1510-089	: 0000	V	1	0/21:25:22 -	0/21:30:17	1	1232296
204	1611+343	: 0000	V	1	0/21:30:22 -	0/21:35:17	1	1238686
205	1633+382	: 0000	V	1	0/21:35:22 -	0/21:40:15	1	1245076
206	3C345	: 0000	V	1	0/21:40:19 -	0/21:45:15	1	1251420
207	1622-297	: 0000	V	1	0/21:45:19 -	0/21:50:15	1	1257810
208	1730-130	: 0000	V	1	0/21:50:19 -	0/21:55:15	1	1264200
209	3C279	: 0000	V	1	0/21:55:17 -	0/22:00:13	1	1270542
210	1406-076	: 0000	V	1	0/22:00:17 -	0/22:05:12	1	1274519
211	1510-089	: 0000	V	1	0/22:05:17 -	0/22:10:10	1	1279551
212	1611+343	: 0000	V	1	0/22:10:14 -	0/22:15:10	1	1285788
213	1633+382	: 0000	V	1	0/22:15:14 -	0/22:20:08	1	1292178
214	3C345	: 0000	V	1	0/22:20:12 -	0/22:25:10	1	1298523
215	1622-297	: 0000	V	1	0/22:25:12 -	0/22:30:08	1	1304909
216	1730-130	: 0000	V	1	0/22:30:12 -	0/22:35:12	1	1310022
217	BLLAC	: 0000	V	1	0/22:36:17 -	0/22:41:08	1	1316368
218	1510-089	: 0000	V	1	0/22:41:10 -	0/22:46:04	1	1321390
219	1611+343	: 0000	V	1	0/22:46:08 -	0/22:51:04	1	1326466

Figure 3.14: Log of the November 2007 observation details.

Scan	Source	Qual	Calcode	Sub	Timerange		FrqID	START
220	1633+382	: 0000	V	1	0/22:51:08 -	0/22:56:04	1	1332748
221	3C345	: 0000	V	1	0/22:56:08 -	0/23:01:06	1	1339138
222	1622-297	: 0000	V	1	0/23:01:08 -	0/23:06:02	1	1345521
223	1730-130	: 0000	V	1	0/23:06:06 -	0/23:11:01	1	1350597
224	BLLAC	: 0000	V	1	0/23:11:29 -	0/23:16:01	1	1356834
225	1510-089	: 0000	V	1	0/23:16:03 -	0/23:20:59	1	1362637
226	1611+343	: 0000	V	1	0/23:21:03 -	0/23:25:57	1	1367749
227	1633+382	: 0000	V	1	0/23:26:01 -	0/23:30:59	1	1373995
228	3C345	: 0000	V	1	0/23:31:03 -	0/23:35:59	1	1380430
229	1622-297	: 0000	V	1	0/23:36:01 -	0/23:40:57	1	1386772
230	1730-130	: 0000	V	1	0/23:41:01 -	0/23:45:54	1	1390759
231	BLLAC	: 0000	V	1	0/23:45:59 -	0/23:50:56	1	1396529
232	1510-089	: 0000	V	1	0/23:50:58 -	0/23:55:54	1	1402804
233	1611+343	: 0000	V	1	0/23:55:58 -	1/00:00:53	1	1406781
234	1633+382	: 0000	V	1	1/00:01:23 -	1/00:05:51	1	1412314
235	3C345	: 0000	V	1	1/00:06:19 -	1/00:10:53	1	1418039
236	1622-297	: 0000	V	1	1/00:10:55 -	1/00:15:49	1	1423883
237	1730-130	: 0000	V	1	1/00:15:53 -	1/00:20:49	1	1427832
238	BLLAC	: 0000	V	1	1/00:20:53 -	1/00:25:53	1	1434026
239	3C446	: 0000	V	1	1/00:27:00 -	1/00:31:47	1	1440431
240	CTA102	: 0000	V	1	1/00:31:52 -	1/00:36:47	1	1446313
241	3C454.3	: 0000	V	1	1/00:36:51 -	1/00:41:45	1	1452696
242	1611+343	: 0000	V	1	1/00:41:49 -	1/00:46:45	1	1459041
243	1633+382	: 0000	V	1	1/00:46:49 -	1/00:51:45	1	1465431
244	3C345	: 0000	V	1	1/00:51:49 -	1/00:56:47	1	1471821
245	1730-130	: 0000	V	1	1/00:56:49 -	1/01:01:43	1	1478204
246	BLLAC	: 0000	V	1	1/01:01:47 -	1/01:06:42	1	1483280
247	3C446	: 0000	V	1	1/01:06:47 -	1/01:11:40	1	1489634
248	CTA102	: 0000	V	1	1/01:11:44 -	1/01:16:40	1	1495979
249	3C454.3	: 0000	V	1	1/01:16:44 -	1/01:21:38	1	1502369
250	1611+343	: 0000	V	1	1/01:21:42 -	1/01:26:40	1	1508714
251	1633+382	: 0000	V	1	1/01:26:44 -	1/01:31:38	1	1515149
252	3C345	: 0000	V	1	1/01:31:42 -	1/01:36:40	1	1521494
253	1730-130	: 0000	V	1	1/01:36:42 -	1/01:41:35	1	1527878
254	BLLAC	: 0000	V	1	1/01:41:40 -	1/01:46:35	1	1532954
255	3C446	: 0000	V	1	1/01:46:39 -	1/01:51:35	1	1539317
256	CTA102	: 0000	V	1	1/01:51:39 -	1/01:56:33	1	1545707

Figure 3.15: Log of the November 2007 observation details.

Scan	Source	Qual	Calcode	Sub	Timerange			FrqID	START
257	3C454.3	: 0000	V	1	1/01:56:37	-	1/02:01:33	1	1552052
258	1611+343	: 0000	V	1	1/02:01:37	-	1/02:06:33	1	1558442
259	1633+382	: 0000	V	1	1/02:07:00	-	1/02:11:35	1	1564793
260	3C345	: 0000	V	1	1/02:12:57	-	1/02:17:31	1	1570607
261	1730-130	: 0000	V	1	1/02:17:33	-	1/02:22:29	1	1576463
262	BLLAC	: 0000	V	1	1/02:22:33	-	1/02:27:29	1	1580442
263	3C446	: 0000	V	1	1/02:27:33	-	1/02:32:29	1	1586566
264	CTA102	: 0000	V	1	1/02:32:33	-	1/02:37:27	1	1592812
265	3C454.3	: 0000	V	1	1/02:37:31	-	1/02:42:29	1	1599157
266	0235+164	: 0000	V	1	1/02:42:31	-	1/02:47:24	1	1605541
267	3C345	: 0000	V	1	1/02:47:29	-	1/02:52:24	1	1610617
268	BLLAC	: 0000	V	1	1/02:52:28	-	1/02:57:24	1	1616971
269	3C446	: 0000	V	1	1/02:57:28	-	1/03:02:22	1	1623361
270	CTA102	: 0000	V	1	1/03:02:26	-	1/03:07:22	1	1629706
271	3C454.3	: 0000	V	1	1/03:07:26	-	1/03:12:24	1	1636096
272	0235+164	: 0000	V	1	1/03:12:26	-	1/03:17:24	1	1642480
273	BLLAC	: 0000	V	1	1/03:18:29	-	1/03:23:18	1	1647607
274	3C446	: 0000	V	1	1/03:23:22	-	1/03:28:18	1	1653624
275	CTA102	: 0000	V	1	1/03:28:22	-	1/03:33:18	1	1660014
276	3C454.3	: 0000	V	1	1/03:33:22	-	1/03:38:20	1	1666404
277	0235+164	: 0000	V	1	1/03:38:22	-	1/03:43:16	1	1672786
278	3C446	: 0000	V	1	1/03:43:20	-	1/03:48:15	1	1677862
279	CTA102	: 0000	V	1	1/03:48:20	-	1/03:53:15	1	1684153
280	3C454.3	: 0000	V	1	1/03:53:20	-	1/03:57:44	1	1690543
281	0235+164	: 0000	V	1	1/03:57:48	-	1/04:02:46	1	1696258
282	0336-019	: 0000	V	1	1/04:02:48	-	1/04:07:41	1	1701565
283	0420-014	: 0000	V	1	1/04:07:46	-	1/04:12:41	1	1706641
284	BLLAC	: 0000	V	1	1/04:12:46	-	1/04:17:41	1	1711753
285	3C446	: 0000	V	1	1/04:17:45	-	1/04:22:39	1	1718107
286	CTA102	: 0000	V	1	1/04:22:43	-	1/04:27:39	1	1724452
287	3C454.3	: 0000	V	1	1/04:27:43	-	1/04:31:57	1	1730842

Figure 3.16: Log of the November 2007 observation details.

3.2.3 January 2008 Epoch

Scan summary listing

Scan	Source	Qual	Calcode	Sub	Timerange	FrqID	START
1	0235+164	: 0000	V	1	0/04:05:50 - 0/04:10:33	1	1
2	0336-019	: 0000	V	1	0/04:10:38 - 0/04:15:33	1	5972
3	3C111	: 0000		1	0/04:15:38 - 0/04:20:31	1	12361
4	0420-014	: 0000	V	1	0/04:20:35 - 0/04:25:31	1	18706
5	0528+134	: 0000	V	1	0/04:25:35 - 0/04:30:31	1	25096
6	0716+714	: 0000	V	1	0/04:30:35 - 0/04:35:29	1	31486
7	0735+178	: 0000	V	1	0/04:35:33 - 0/04:40:31	1	37831
8	0829+046	: 0000	V	1	0/04:40:33 - 0/04:45:28	1	44218
9	0827+243	: 0000	V	1	0/04:45:33 - 0/04:50:26	1	49331
10	0836+710	: 0000	V	1	0/04:50:30 - 0/04:55:26	1	55577
11	0954+658	: 0000	V	1	0/04:55:30 - 0/05:00:26	1	61967
12	OJ287	: 0000	V	1	0/05:00:28 - 0/05:05:24	1	68313
13	0235+164	: 0000	V	1	0/05:05:28 - 0/05:10:24	1	73426
14	0336-019	: 0000	V	1	0/05:10:28 - 0/05:15:24	1	79717
15	3C111	: 0000		1	0/05:15:28 - 0/05:20:21	1	86107
16	0420-014	: 0000	V	1	0/05:20:26 - 0/05:25:21	1	92452
17	0528+134	: 0000	V	1	0/05:25:26 - 0/05:30:19	1	98842
18	0716+714	: 0000	V	1	0/05:30:23 - 0/05:35:19	1	105185
19	0735+178	: 0000	V	1	0/05:35:23 - 0/05:40:19	1	111575
20	0829+046	: 0000	V	1	0/05:40:23 - 0/05:45:19	1	117965
21	0827+243	: 0000	V	1	0/05:45:23 - 0/05:50:17	1	124355
22	0836+710	: 0000	V	1	0/05:50:21 - 0/05:55:17	1	130700
23	0954+658	: 0000	V	1	0/05:55:21 - 0/06:00:14	1	137090
24	OJ287	: 0000	V	1	0/06:00:46 - 0/06:05:16	1	143430
25	1156+295	: 0000	V	1	0/06:05:18 - 0/06:10:14	1	149192
26	1219+285	: 0000	V	1	0/06:10:18 - 0/06:15:12	1	154385
27	1222+216	: 0000	V	1	0/06:15:16 - 0/06:20:16	1	159381
28	3C111	: 0000		1	0/06:21:21 - 0/06:26:10	1	164535
29	0528+134	: 0000	V	1	0/06:26:15 - 0/06:31:10	1	170440
30	0716+714	: 0000	V	1	0/06:31:14 - 0/06:36:10	1	176830
31	0735+178	: 0000	V	1	0/06:36:14 - 0/06:41:08	1	183220
32	0829+046	: 0000	V	1	0/06:41:12 - 0/06:46:08	1	189565
33	0827+243	: 0000	V	1	0/06:46:12 - 0/06:51:08	1	195955
34	0836+710	: 0000	V	1	0/06:51:12 - 0/06:56:06	1	202345

Figure 3.17: Log of the January 2008 observation details.

Scan	Source	Qual	Calcode	Sub	Timerange		FrqID	START
35	0954+658	: 0000	V	1	0/06:56:10 -	0/07:01:05	1	208690
36	OJ287	: 0000	V	1	0/07:01:10 -	0/07:06:05	1	215080
37	3C111	: 0000		1	0/07:06:10 -	0/07:11:03	1	221470
38	0528+134	: 0000	V	1	0/07:11:07 -	0/07:16:03	1	227815
39	0716+714	: 0000	V	1	0/07:16:07 -	0/07:21:03	1	234205
40	0735+178	: 0000	V	1	0/07:21:07 -	0/07:26:01	1	240595
41	0829+046	: 0000	V	1	0/07:26:05 -	0/07:31:01	1	246940
42	0827+243	: 0000	V	1	0/07:31:05 -	0/07:36:00	1	253330
43	0836+710	: 0000	V	1	0/07:36:05 -	0/07:41:00	1	259720
44	1127-145	: 0000	V	1	0/07:41:02 -	0/07:45:58	1	266066
45	3C273	: 0000	V	1	0/07:46:02 -	0/07:50:56	1	271179
46	OJ287	: 0000	V	1	0/07:51:00 -	0/07:55:56	1	276255
47	0716+714	: 0000	V	1	0/07:56:00 -	0/08:00:56	1	282618
48	0954+658	: 0000	V	1	0/08:01:23 -	0/08:05:58	1	288993
49	1127-145	: 0000	V	1	0/08:06:00 -	0/08:10:53	1	294830
50	1156+295	: 0000	V	1	0/08:10:58 -	0/08:15:55	1	299907
51	1219+285	: 0000	V	1	0/08:15:58 -	0/08:20:51	1	306092
52	1222+216	: 0000	V	1	0/08:20:55 -	0/08:25:51	1	311168
53	3C273	: 0000	V	1	0/08:25:55 -	0/08:30:51	1	316280
54	3C279	: 0000	V	1	0/08:30:55 -	0/08:34:52	1	321360
55	1406-076	: 0000	V	1	0/08:34:54 -	0/08:39:50	1	325426
56	1127-145	: 0000	V	1	0/08:39:54 -	0/08:44:52	1	328488
57	3C111	: 0000		1	0/08:45:57 -	0/08:50:46	1	334555
58	0528+134	: 0000	V	1	0/08:50:50 -	0/08:55:46	1	339283
59	0735+178	: 0000	V	1	0/08:55:50 -	0/09:00:46	1	344395
60	0829+046	: 0000	V	1	0/09:00:50 -	0/09:05:44	1	350784
61	0827+243	: 0000	V	1	0/09:05:48 -	0/09:10:44	1	357049
62	OJ287	: 0000	V	1	0/09:10:48 -	0/09:15:44	1	363439
63	0836+710	: 0000	V	1	0/09:15:48 -	0/09:20:44	1	369829
64	0716+714	: 0000	V	1	0/09:20:48 -	0/09:25:41	1	376209
65	0735+178	: 0000	V	1	0/09:25:46 -	0/09:30:41	1	382554
66	0829+046	: 0000	V	1	0/09:30:45 -	0/09:35:39	1	388944
67	0827+243	: 0000	V	1	0/09:35:43 -	0/09:40:39	1	395289
68	OJ287	: 0000	V	1	0/09:40:43 -	0/09:45:39	1	401679
69	0836+710	: 0000	V	1	0/09:45:43 -	0/09:50:39	1	408042
70	0954+658	: 0000	V	1	0/09:50:43 -	0/09:55:37	1	414432
71	1127-145	: 0000	V	1	0/09:55:41 -	0/10:00:36	1	420777

Figure 3.18: Log of the January 2008 observation details.

Scan	Source	Qual	Calcode	Sub	Timerange		FrqID	START
72	1156+295	: 0000	V	1	0/10:01:04 -	0/10:05:34	1	427140
73	1219+285	: 0000	V	1	0/10:05:38 -	0/10:10:34	1	432820
74	1222+216	: 0000	V	1	0/10:10:38 -	0/10:15:34	1	439210
75	3C273	: 0000	V	1	0/10:15:38 -	0/10:20:34	1	445600
76	3C279	: 0000	V	1	0/10:20:38 -	0/10:25:34	1	451990
77	1406-076	: 0000	V	1	0/10:25:36 -	0/10:30:32	1	458331
78	0716+714	: 0000	V	1	0/10:30:36 -	0/10:35:31	1	463443
79	0735+178	: 0000	V	1	0/10:35:34 -	0/10:40:29	1	469696
80	0829+046	: 0000	V	1	0/10:40:33 -	0/10:45:29	1	474809
81	0827+243	: 0000	V	1	0/10:45:33 -	0/10:50:27	1	481093
82	OJ287	: 0000	V	1	0/10:50:31 -	0/10:55:27	1	487438
83	0836+710	: 0000	V	1	0/10:55:31 -	0/11:00:27	1	493828
84	0954+658	: 0000	V	1	0/11:00:31 -	0/11:05:25	1	499363
85	1127-145	: 0000	V	1	0/11:05:29 -	0/11:10:24	1	504439
86	1156+295	: 0000	V	1	0/11:10:29 -	0/11:15:24	1	509551
87	1219+285	: 0000	V	1	0/11:15:29 -	0/11:20:22	1	514663
88	1222+216	: 0000	V	1	0/11:20:26 -	0/11:25:22	1	519739
89	3C273	: 0000	V	1	0/11:25:26 -	0/11:30:22	1	524851
90	3C279	: 0000	V	1	0/11:30:26 -	0/11:35:20	1	529843
91	1406-076	: 0000	V	1	0/11:35:24 -	0/11:40:24	1	534919
92	OJ287	: 0000	V	1	0/11:41:29 -	0/11:46:18	1	540866
93	0836+710	: 0000	V	1	0/11:46:22 -	0/11:51:18	1	544267
94	0954+658	: 0000	V	1	0/11:51:22 -	0/11:56:16	1	549379
95	1127-145	: 0000	V	1	0/11:56:20 -	0/12:01:16	1	554455
96	1156+295	: 0000	V	1	0/12:01:20 -	0/12:06:16	1	559567
97	1219+285	: 0000	V	1	0/12:06:20 -	0/12:11:16	1	564679
98	1222+216	: 0000	V	1	0/12:11:20 -	0/12:16:13	1	569791
99	3C273	: 0000	V	1	0/12:16:18 -	0/12:21:13	1	574867
100	3C279	: 0000	V	1	0/12:21:17 -	0/12:26:11	1	579979
101	1406-076	: 0000	V	1	0/12:26:15 -	0/12:31:11	1	585055
102	1510-089	: 0000	V	1	0/12:31:15 -	0/12:36:09	1	590167
103	1611+343	: 0000	V	1	0/12:36:38 -	0/12:41:11	1	595231
104	1633+382	: 0000	V	1	0/12:41:15 -	0/12:46:09	1	599424
105	3C345	: 0000	V	1	0/12:46:13 -	0/12:51:11	1	604500
106	OJ287	: 0000	V	1	0/12:51:13 -	0/12:56:06	1	609607
107	0836+710	: 0000	V	1	0/12:56:10 -	0/13:01:06	1	613556
108	0954+658	: 0000	V	1	0/13:01:10 -	0/13:06:06	1	618580

Figure 3.19: Log of the January 2008 observation details.

Scan	Source	Qual	Calcode	Sub	Timerange		FrqID	START
109	1127-145	: 0000	V	1	0/13:06:10 -	0/13:11:06	1	623692
110	1156+295	: 0000	V	1	0/13:11:10 -	0/13:16:04	1	628804
111	1219+285	: 0000	V	1	0/13:16:08 -	0/13:21:04	1	633880
112	1222+216	: 0000	V	1	0/13:21:08 -	0/13:26:01	1	638992
113	3C273	: 0000	V	1	0/13:26:06 -	0/13:31:01	1	644068
114	3C279	: 0000	V	1	0/13:31:05 -	0/13:36:01	1	649180
115	1406-076	: 0000	V	1	0/13:36:05 -	0/13:40:59	1	654292
116	1510-089	: 0000	V	1	0/13:41:03 -	0/13:45:59	1	659368
117	1611+343	: 0000	V	1	0/13:46:03 -	0/13:50:59	1	664456
118	1633+382	: 0000	V	1	0/13:51:03 -	0/13:55:57	1	669568
119	3C345	: 0000	V	1	0/13:56:01 -	0/14:00:56	1	674644
120	1622-297	: 0000	V	1	0/14:01:01 -	0/14:06:01	1	679756
121	1127-145	: 0000	V	1	0/14:07:06 -	0/14:11:55	1	684673
122	1156+295	: 0000	V	1	0/14:11:59 -	0/14:16:55	1	688354
123	1219+285	: 0000	V	1	0/14:16:59 -	0/14:21:53	1	693386
124	1222+216	: 0000	V	1	0/14:21:57 -	0/14:26:53	1	698462
125	3C273	: 0000	V	1	0/14:26:57 -	0/14:31:50	1	703574
126	3C279	: 0000	V	1	0/14:31:54 -	0/14:36:50	1	708650
127	1406-076	: 0000	V	1	0/14:36:54 -	0/14:41:50	1	713762
128	1510-089	: 0000	V	1	0/14:41:54 -	0/14:46:48	1	718874
129	1611+343	: 0000	V	1	0/14:46:52 -	0/14:51:48	1	723950
130	1633+382	: 0000	V	1	0/14:51:52 -	0/14:56:48	1	729062
131	3C345	: 0000	V	1	0/14:56:52 -	0/15:01:48	1	734174
132	1622-297	: 0000	V	1	0/15:01:52 -	0/15:06:45	1	739286
133	1730-130	: 0000	V	1	0/15:06:50 -	0/15:11:43	1	744362
134	1156+295	: 0000	V	1	0/15:12:00 -	0/15:16:43	1	749434
135	1219+285	: 0000	V	1	0/15:16:47 -	0/15:21:43	1	752856
136	1222+216	: 0000	V	1	0/15:22:00 -	0/15:26:43	1	757856
137	3C273	: 0000	V	1	0/15:26:47 -	0/15:31:43	1	760655
138	3C279	: 0000	V	1	0/15:31:47 -	0/15:36:41	1	764631
139	1406-076	: 0000	V	1	0/15:36:45 -	0/15:41:40	1	768579
140	1510-089	: 0000	V	1	0/15:41:59 -	0/15:46:38	1	773588
141	1611+343	: 0000	V	1	0/15:46:42 -	0/15:51:38	1	777903
142	1633+382	: 0000	V	1	0/15:51:42 -	0/15:56:38	1	783015
143	3C345	: 0000	V	1	0/15:56:55 -	0/16:01:38	1	788111
144	1622-297	: 0000	V	1	0/16:01:42 -	0/16:06:36	1	791839
145	1730-130	: 0000	V	1	0/16:06:40 -	0/16:11:40	1	796915

Figure 3.20: Log of the January 2008 observation details.

Scan	Source	Qual	Calcode	Sub	Timerange	FrqID	START
146	3C279	: 0000	V	1	0/16:12:45 - 0/16:17:34	1	802066
147	1406-076	: 0000	V	1	0/16:17:38 - 0/16:22:32	1	805732
148	1510-089	: 0000	V	1	0/16:22:36 - 0/16:27:32	1	810937
149	1611+343	: 0000	V	1	0/16:27:36 - 0/16:32:32	1	817327
150	1633+382	: 0000	V	1	0/16:32:36 - 0/16:37:32	1	823717
151	3C345	: 0000	V	1	0/16:37:36 - 0/16:42:29	1	830107
152	1622-297	: 0000	V	1	0/16:42:34 - 0/16:47:29	1	836452
153	1730-130	: 0000	V	1	0/16:47:34 - 0/16:52:29	1	842842
154	3C279	: 0000	V	1	0/16:52:31 - 0/16:57:27	1	849187
155	1406-076	: 0000	V	1	0/16:57:31 - 0/17:02:27	1	853166
156	1510-089	: 0000	V	1	0/17:02:31 - 0/17:07:27	1	857142
157	1611+343	: 0000	V	1	0/17:07:31 - 0/17:12:25	1	863353
158	1633+382	: 0000	V	1	0/17:12:29 - 0/17:17:25	1	869698
159	3C345	: 0000	V	1	0/17:17:29 - 0/17:22:22	1	876088
160	1622-297	: 0000	V	1	0/17:22:27 - 0/17:27:22	1	882433
161	1730-130	: 0000	V	1	0/17:27:49 - 0/17:32:26	1	887524
162	BLLAC	: 0000	V	1	0/17:33:31 - 0/17:38:23	1	894545
163	1510-089	: 0000	V	1	0/17:38:25 - 0/17:43:21	1	901109
164	1611+343	: 0000	V	1	0/17:43:25 - 0/17:48:18	1	906222
165	1633+382	: 0000	V	1	0/17:48:23 - 0/17:53:18	1	913758
166	3C345	: 0000	V	1	0/17:53:22 - 0/17:58:20	1	921568
167	1622-297	: 0000	V	1	0/17:58:22 - 0/18:03:16	1	929372
168	1730-130	: 0000	V	1	0/18:03:20 - 0/18:08:16	1	935717
169	BLLAC	: 0000	V	1	0/18:08:20 - 0/18:13:18	1	943417
170	1510-089	: 0000	V	1	0/18:13:20 - 0/18:18:14	1	951214
171	1611+343	: 0000	V	1	0/18:18:18 - 0/18:23:13	1	956290
172	1633+382	: 0000	V	1	0/18:23:18 - 0/18:28:13	1	963891
173	3C345	: 0000	V	1	0/18:28:18 - 0/18:33:13	1	971701
174	1622-297	: 0000	V	1	0/18:33:15 - 0/18:38:11	1	979457
175	1730-130	: 0000	V	1	0/18:38:15 - 0/18:43:11	1	983439
176	BLLAC	: 0000	V	1	0/18:43:15 - 0/18:48:11	1	990960
177	1510-089	: 0000	V	1	0/18:48:13 - 0/18:53:09	1	998711
178	1611+343	: 0000	V	1	0/18:53:13 - 0/18:58:09	1	1002690
179	1633+382	: 0000	V	1	0/18:58:13 - 0/19:03:06	1	1010211
180	3C345	: 0000	V	1	0/19:03:11 - 0/19:08:08	1	1017966
181	1622-297	: 0000	V	1	0/19:08:10 - 0/19:13:04	1	1025765
182	1730-130	: 0000	V	1	0/19:13:08 - 0/19:18:04	1	1029714

Figure 3.21: Log of the January 2008 observation details.

Scan	Source	Qual	Calcode	Sub	Timerange	FrqID	START
183	BLLAC	: 0000	V	1	0/19:18:08 - 0/19:23:08	1	1037190
184	3C446	: 0000	V	1	0/19:24:13 - 0/19:29:02	1	1045070
185	CTA102	: 0000	V	1	0/19:29:32 - 0/19:34:02	1	1052272
186	3C454.3	: 0000	V	1	0/19:34:06 - 0/19:39:02	1	1059422
187	1611+343	: 0000	V	1	0/19:39:04 - 0/19:44:00	1	1067176
188	1633+382	: 0000	V	1	0/19:44:04 - 0/19:49:00	1	1073567
189	3C345	: 0000	V	1	0/19:49:04 - 0/19:54:02	1	1081267
190	1730-130	: 0000	V	1	0/19:54:04 - 0/19:58:58	1	1089064
191	BLLAC	: 0000	V	1	0/19:59:02 - 0/20:03:57	1	1094140
192	3C446	: 0000	V	1	0/20:04:02 - 0/20:08:55	1	1101741
193	CTA102	: 0000	V	1	0/20:08:59 - 0/20:13:55	1	1109496
194	3C454.3	: 0000	V	1	0/20:13:59 - 0/20:18:55	1	1117306
195	1611+343	: 0000	V	1	0/20:18:57 - 0/20:23:55	1	1125060
196	1633+382	: 0000	V	1	0/20:23:59 - 0/20:28:53	1	1131496
197	3C345	: 0000	V	1	0/20:28:57 - 0/20:33:55	1	1137841
198	1730-130	: 0000	V	1	0/20:33:57 - 0/20:38:50	1	1144225
199	BLLAC	: 0000	V	1	0/20:38:55 - 0/20:43:50	1	1149301
200	3C446	: 0000	V	1	0/20:43:54 - 0/20:48:50	1	1156892
201	CTA102	: 0000	V	1	0/20:48:54 - 0/20:53:48	1	1164702
202	3C454.3	: 0000	V	1	0/20:53:52 - 0/20:58:50	1	1172417
203	1611+343	: 0000	V	1	0/20:58:52 - 0/21:03:48	1	1180222
204	1633+382	: 0000	V	1	0/21:03:52 - 0/21:08:50	1	1186612
205	3C345	: 0000	V	1	0/21:10:01 - 0/21:14:46	1	1193005
206	1730-130	: 0000	V	1	0/21:14:48 - 0/21:19:44	1	1198879
207	BLLAC	: 0000	V	1	0/21:19:48 - 0/21:24:44	1	1202858
208	3C446	: 0000	V	1	0/21:24:48 - 0/21:29:44	1	1210472
209	CTA102	: 0000	V	1	0/21:30:01 - 0/21:34:42	1	1218234
210	3C454.3	: 0000	V	1	0/21:34:46 - 0/21:39:44	1	1225426
211	0235+164	: 0000	V	1	0/21:39:46 - 0/21:44:41	1	1233229
212	3C345	: 0000	V	1	0/21:44:44 - 0/21:49:39	1	1239572
213	BLLAC	: 0000	V	1	0/21:49:43 - 0/21:54:39	1	1245863
214	3C446	: 0000	V	1	0/21:54:43 - 0/21:59:37	1	1253583
215	CTA102	: 0000	V	1	0/21:59:41 - 0/22:04:37	1	1261338
216	3C454.3	: 0000	V	1	0/22:04:41 - 0/22:09:39	1	1269148
217	0235+164	: 0000	V	1	0/22:09:41 - 0/22:14:39	1	1276950
218	BLLAC	: 0000	V	1	0/22:15:44 - 0/22:20:33	1	1283355
219	3C446	: 0000	V	1	0/22:21:02 - 0/22:25:33	1	1290612

Figure 3.22: Log of the January 2008 observation details.

Scan	Source	Qual	Calcode	Sub	Timerange			FrqID	START
220	CTA102	: 0000	V	1	0/22:25:37	-	0/22:30:33	1	1296671
221	3C454.3	: 0000	V	1	0/22:30:37	-	0/22:35:35	1	1304481
222	0235+164	: 0000	V	1	0/22:35:37	-	0/22:40:31	1	1312282
223	3C446	: 0000	V	1	0/22:40:35	-	0/22:45:30	1	1318627
224	CTA102	: 0000	V	1	0/22:45:35	-	0/22:50:30	1	1326337
225	3C454.3	: 0000	V	1	0/22:50:35	-	0/22:54:59	1	1334147
226	0235+164	: 0000	V	1	0/22:55:03	-	0/23:00:01	1	1341132
227	0336-019	: 0000	V	1	0/23:00:03	-	0/23:04:57	1	1348054
228	0420-014	: 0000	V	1	0/23:05:01	-	0/23:09:56	1	1354399
229	BLLAC	: 0000	V	1	0/23:10:01	-	0/23:14:56	1	1360789
230	3C446	: 0000	V	1	0/23:15:00	-	0/23:19:54	1	1368569
231	CTA102	: 0000	V	1	0/23:19:58	-	0/23:24:54	1	1376324
232	3C454.3	: 0000	V	1	0/23:24:58	-	0/23:29:22	1	1384114
233	0235+164	: 0000	V	1	0/23:29:27	-	0/23:34:22	1	1391099
234	3C446	: 0000	V	1	0/23:34:27	-	0/23:39:20	1	1398909
235	CTA102	: 0000	V	1	0/23:39:24	-	0/23:44:20	1	1406664
236	3C454.3	: 0000	V	1	0/23:44:24	-	0/23:49:20	1	1414474
237	0235+164	: 0000	V	1	0/23:49:24	-	0/23:54:20	1	1422284
238	0336-019	: 0000	V	1	0/23:54:24	-	0/23:59:18	1	1430084
239	0420-014	: 0000	V	1	0/23:59:22	-	1/00:04:17	1	1436429
240	3C111	: 0000		1	1/00:04:21	-	1/00:09:17	1	1442086
241	BLLAC	: 0000	V	1	1/00:09:21	-	1/00:14:17	1	1449785
242	3C446	: 0000	V	1	1/00:14:21	-	1/00:19:14	1	1457595
243	CTA102	: 0000	V	1	1/00:19:19	-	1/00:24:14	1	1465350
244	3C454.3	: 0000	V	1	1/00:24:19	-	1/00:29:12	1	1473160
245	0235+164	: 0000	V	1	1/00:29:16	-	1/00:34:12	1	1480915
246	0336-019	: 0000	V	1	1/00:34:16	-	1/00:39:12	1	1488725
247	3C111	: 0000		1	1/00:39:16	-	1/00:44:14	1	1496535
248	0420-014	: 0000	V	1	1/00:44:16	-	1/00:49:14	1	1504337
249	BLLAC	: 0000	V	1	1/00:50:21	-	1/00:55:10	1	1510724
250	3C446	: 0000	V	1	1/00:55:12	-	1/01:00:08	1	1517902
251	CTA102	: 0000	V	1	1/01:00:12	-	1/01:05:06	1	1523294
252	3C454.3	: 0000	V	1	1/01:05:10	-	1/01:10:08	1	1530929
253	0235+164	: 0000	V	1	1/01:10:12	-	1/01:15:06	1	1538794
254	0336-019	: 0000	V	1	1/01:15:10	-	1/01:20:06	1	1546549
255	3C111	: 0000		1	1/01:20:10	-	1/01:25:03	1	1554359
256	0420-014	: 0000	V	1	1/01:25:08	-	1/01:30:05	1	1562114

Figure 3.23: Log of the January 2008 observation details.

Scan	Source	Qual	Calcode	Sub	Timerange			FrqID	START
257	0528+134	: 0000	V	1	1/01:30:08	-	1/01:35:03	1	1569917
258	BLLAC	: 0000	V	1	1/01:35:05	-	1/01:40:03	1	1576261
259	3C446	: 0000	V	1	1/01:40:05	-	1/01:45:01	1	1582554
260	CTA102	: 0000	V	1	1/01:45:05	-	1/01:50:01	1	1587667
261	3C454.3	: 0000	V	1	1/01:50:05	-	1/01:54:59	1	1593958
262	0235+164	: 0000	V	1	1/01:55:03	-	1/01:59:58	1	1600303
263	0336-019	: 0000	V	1	1/02:00:28	-	1/02:04:58	1	1607962
264	3C111	: 0000		1	1/02:05:03	-	1/02:09:56	1	1614605
265	0420-014	: 0000	V	1	1/02:10:00	-	1/02:14:56	1	1622360
266	0528+134	: 0000	V	1	1/02:15:00	-	1/02:19:56	1	1630170
267	0716+714	: 0000	V	1	1/02:20:00	-	1/02:24:56	1	1637980
268	0735+178	: 0000	V	1	1/02:24:58	-	1/02:29:54	1	1645730
269	0827+243	: 0000	V	1	1/02:29:58	-	1/02:34:54	1	1652120
270	0829+046	: 0000	V	1	1/02:34:58	-	1/02:39:51	1	1658510
271	0235+164	: 0000	V	1	1/02:39:56	-	1/02:44:51	1	1663958
272	0336-019	: 0000	V	1	1/02:44:55	-	1/02:49:49	1	1671668
273	3C111	: 0000		1	1/02:49:53	-	1/02:54:49	1	1679423
274	0420-014	: 0000	V	1	1/02:54:53	-	1/02:59:49	1	1687233
275	0528+134	: 0000	V	1	1/02:59:53	-	1/03:04:49	1	1695043
276	0716+714	: 0000	V	1	1/03:04:53	-	1/03:09:49	1	1702853
277	BLLAC	: 0000	V	1	1/03:09:51	-	1/03:14:48	1	1710604
278	3C454.3	: 0000	V	1	1/03:14:51	-	1/03:19:44	1	1716989
279	0235+164	: 0000	V	1	1/03:19:48	-	1/03:24:44	1	1722065
280	0336-019	: 0000	V	1	1/03:24:48	-	1/03:29:44	1	1729713
281	3C111	: 0000		1	1/03:29:48	-	1/03:34:44	1	1737523
282	0420-014	: 0000	V	1	1/03:34:48	-	1/03:39:42	1	1745333
283	0528+134	: 0000	V	1	1/03:39:46	-	1/03:44:44	1	1753048
284	0735+178	: 0000	V	1	1/03:44:46	-	1/03:49:39	1	1760851
285	0827+243	: 0000	V	1	1/03:49:44	-	1/03:54:39	1	1767196
286	0829+046	: 0000	V	1	1/03:54:43	-	1/03:59:39	1	1773586
287	0954+658	: 0000	V	1	1/03:59:43	-	1/04:04:37	1	1779976

Figure 3.24: Log of the January 2008 observation details.

3.3 VLBI Maps

VLBI maps were produced for three distinct epochs of observation: August 2007, November 2007 and January 2008. The results are shown in terms of each source and prior to calibration of their EVPAs. The goal of this work does not involve the analysis of polarisation structures. They appear only to demonstrate the polarisation results that were obtained in the process of making VLBI maps. Nothing further will be added to describe the calibration of EVPAs, as it is not a necessary part of this work.

For all of the sources, there are more epochs of observation available to be viewed at www.bu.edu/blazars/VLBAproject.html. This is a part of the Boston University Blazar Group website.

Some of the mapping work that I present in this thesis (for 3C279) was included in Larionov et al. (2008). This work indicates that the source may contain a helical magnetic field that extends 20 pc past the 43 GHz core.

Polarisation structure can be seen in the core of this source in all but the January 2008 epoch. The core dominates the images, with more diffuse emission also visible. There is a significant drop in the peak flux of the source in the January 2008 epoch.

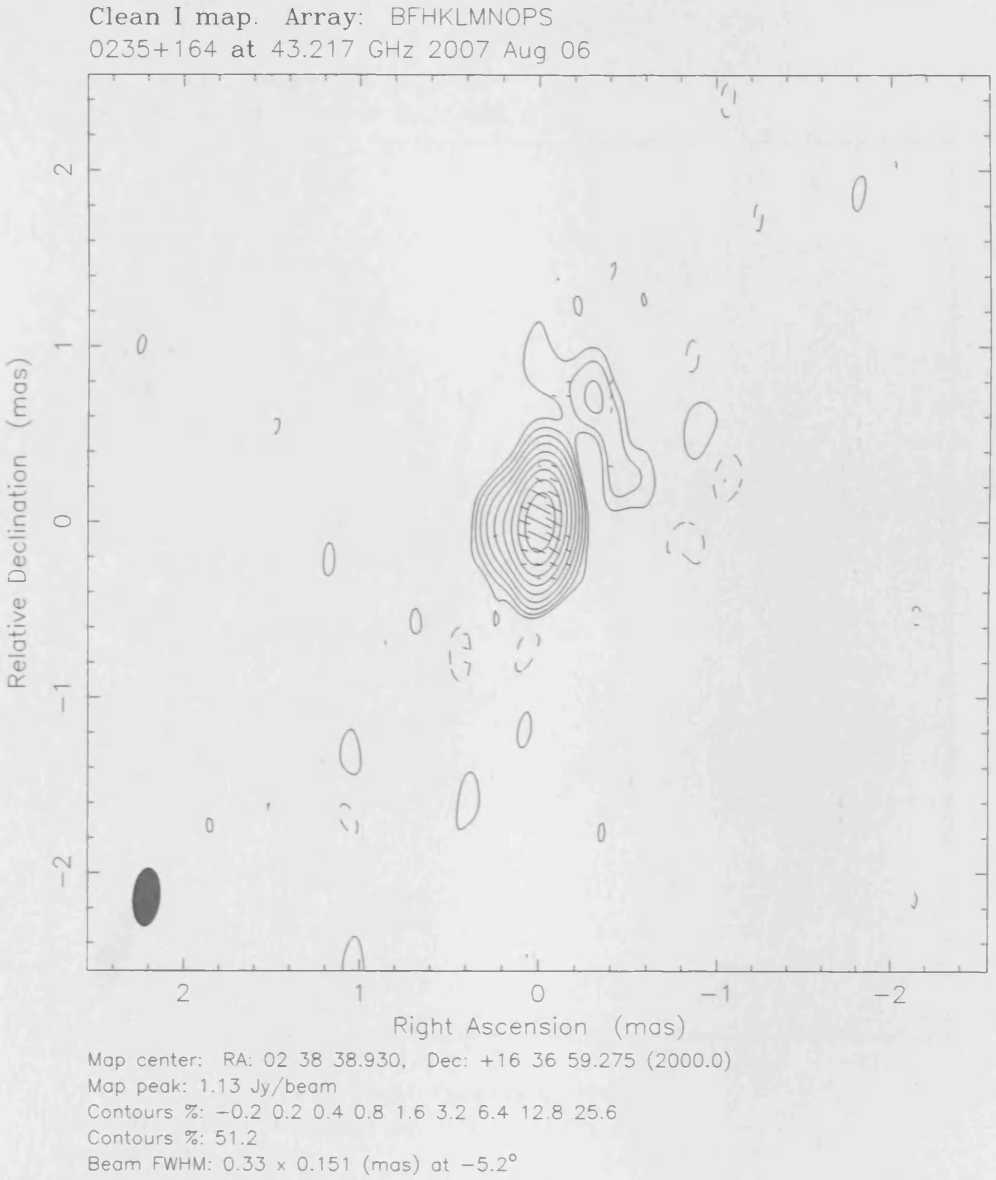

Figure 3.25: August 2007 VLBI Map of 0235+164. For polarisation vectors: 1 mas = $3.57\text{x}10^{-1}$ Jy/beam.

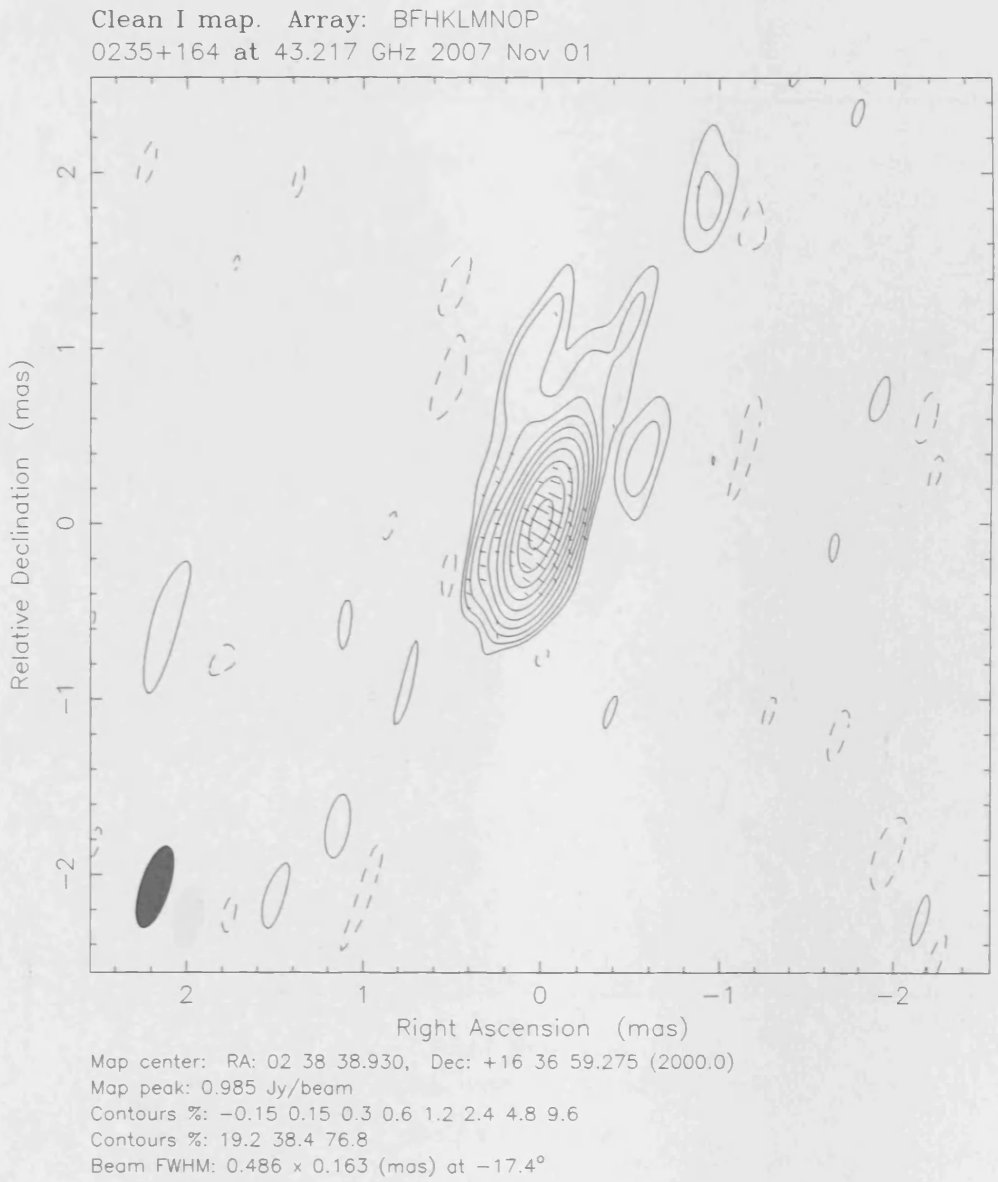

Figure 3.26: November 2007 VLBI Map of 0235+164. For polarisation vectors: 1 mas = $3.57 \text{x} 10^{-1}$ Jy/beam.

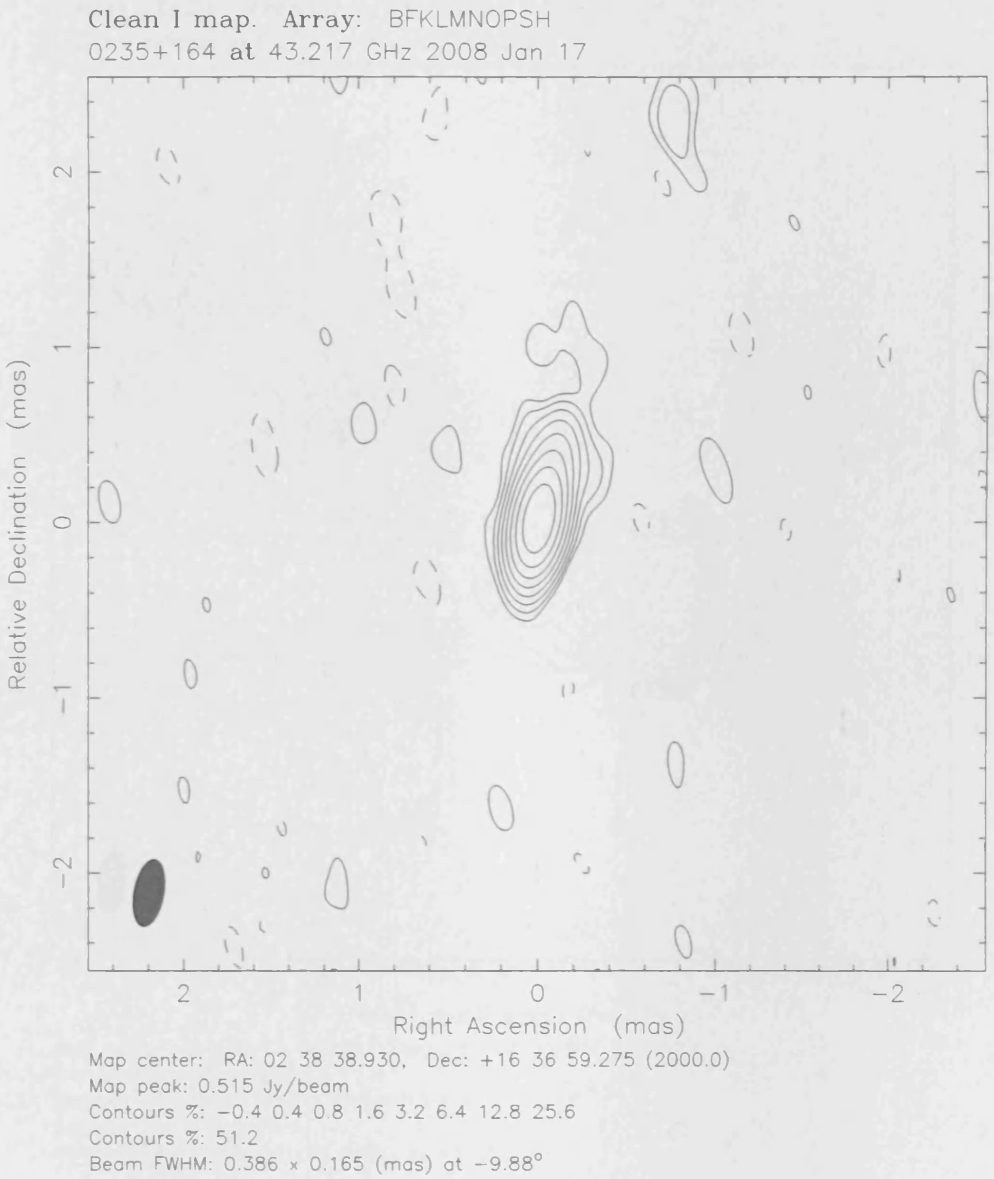

Figure 3.27: January 2008 VLBI Map of 0235+164.

0336-019

This is a more extended source. Many components can be seen in the images, although less structure separated from the core is visible. Polarisation can be seen in the core and first component in the August and November 2007 images. Judging by the angles of the polarisation vectors around the core in January 2008 however, it is not as clear as to whether real polarisation is present along the jet.

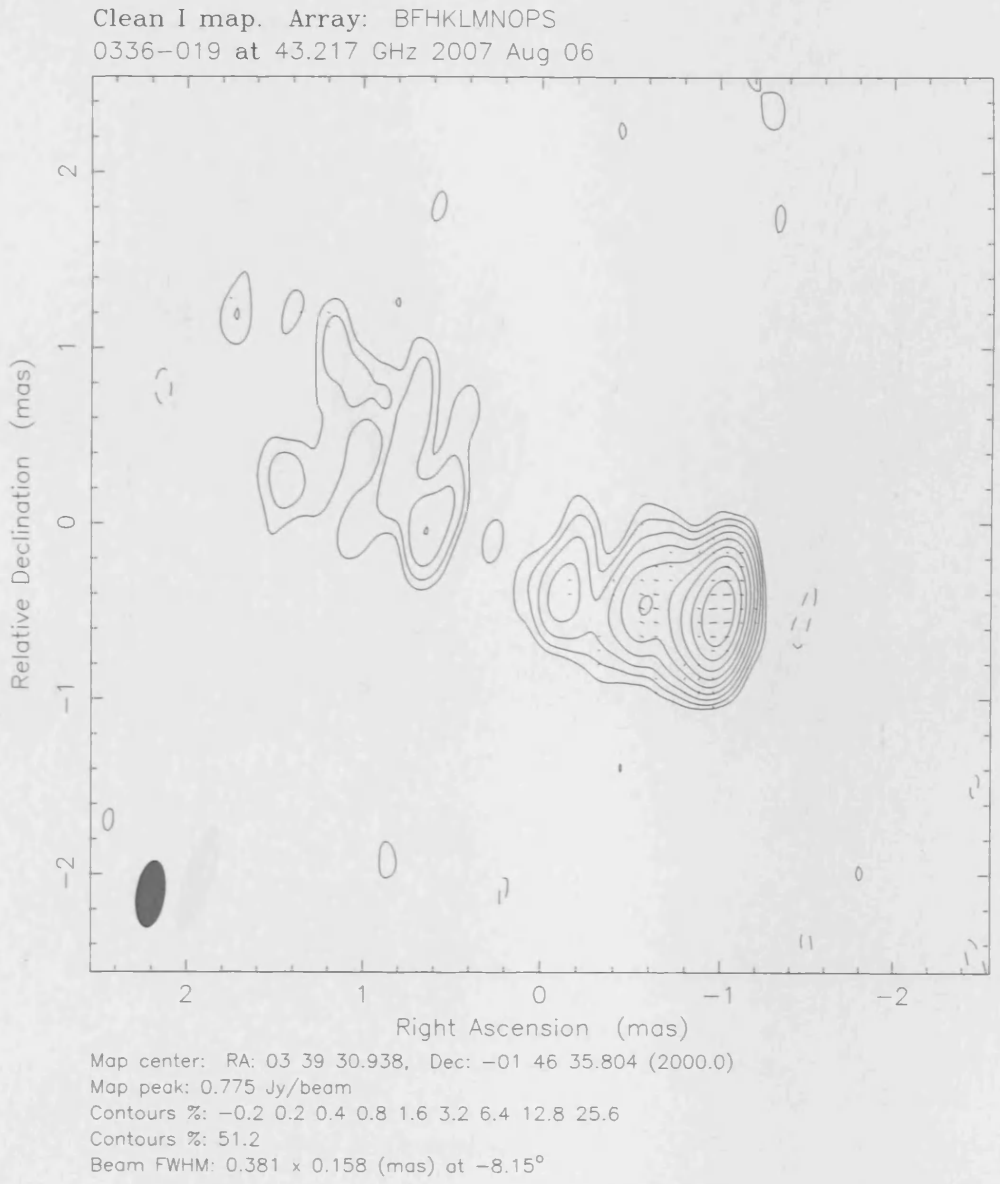

Figure 3.28: August 2007 VLBI Map of 0336-019. For polarisation vectors: 1 mas = 5.00×10^{-1} Jy/beam.

Figure 3.29: November 2007 VLBI Map of 0336-019. For polarisation vectors: 1 mas = $5.00 \text{x} 10^{-1}$ Jy/beam.

Figure 3.30: January 2008 VLBI Map of 0336-019. For polarisation vectors: 1 mas = 2.50×10^{-1} Jy/beam.

0420-014

The most interesting feature of the three images of this source is manifest in the apparent yet significant swing of the jet in the January 2008 epoch. There is a drop in the peak flux of about $0.5Jy$ that accompanies the drop. Polarisation is prominent in the core of the source across the three epochs.

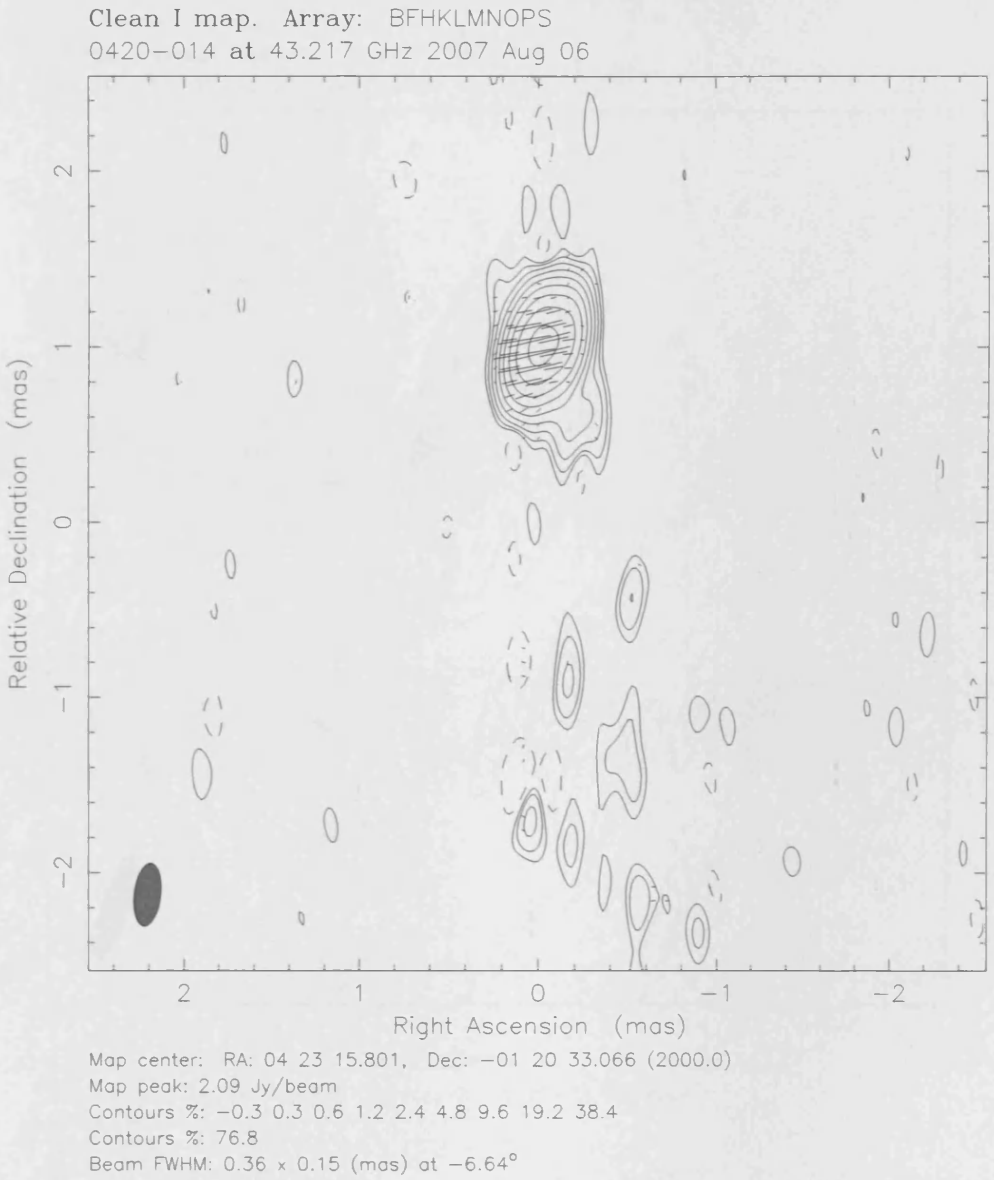

Figure 3.31: August 2007 VLBI Map of 0420-014. For polarisation vectors: 1 mas = 1.00×10^0 Jy/beam.

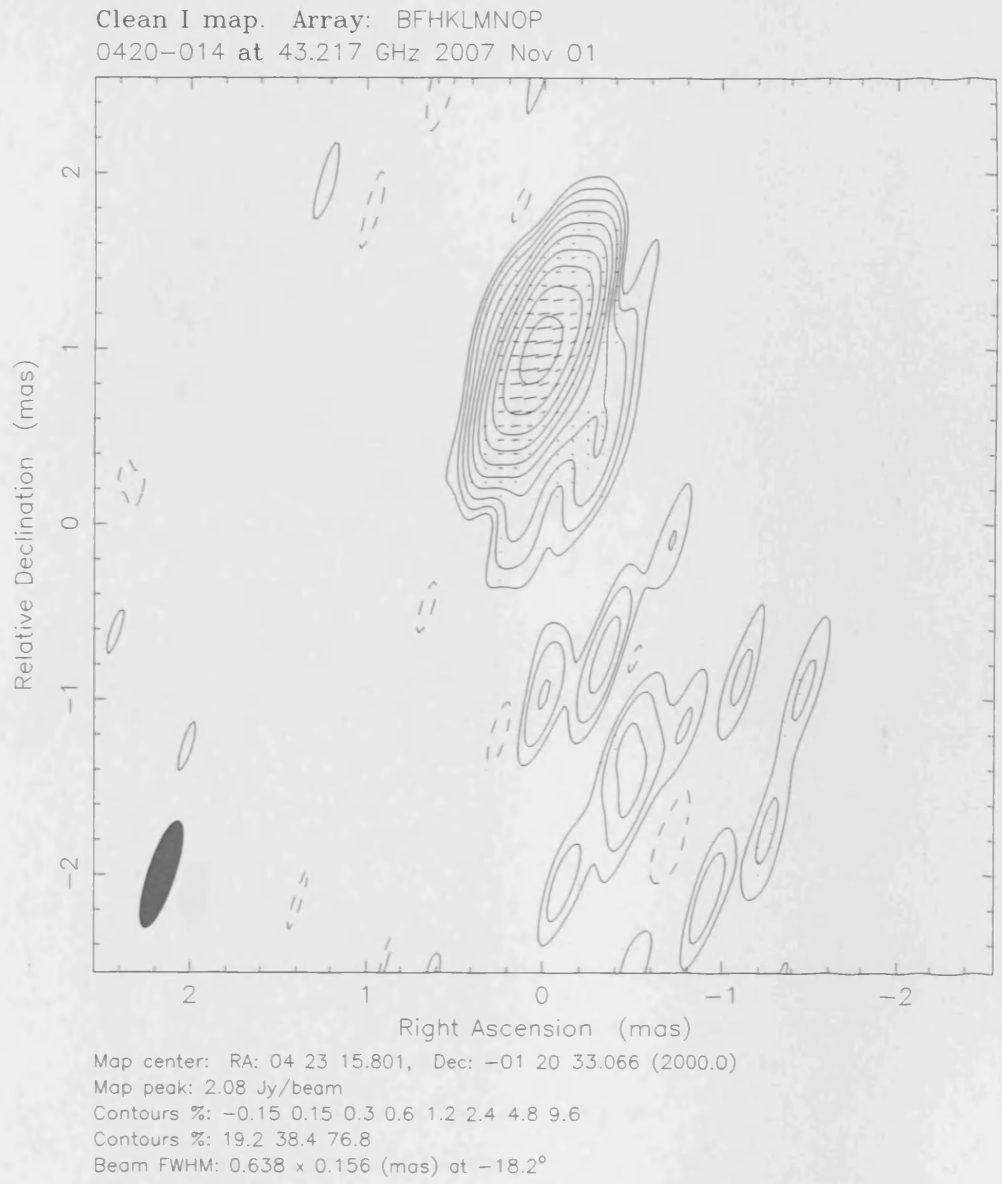

Figure 3.32: November 2007 VLBI Map of 0420-014. For polarisation vectors: 1 mas = 6.25×10^{-1} Jy/beam.

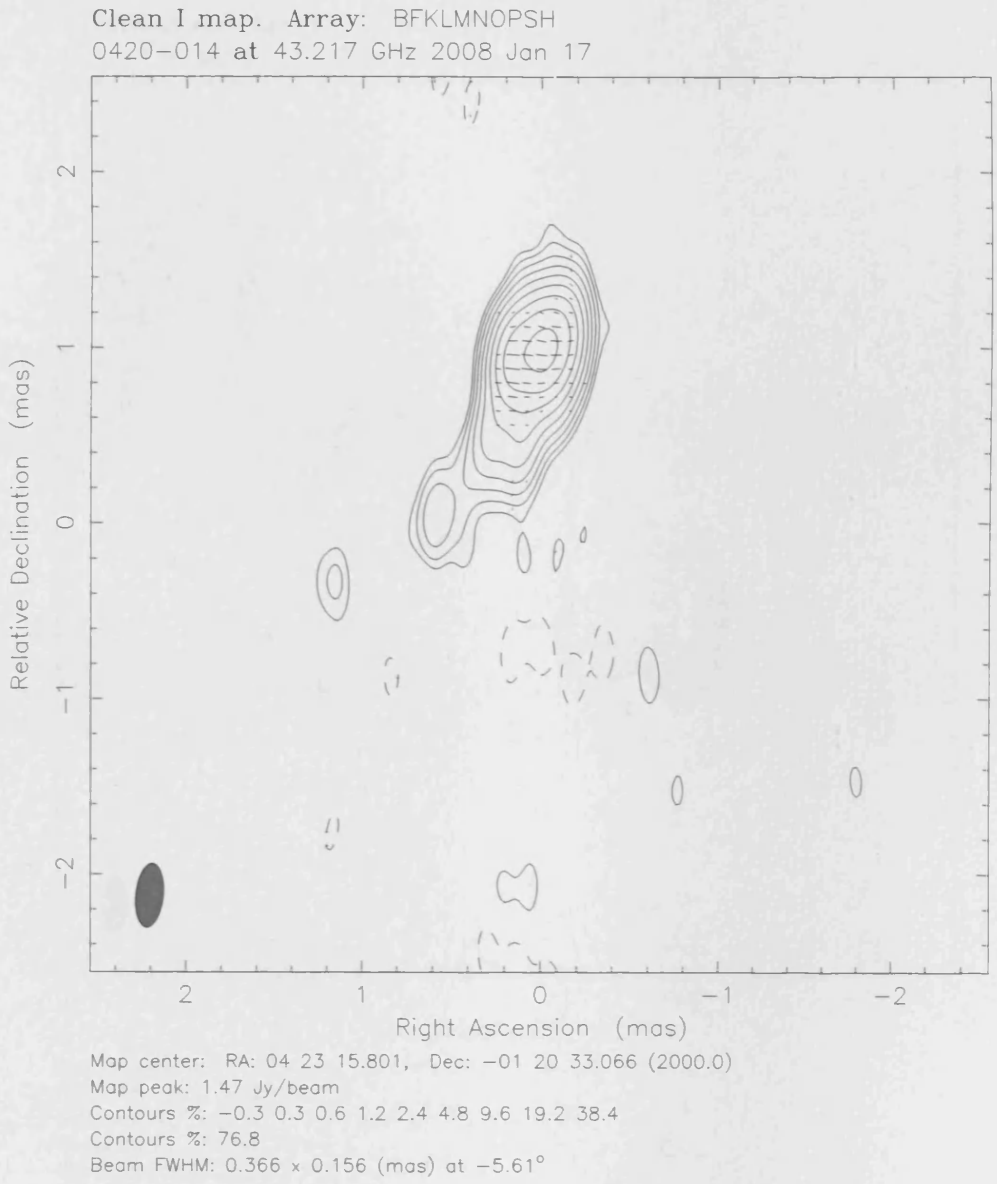

Figure 3.33: January 2008 VLBI Map of 0420-014. For polarisation vectors: 1 mas = 5.00×10^{-1} Jy/beam.

0528+134

The peak flux for this source exhibits a drop that can be seen in the final VLBI map. Polarisation appears to occupy the core and (tentatively) the first component in August and November 2007 though there is no polarisation seen in the first component in the January 2008 epoch. In terms of the core polarisation, there appears to be a gradual anticlockwise rotation of the EVPAs across the epochs.

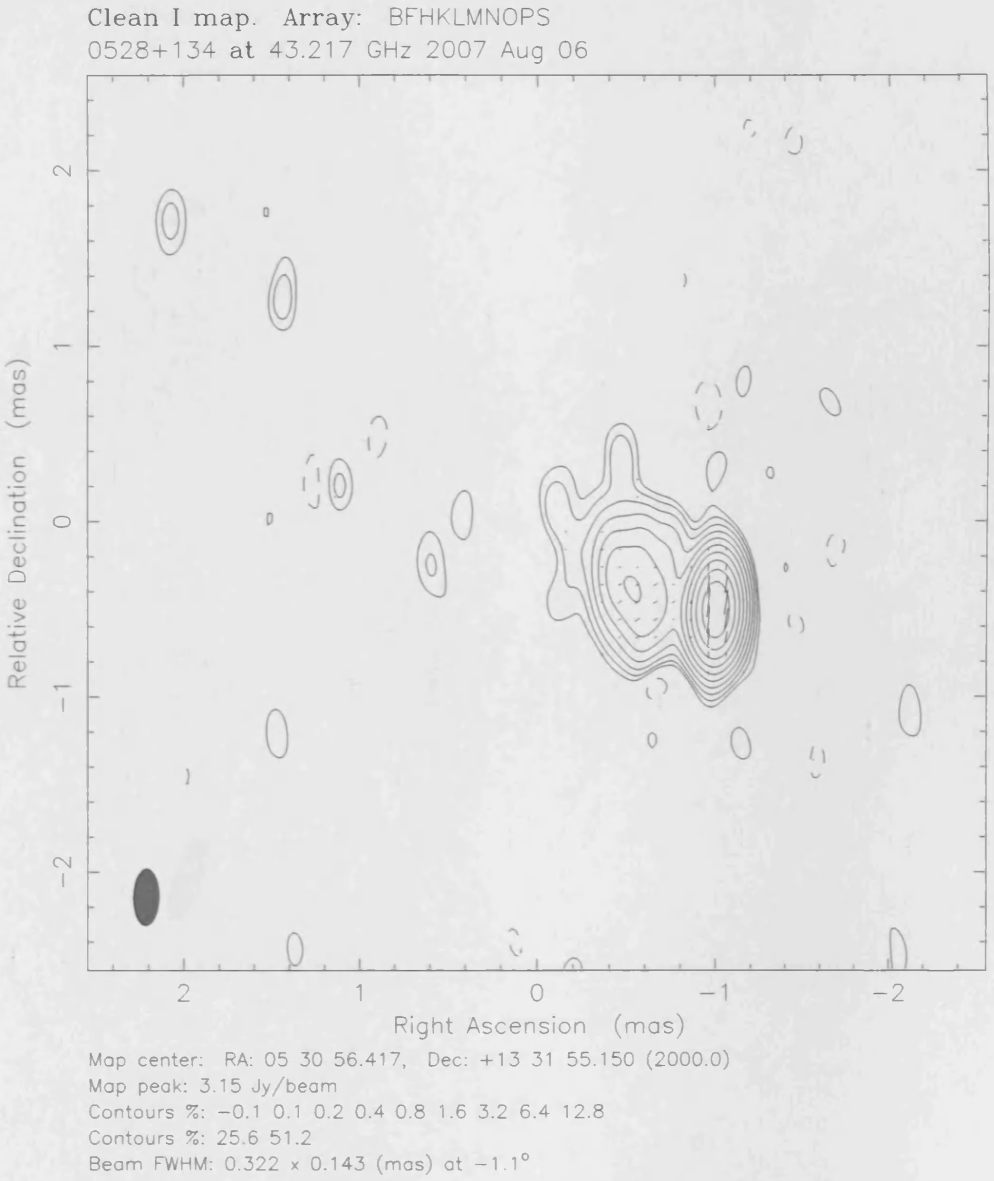

Figure 3.34: August 2007 VLBI Map of 0528+134. For polarisation vectors: 1 mas = 1.00×10^0 Jy/beam.

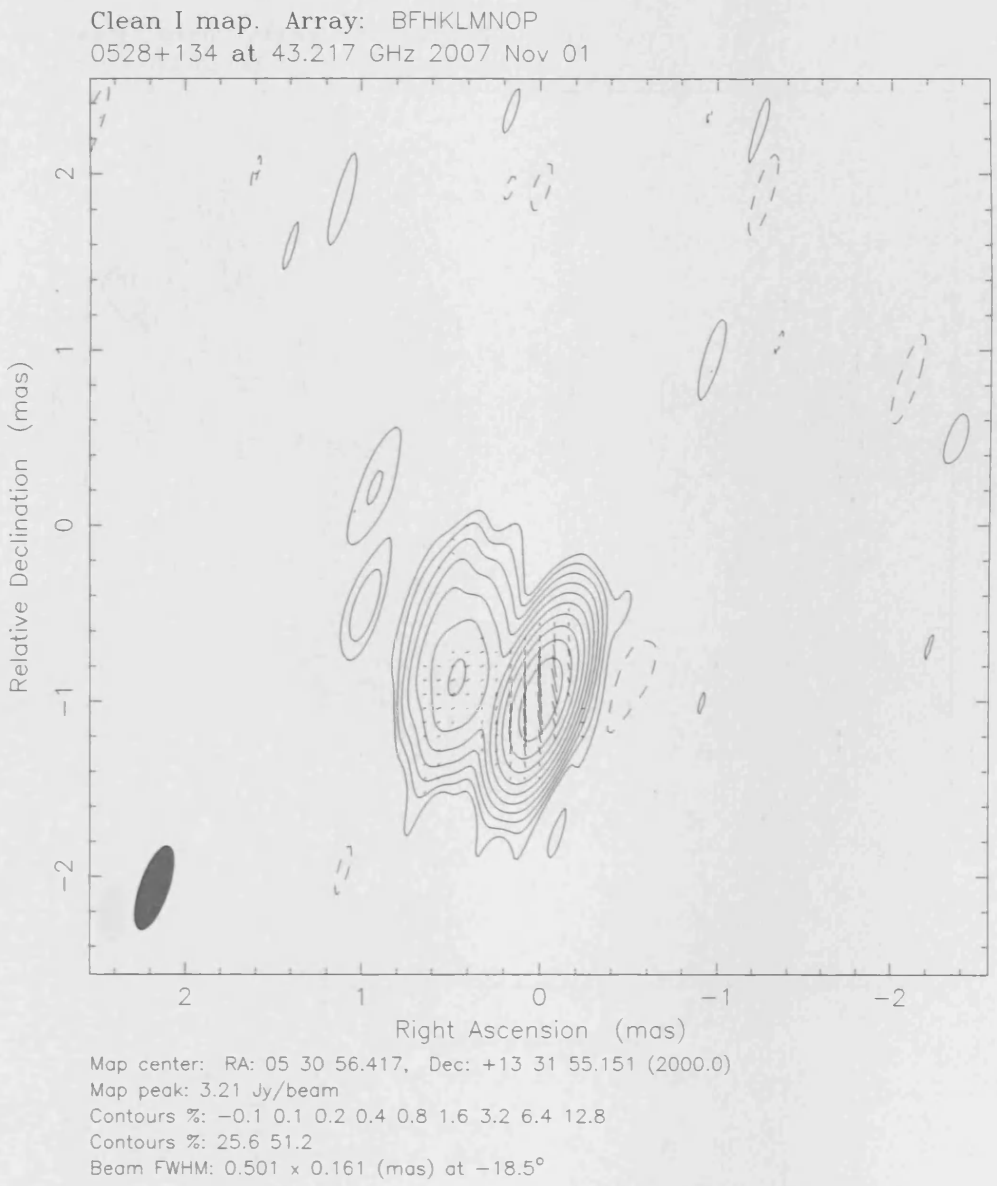

Figure 3.35: November 2007 VLBI Map of 0528+134. For polarisation vectors: 1 mas = 1.25×10^0 Jy/beam.

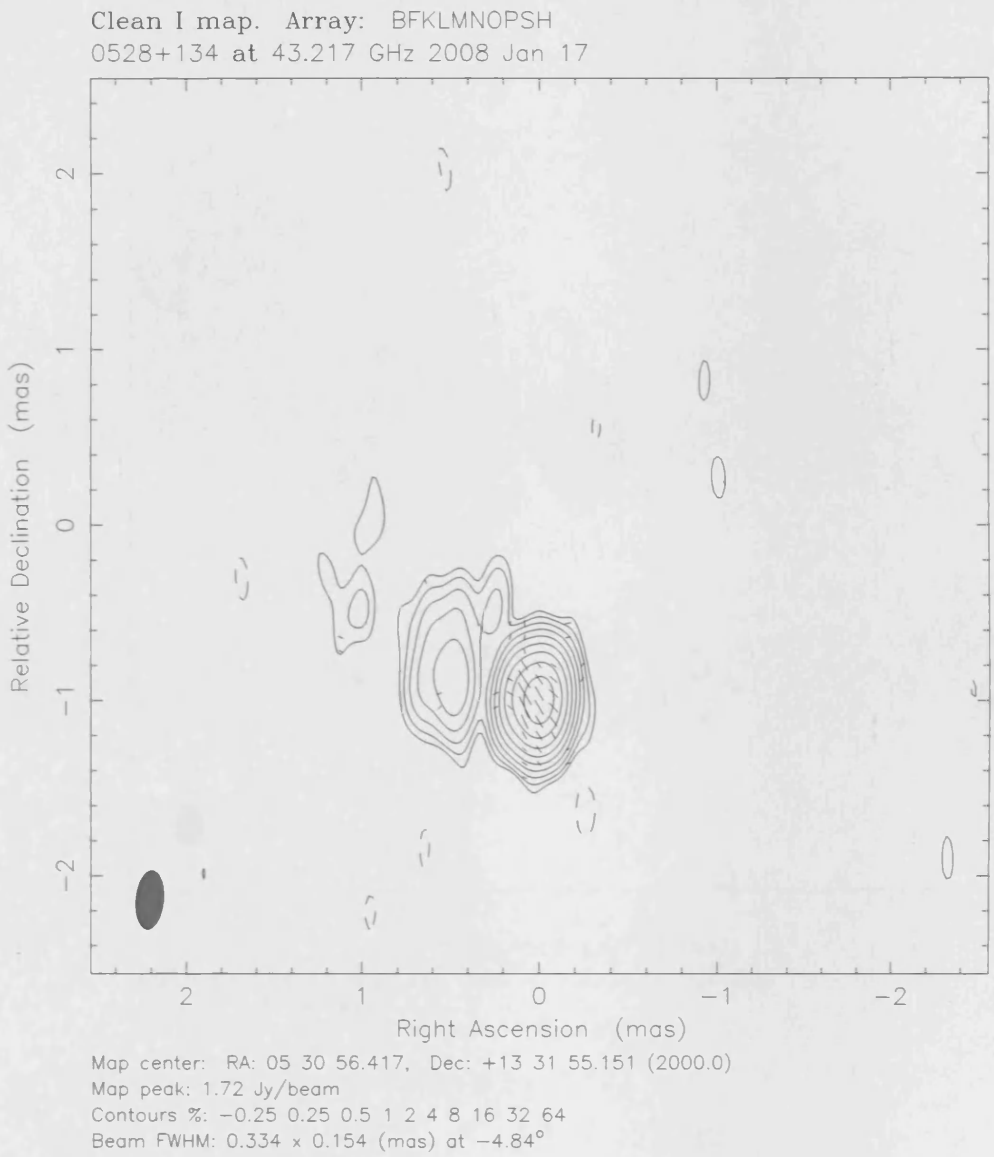

Figure 3.36: January 2008 VLBI Map of 0528+134. For polarisation vectors: 1 mas = 2.50×10^{-1} Jy/beam.

Over the three epochs, the peak flux jumps from $1.02Jy$ to $2.61Jy$ before falling to $0.738Jy$. Again, no polarisation vectors can be seen in the January 2008 epoch, though the core is clearly polarised in August 2007 and November 2007.

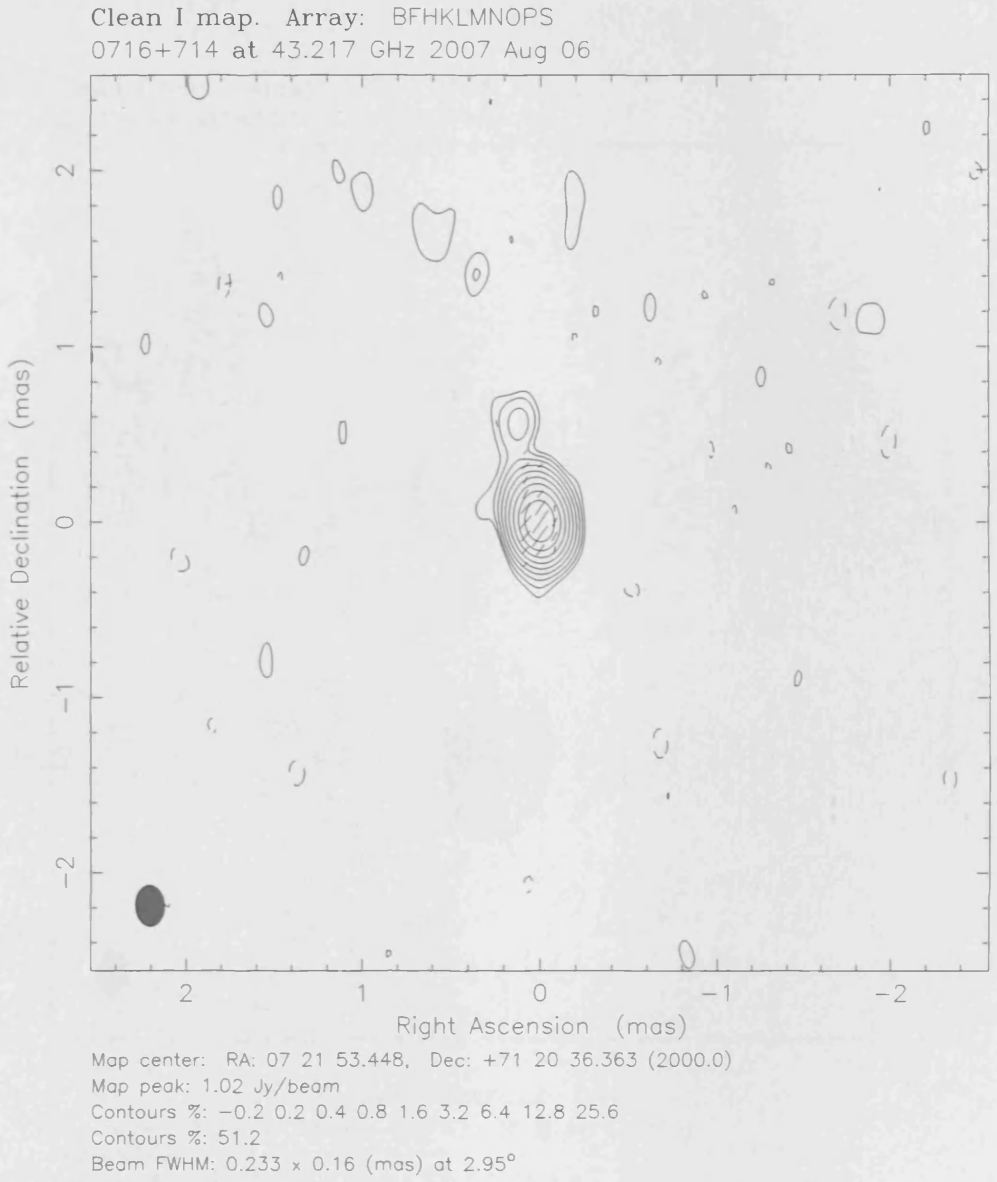

Figure 3.37: August 2007 VLBI Map of 0716+714. For polarisation vectors: 1 mas = $5.00\text{x}10^{-1}$ Jy/beam.

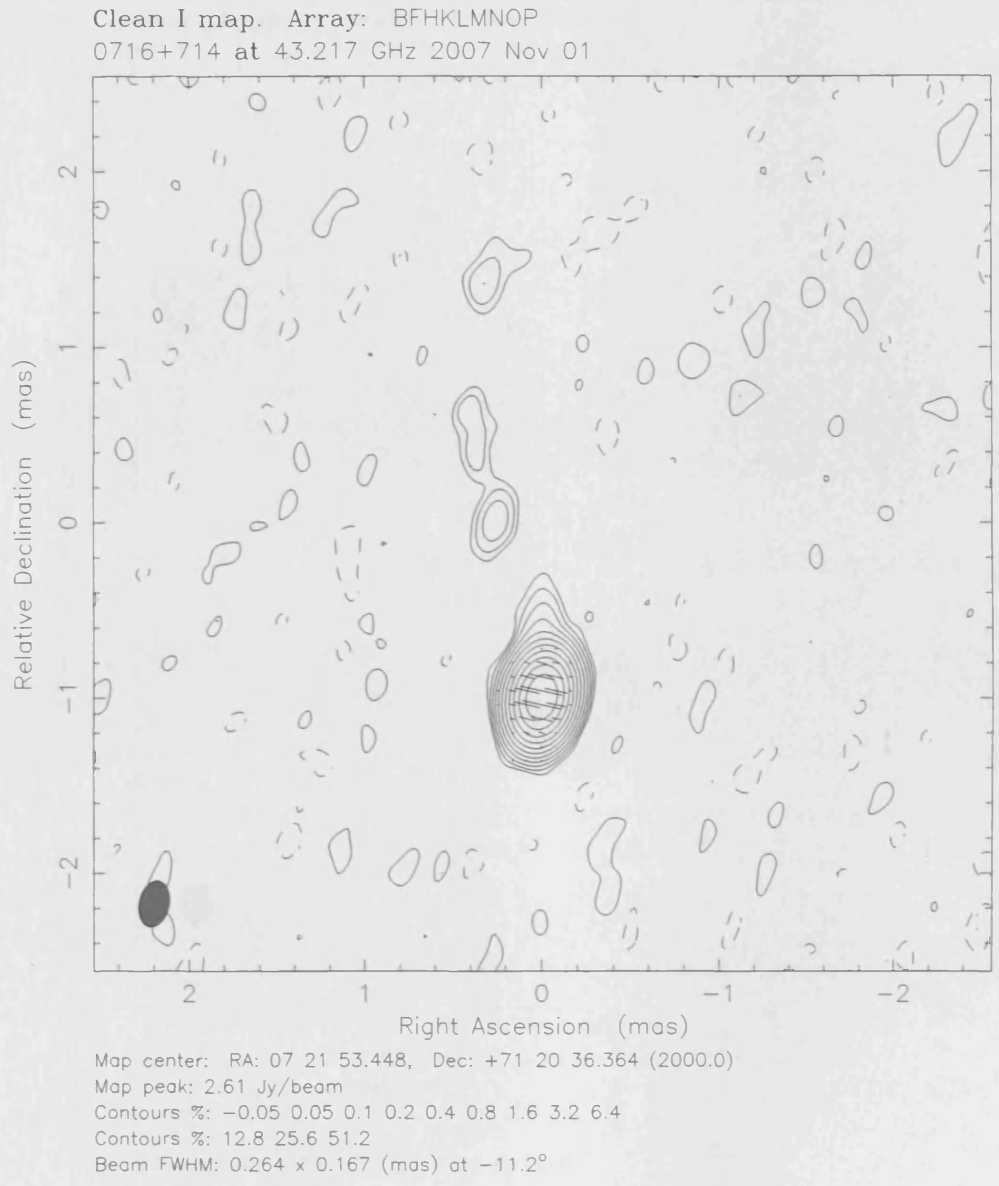

Figure 3.38: November 2007 VLBI Map of 0716+714. For polarisation vectors: 1 mas = 8.33×10^{-1} Jy/beam.

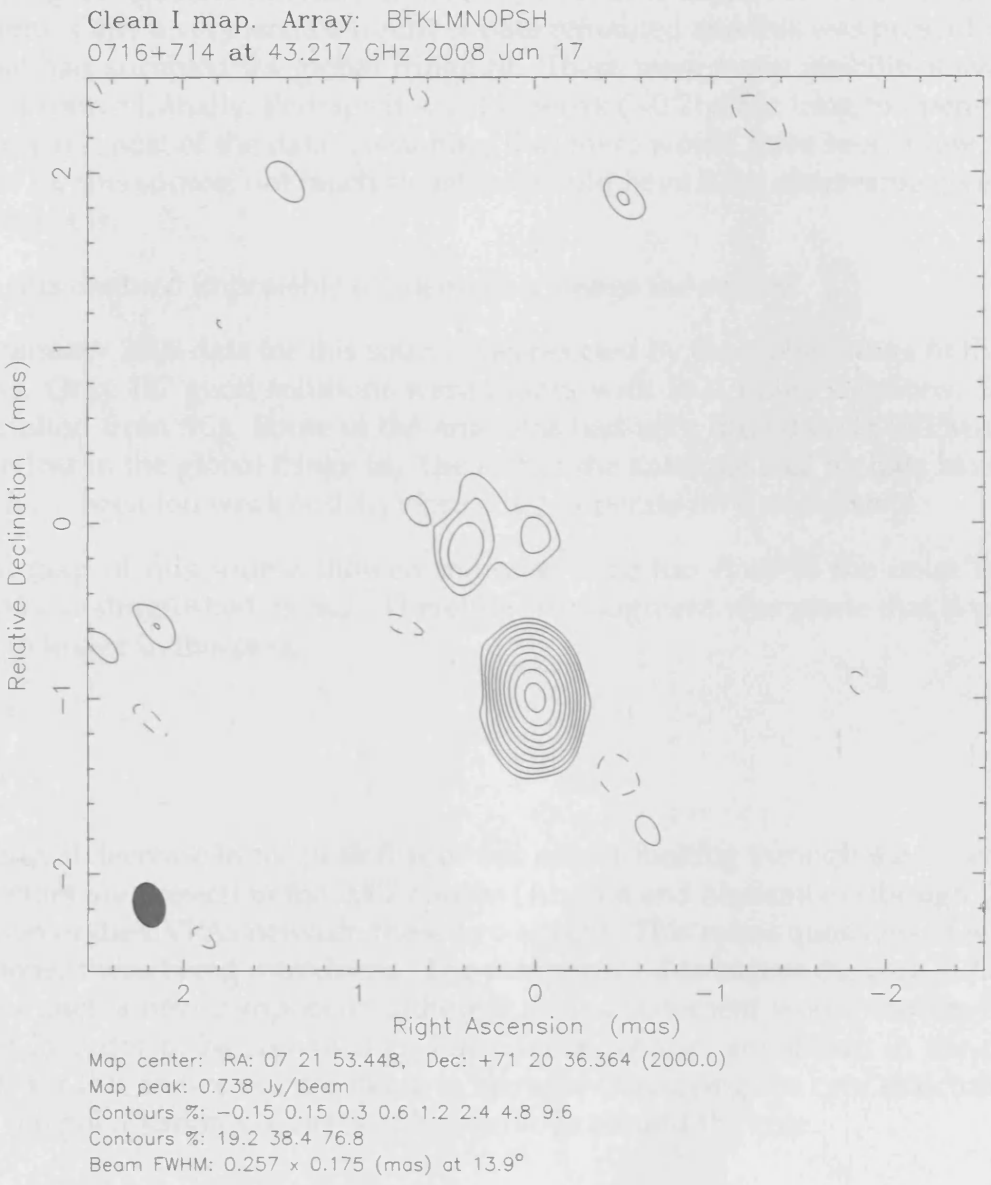

Figure 3.39: January 2008 VLBI Map of 0716+714. For polarisation vectors: 1 mas = $3.57 \text{x} 10^{-1}$ Jy/beam.

0735+178

An image from the November 2007 epoch was the only success in terms of mapping this source. As can be seen, the beam size is very large. This is likely a reflection of how much data was rejected by the global fringe fit in AIPS.

Most of the data for the source in August 2007 was rejected by the global fringe fit (AIPS task fring). Only 150 good solutions were found, with 1146 failed solutions. This caused major problems. Only a very small amount of data remained and this was present in only a few IFs that had survived the global fringe fit. There were many visibilities available to use for this source initially. Perhaps it was too weak ($\sim$0.2Jy) for fring to operate on it without removing most of the data. Assuming that there would have been a low signal-to-noise ratio for this source, not much structure would have been observable given how relatively weak it is.

Therefore it was deemed impossible to adequately image the source.

Most of the January 2008 data for this source was rejected by the global fringe fit that was implemented. Only 187 good solutions were found, with 1021 failed solutions. Serious problems resulted from this. Some of the antennas had very little data in DIFMAP that had not been lost in the global fringe fit. The rest of the antennas had no data at all. The source may have been too weak ($<$0.3Jy) for fring to operate on it adequately.

The residual map of this source showed the core to be too close to the noise level of the image to be distinguished as real. Therefore the judgment was made that it was not worthwhile to image in this case.

0827+243

There is a general decrease in the peak flux of this source looking through the epochs. Polarisation vectors are present in the 2007 epochs (August and November) though there is a large rotation of the EVPAs between these two epochs. This raises questions of whether a new component was being introduced. The component due east of the core in January 2008 could be such a new component, although such a statement would require further investigation in order to be convincing. Polarisation vectors are shown in the core in January 2008 for this source but are likely to be noise overlaying the core structure. The structure of the polarisation vectors is rather tenuous around the core.

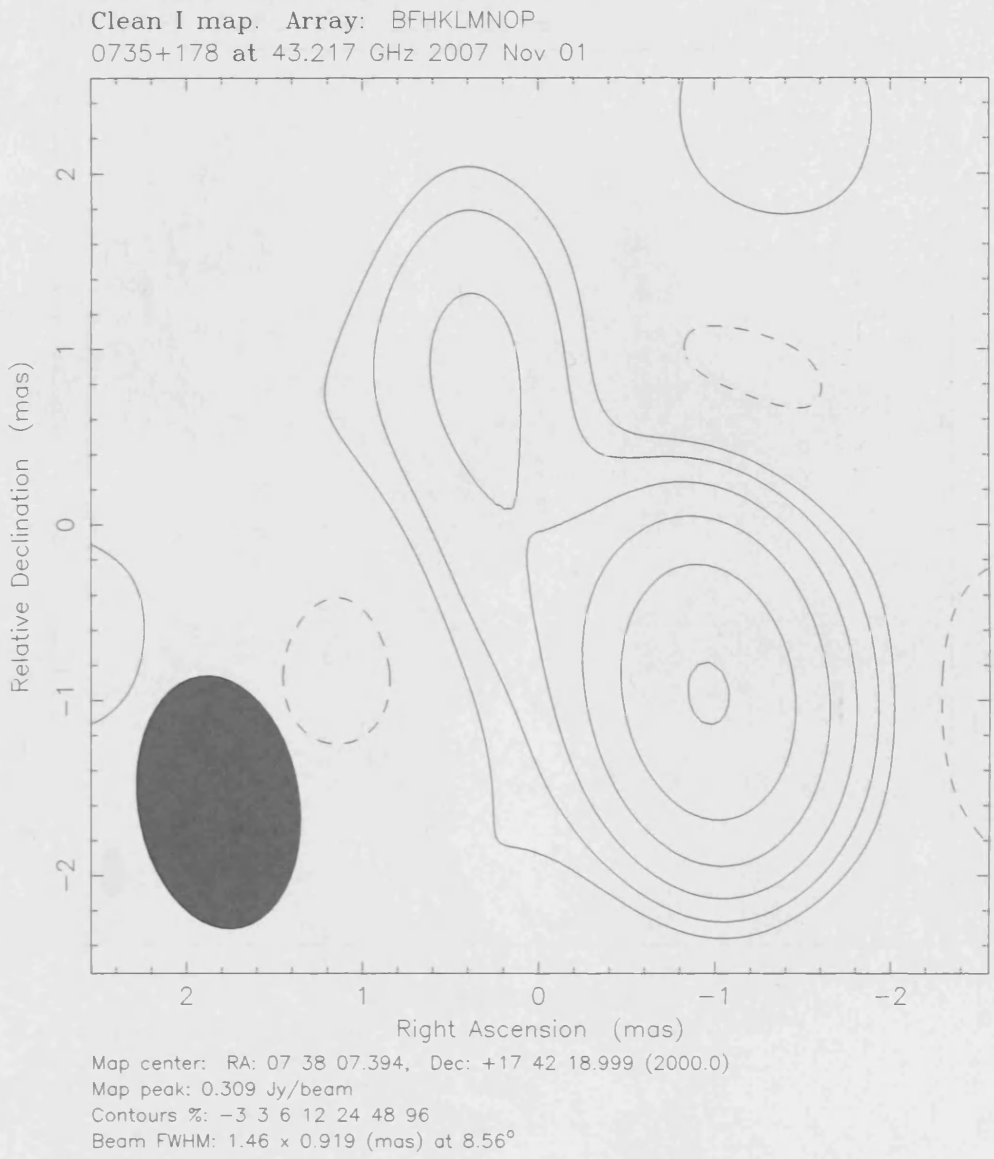

Figure 3.40: November 2007 VLBI Map of 0735+178.

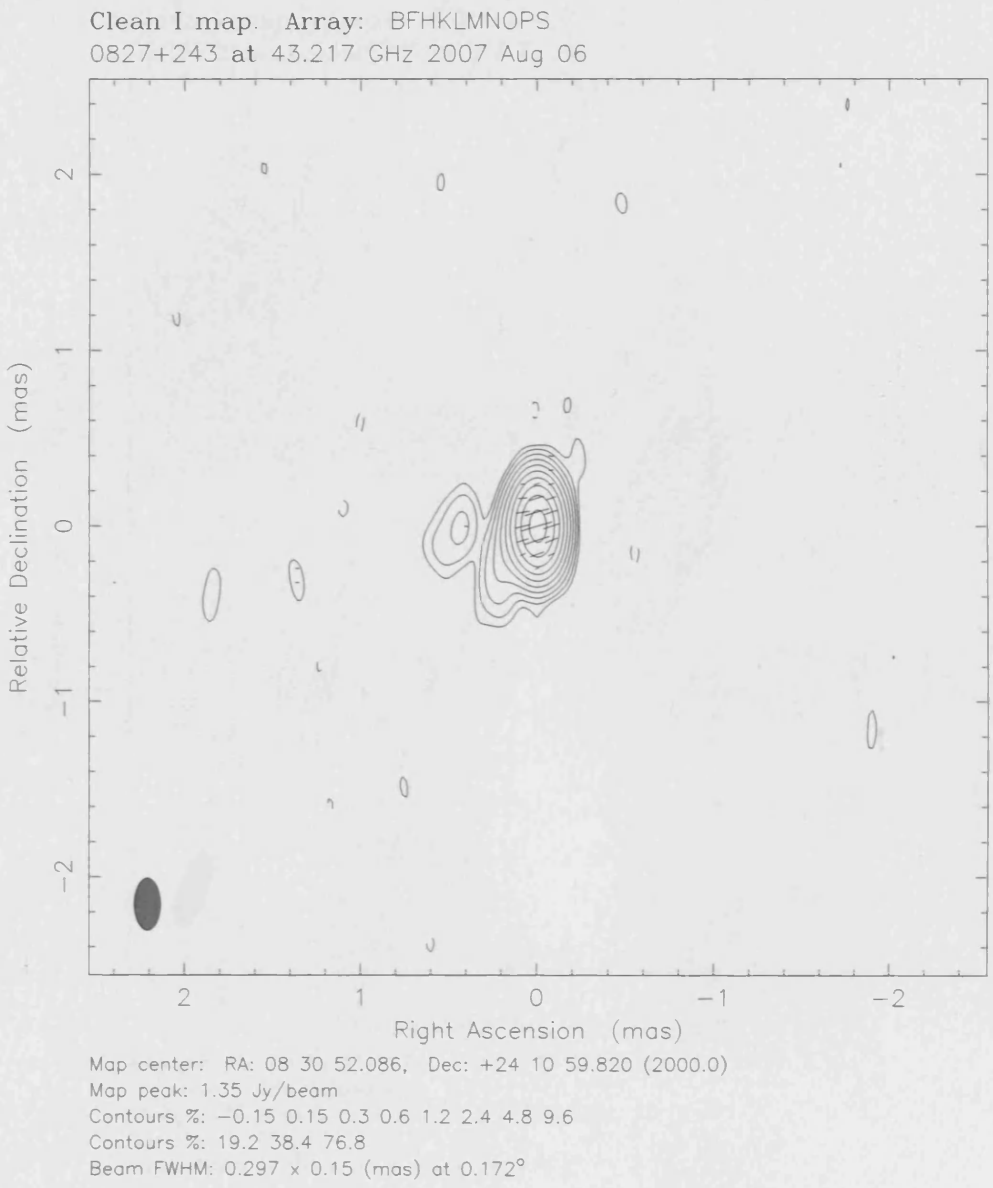

Figure 3.41: Final VLBI Map of 0827+243. For polarisation vectors: 1 mas = 5.00×10^{-1} Jy/beam.

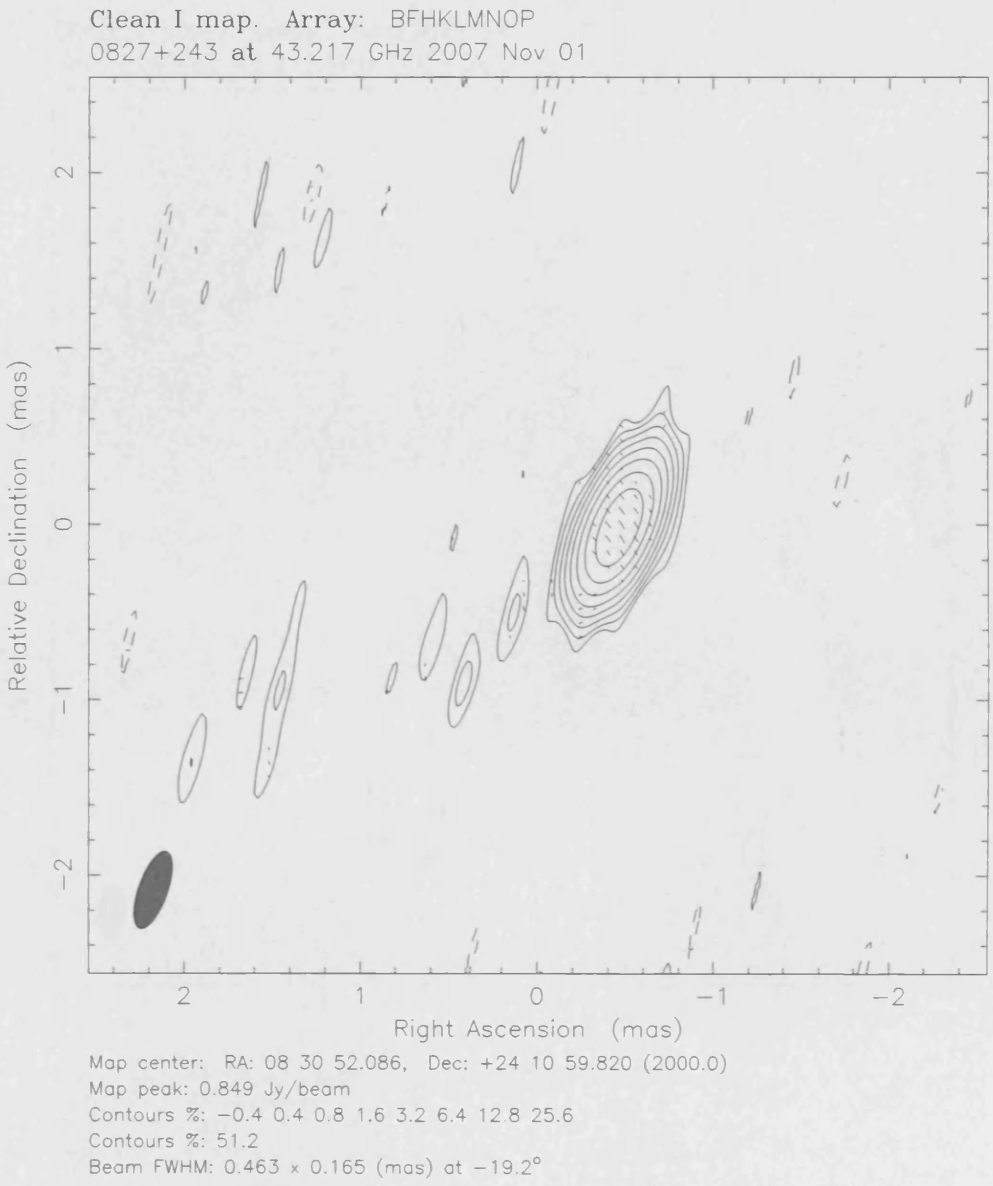

Figure 3.42: November 2007 VLBI Map of 0827+243. For polarisation vectors: 1 mas = $2.50 \text{x} 10^{-1}$ Jy/beam.

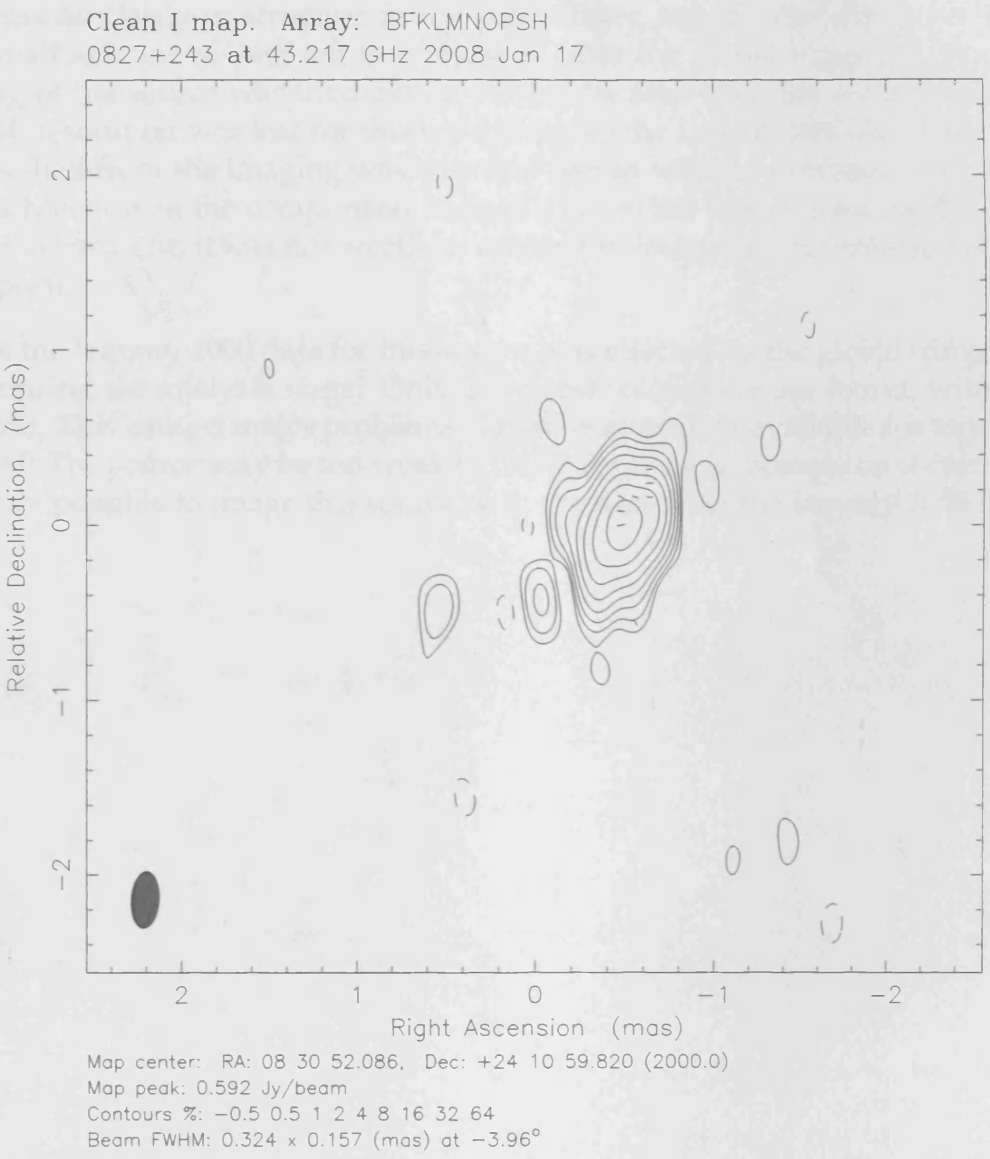

Figure 3.43: January 2008 VLBI Map of 0827+243. For polarisation vectors: 1 mas = 2.50×10^{-1} Jy/beam.

0829+046

No polarisation could be imaged for this source and furthermore imaging was not possible at all for the January 2008 epoch. The maps that were produced have poor resolution resulting from large beam sizes. The cause of this is likely to be the loss of data following the global fringe fit for this source.

Initially, work on this source in the August 2007 epoch was halted due to the fact that there was no clarity or structure in the preliminary image. The reason for this was the very small amount of data left to work with after the global fringe fit. In spite of this, imaging of the source was tried again. As can be seen from the large beam size in Figure 3.44, resolution was lost for this source due to the lack of data mentioned above. All that resulted from the imaging was a central region with no extended emission (some is present however in the comparison image). Due to the lack of data for this source after the global fringe fit, it was not worth an attempt to image any polarisation in the August 2007 epoch.

A lot of the January 2008 data for this source was rejected by the global fringe fit that was made during the analysis stage. Only 153 good solutions were found, with 1111 failed solutions. This caused major problems. There was no data available for any antennas in DIFMAP. The source may be too weak (<0.3Jy) for fring to operate on it currently. It was hence not possible to image this source with the data from the January 2008 epoch.

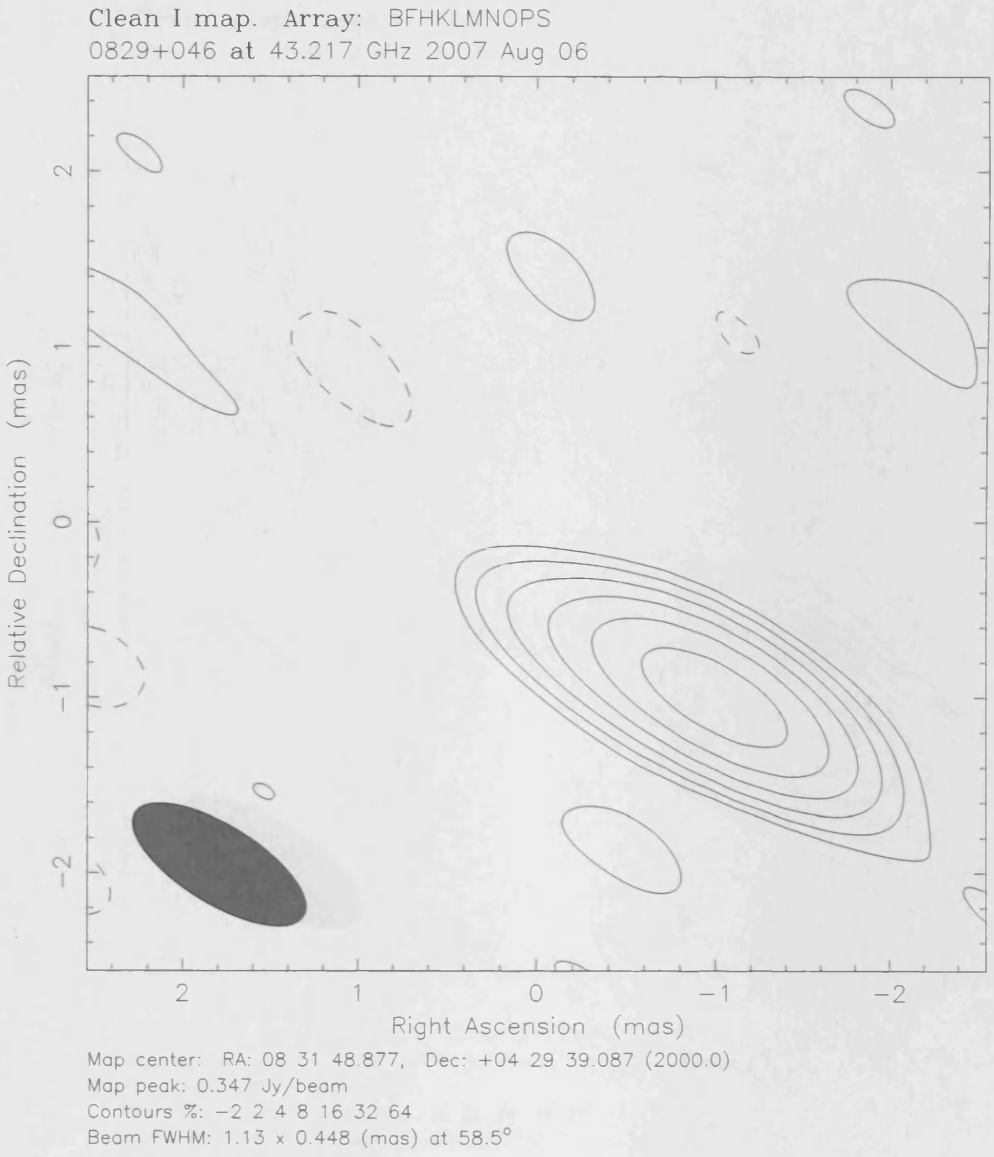

Figure 3.44: August 2007 VLBI Map of 0829+046.

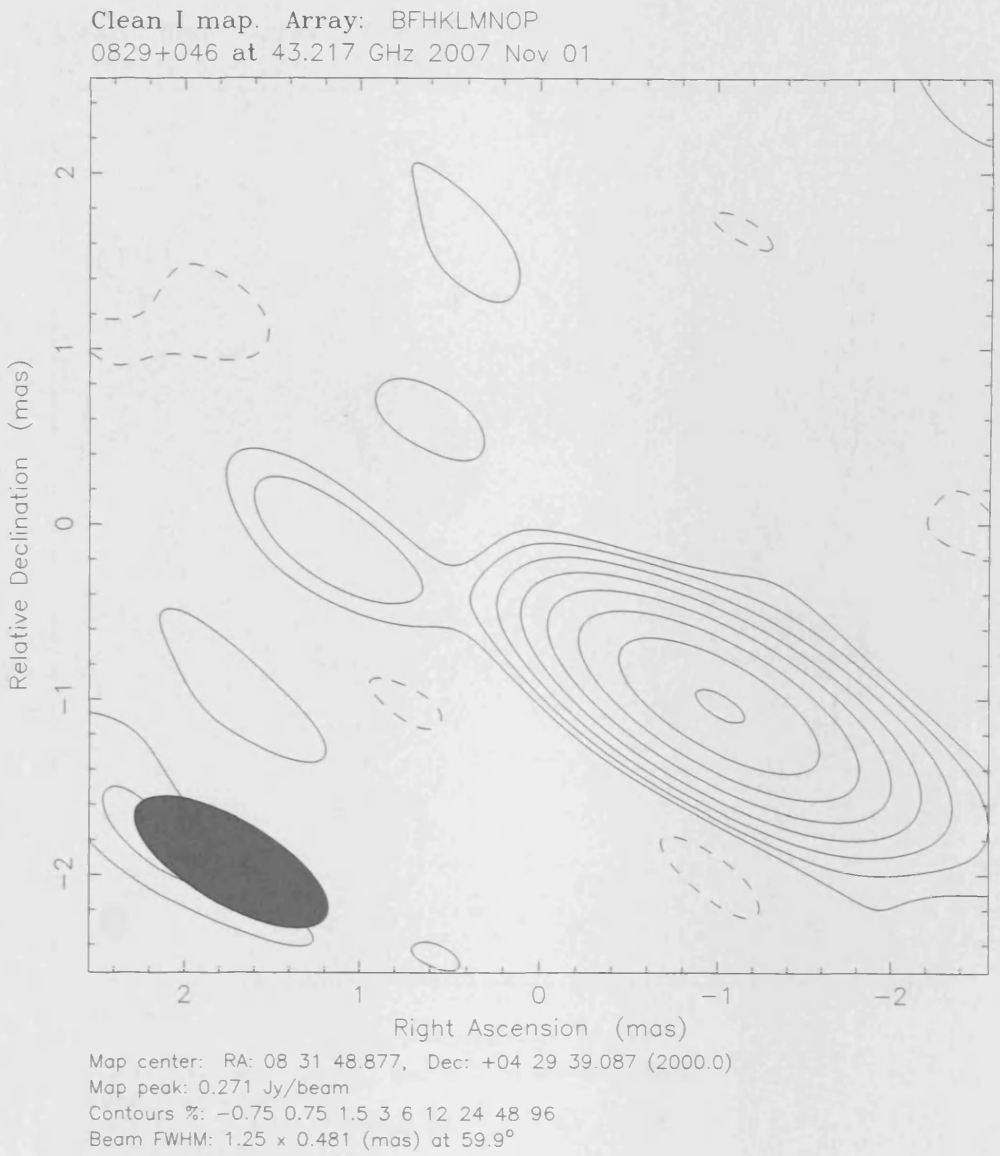

Figure 3.45: November 2007 VLBI Map of 0829+046.

0836+710

This source appears as a dominant core with extended weak emission in August 2007. In the latter two epochs some components can be seen to be emerging from the core region; they are beginning to separate from it. There is not evidence of particularly strong polarisation in the core across the epochs shown. In fact, in the August 2007 image the polarisation is likely to be noise judging by the distribution of the vectors in the core region.

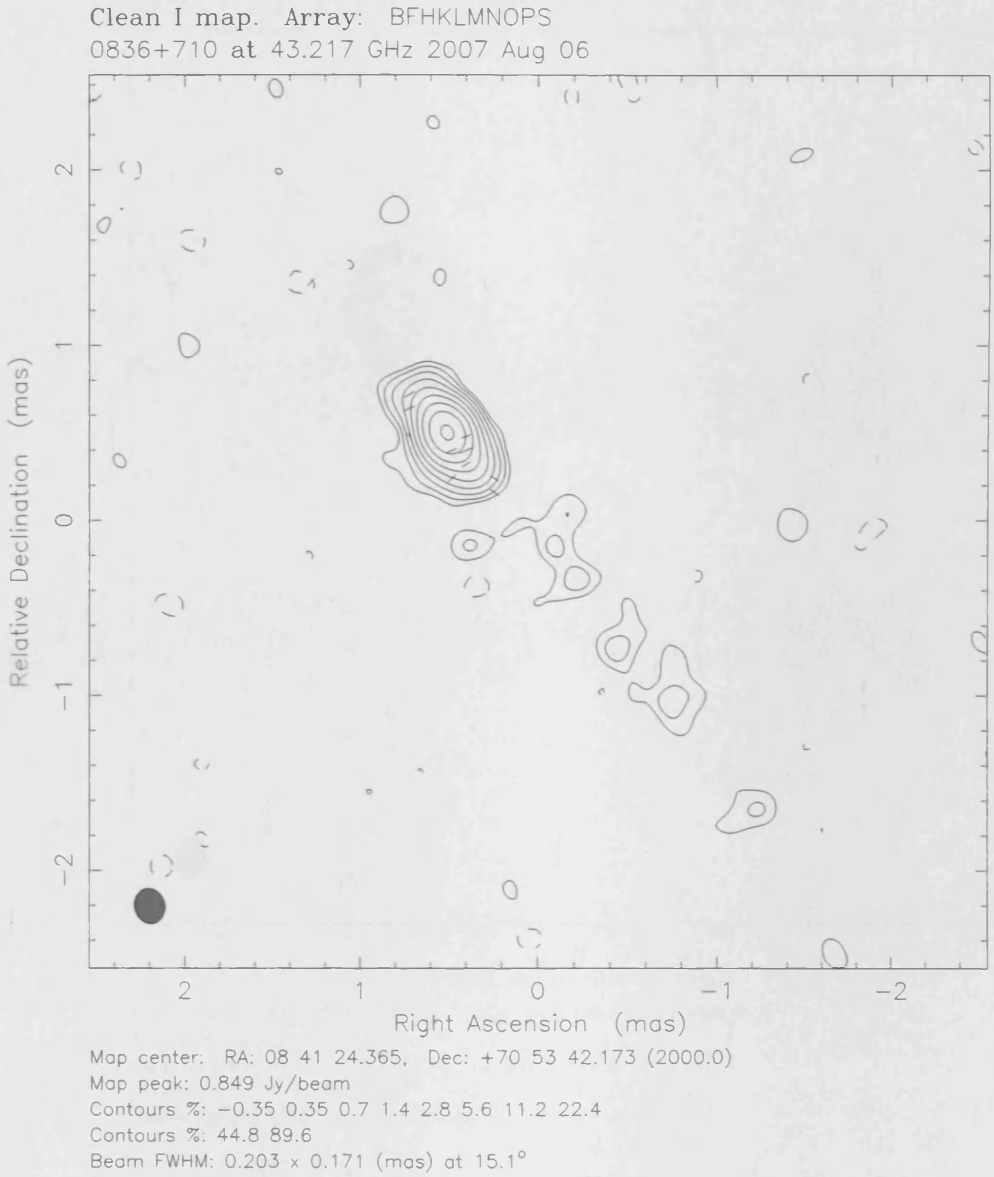

Figure 3.46: August 2007 VLBI Map of 0836+710. For polarisation vectors: 1 mas = $3.57\text{x}10^{-1} Jy/beam$.

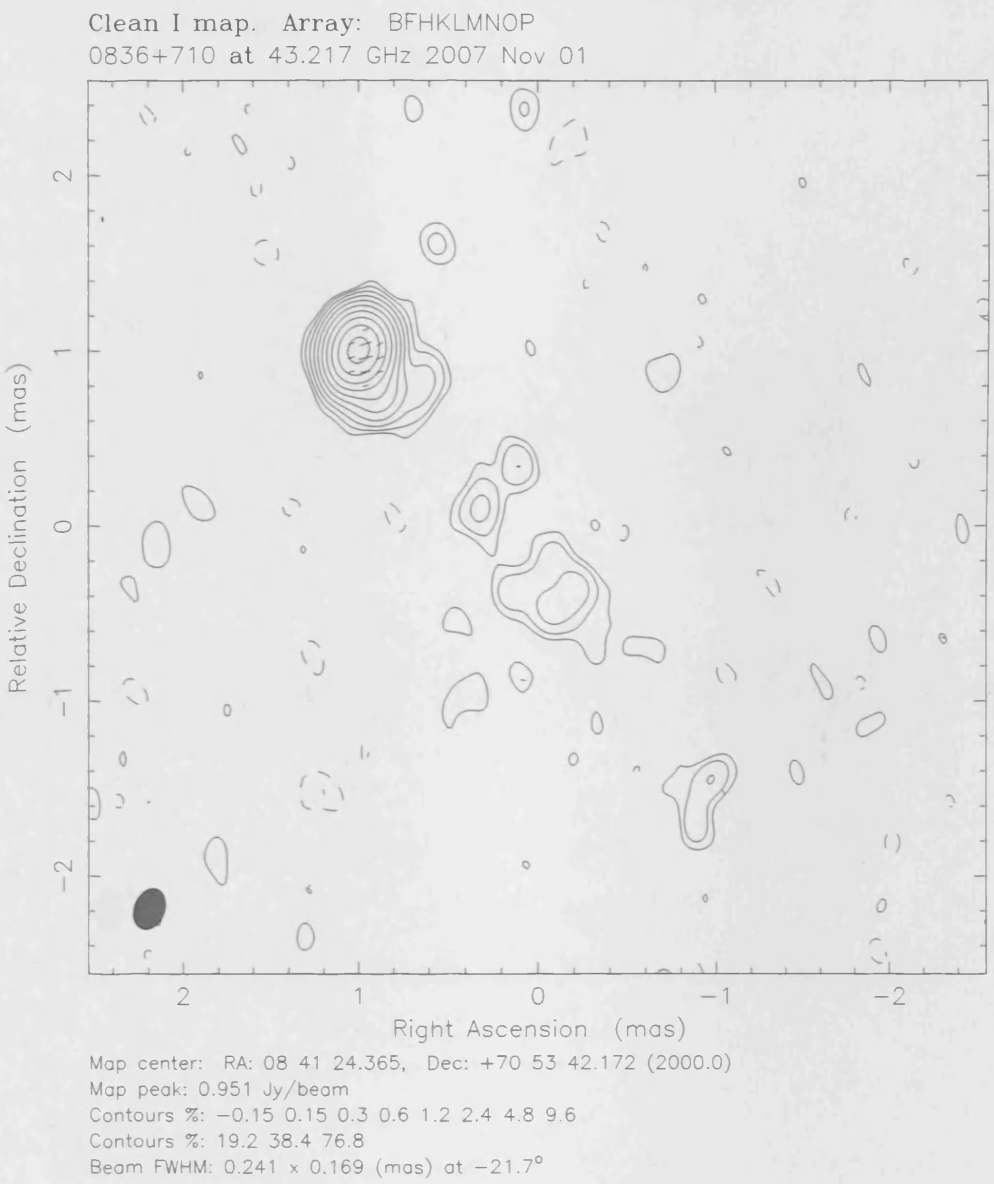

Figure 3.47: November 2007 VLBI Map of 0836+710. For polarisation vectors: 1 mas = 2.50x10^{-1} $Jy/beam$.

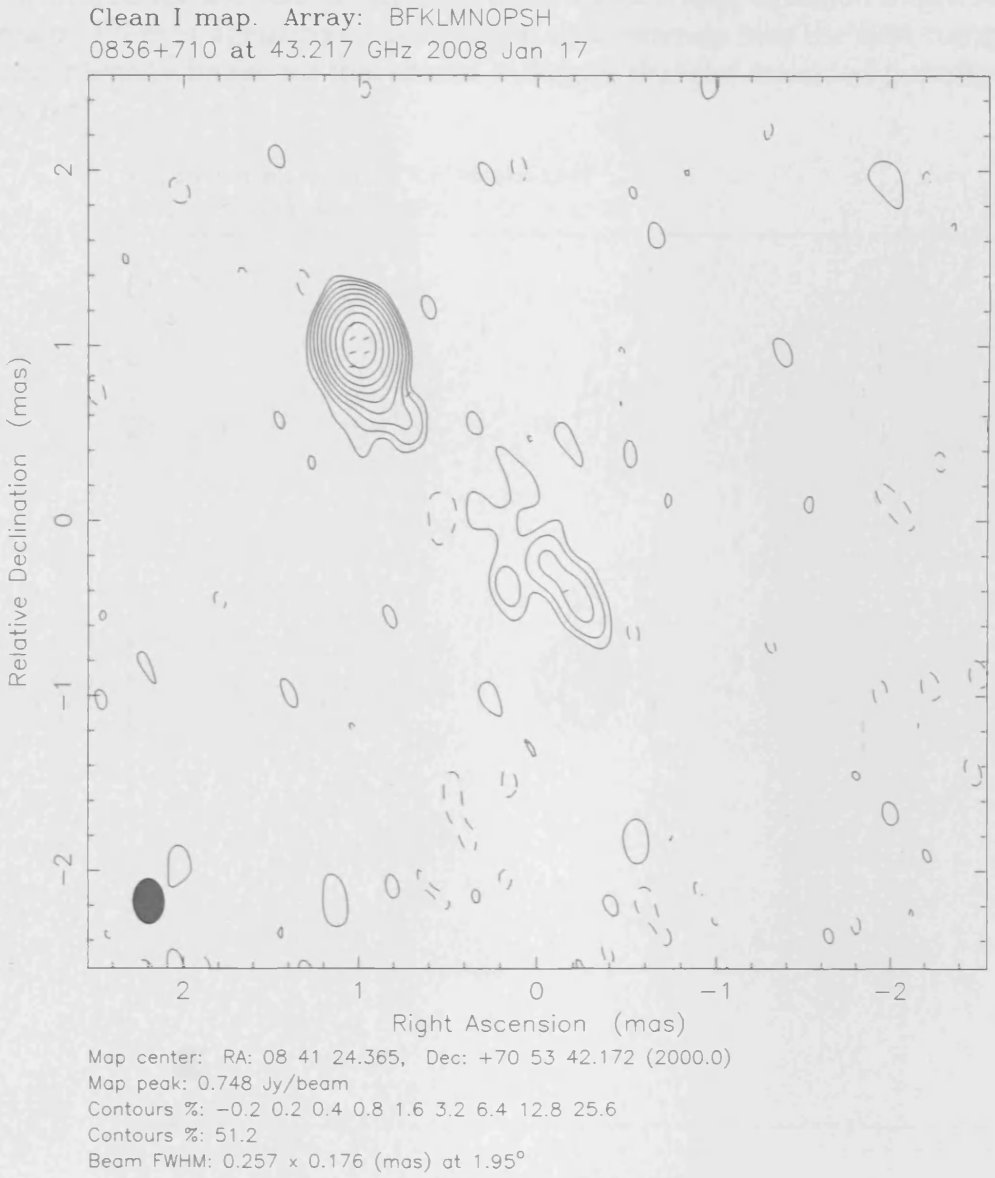

Figure 3.48: January 2008 VLBI Map of 0836+710. For polarisation vectors: 1 mas = $2.50\text{x}10^{-1} Jy/beam$.

Again there is a significant drop in the peak flux going into the January 2008 epoch. For this source the drop is from $1.12Jy$ to $0.495Jy$. The polarisation in August 2007 resides predominantly in the core with some vectors in the first component (these are too weak to be realistically considered as noise). In the November 2007 epoch there is also core polarisation but this appears to extend into the first component. The polarised intensity image produced for this source suggests that this extended emission might be real. In the final image, there is again core polarisation that extends into the first component. The polarised intensity image for this source indicates that the extended polarisation is quite possibly real.

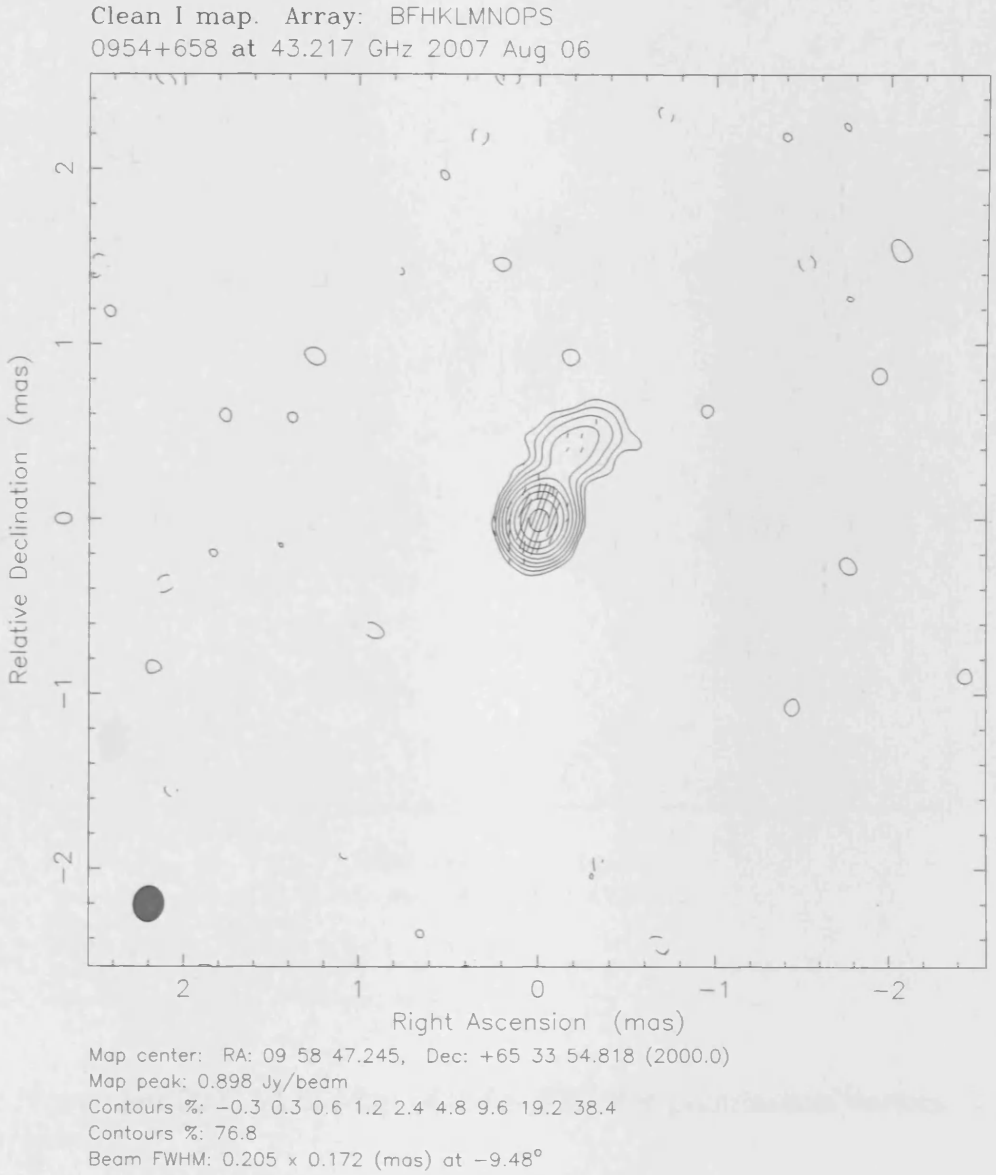

Figure 3.49: August 2007 VLBI Map of 0954+658. For polarisation vectors: 1 mas = 5.00x10^{-1} $Jy/beam$.

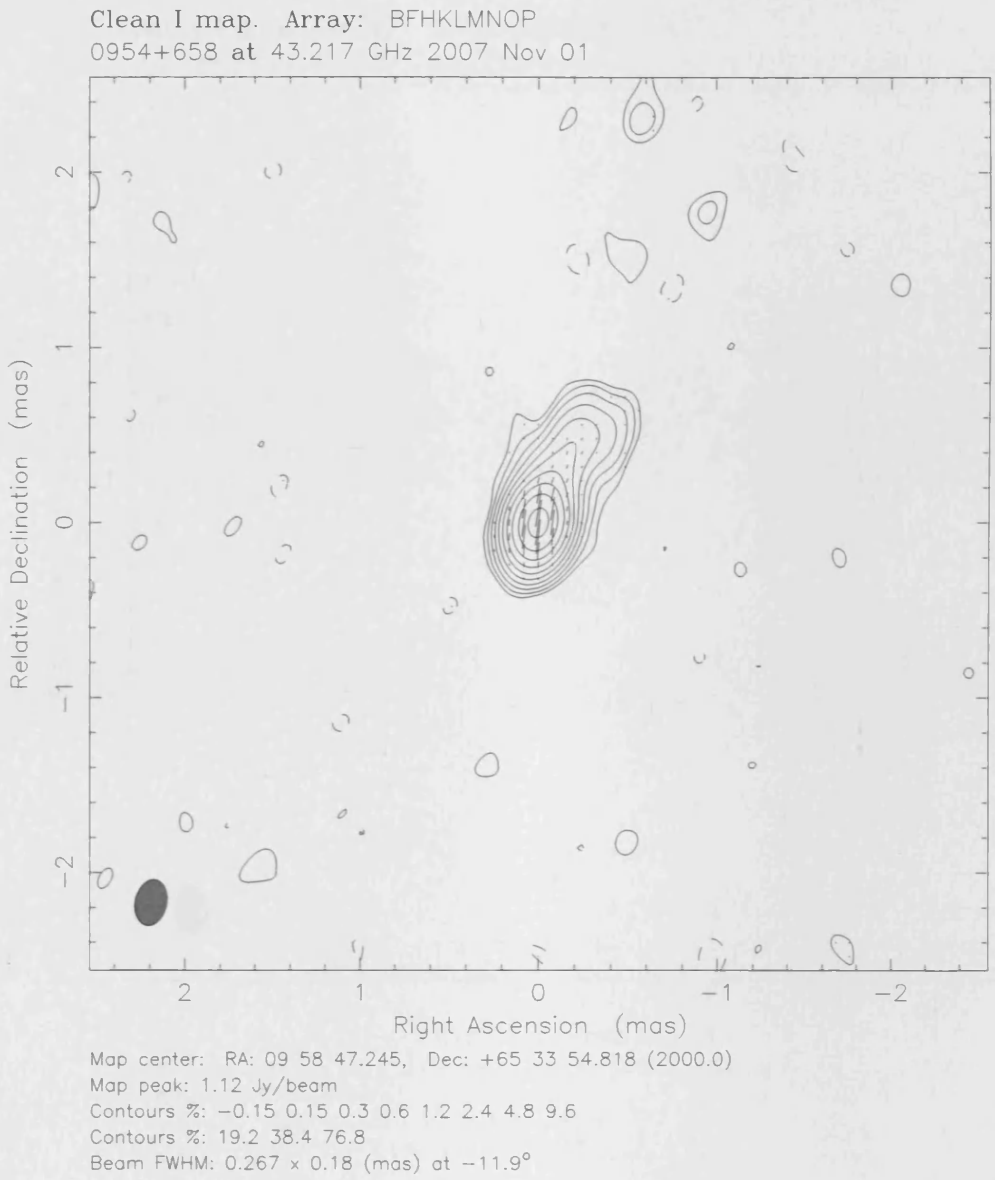

Figure 3.50: November 2007 VLBI Map of 0954+658. For polarisation vectors: 1 mas = $8.33\text{x}10^{-1} Jy/beam$.

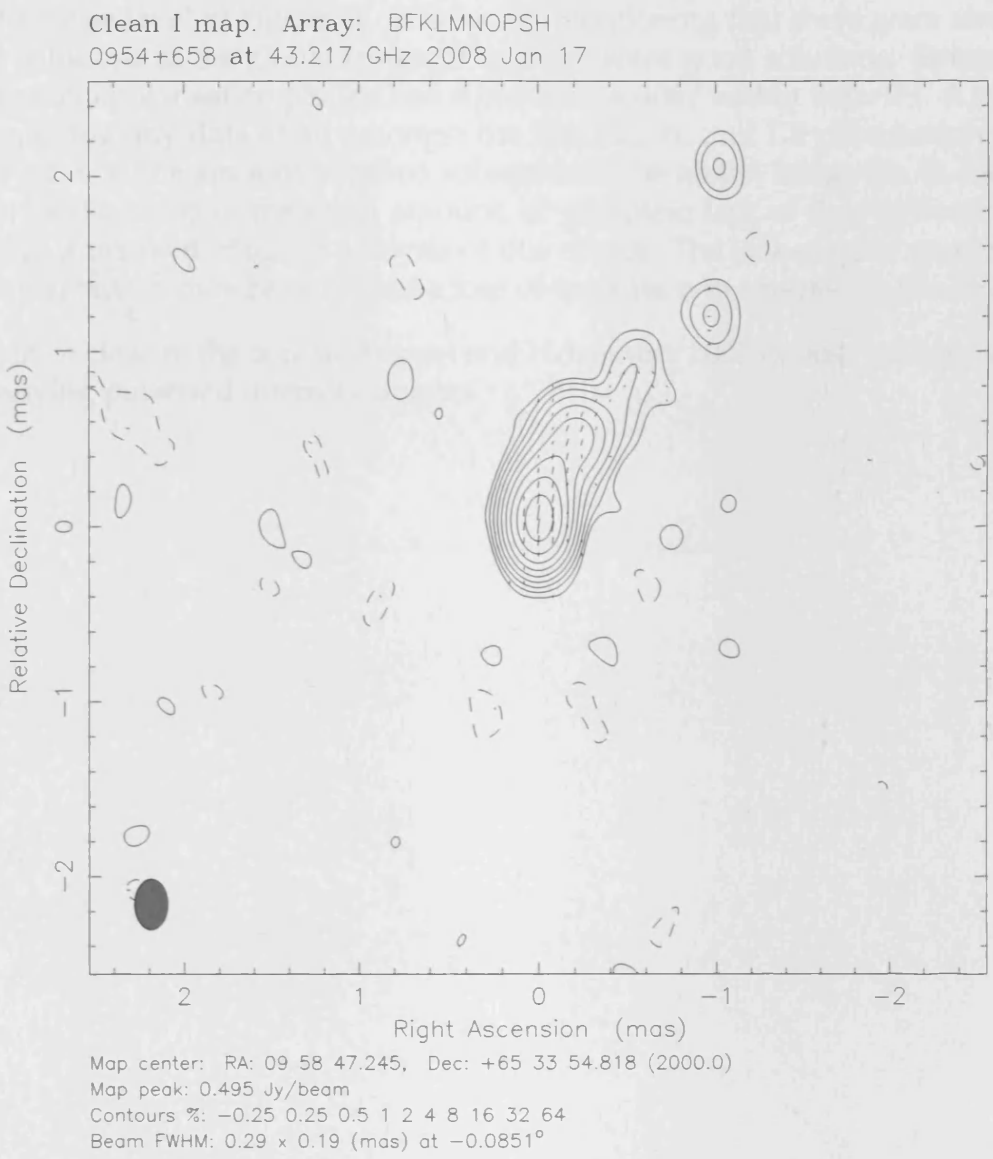

Figure 3.51: January 2008 VLBI Map of 0954+658. For polarisation vectors: 1 mas = $3.13\text{x}10^{-1} Jy/beam$.

1127-145

The January 2008 image has a very large beam size that has caused poor resolution. As has been mentioned before, this is likely due to a loss of data following the global fringe fit for this source in January 2008.

Extended weak structure was seen in this source several mas from the core. The polarised intensity in the core appears to be real, but the other polarisation structures are approximately at the noise level of Figure **??**. It is worth mentioning that there were almost as many failed solutions in the global fringe fit as there were good solutions. Some of the RR and LL parallel polarisation phases had significant scatter within their IFs. A handful of IFs were missing any data at all amongst the RR, LL, RL and LR polarisations. This was probably due to the amount of failed solutions in the global fringe fit. In turn, *this* was likely to be the cause of the small amount, or complete lack of data left over when inspecting each antenna during the analysis of this source. The lack of good quantities of data for many antennas may have caused a loss of resolution in images for this source.

Polarisation in or close to the core in August and November 2007 is close to noise level in the accompanying polarised intensity images.

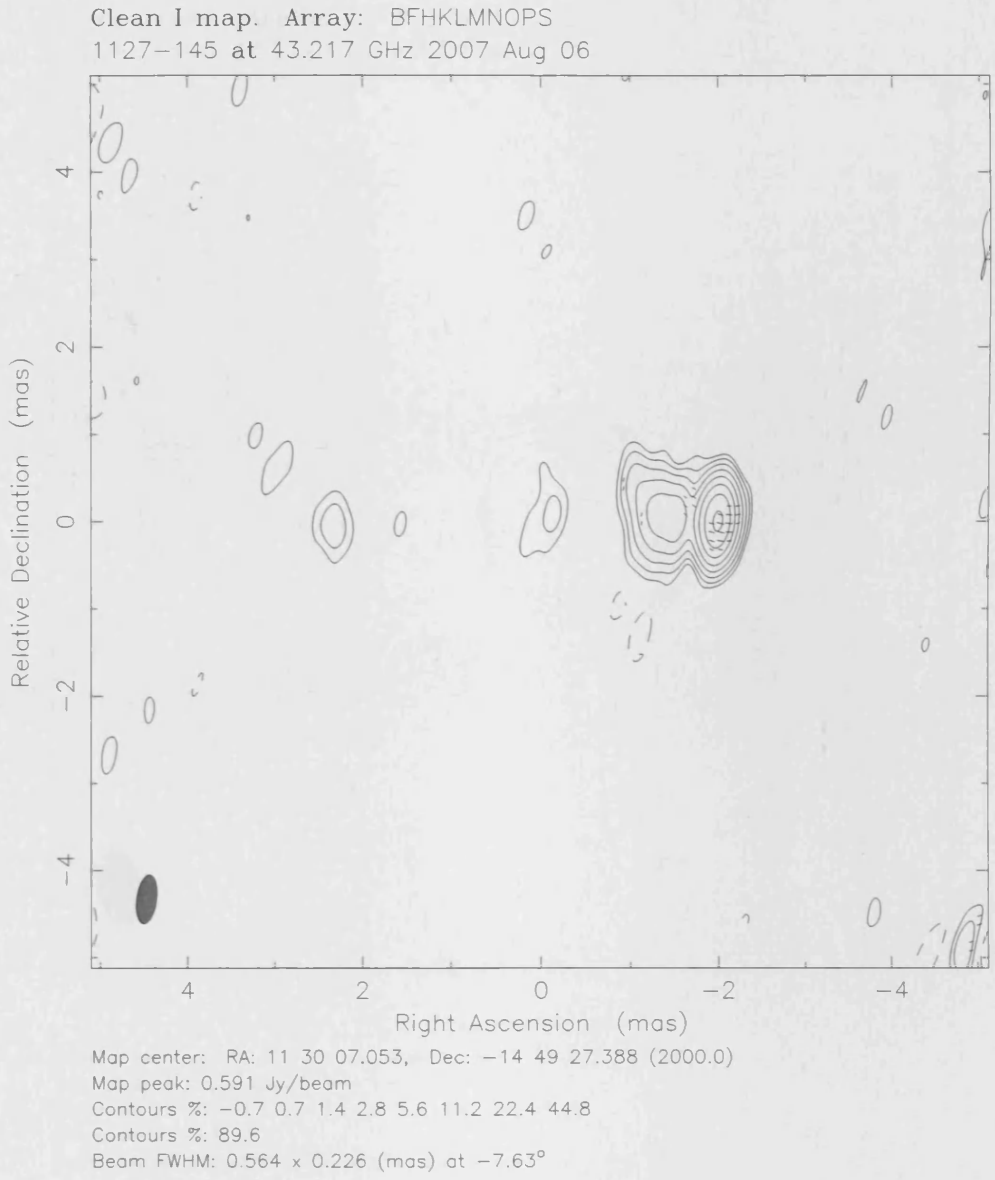

Figure 3.52: August 2007 VLBI Map of 1127-145. For polarisation vectors: 1 mas = 5.00x10^{-1}*Jy/beam*.

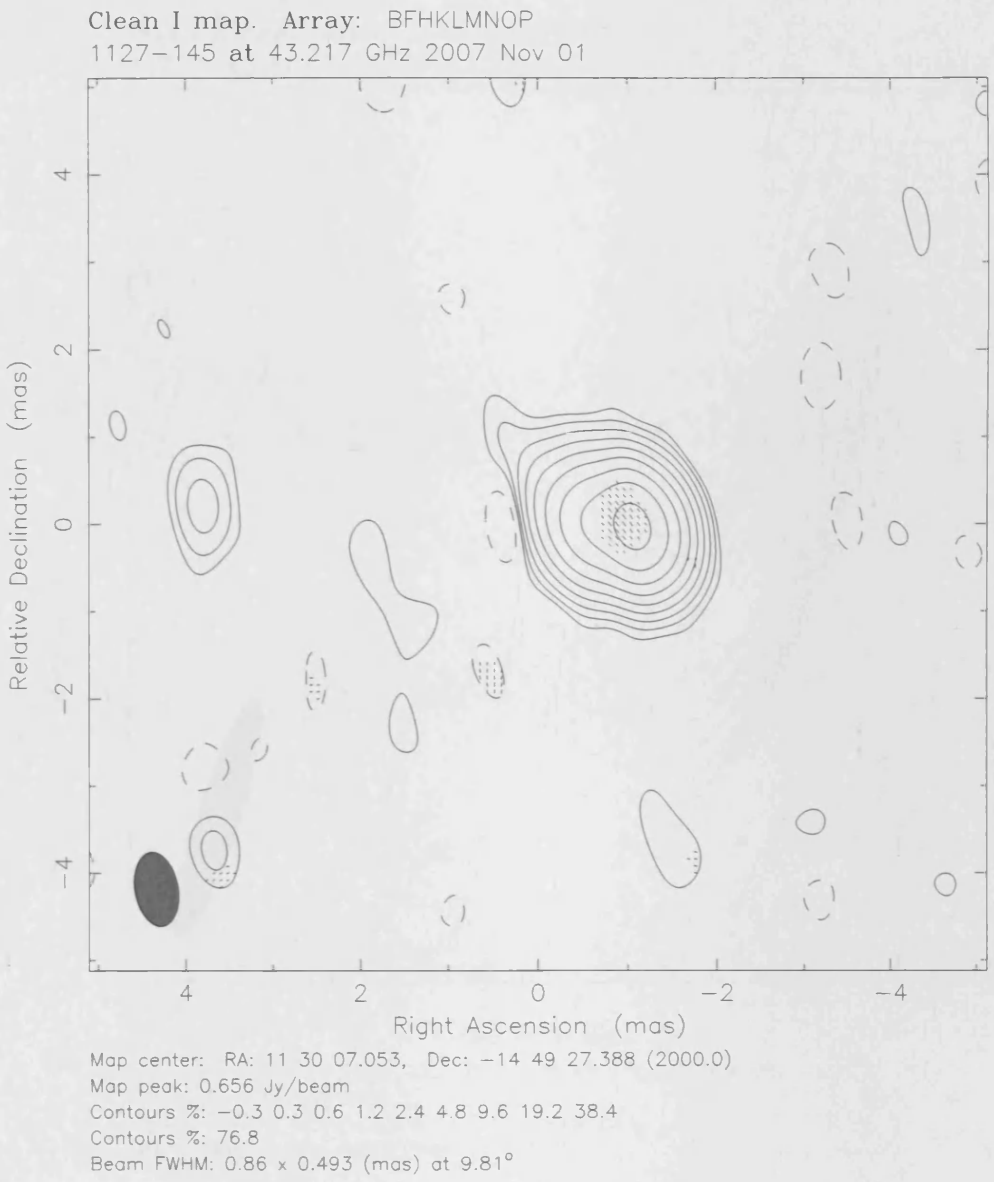

Figure 3.53: November 2007 VLBI Map of 1127-145. For polarisation vectors: 1 mas = 5.00x10^{-1} $Jy/beam$.

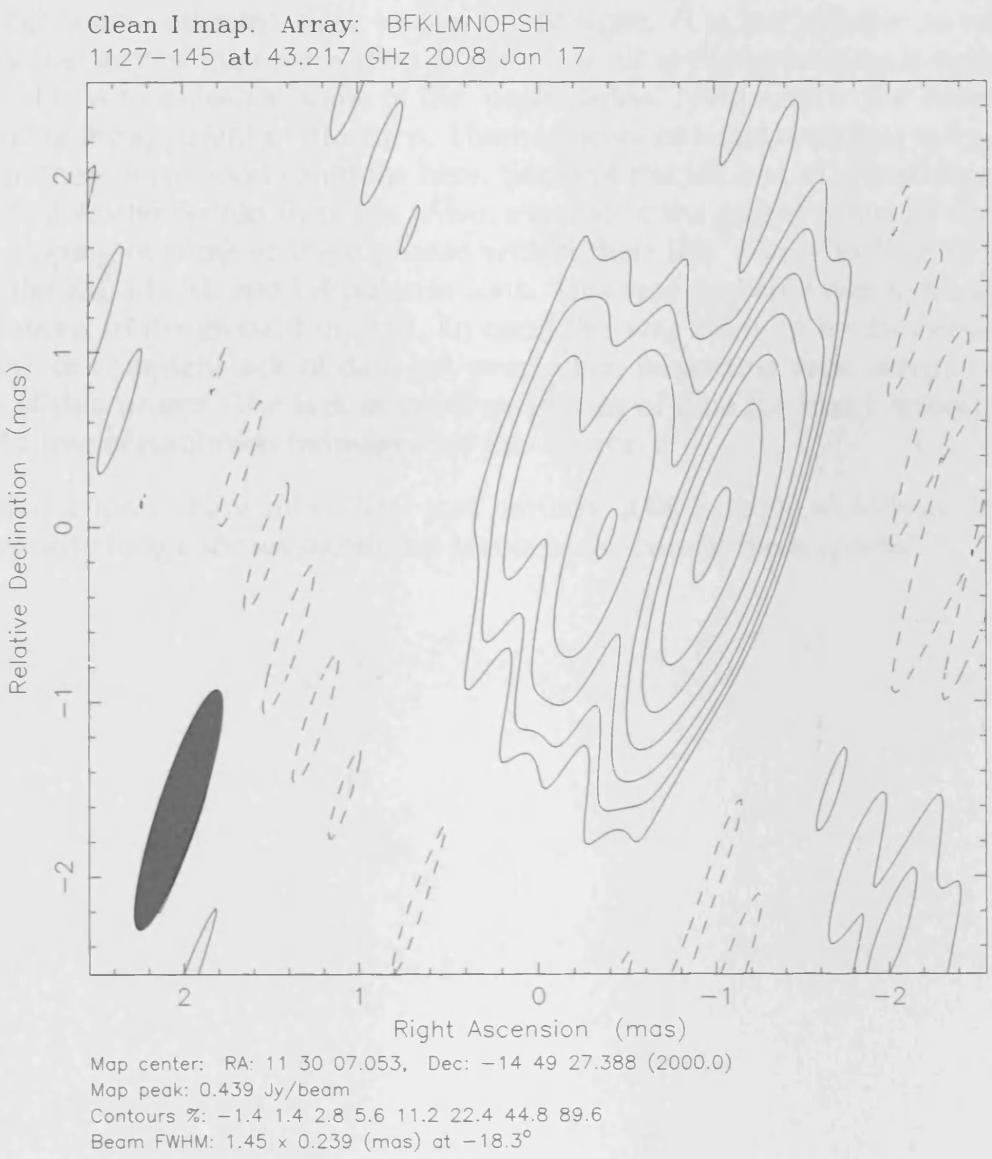

Figure 3.54: January 2008 VLBI Map of 1127-145. For polarisation vectors: 1 mas = 3.57x$10^{-1} Jy/beam$.

1156+295

The extended emission in January 2008 for this source is strange in that it is directed in two directions away from the core. The extended emission nearly due east of the core is rather weak so might not be real. The slightly stronger emission moving away from the core in a northwesterly direction might demonstrate a swing in the jet from its general direction in the other two earlier epochs.

This is another source oriented close to the line of sight. It is not possible to say with any certainty that any of the polarisation is real. It is all at the approximate noise level of the map. This is true despite some of the 'polarisation' lying near to the central core region and along the apparent jet direction. There were more failed solutions in the global fringe fit than there were good solutions here. Some of the RR and LL parallel polarisation phases had scatter within their IFs. Also, even after the global fringe fit there was some slight sloping of some of these phases within their IFs. Some IFs had no data at all amongst the RR, LL, RL and LR polarisations. This was probably due to the amount of failed solutions in the global fringe fit. In turn, *this* was likely to be the cause of the small amount, or complete lack of data left over when inspecting each antenna during the analysis of this source. The lack of good quantities of data for many antennas may have caused a loss of resolution in images for this source.

The core polarisation in November 2007 and January 2008 is likely to be real since the polarised intensity image shows significant levels in the core in these epochs.

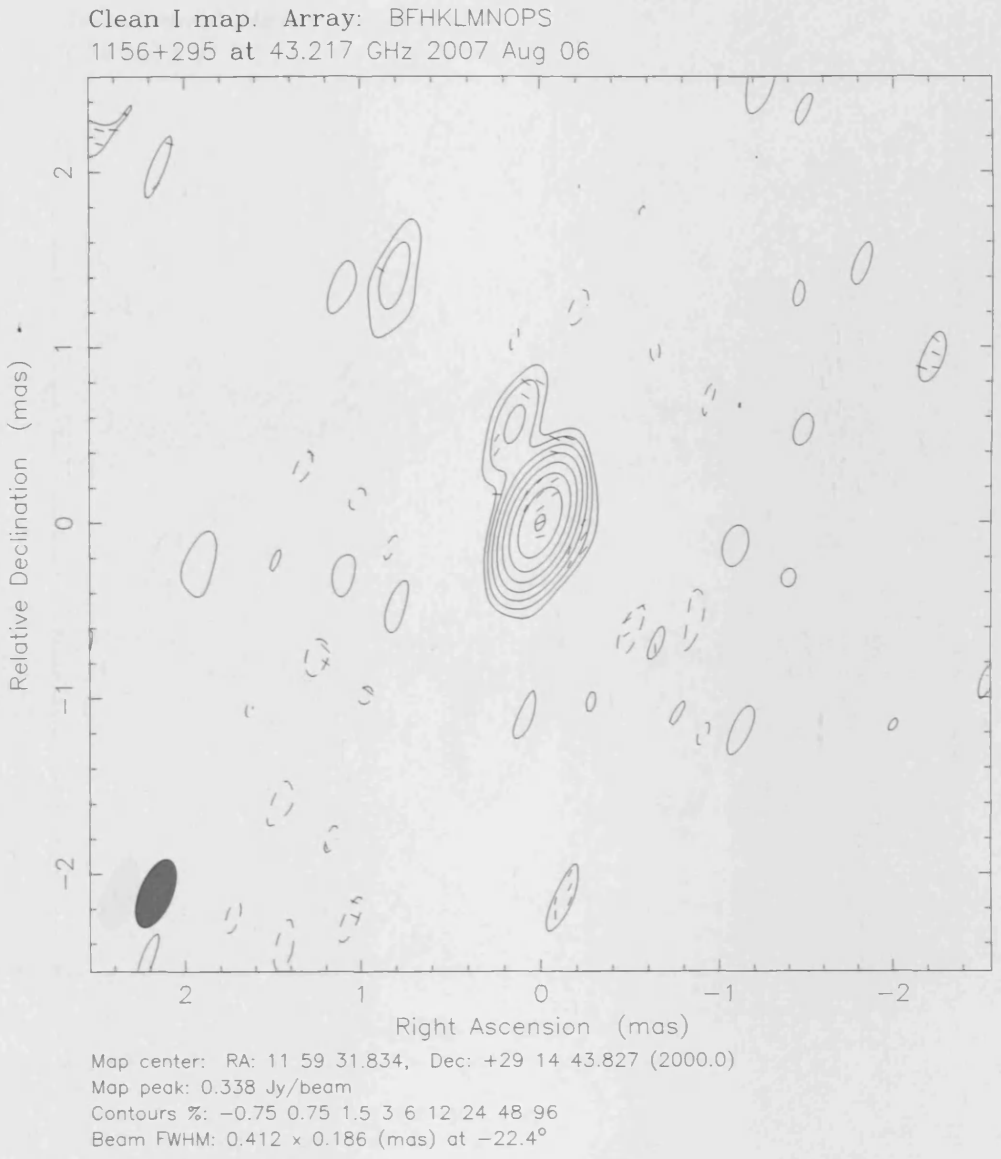

Figure 3.55: August 2007 VLBI Map of 1156+295. For polarisation vectors: 1 mas = 5.00x10^{-1}*Jy/beam*.

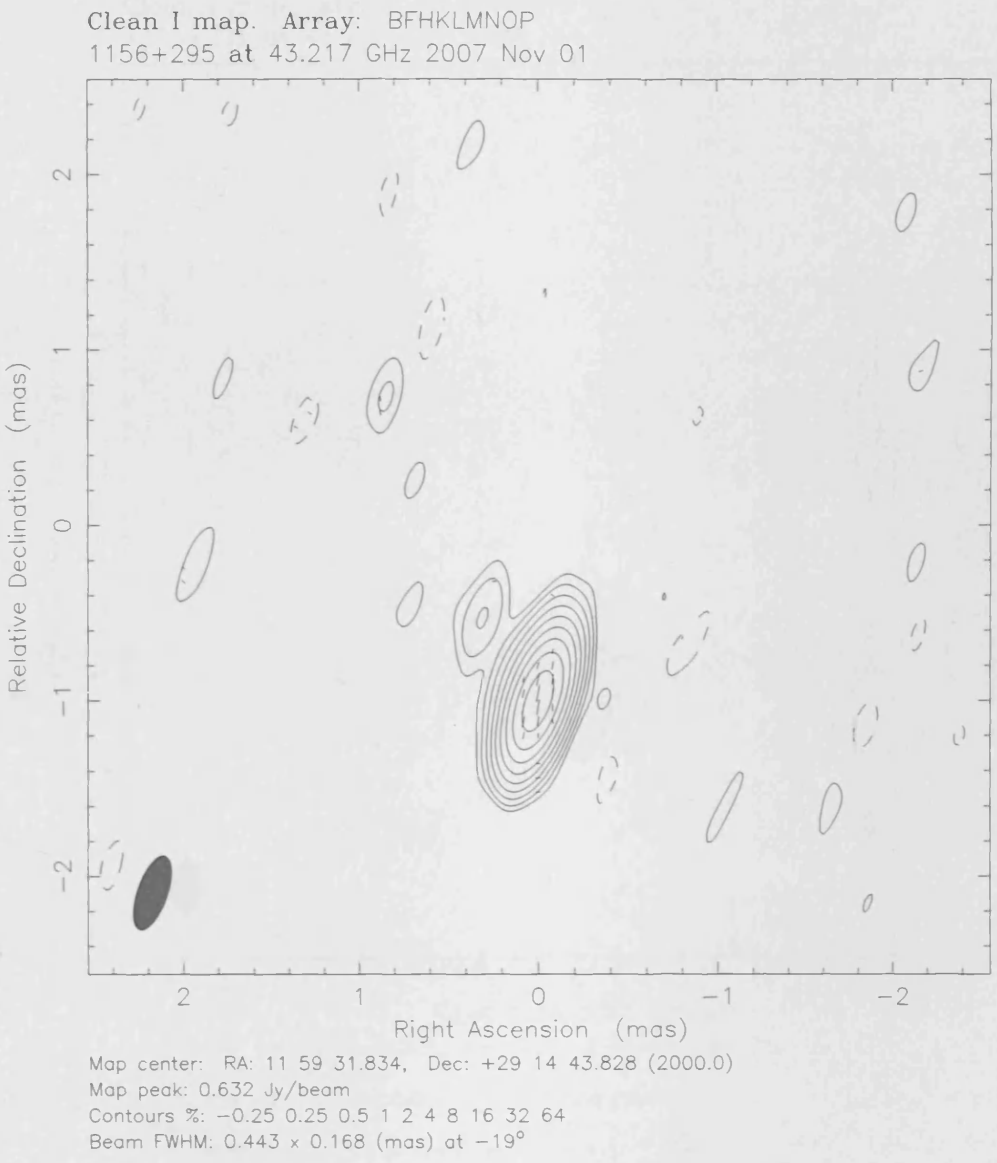

Figure 3.56: November 2007 VLBI Map of 1156+295. For polarisation vectors: 1 mas = 2.50x10^{-1} $Jy/beam$.

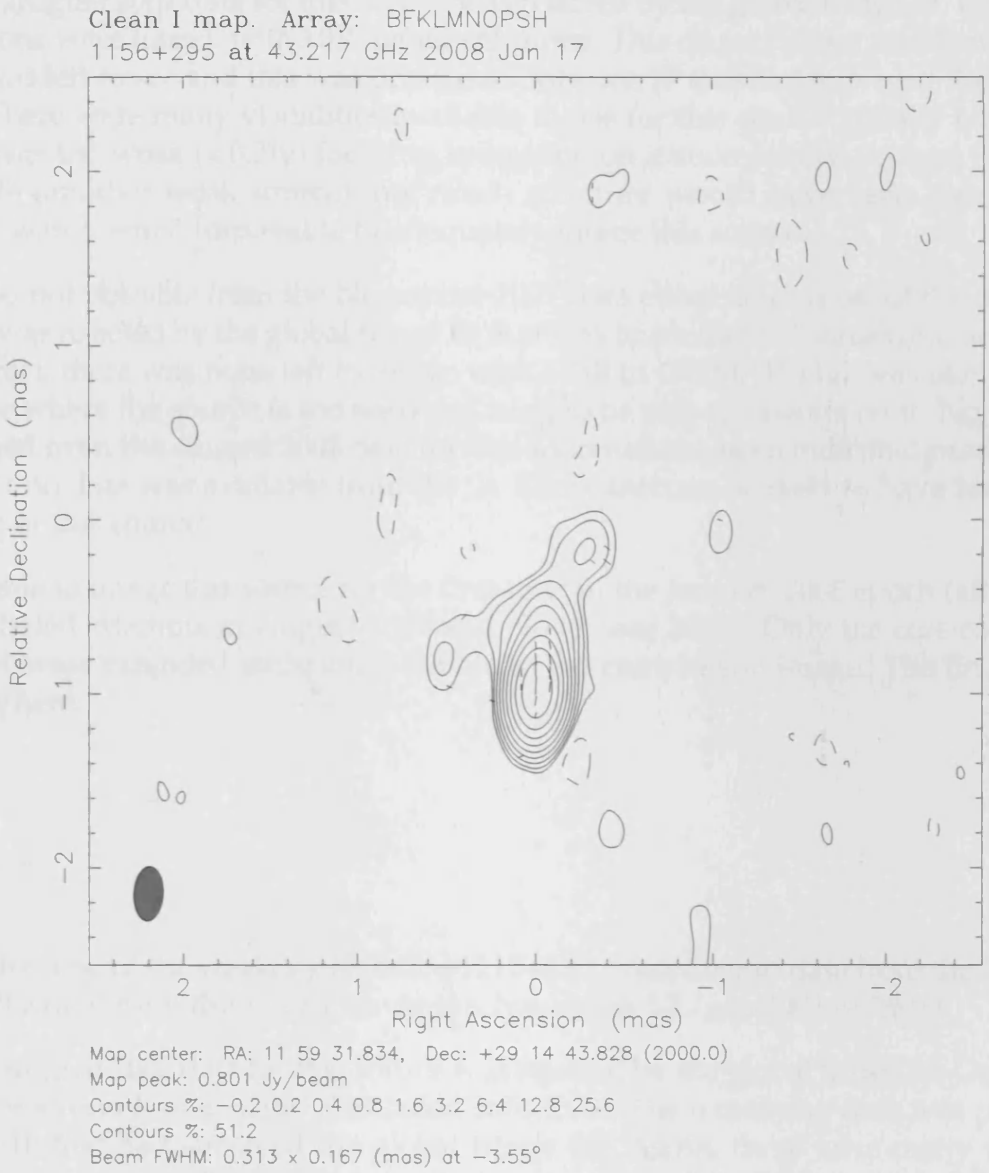

Figure 3.57: January 2008 VLBI Map of 1156+295. For polarisation vectors: 1 mas = $3.13\text{x}10^{-1} Jy/beam$.

1219+285

This is one of the weaker jets (according to data from the Boston University Blazar Group this source never reaches above $0.5Jy$ in 2007 or 2008). It was only possible to image this source from the January 2008 data. As can be seen in Figure 3.58 the resolution is very poor.

Most of the August 2007 data for this source was rejected by the global fringe fit. Only 129 good solutions were found, with 1039 failed solutions. This caused major problems. Very little data was left to see and this was present in only one IF that had survived the global fringe fit. There were many visibilities available to use for this source initially however. Perhaps it was too weak (<0.2Jy) for fring to operate on it successfully. As was the case for 0735+178 (another weak source), not much structure would have been observable. Therefore it was deemed impossible to adequately image this source.

Imaging was not possible from the November 2007 data either since most of the data for this source was rejected by the global fringe fit that was implemented, causing a large loss of data. In fact, there was none left to image with at all in DIFMAP. This was likely to be another case where the source is too weak for fring to be able to operate on it. No results were obtained from the August 2007 data for this source as has been indicated previously. The fact that no data was available from the St. Croix antenna is likely to have hindered the imaging of this source.

It was possible to image this source for the first time in the January 2008 epoch (after two previously failed attempts in August 2007 and November 2007). Only the core could be resolved, whereas extended emission is visible in the comparison image. The final map is very poor here.

1222+216

This is another one of the weaker jets (as for 1219+285, according to data from the Boston University Blazar Group this source never reaches above $0.5Jy$ in 2007 or 2008).

Most of the August 2007 data for this source was rejected by the global fringe fit. Only 128 good solutions were found, with 1040 failed solutions. The remaining data was present in only one IF that had survived the global fringe fit. Again, there were many visibilities available to use for this source initially but it was probably too weak (<0.2Jy) for fring to adequately operate on it. Not much structure would have been observable for such a weak source. Therefore it was also deemed impossible to image this source to a satisfactory standard.

Imaging was not possible for this source in November 2007 either. Again, a large loss of data resulted from the global fringe fit. Not enough data remained for imaging to take place.

This was the second source that I managed to image for the first time in January 2008 (after two unsuccessful attempts in August 2007 and November 2007). Again, it was only possible to resolve the core, but structure separated from the central region is seen in Figure ??.

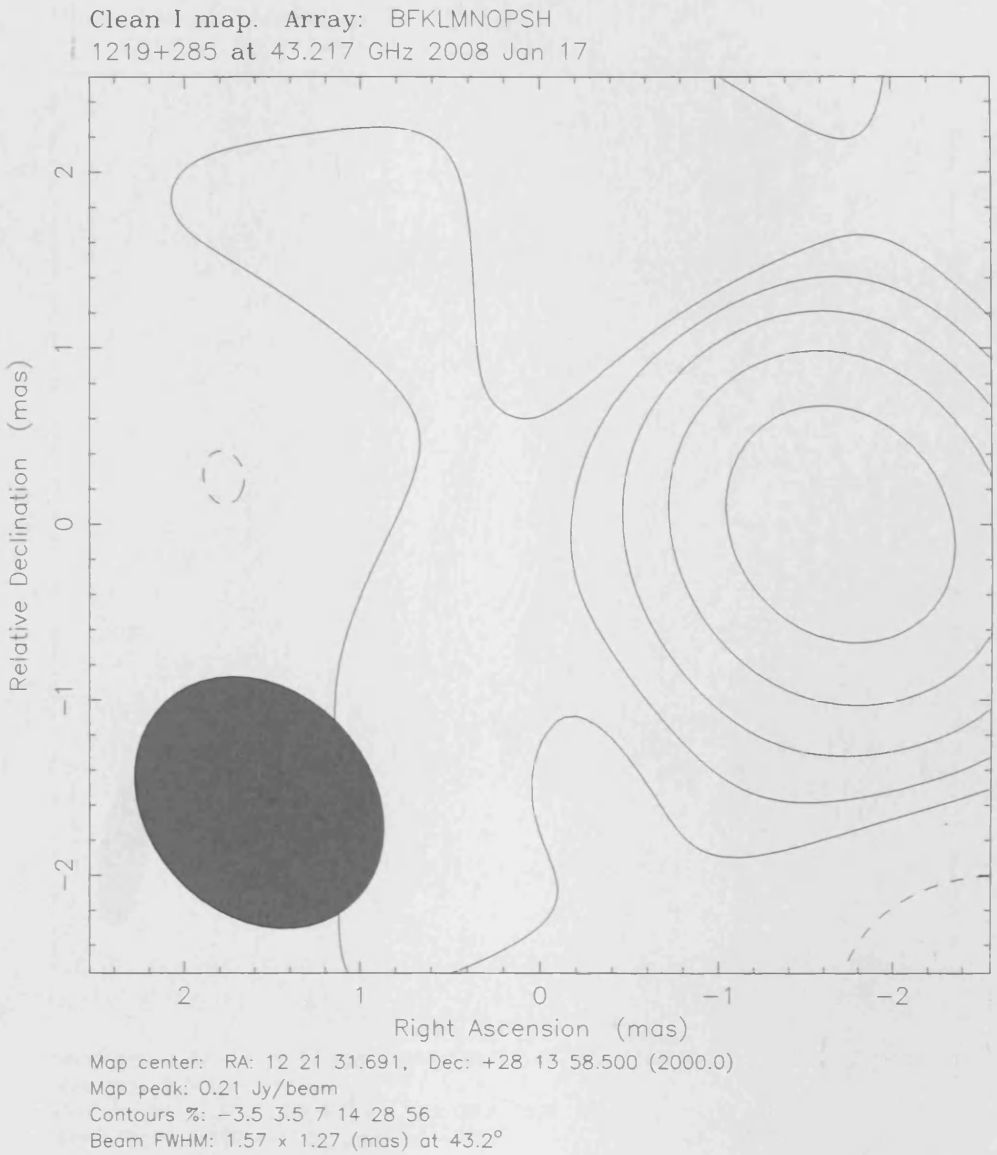

Figure 3.58: January 2008 VLBI Map of 1219+285. For polarisation vectors: 1 mas = $1.25\text{x}10^0 Jy/beam$.

1406-076

This source maintains a fairly steady peak flux in the epochs shown. A large beam size for the January 2008 epoch yields a poor resolution image with no significant structure. The lack of any data from a handful of the contributing antennas in this epoch likely played a large part in this problem. This is in constrast to the 2007 images, which show some extended compact structure.

In August 2007, there were many more failed solutions in the global fringe fit than there were good solutions here. Most of the RR and LL parallel polarisation phases had significant scatter within their IFs. Also, even after the global fringe fit there was some slight sloping of most of these phases within their IFs. All of the RL and LR cross polarisation phases were random, which may account for the lack of measurable polarisation for this source. A handful of IFs were missing any data at all amongst the RR, LL, RL and LR polarisations. This was probably due to the amount of failed solutions in the global fringe

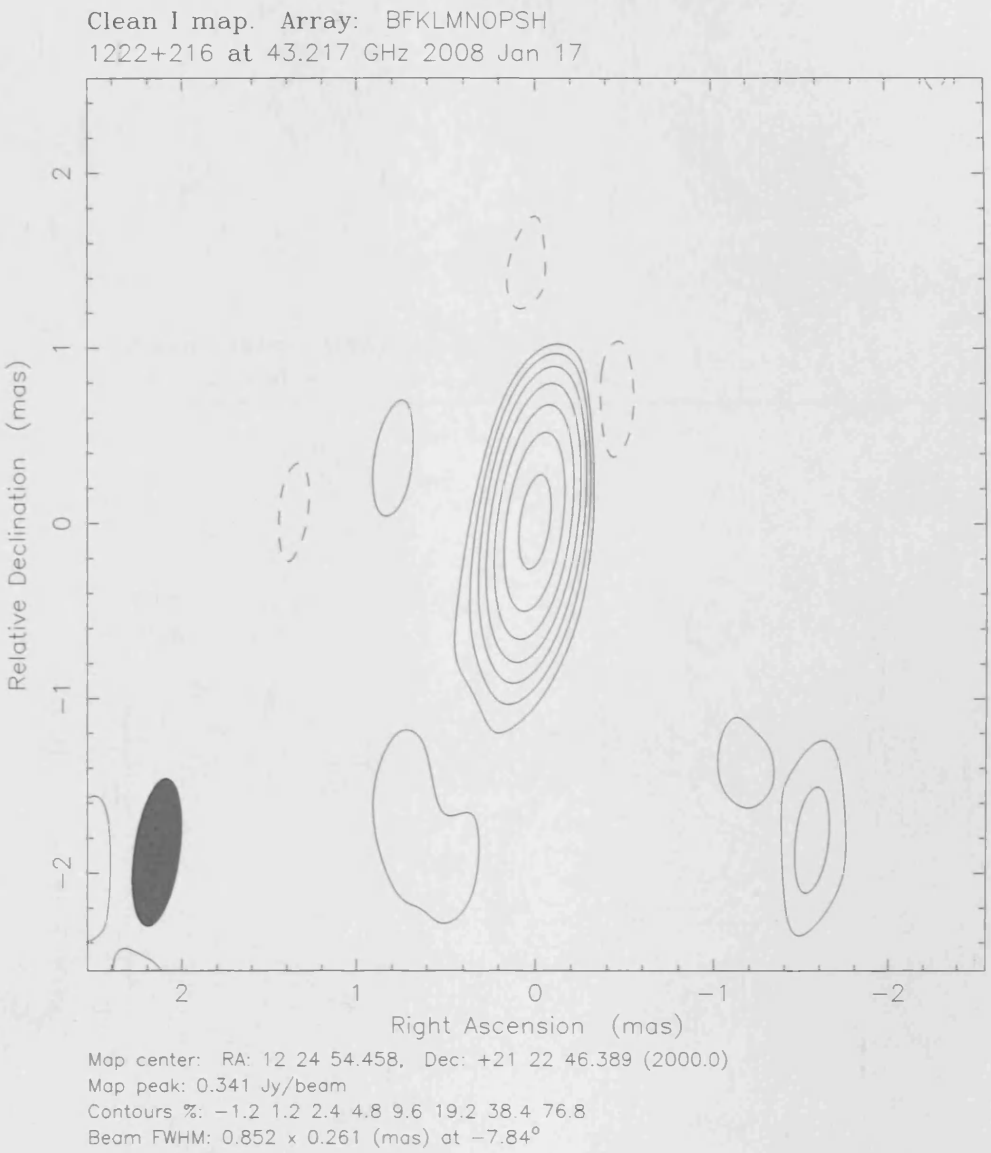

Figure 3.59: January 2008 VLBI Map of 1222+216. For polarisation vectors: 1 mas = 5.99x$10^{-1} Jy/beam$.

fit. In turn, *this* was likely to be the cause of the small amount, or complete lack of data left over when inspecting each antenna during the analysis of this source. The lack of good quantities of data for many antennas may have caused a loss of resolution in images for this source.

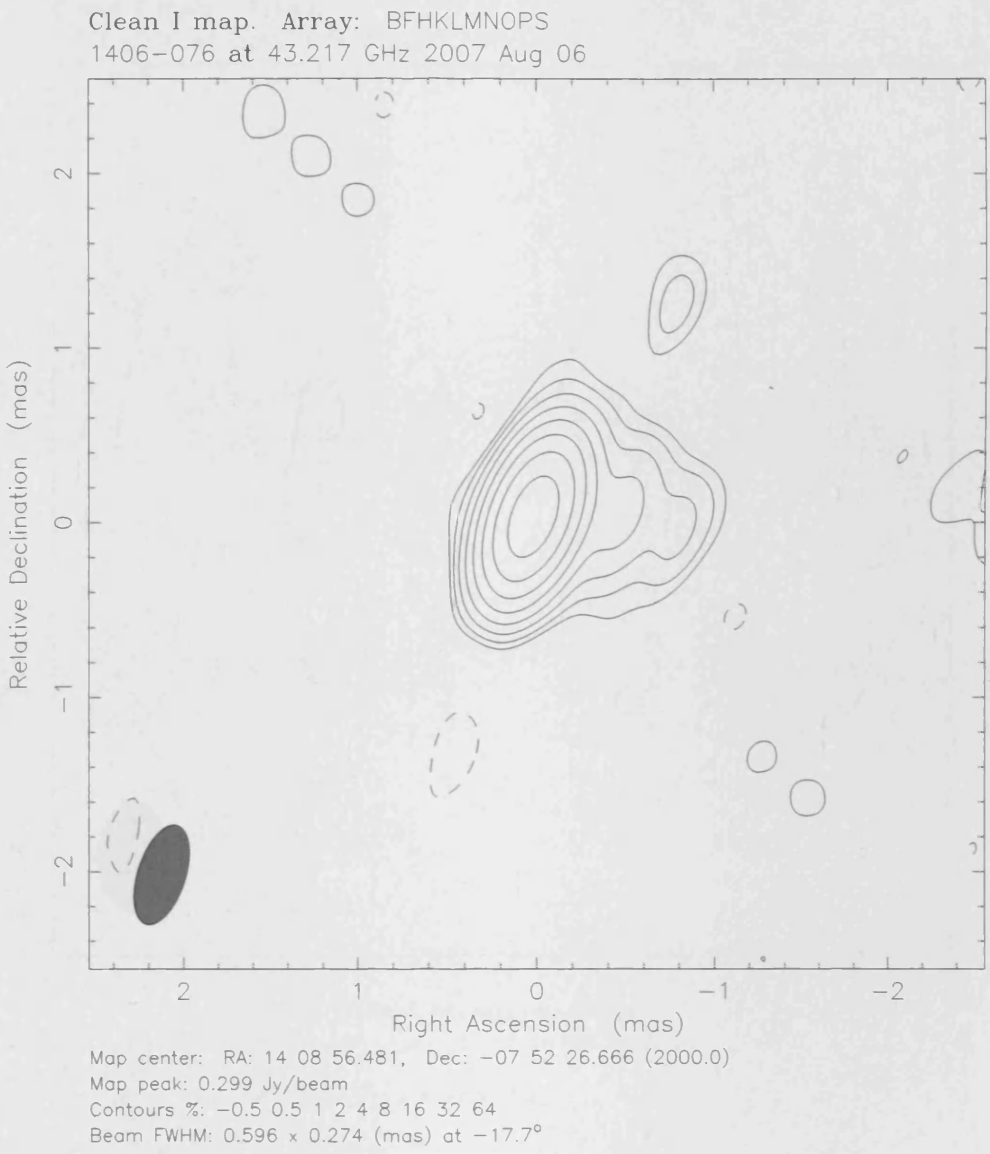

Figure 3.60: August 2007 VLBI Map of 1406-076. For polarisation vectors: 1 mas = 5.00x10^{-1} $Jy/beam$.

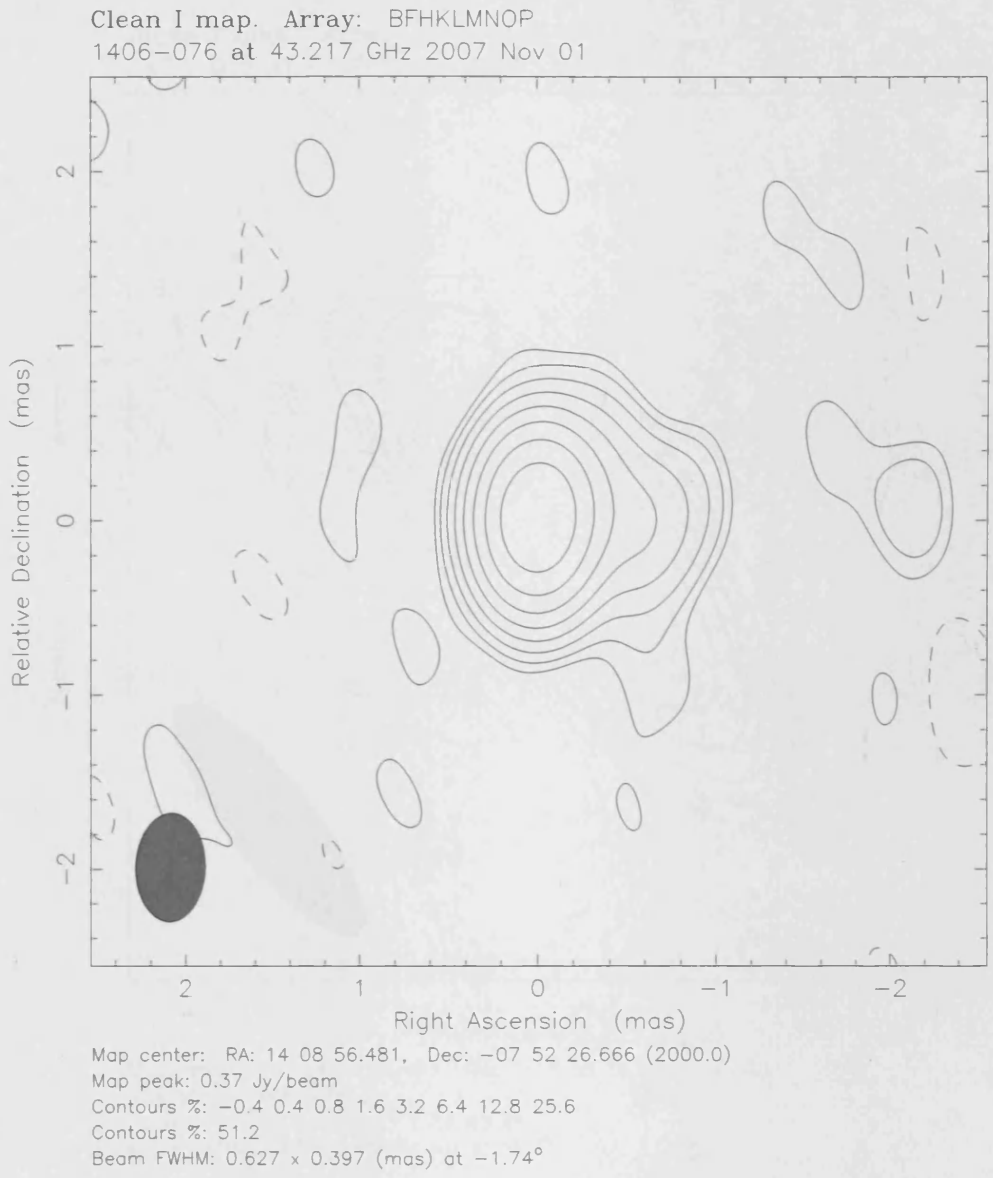

Figure 3.61: November 2007 VLBI Map of 1406-076. For polarisation vectors: 1 mas = 5.00x10^{-1} $Jy/beam$.

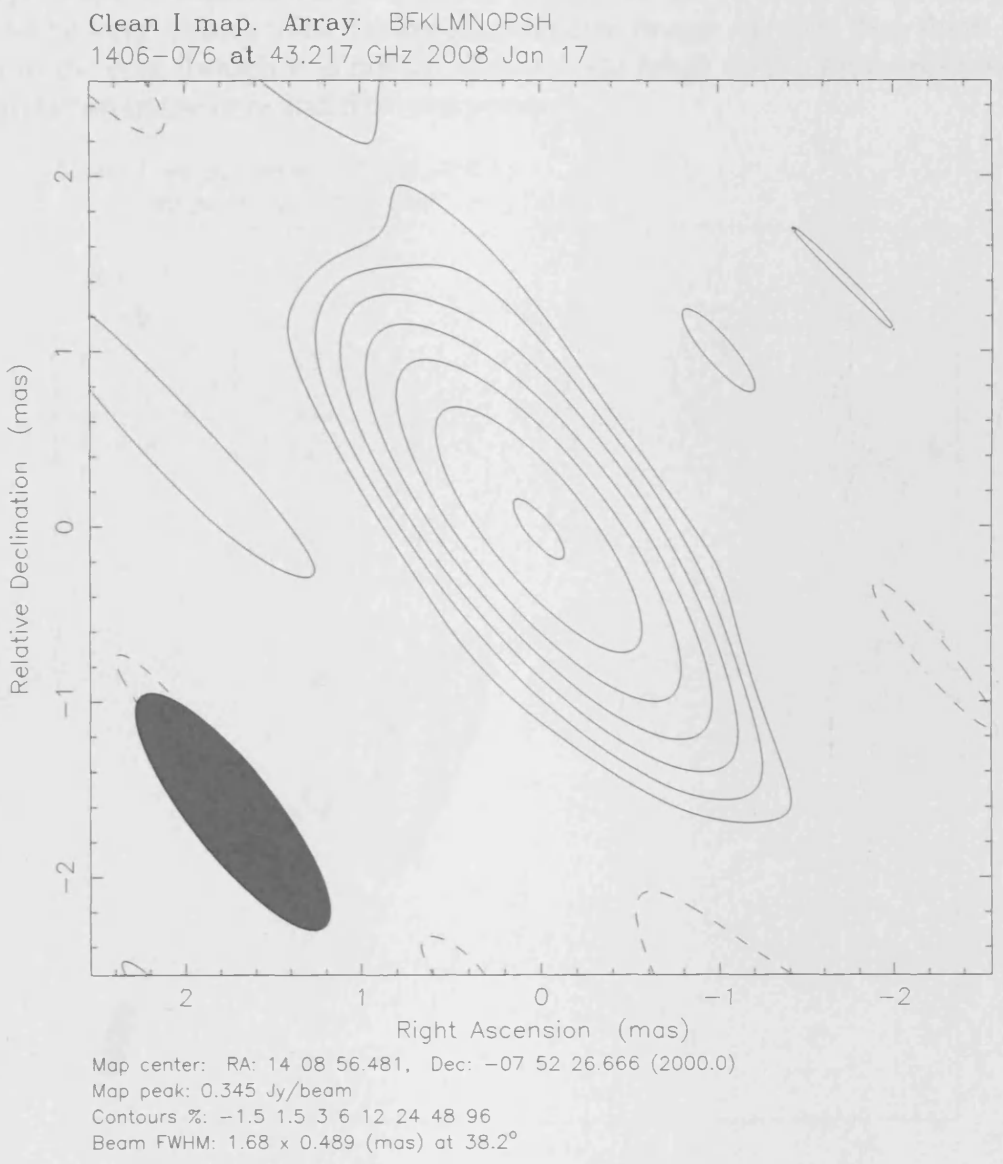

Figure 3.62: January 2008 VLBI Map of 1406-076. For polarisation vectors: 1 mas = $8.33\text{x}10^{-1} Jy/beam$.

The more intense emission from this source is confined to a compact area near the core, with examples of some lower intensity emission further from the core. The polarisation in the core in the August 2007 map is strange in that it does not maintain the same position angle in this region. The polarised intensity map that accompanies this image reveals two areas of polarised intensity around the core, which partially explains this feature of the final map. There is polarisation in the core of the November 2007 image but it does not appear to be very strong. The polarised intensity image *suggests* that there is real polarisation in the core though it is not far above noise level. In the final epoch shown, there is polarisation in the core and first component.

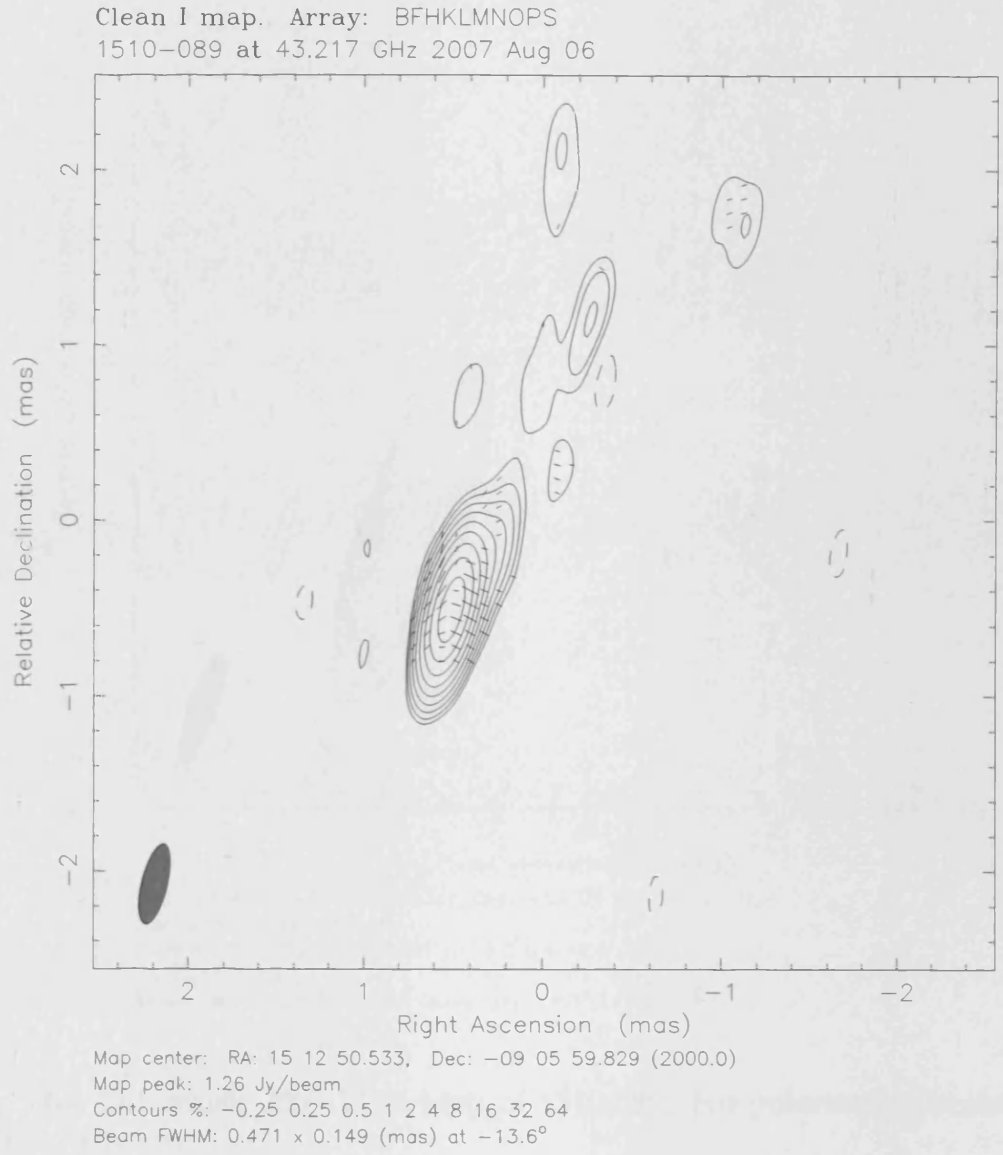

Figure 3.63: August 2007 VLBI Map of 1510-089. For polarisation vectors: 1 mas = 5.00x10^{-1} $Jy/beam$.

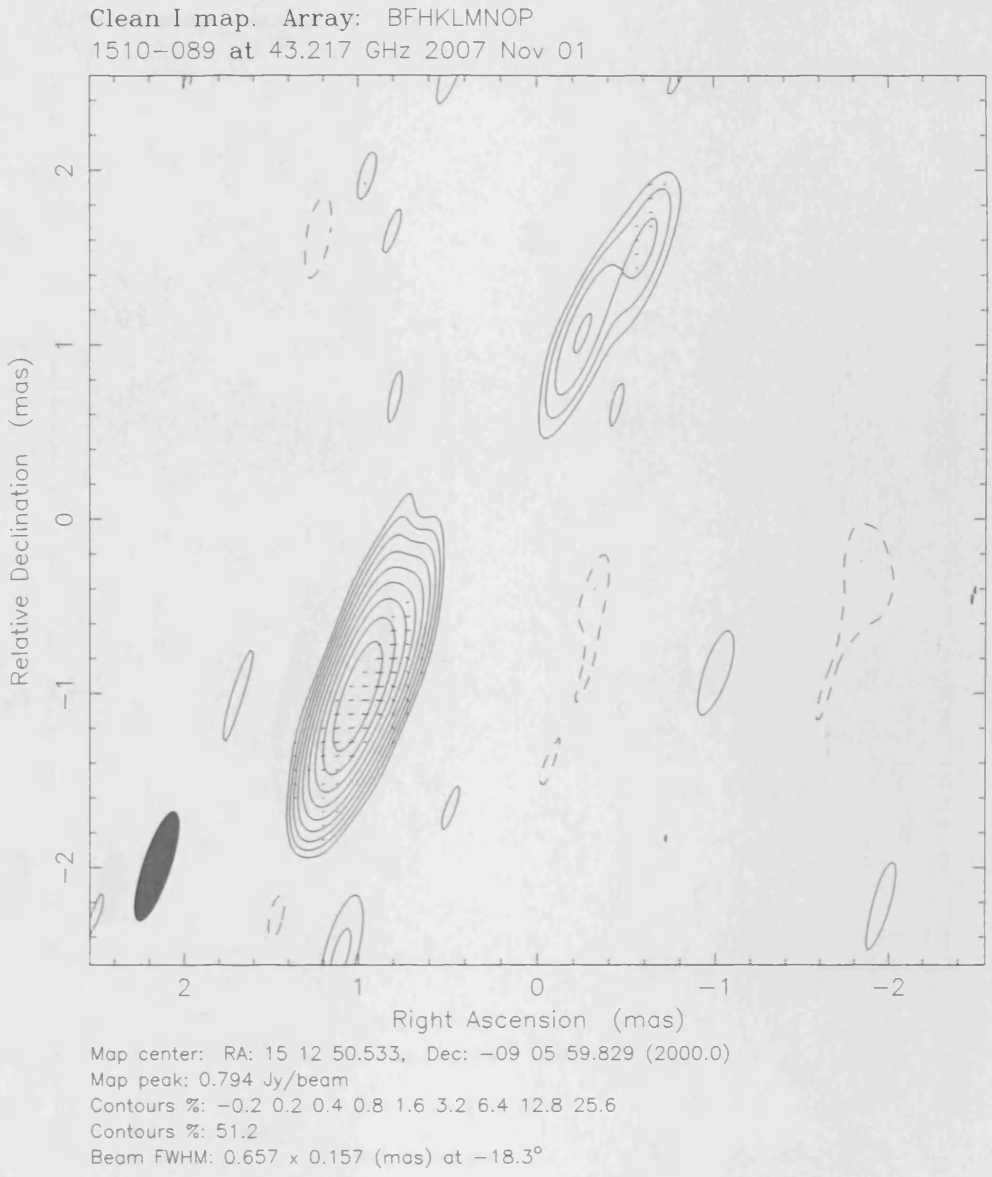

Figure 3.64: November 2007 VLBI Map of 1510-089. For polarisation vectors: 1 mas = 2.50x10^{-1} $Jy/beam$.

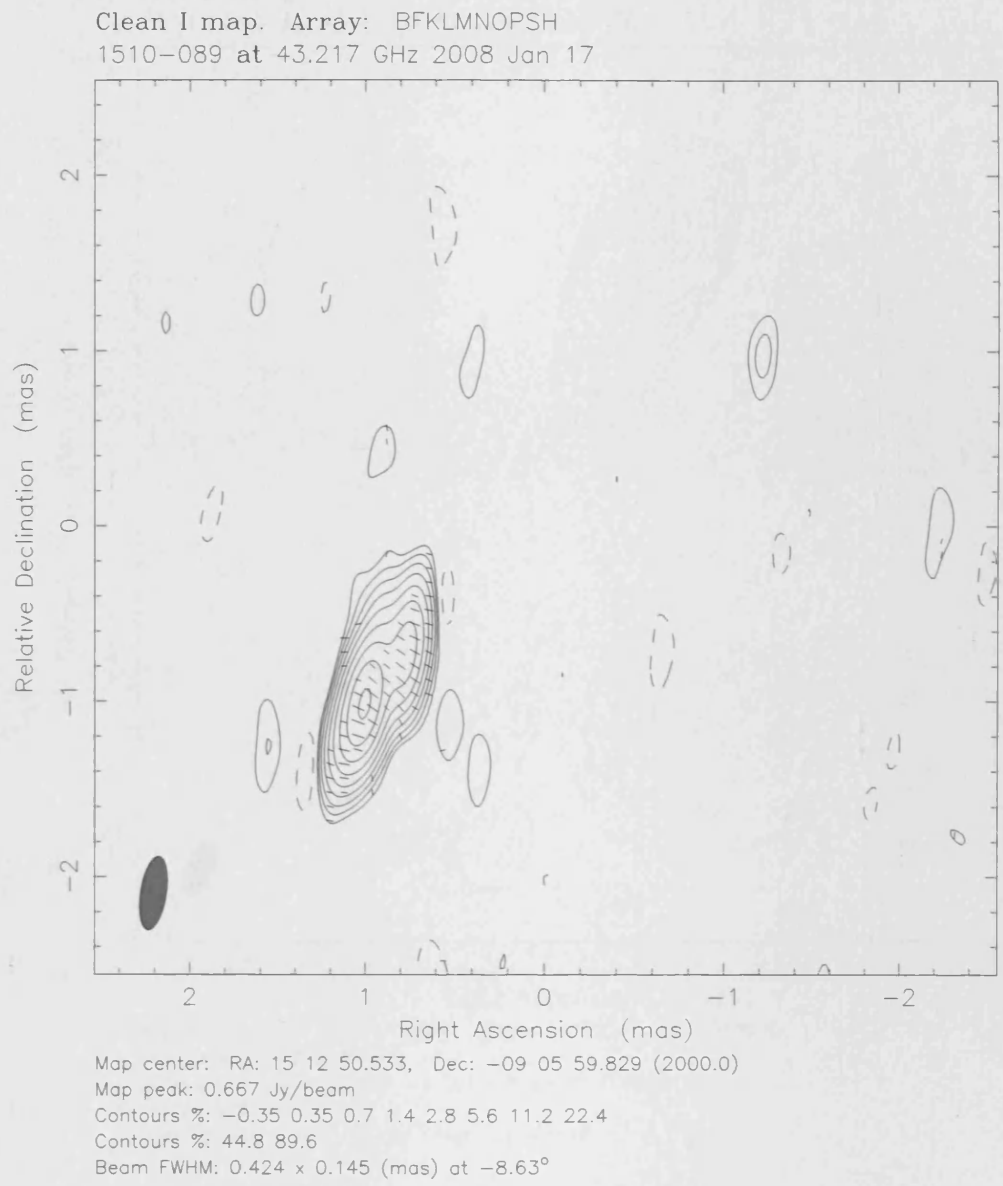

Figure 3.65: January 2008 VLBI Map of 1510-089. For polarisation vectors: 1 mas = $3.13\text{x}10^{-1} Jy/beam$.

1611+343

The January 2008 image shows some interesting structure near to the core; the emission appearing to bend and wave. The core appears to be polarised in all of the epochs though in the November 2007 case this emission does not seem to be very strong. Also, in the January 2008 epoch the polarisation appears to be quite weak and may not be real.

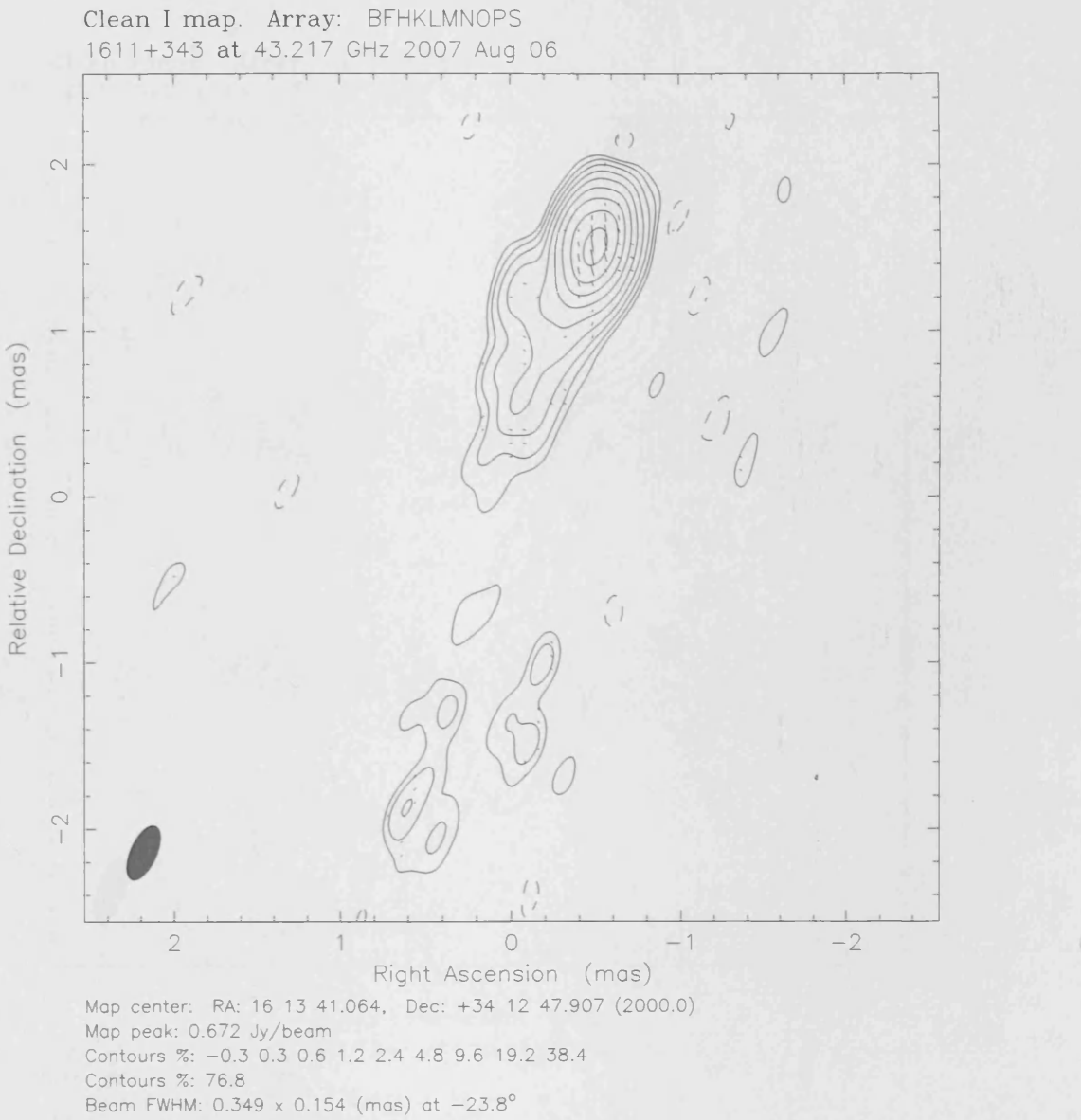

Figure 3.66: August 2007 VLBI Map of 1611+343. For polarisation vectors: 1 mas = $6.25\text{x}10^{-1} Jy/beam$.

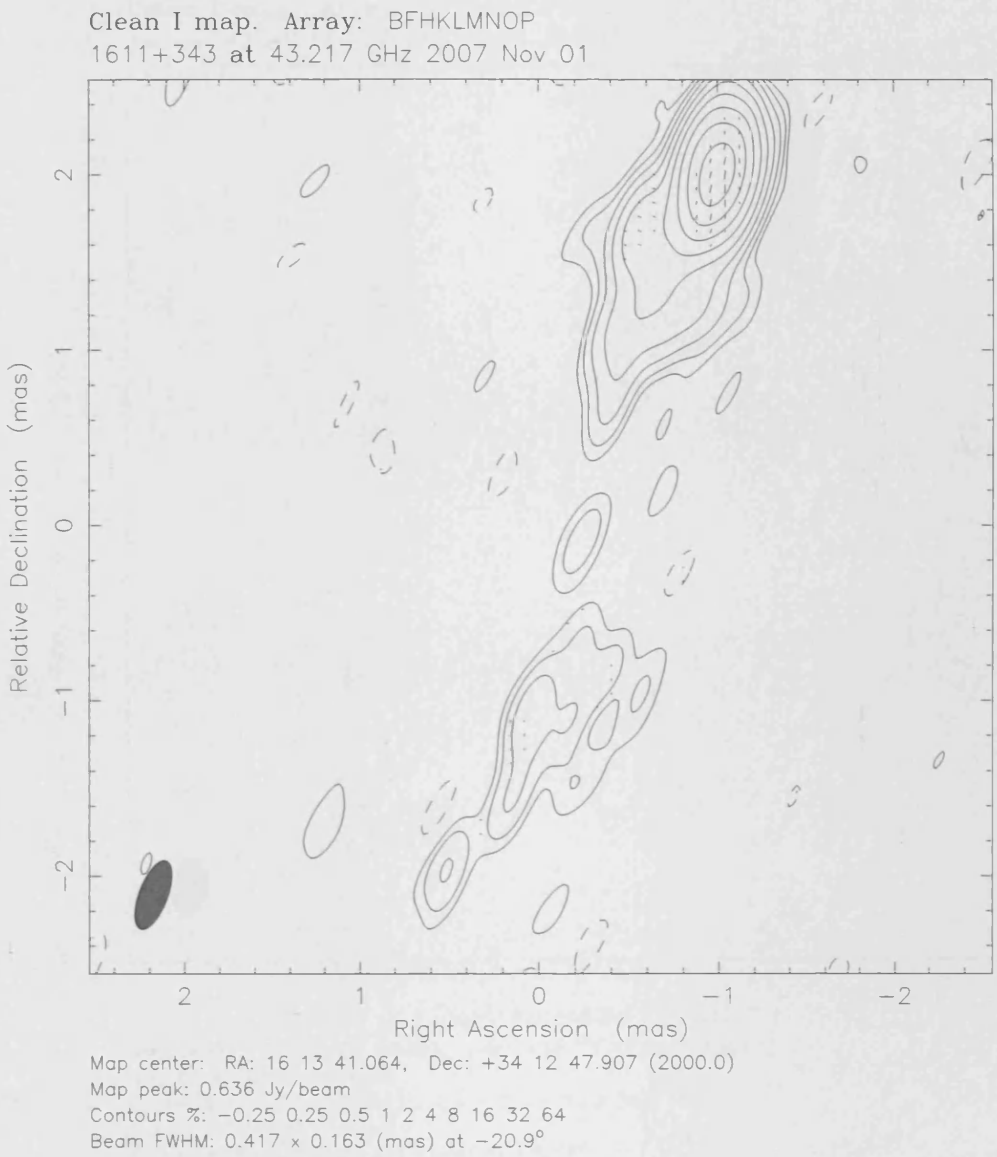

Figure 3.67: November 2007 VLBI Map of 1611+343. For polarisation vectors: 1 mas = 4.17x10^{-1} $Jy/beam$.

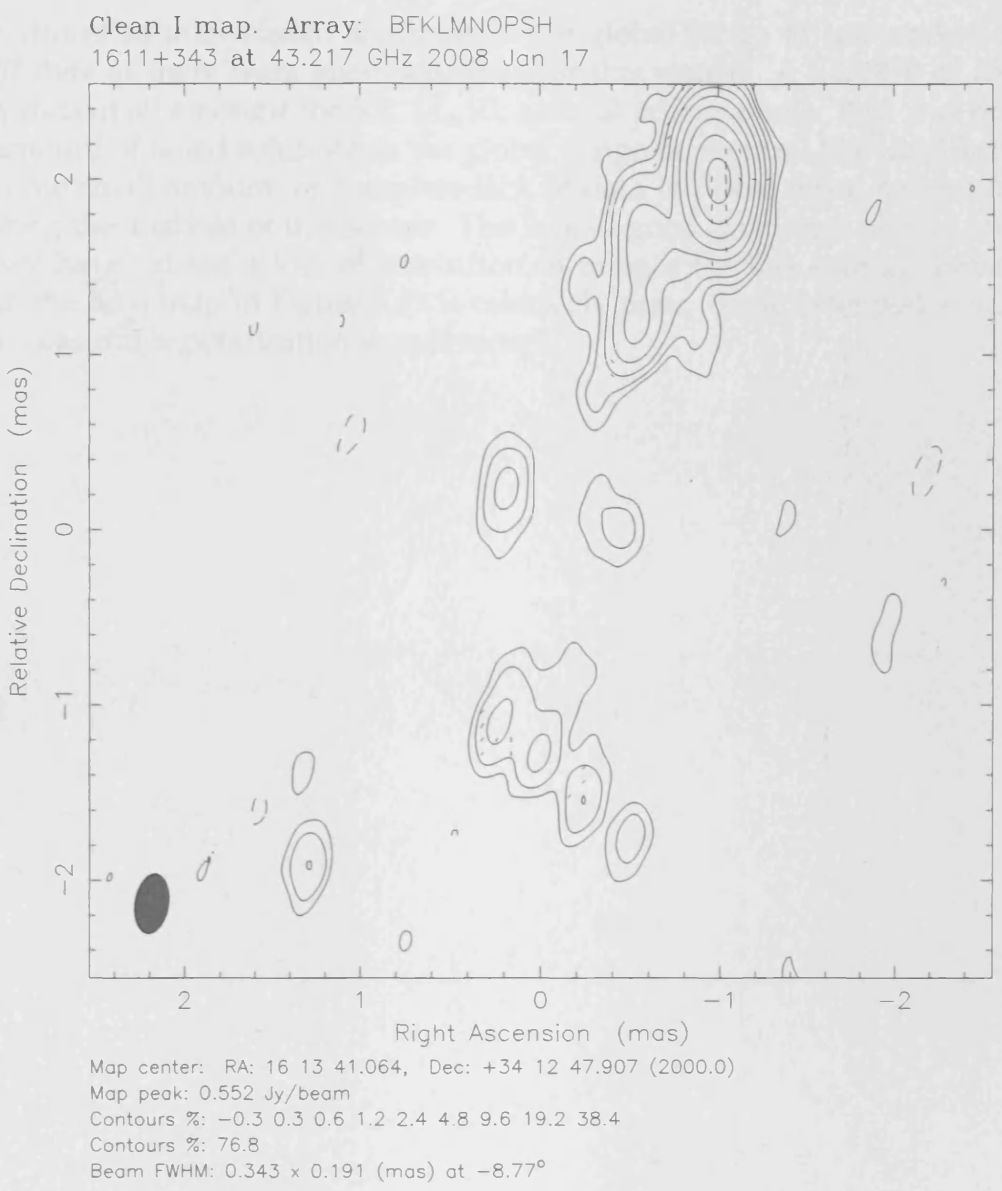

Figure 3.68: January 2008 VLBI Map of 1611+343. For polarisation vectors: 1 mas = $3.57\text{x}10^{-1} Jy/beam$.

1622-297

There is a possibility that the core may lie due east of the brightest component in the January 2008 image. However this is difficult to say with any certainty.This image suffers from a large beam size. With a smaller beam it might be possible to gain a better incite into where the core is situated. It was not possible to image any polarisation at all for this source.

There were almost as many failed solutions in the global fringe fit undertaken for the August 2007 data as there were good solutions for this source. A handful of IFs were missing any data at all amongst the RR, LL, RL and LR polarisations. This was probably due to the amount of failed solutions in the global fringe fit. In turn, *this* was likely to be the cause of the small amount, or complete lack of data left over when inspecting each antenna during the analysis of this source. The lack of good quantities of data for many antennas may have caused a loss of resolution in images for this source. Indeed, the resolution in the final map in Figure 3.69 is relatively poor. Some extended structure is seen but no measurable polarisation was detected.

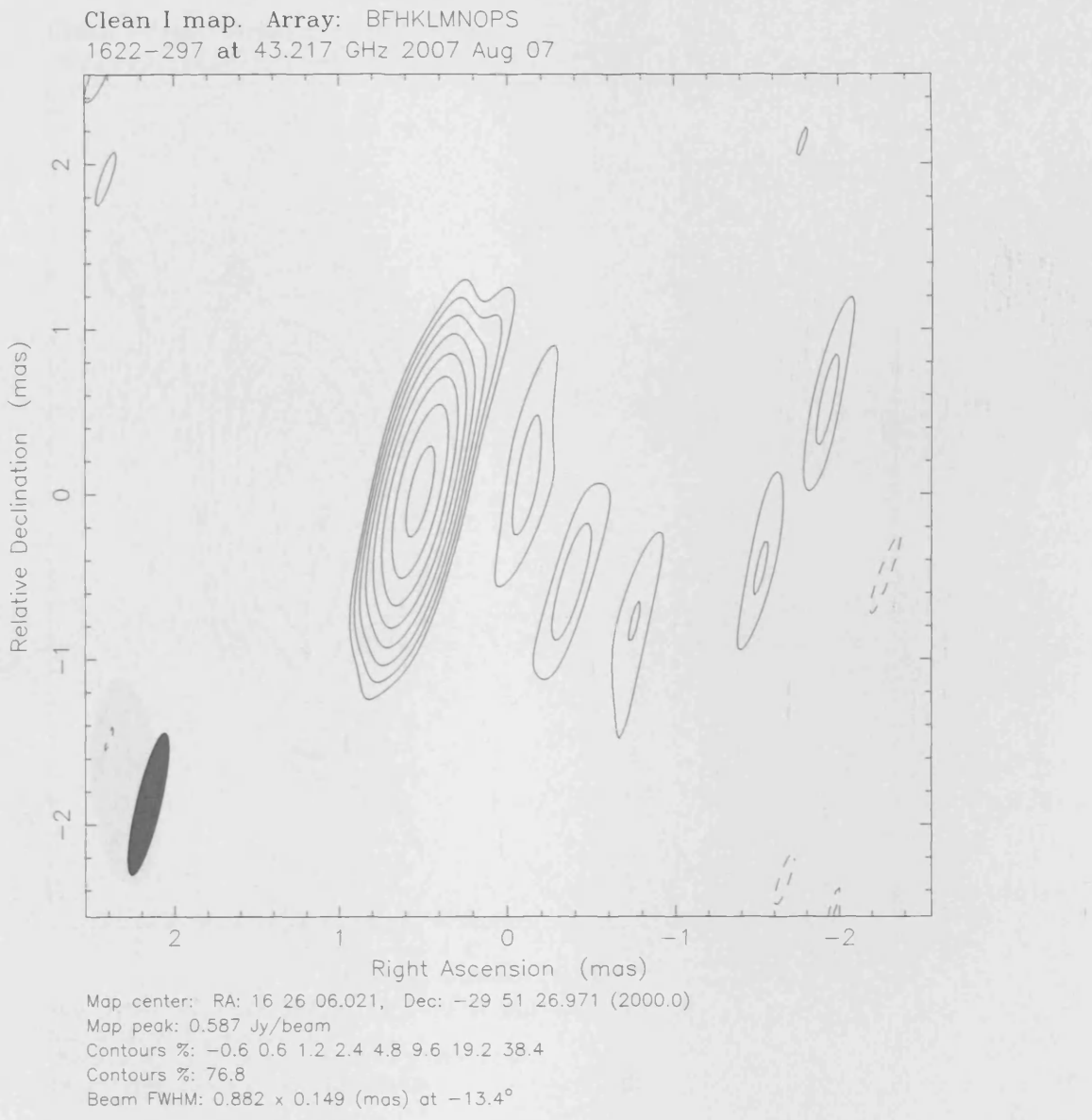

Figure 3.69: August 2007 VLBI Map of 1622-297. For polarisation vectors: 1 mas = $6.25\text{x}10^{-1} Jy/beam$.

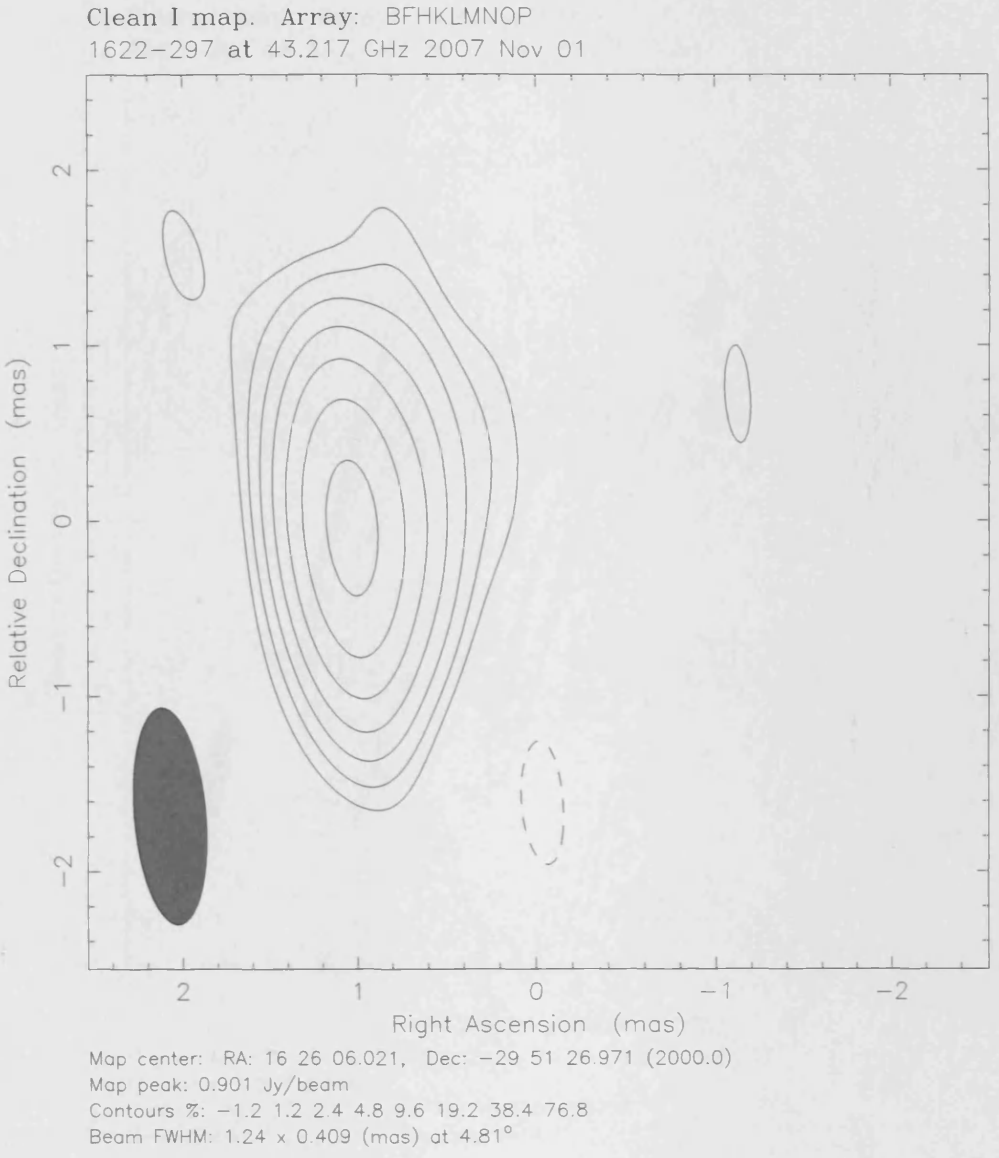

Figure 3.70: November 2007 VLBI Map of 1622-297. For polarisation vectors: 1 mas = 5.00x10^{-1} $Jy/beam$.

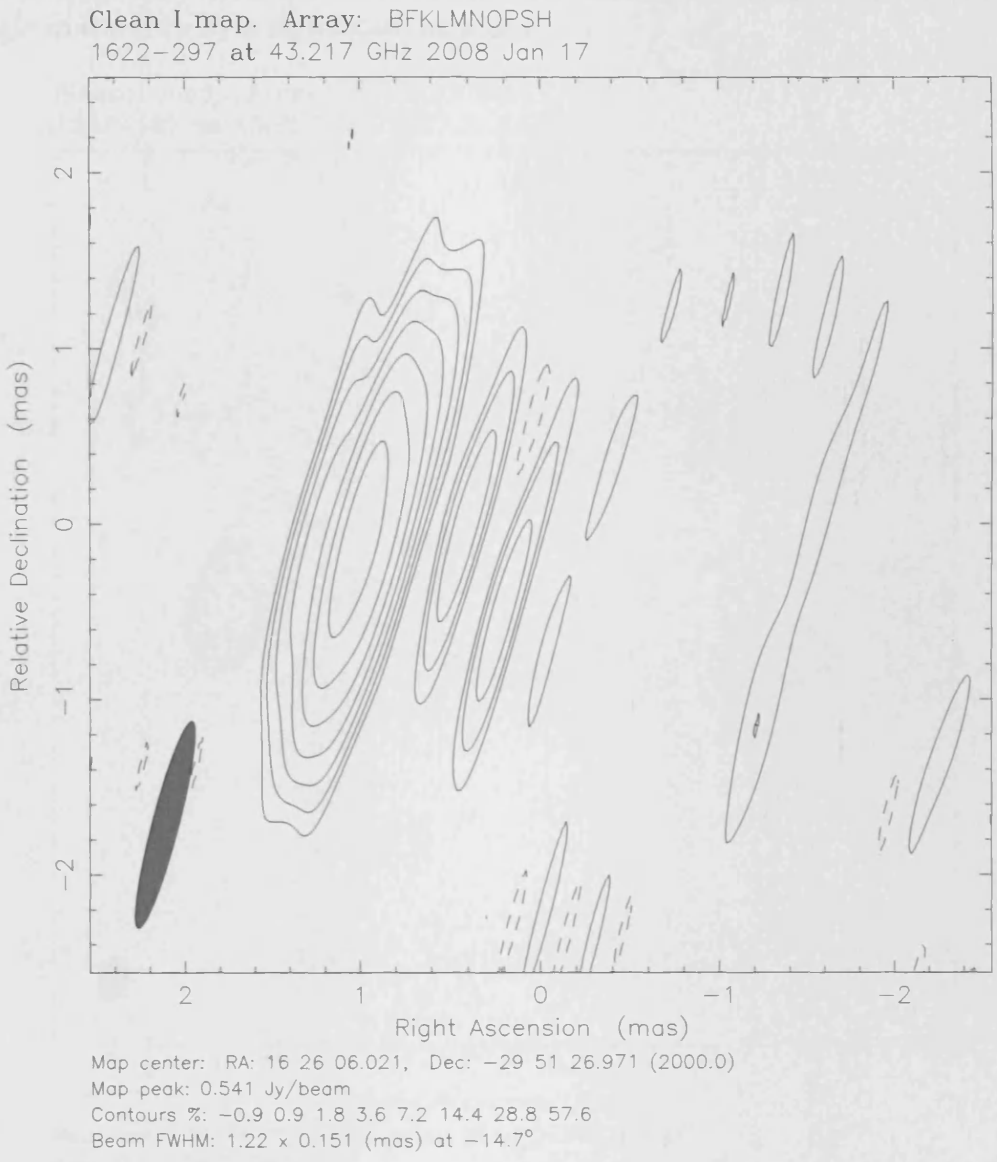

Figure 3.71: January 2008 VLBI Map of 1622-297. For polarisation vectors: 1 mas = 8.33x10^{-1} $Jy/beam$.

1633+382

This source has emission that appears to bend sharply near the core. This is perhaps most prominent in the August 2007 and January 2008 epochs. Weak emission appears to entend far from the core though much of what could be construed as jet emission could be noise. The core appears polarised in August 2007 and January 2008. There is polarisation around the core in November 2007 but it appears weak and may well be noise. Considering the August 2007 and January 2008 epochs on their own, there is a rotation in the polarisation position angle in the core by a significant amount.

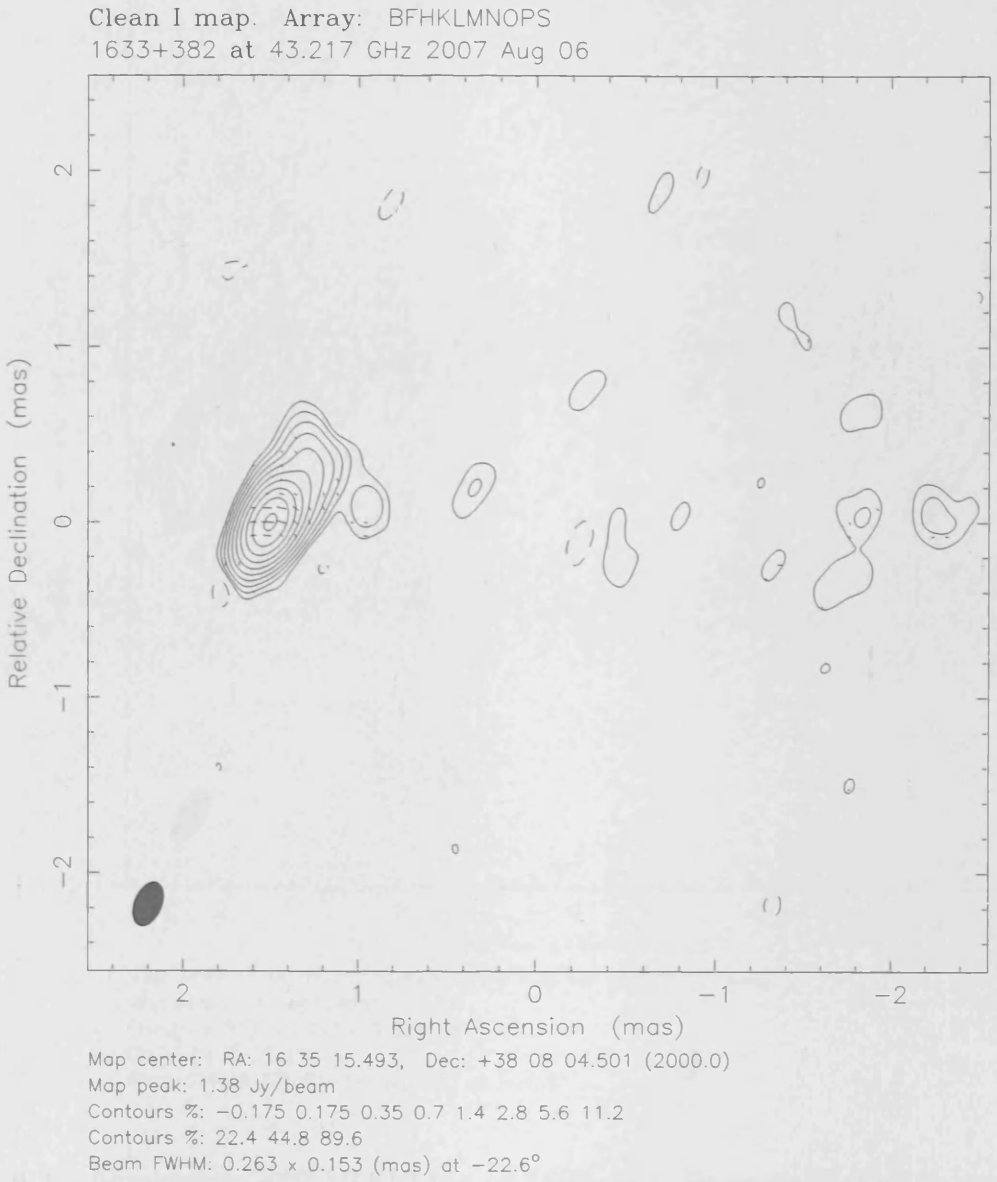

Figure 3.72: August 2007 VLBI Map of 1633+382. For polarisation vectors: 1 mas = $3.57\text{x}10^{-1} Jy/beam$.

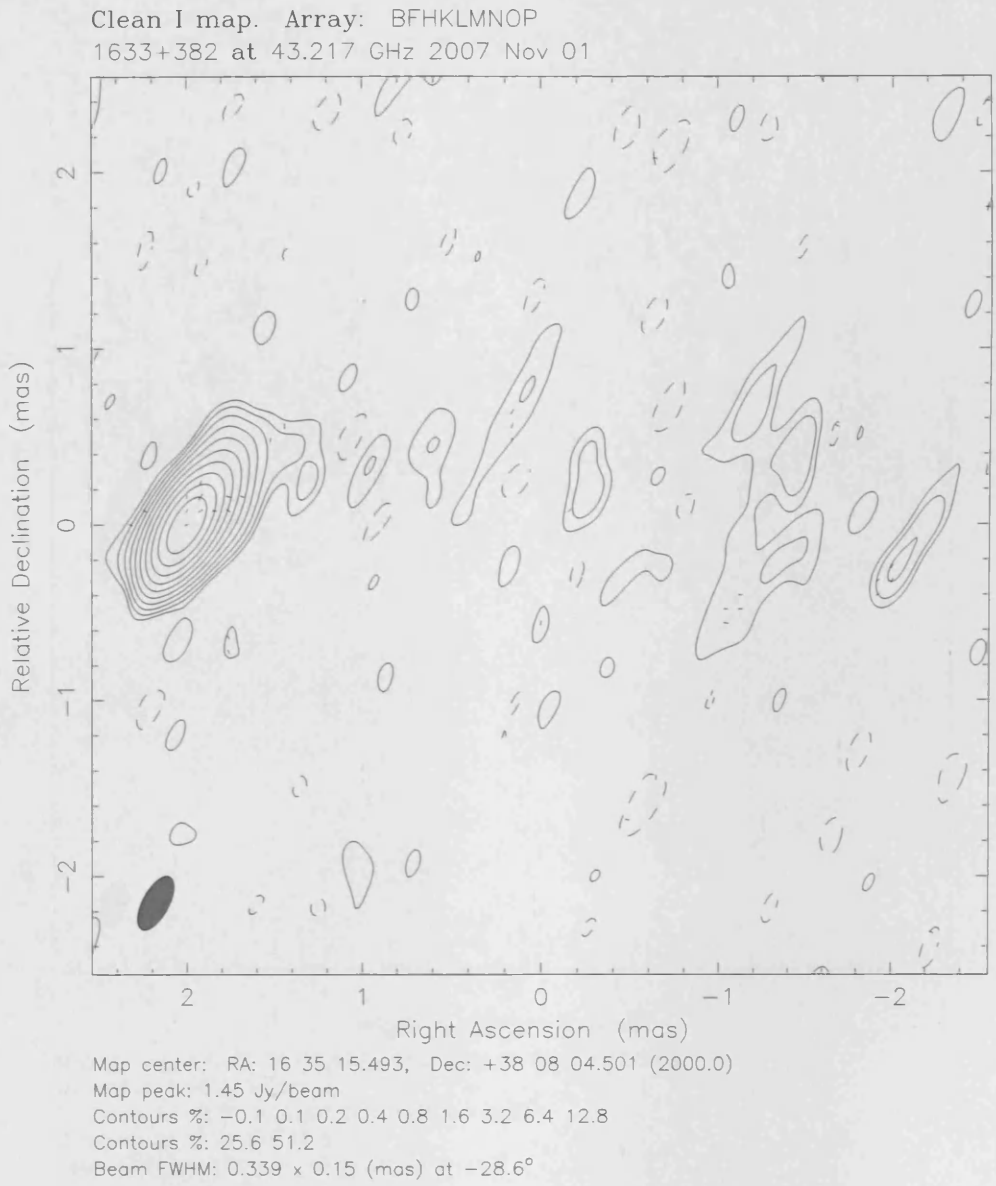

Figure 3.73: November 2007 VLBI Map of 1633+382. For polarisation vectors: 1 mas = 2.50x10^{-1} $Jy/beam$.

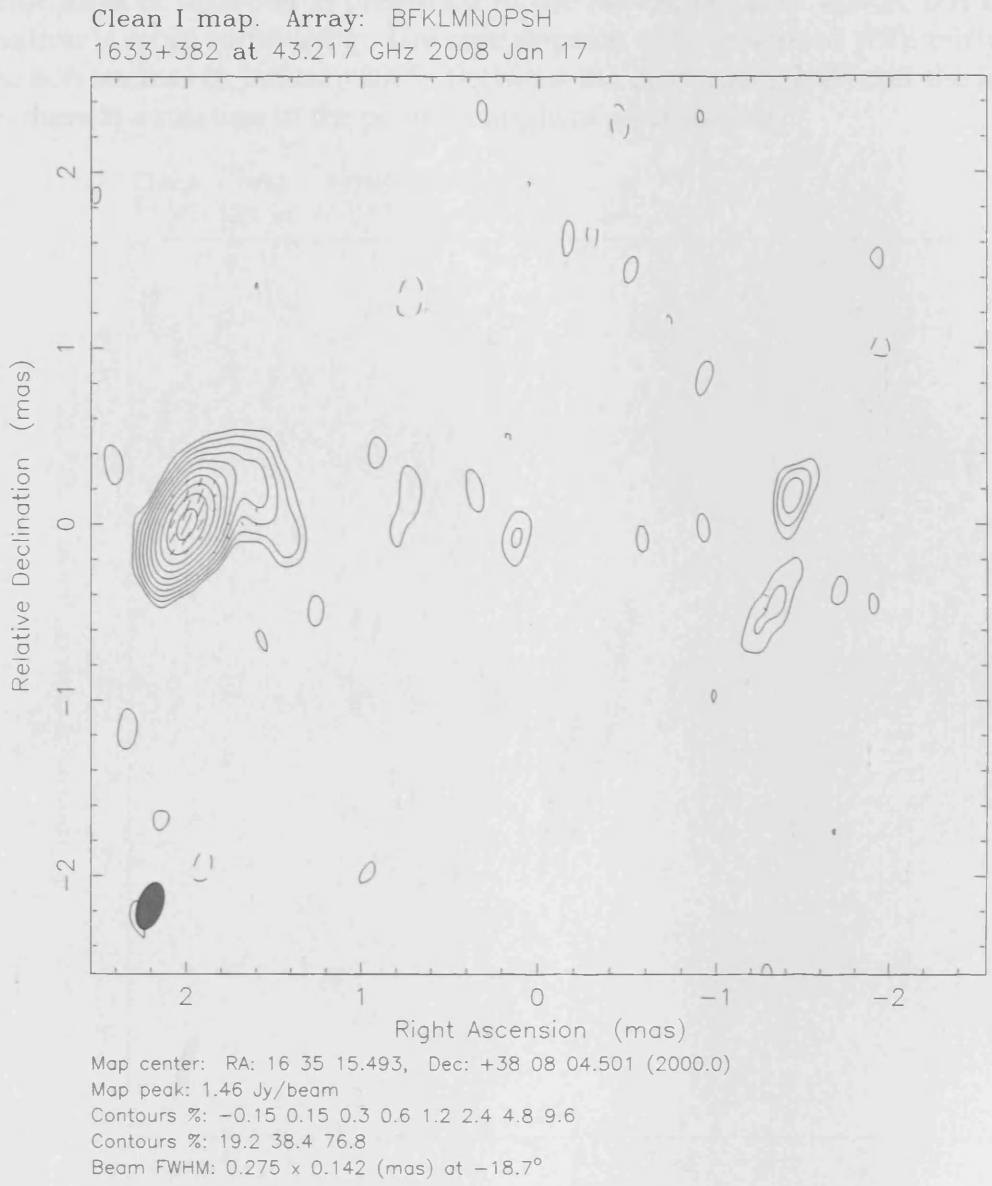

Figure 3.74: January 2008 VLBI Map of 1633+382. For polarisation vectors: 1 mas = $3.57\text{x}10^{-1} Jy/beam$.

1730-130

This source brightens by roughly $0.5Jy$ between the August and November 2007 epochs. The jet itself appears to bend towards an easterly direction in the first two epochs shown, then straighten up somewhat in January 2008. The polarisation in August 2007 appears to reside in the core and a component approximately due north of the core. However the polarised intensity map reveals that this polarisation is likely to be noise in both cases. The same kind of situation is presented in the November 2007 epoch, but this time the polarisation is more convincing. The core appears to be polarised with fairly prominent polarisation vectors in January 2008. Between the November 2007 and the January 2008 epochs there is a rotation in the position angle of polarisation.

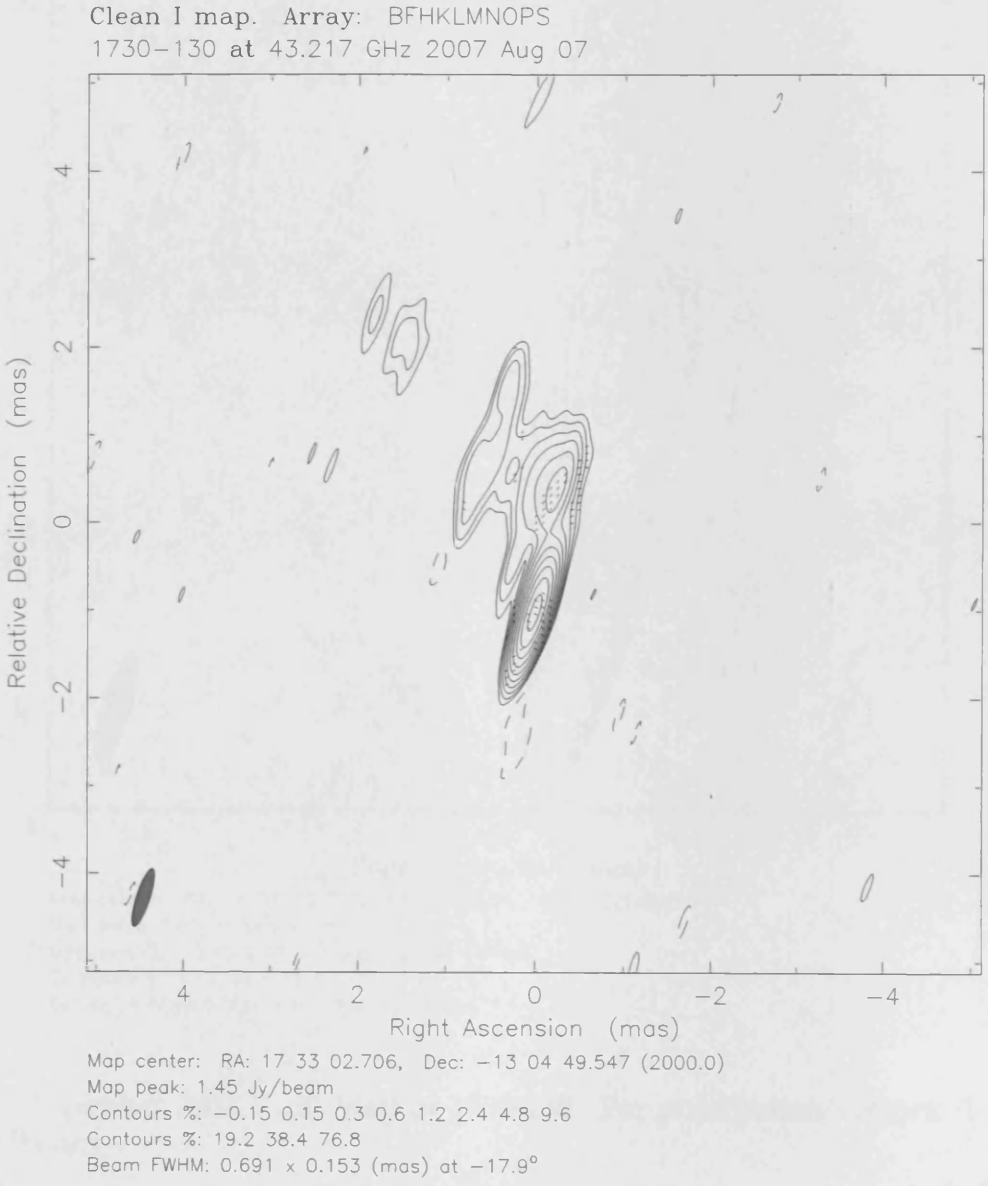

Figure 3.75: August 2007 VLBI Map of 1730-130. For polarisation vectors: 1 mas = $3.57\text{x}10^{-1}$ Jy/beam.

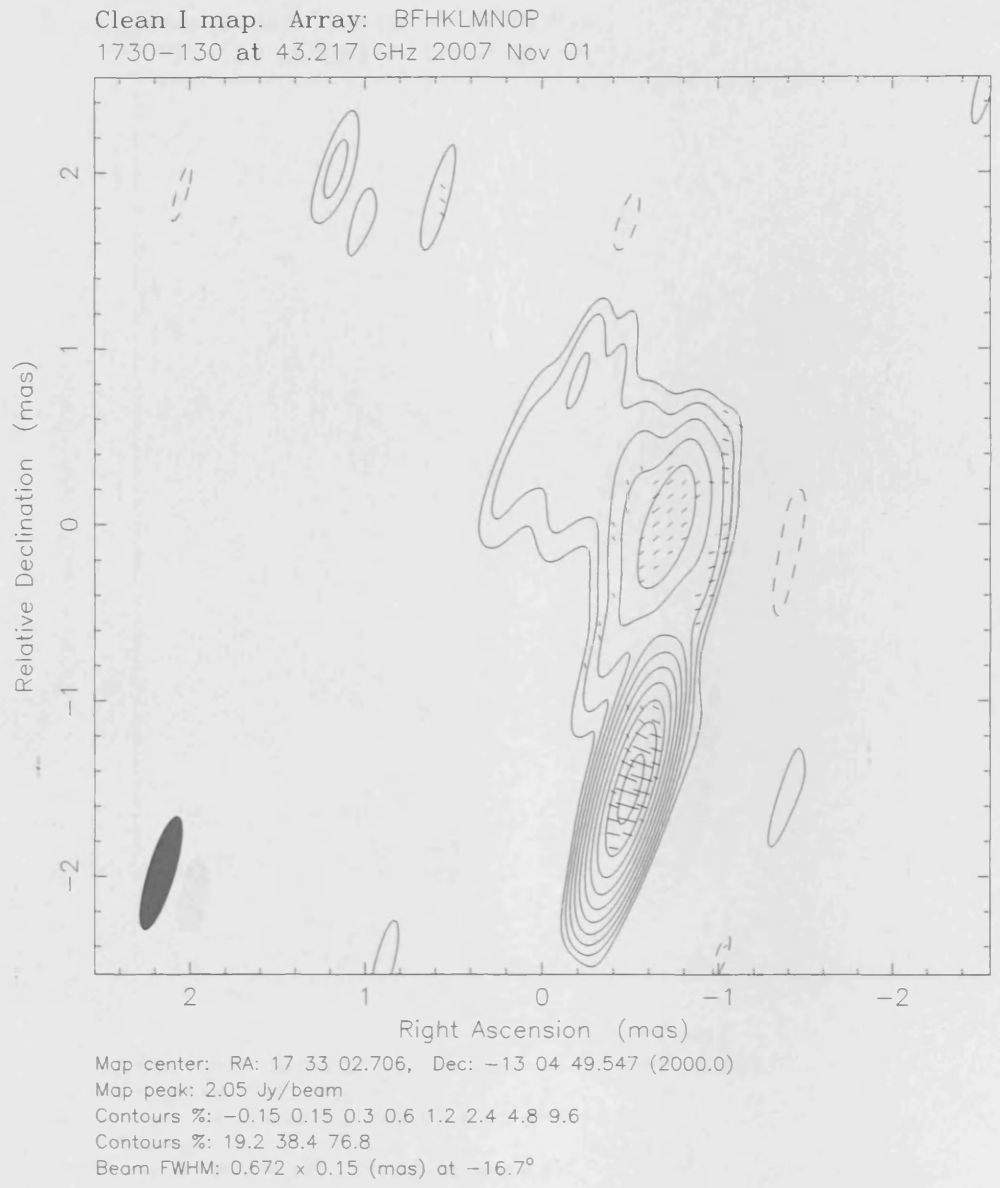

Figure 3.76: November 2007 VLBI Map of 1730-130. For polarisation vectors: 1 mas = $4.17 \text{x} 10^{-1}$ Jy/beam.

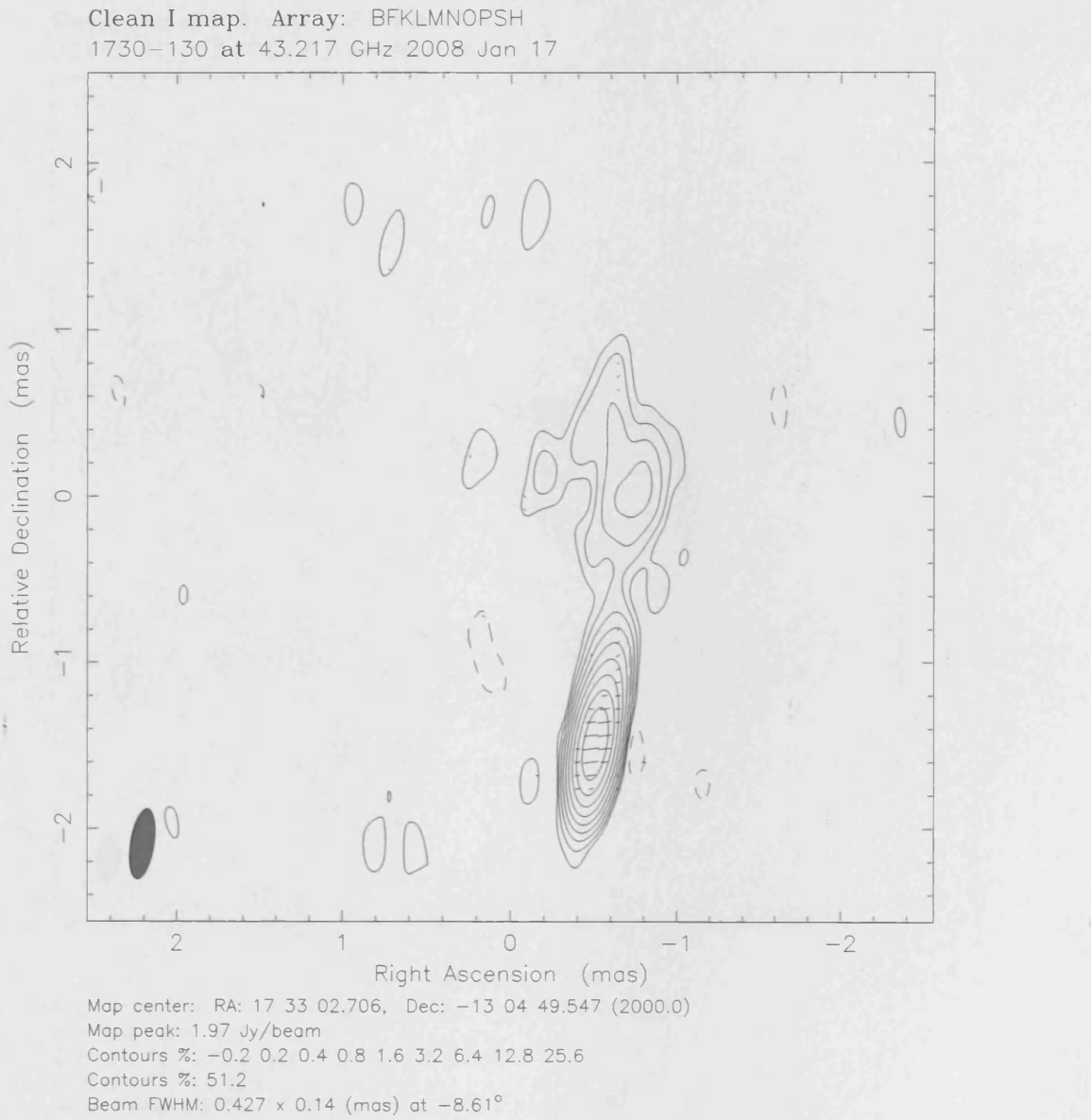

Figure 3.77: January 2008 VLBI Map of 1730-130. For polarisation vectors: 1 mas = $8.33\text{x}10^{-1} Jy/beam$.

3C111

This source undergoes a flux increase of around $1Jy$ before dropping down to $1.89Jy$ in the final epoch shown. This is one of the more extended sources imaged. There is some nice helical structure near the core in January 2008. There is polarised intensity indicated in each of the images of this source. However, the polarised intensity maps indicate that the only strong polarisation in this source is to be found in November 2007.

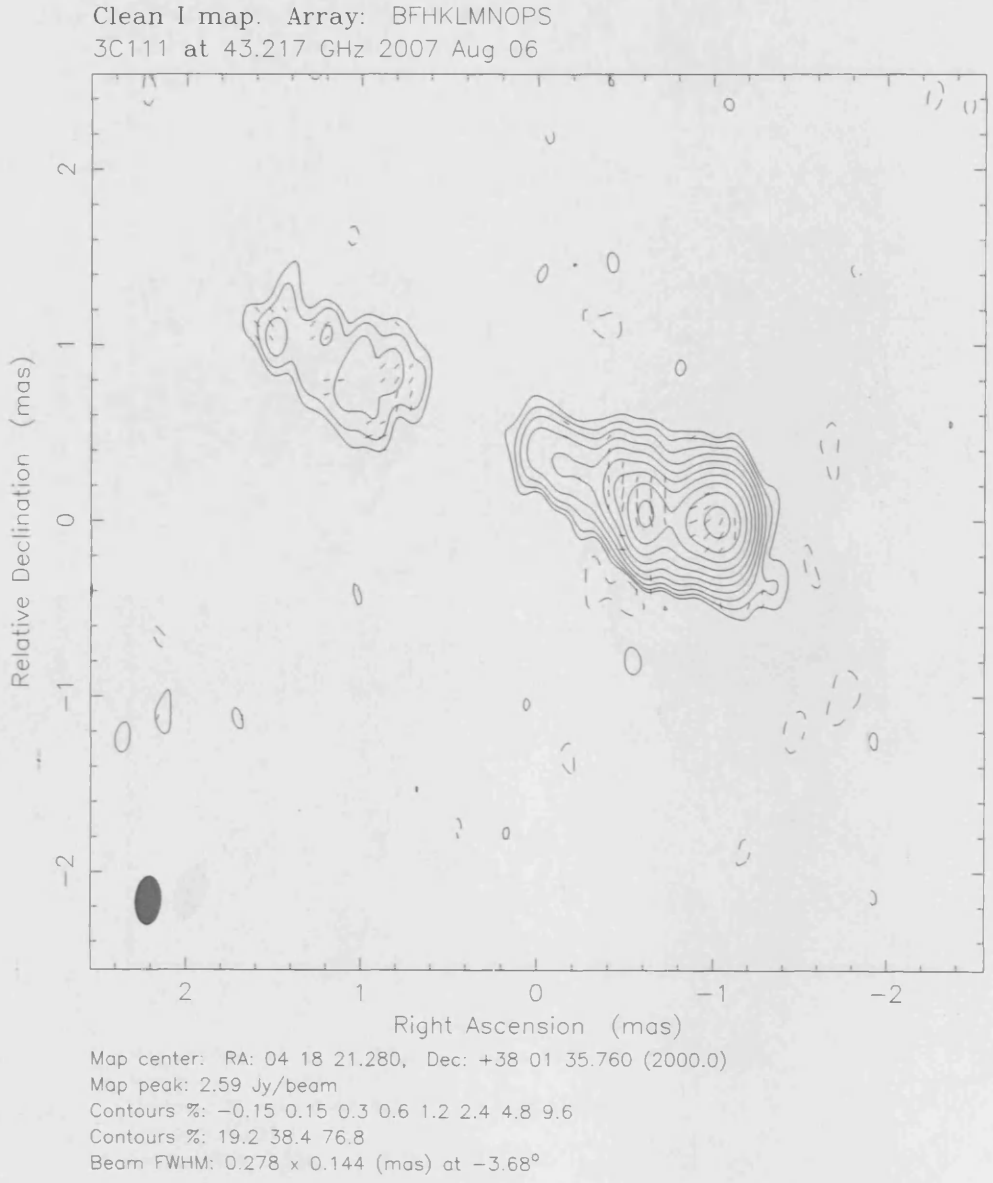

Figure 3.78: August 2007 VLBI Map of 3C111. For polarisation vectors: 1 mas = 3.57x10^{-1} Jy/beam.

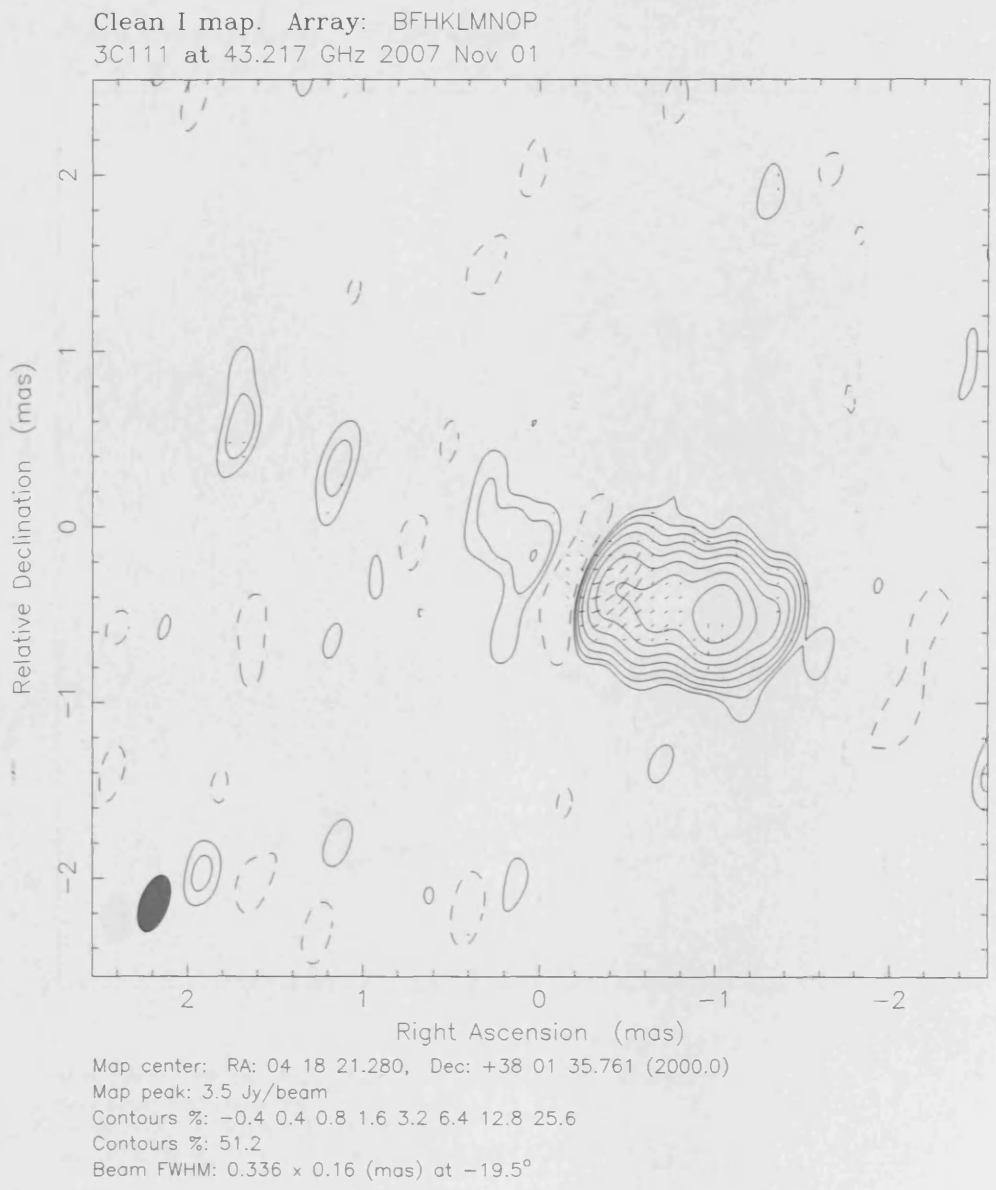

Figure 3.79: November 2007 VLBI Map of 3C111. For polarisation vectors: 1 mas = 5.00×10^{-1} Jy/beam.

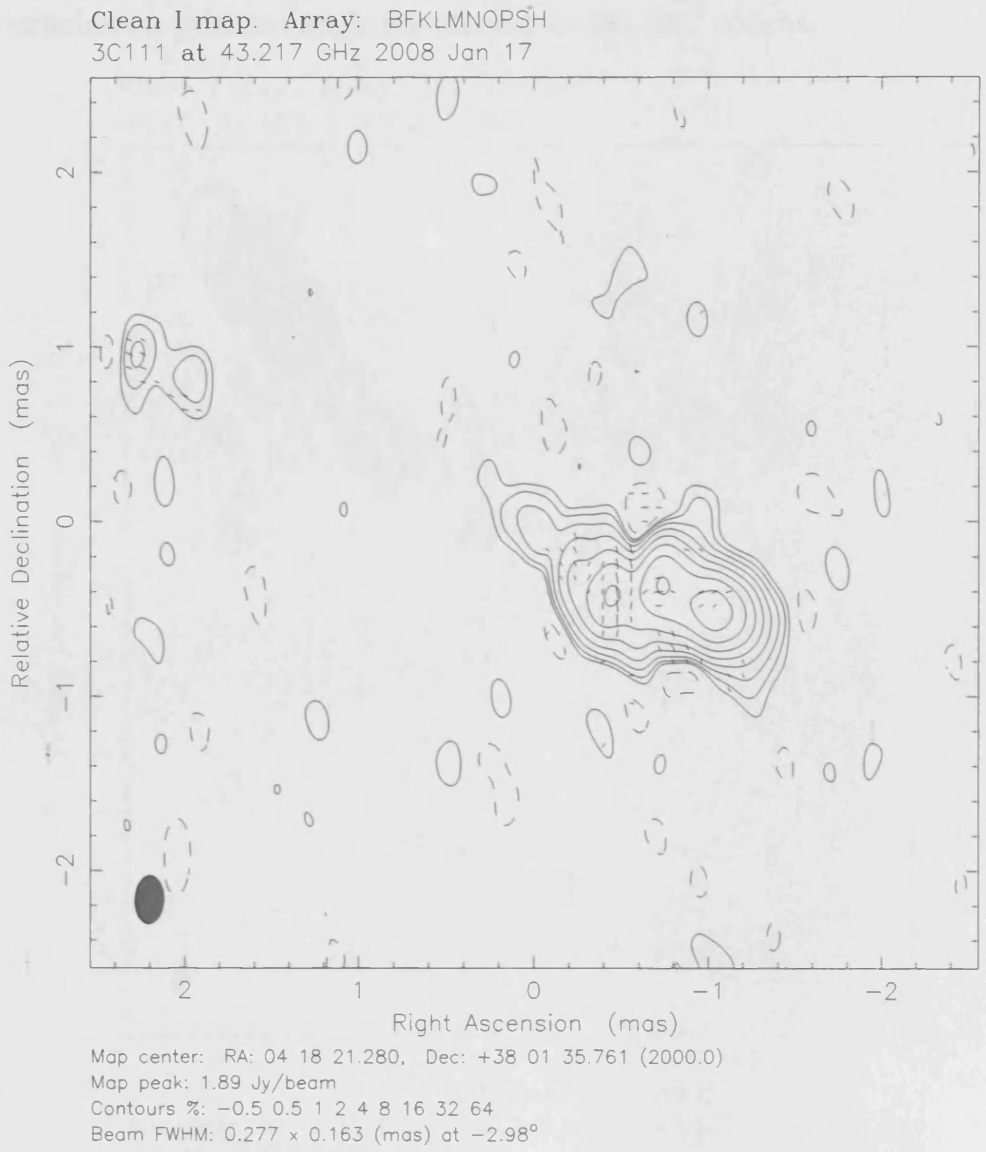

Figure 3.80: January 2008 VLBI Map of 3C111. For polarisation vectors: 1 mas = 2.50x10^{-1} Jy/beam.

3C273

This source demonstrates some signs of interesting helical structure in all of the epochs shown. This can be seen along each of the jets in places where the structure appears to meander. This source exhibits a great deal of polarised intensity and this is extended beyond the core in each of the epochs shown. The core polarisation appears to maintain a fairly constant position angle in the 2007 epochs. In the January 2008 epoch the polarisation in the core appears to fall into two regions, although the polarisation actually in the core maintains the position angle mentioned for the 2007 epochs.

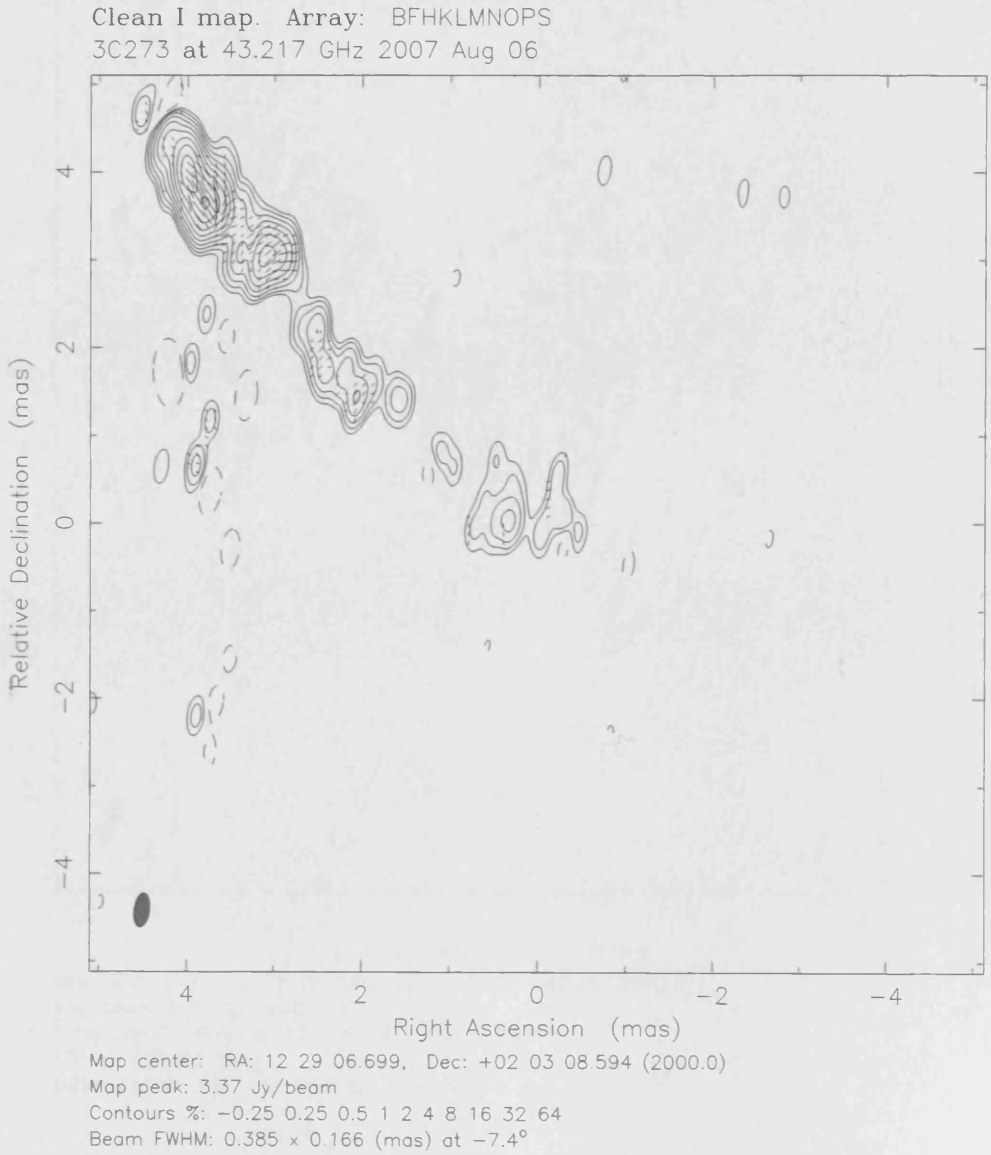

Figure 3.81: August 2007 VLBI Map of 3C273. For polarisation vectors: 1 mas = 7.14×10^{-1} Jy/beam.

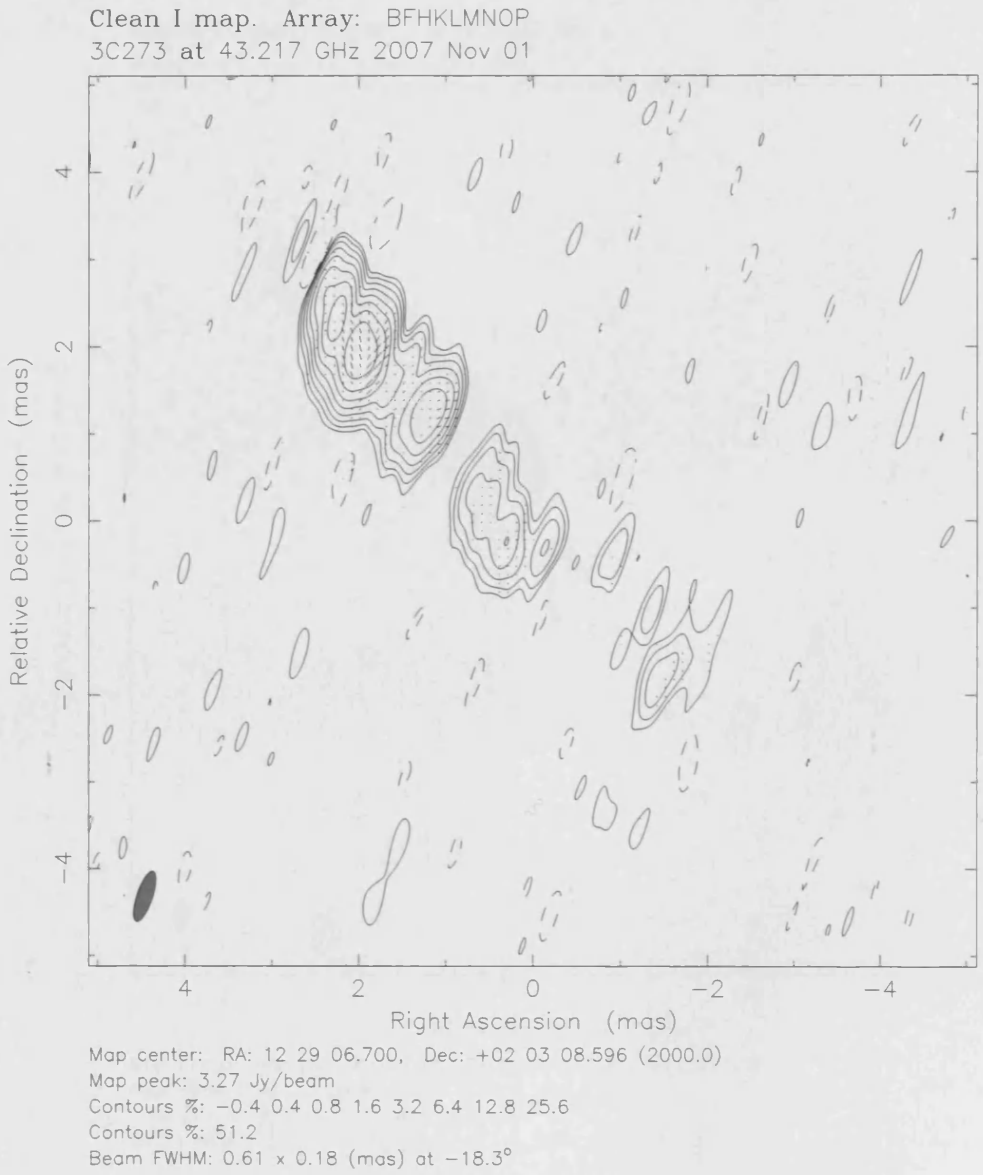

Figure 3.82: November 2007 VLBI Map of 3C273. For polarisation vectors: 1 mas = 2.50×10^0 Jy/beam.

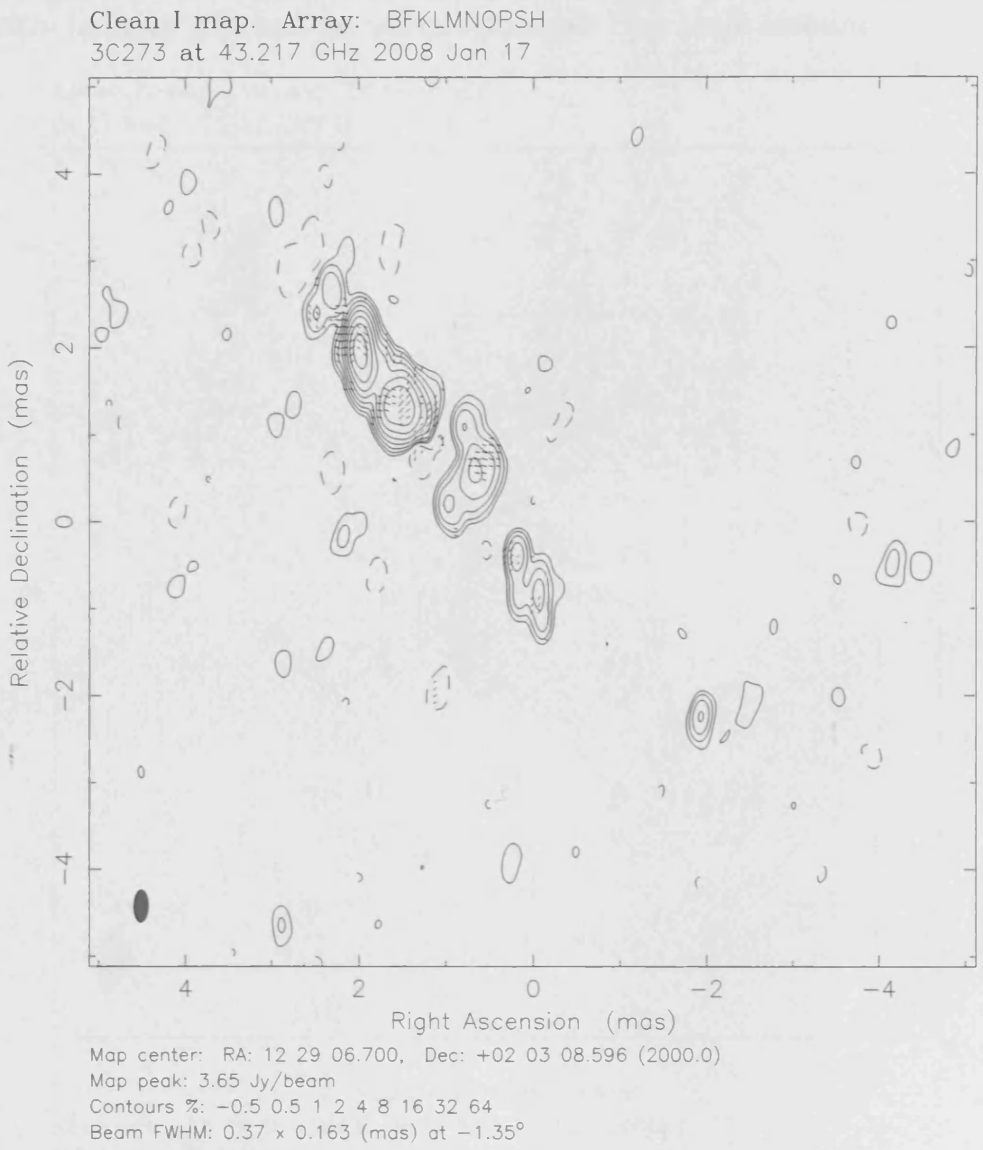

Figure 3.83: January 2008 VLBI Map of 3C273. For polarisation vectors: 1 mas = 6.25x10^{-1} Jy/beam.

The peak flux for this source changes by a significant amount between each of the epochs. The initial $6.86Jy$ rises to $10.7Jy$ before the final figure of $8.25Jy$ is reached. The overall structure of this source is fairly constant throughout the three epochs. There is very strong levels of polarised intensity in the August 2007 epoch that appears to abruptly rotate between the core and first component. In the same area in November 2007, a rotation of the position angle of polarisation can be seen as well. There is polarisation extending out from the core in January 2008 and the vectors do rotate by a small amount.

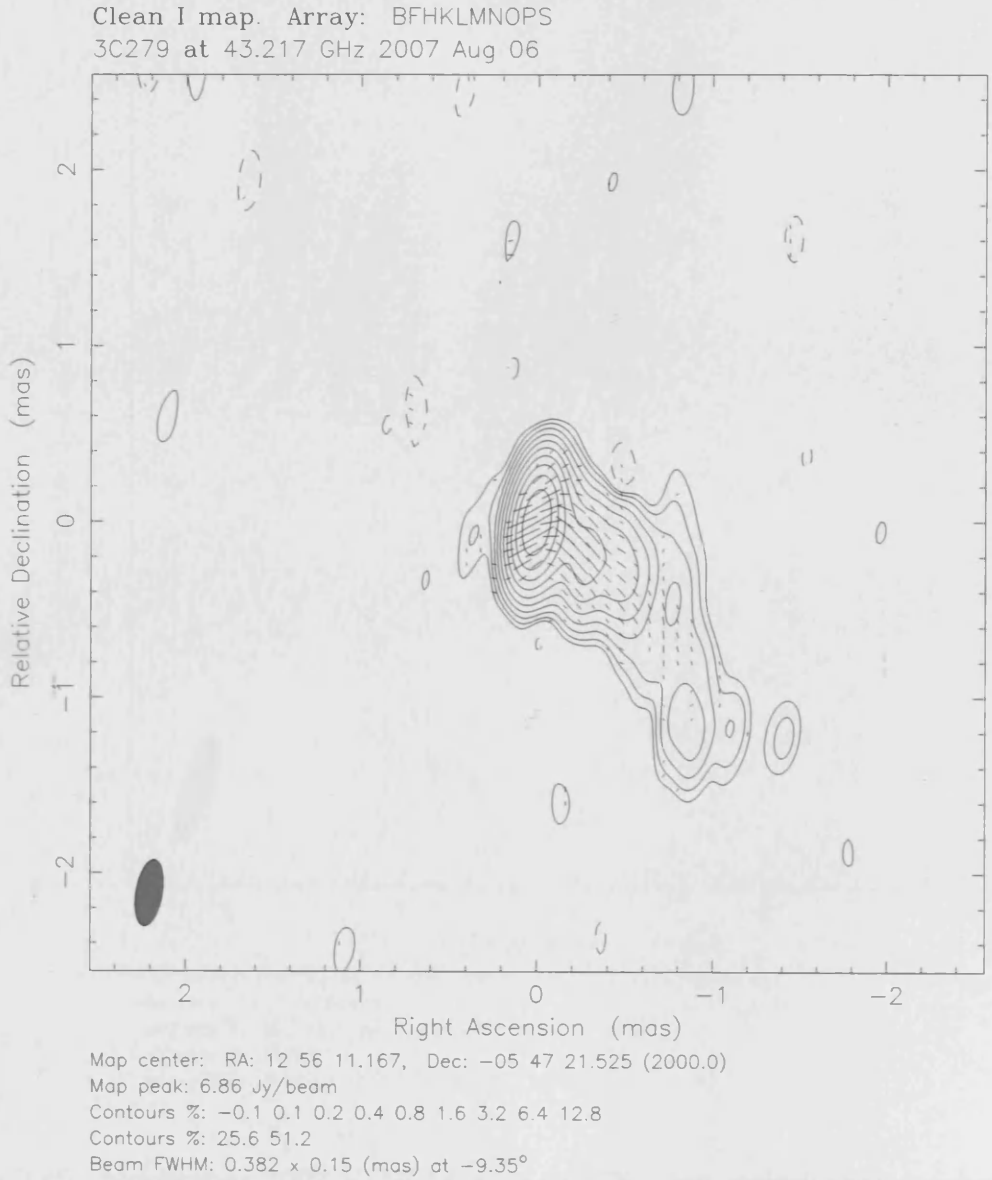

Figure 3.84: August 2007 VLBI Map of 3C279. For polarisation vectors: 1 mas = 8.33x10^{-1} Jy/beam.

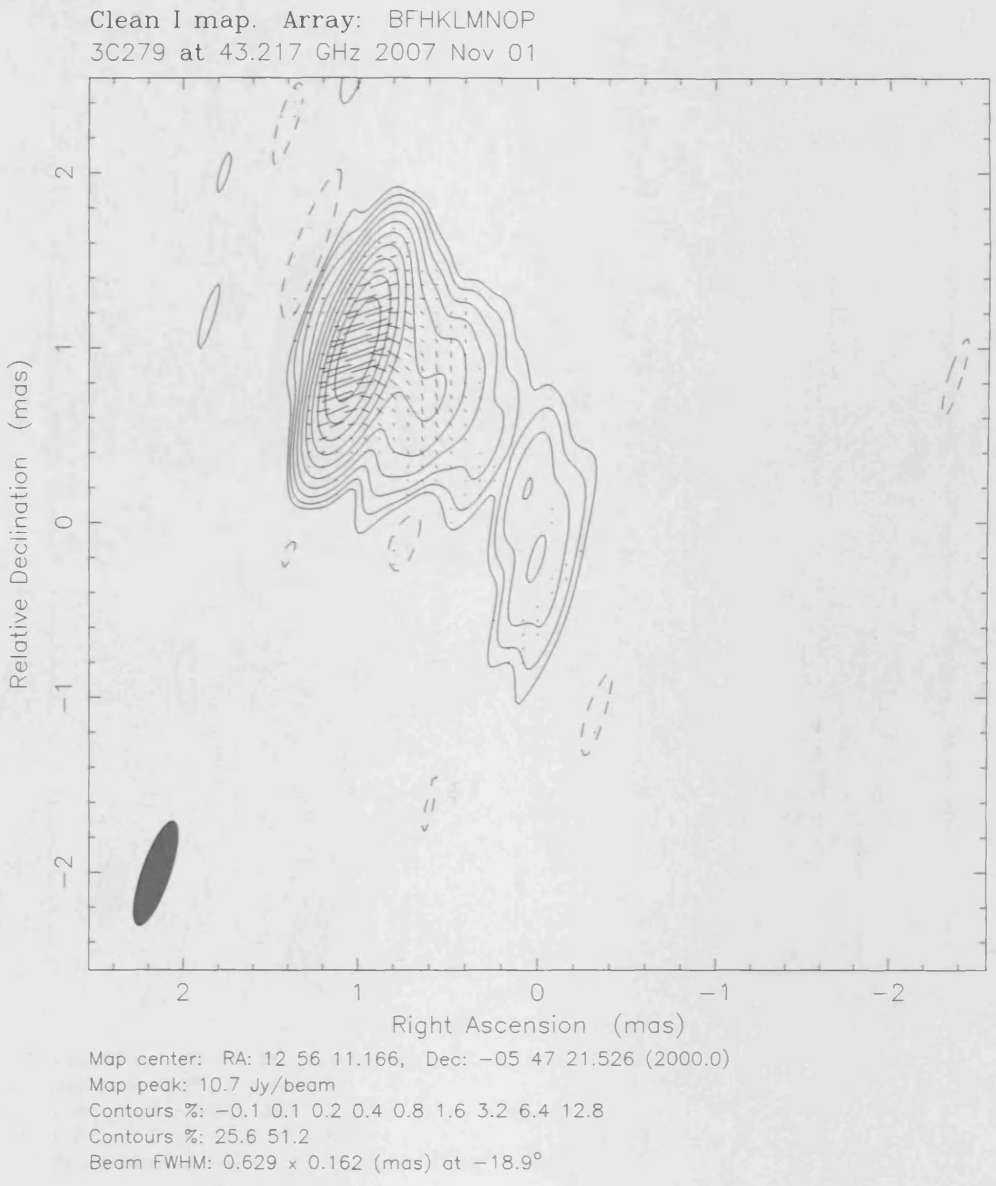

Figure 3.85: November 2007 VLBI Map of 3C279. For polarisation vectors: 1 mas = 2.50×10^0 Jy/beam.

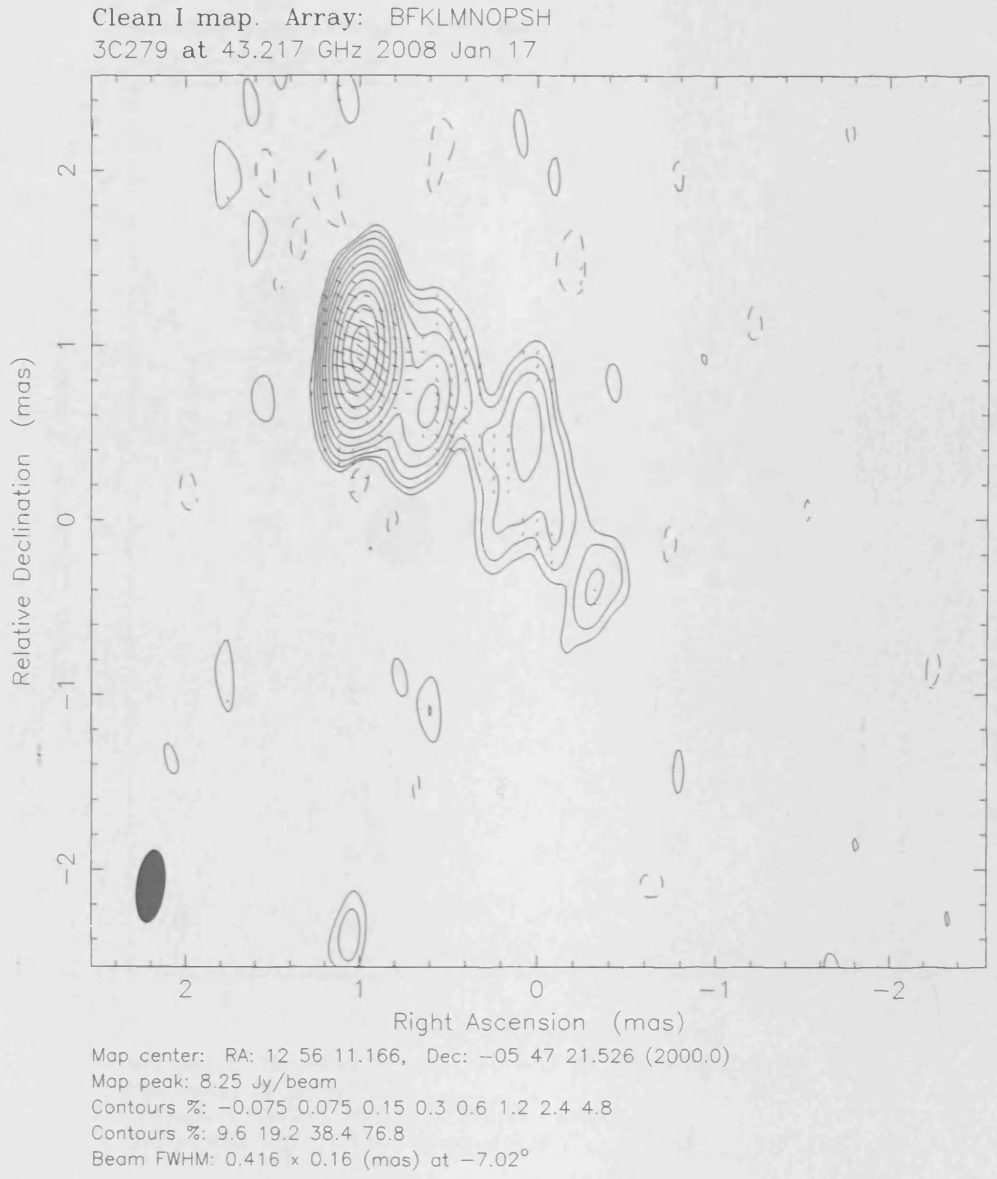

Figure 3.86: January 2008 VLBI Map of 3C279. For polarisation vectors: 1 mas = 1.00×10^0 Jy/beam.

3C345

This is a second source for which there are indications of a helical jet structure in all of the epochs shown. As has been the case for a number of sources, 3C345 reaches its lowest peak flux in the January 2008 epoch. In terms of polarisation, it appears from the polarised intensity maps that it is only the 2007 epochs that harbour any polarisation of significant strength.

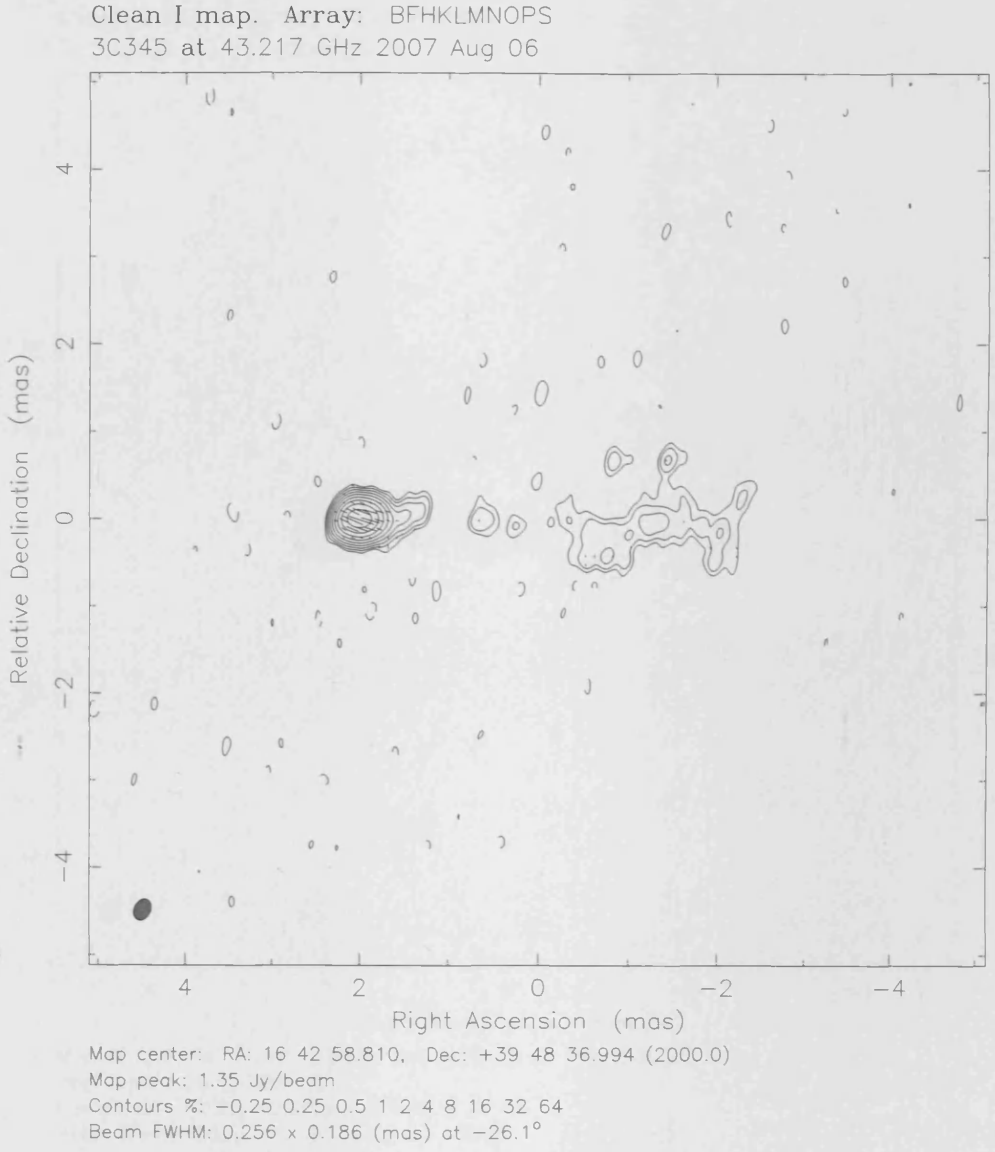

Figure 3.87: August 2007 VLBI Map of 3C345. For polarisation vectors: 1 mas = 7.14×10^{-1} Jy/beam.

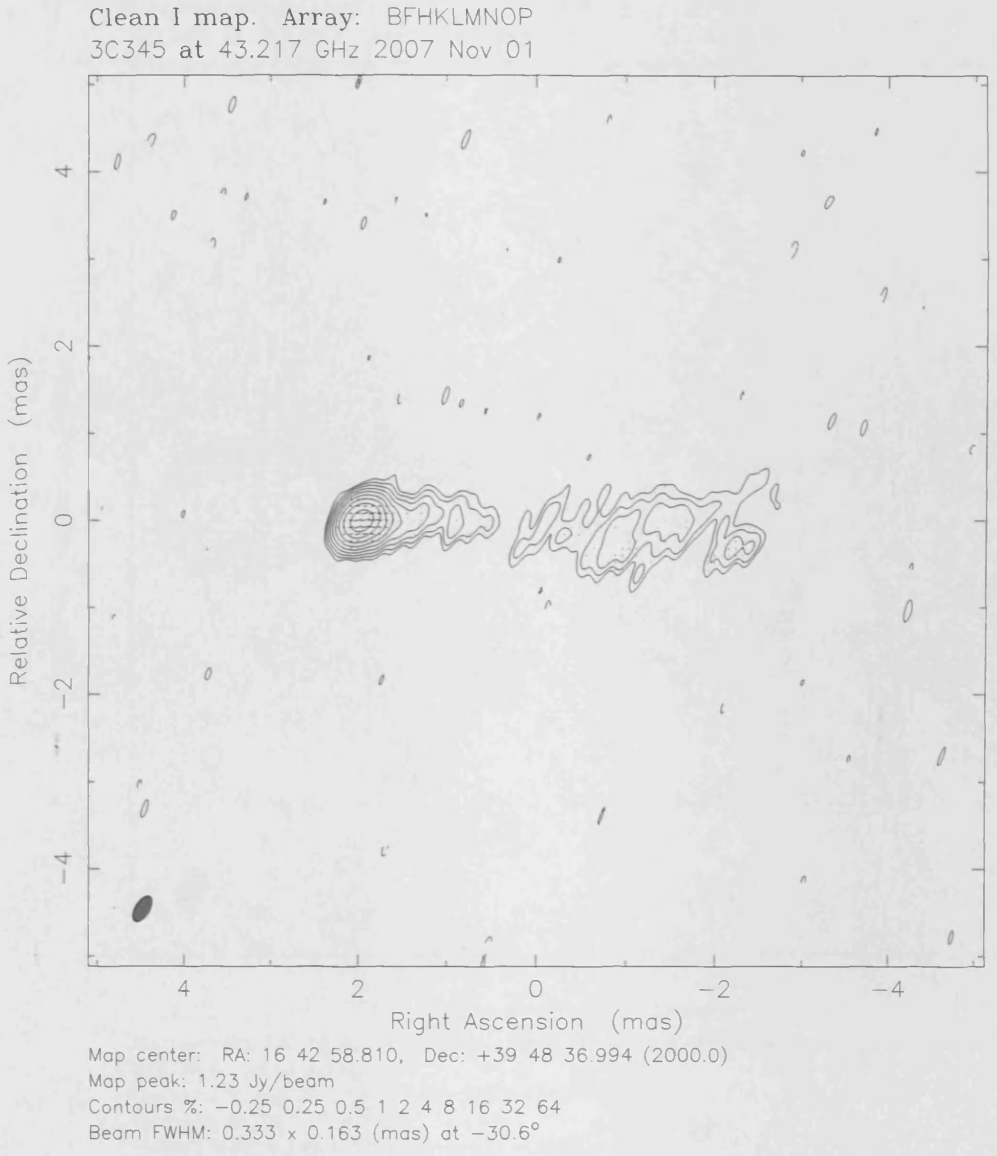

Figure 3.88: November 2007 VLBI Map of 3C345. For polarisation vectors: 1 mas = 1.00×10^0 Jy/beam.

Figure 3.89: January 2008 VLBI Map of 3C345. For polarisation vectors: 1 mas = 2.50×10^{-1} Jy/beam.

3C446

This source brightens by around $1Jy$ between the 2007 epochs shown. Polarisation is present in the core and maintains a fairly steady position angle throughout the three epochs. There is extended polarisation in the August 2007 epoch that may well be real but is weak. The November 2007 polarised intensity map reveals some extended polarisation as well.

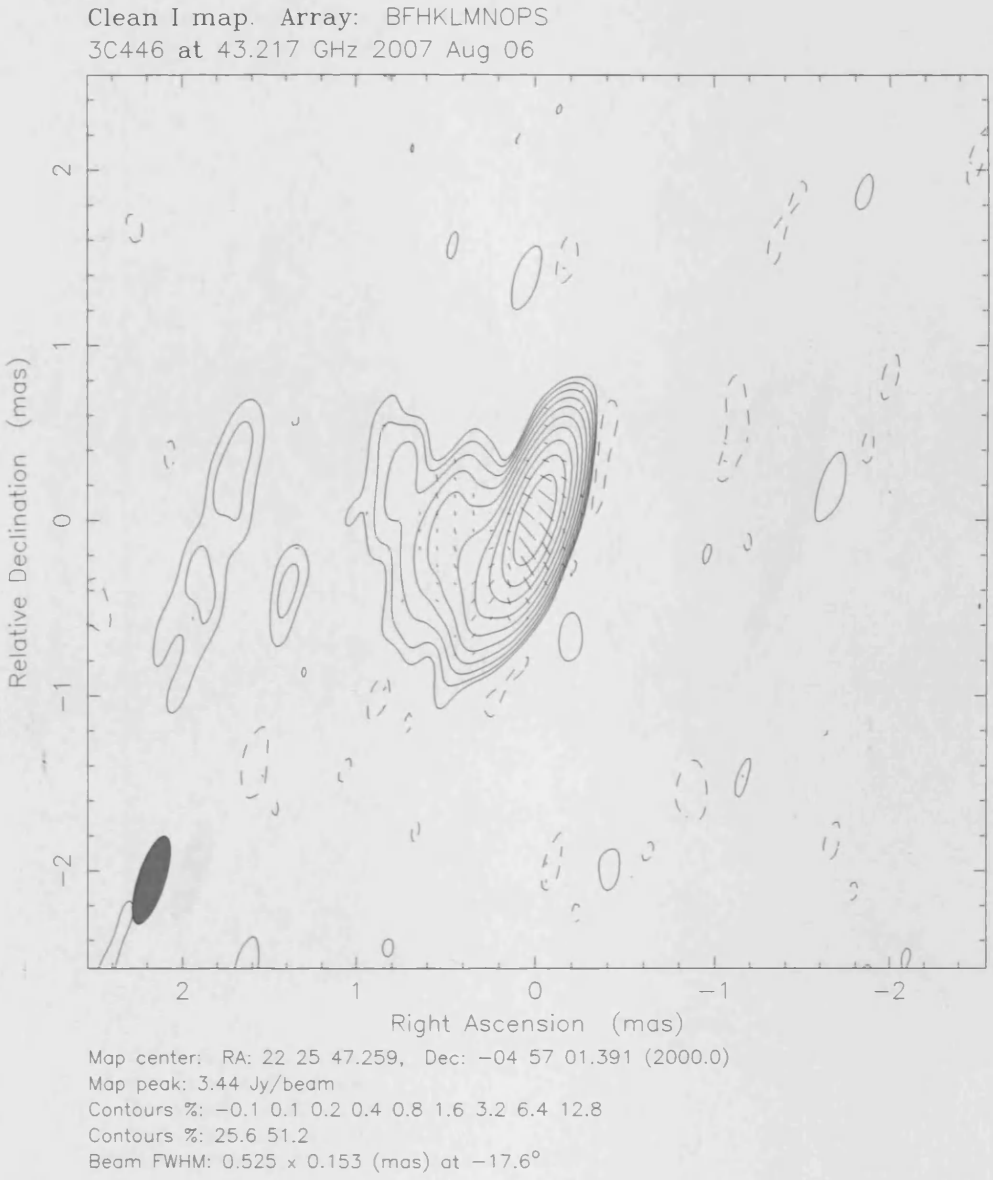

Figure 3.90: August 2007 VLBI Map of 3C446. For polarisation vectors: 1 mas = 7.14x10^{-1} Jy/beam.

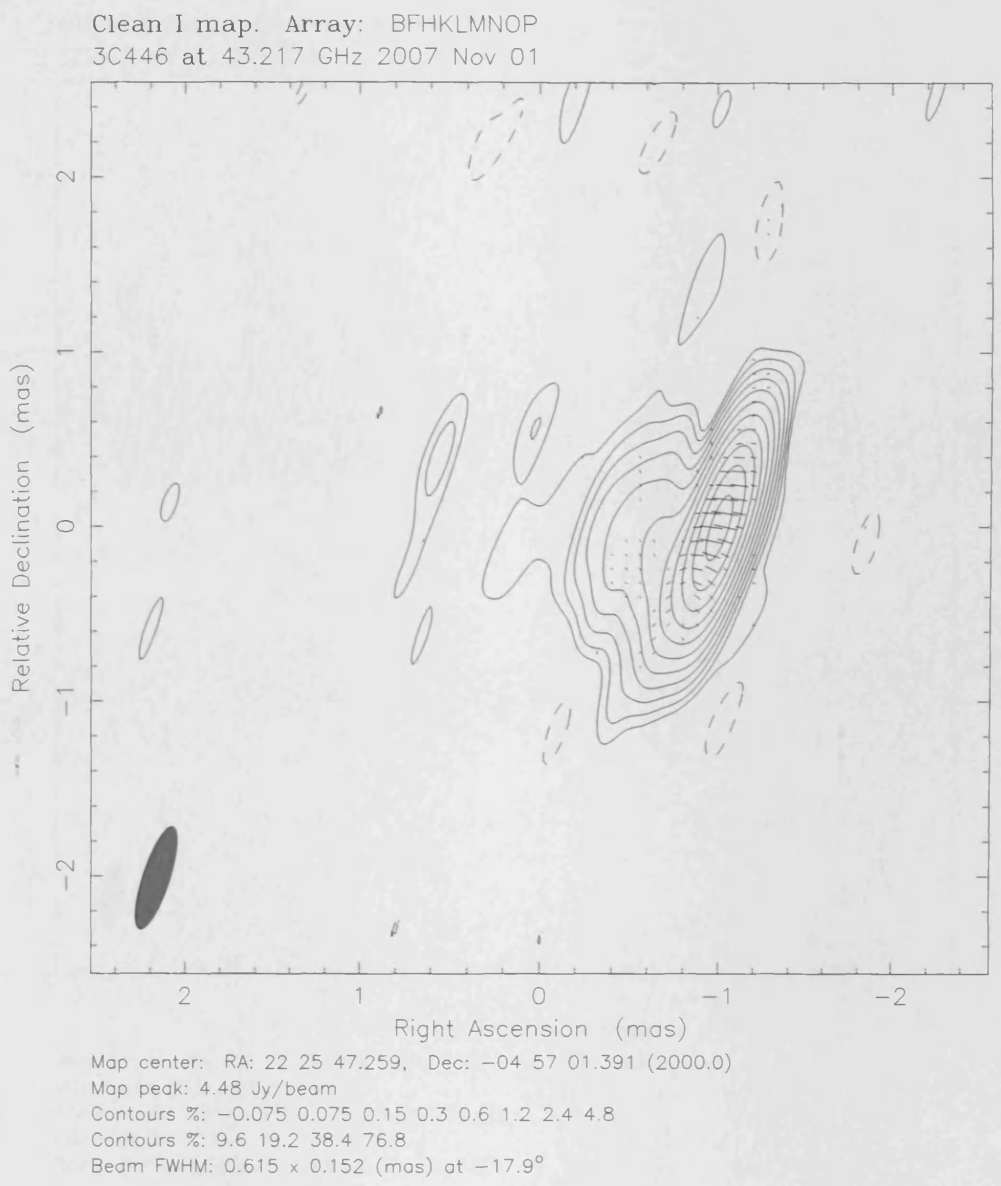

Figure 3.91: November 2007 VLBI Map of 3C446. For polarisation vectors: 1 mas = 1.25×10^0 Jy/beam.

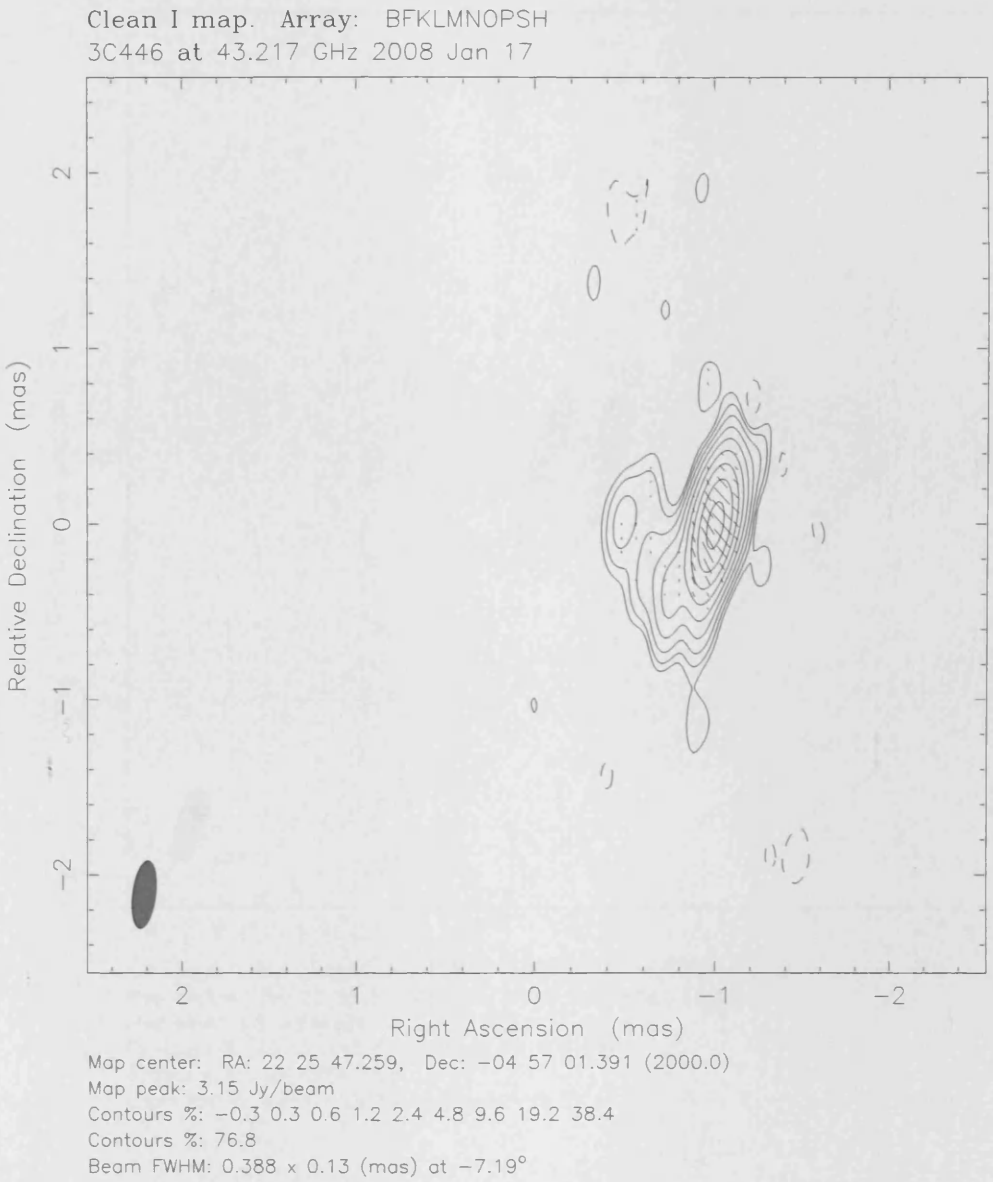

Figure 3.92: January 2008 VLBI Map of 3C446. For polarisation vectors: 1 mas = 5.00x10^{-1} Jy/beam.

3C454.3

There is a notable increase in flux between the 2007 epochs ($5.8Jy$ to $7.05Jy$). There are signs of helical structure in the January 2008 epoch. There is strong polarisation in the core in the 2007 epochs.

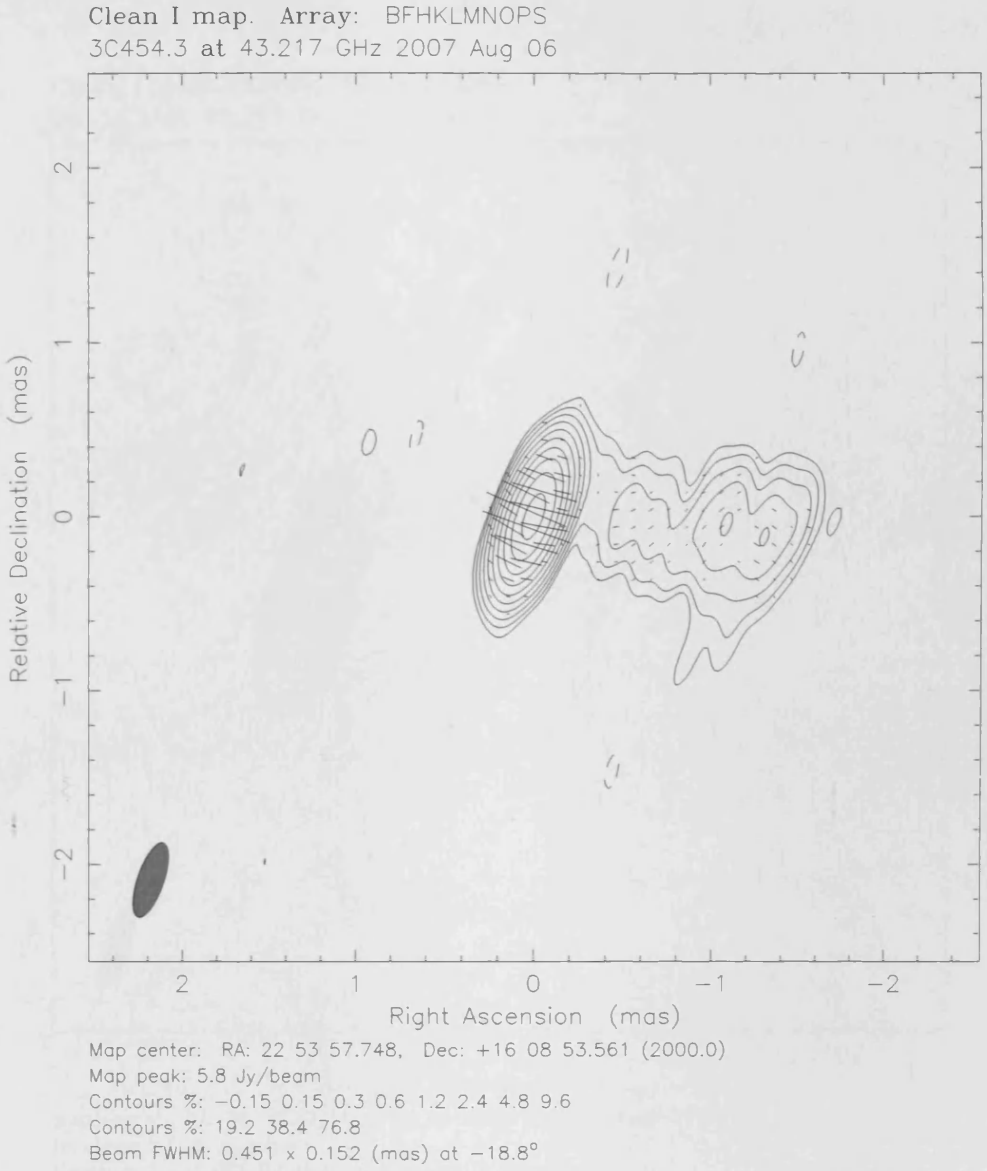

Figure 3.93: August 2007 VLBI Map of 3C454.3. For polarisation vectors: 1 mas = $8.33 \text{x} 10^{-1}$ Jy/beam.

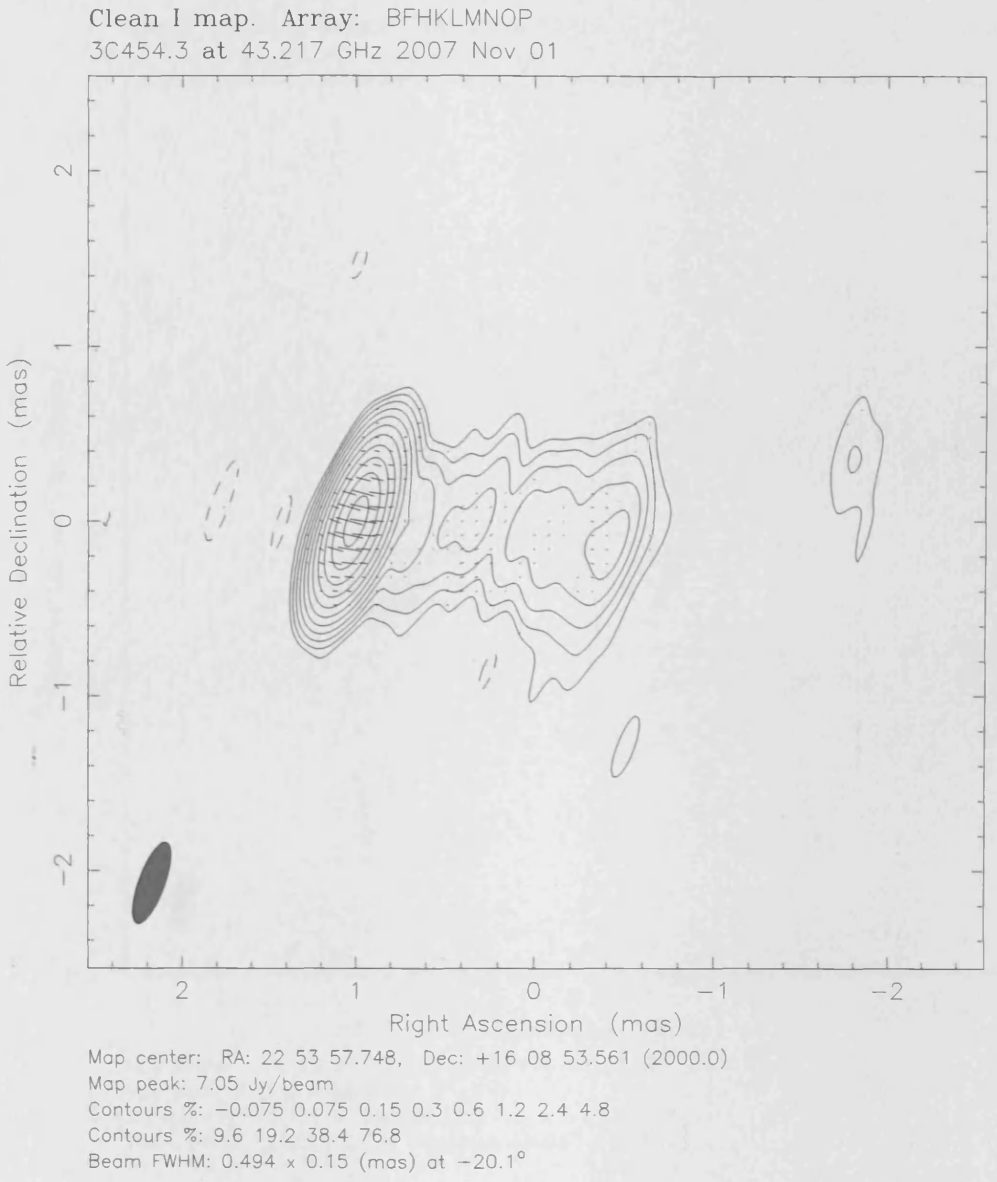

Figure 3.94: November 2007 VLBI Map of 3C454.3. For polarisation vectors: 1 mas = 1.25×10^0 Jy/beam.

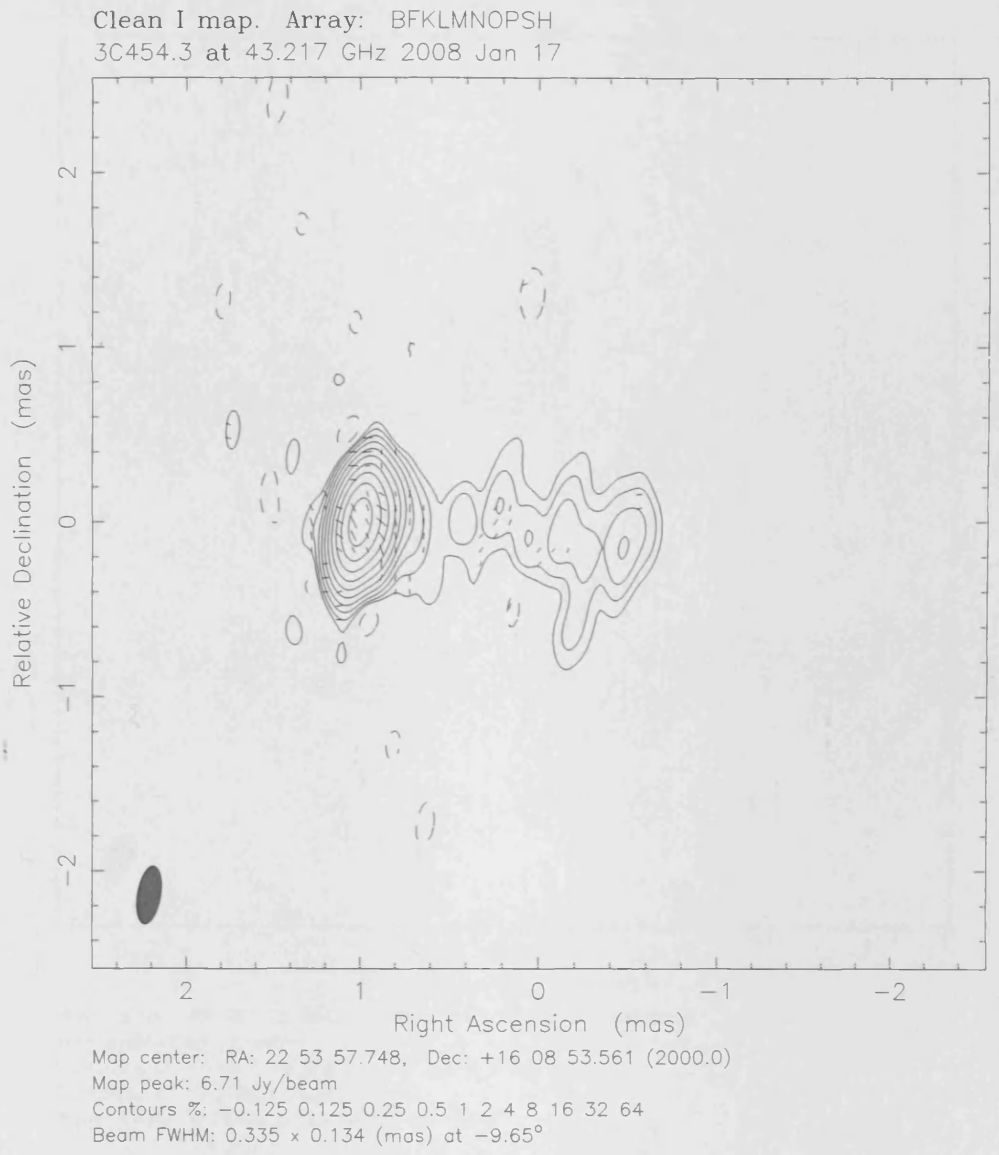

Figure 3.95: January 2008 VLBI Map of 3C454.3. For polarisation vectors: 1 mas = 2.50×10^{-1} Jy/beam.

BL Lac

There is a drop of roughly $1Jy$ between the November 2007 and January 2008 epochs. The polarised intensity maps for this source show strongly polarised cores across the three epochs shown, with some extended polarisation close to the core in January 2008. The core polarisation position angle is very consistent in all of the epochs shown.

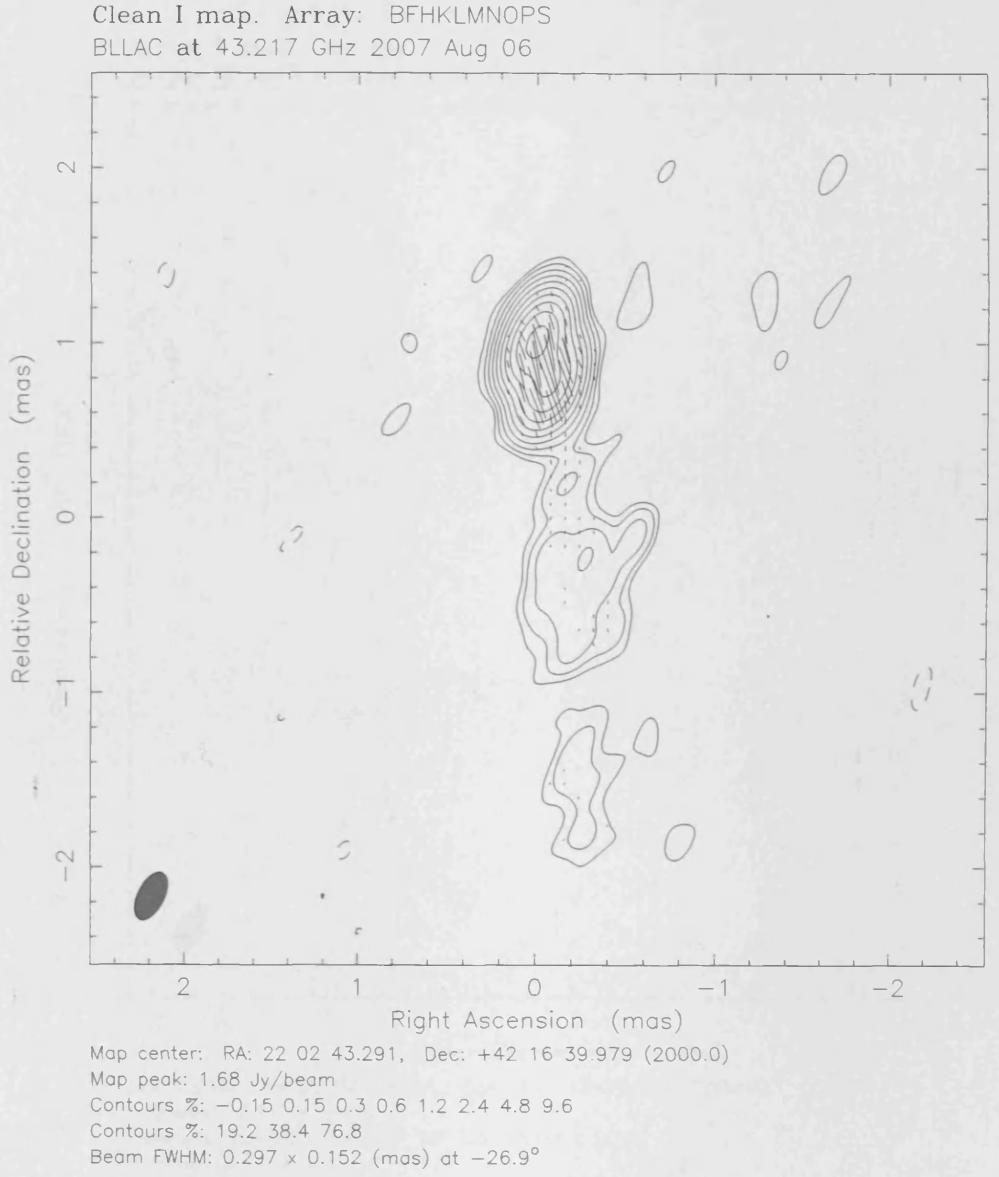

Figure 3.96: August 2007 VLBI Map of BL Lac. For polarisation vectors: 1 mas = 8.33×10^{-1} Jy/beam.

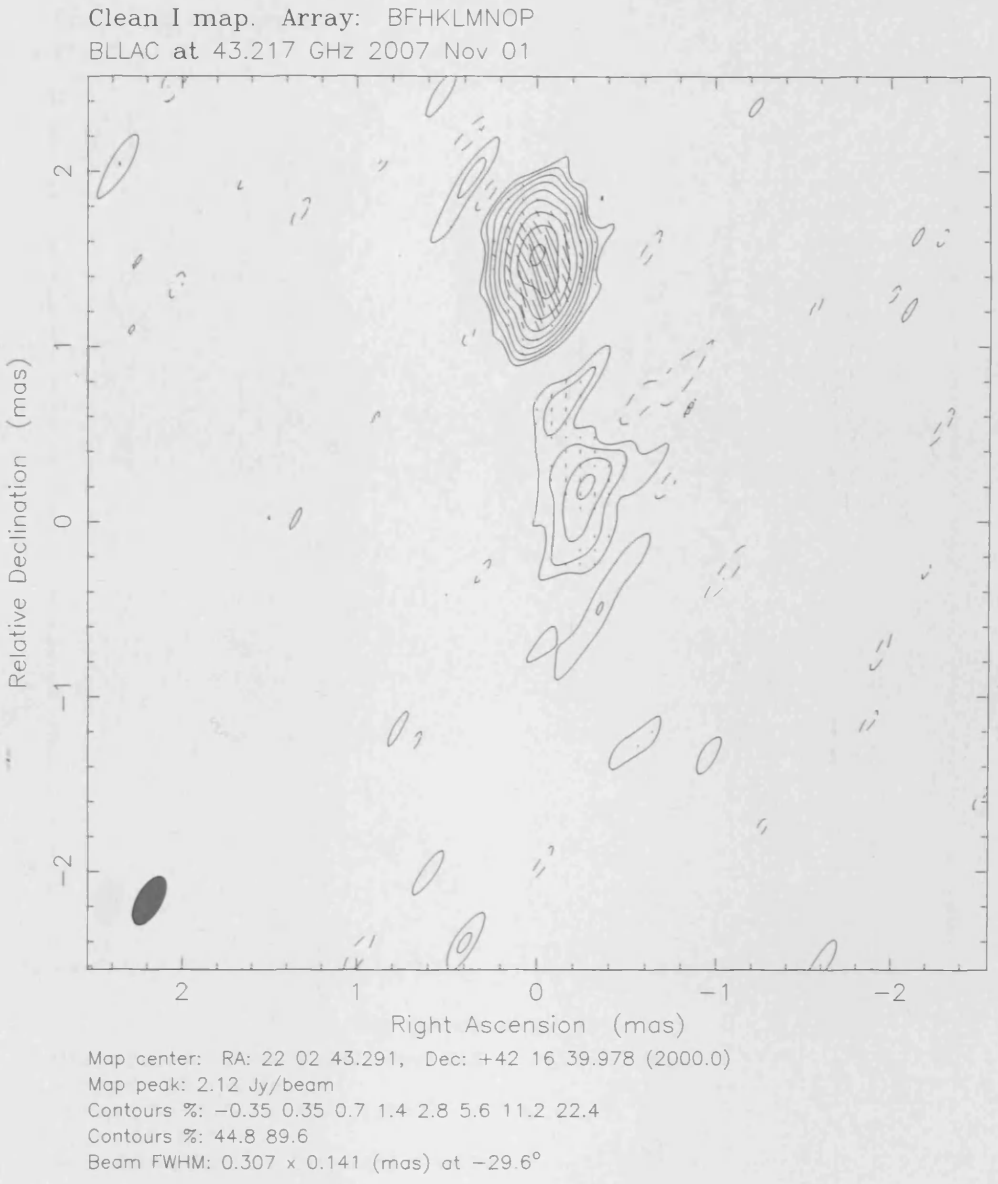

Figure 3.97: November 2007 VLBI Map of BL Lac. For polarisation vectors: 1 mas = 8.33×10^{-1} Jy/beam.

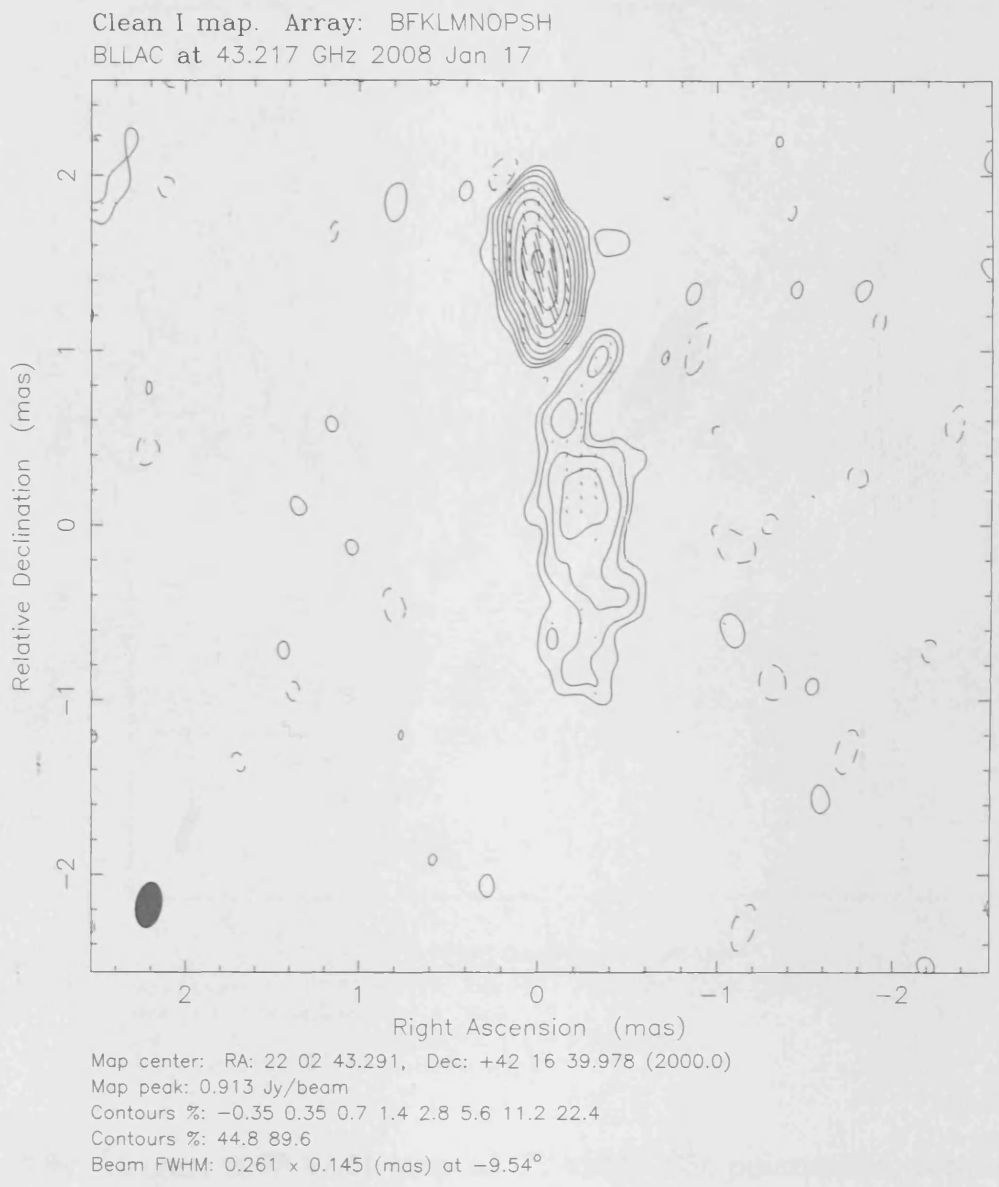

Figure 3.98: January 2008 VLBI Map of BL Lac. For polarisation vectors: 1 mas = 5.00×10^{-1} Jy/beam.

CTA102

The peak flux for this source has remained fairly constant through the three epochs shown. The polarised intensity maps for this source indicate significant polarisation in the core for this source across all of the epochs shown.

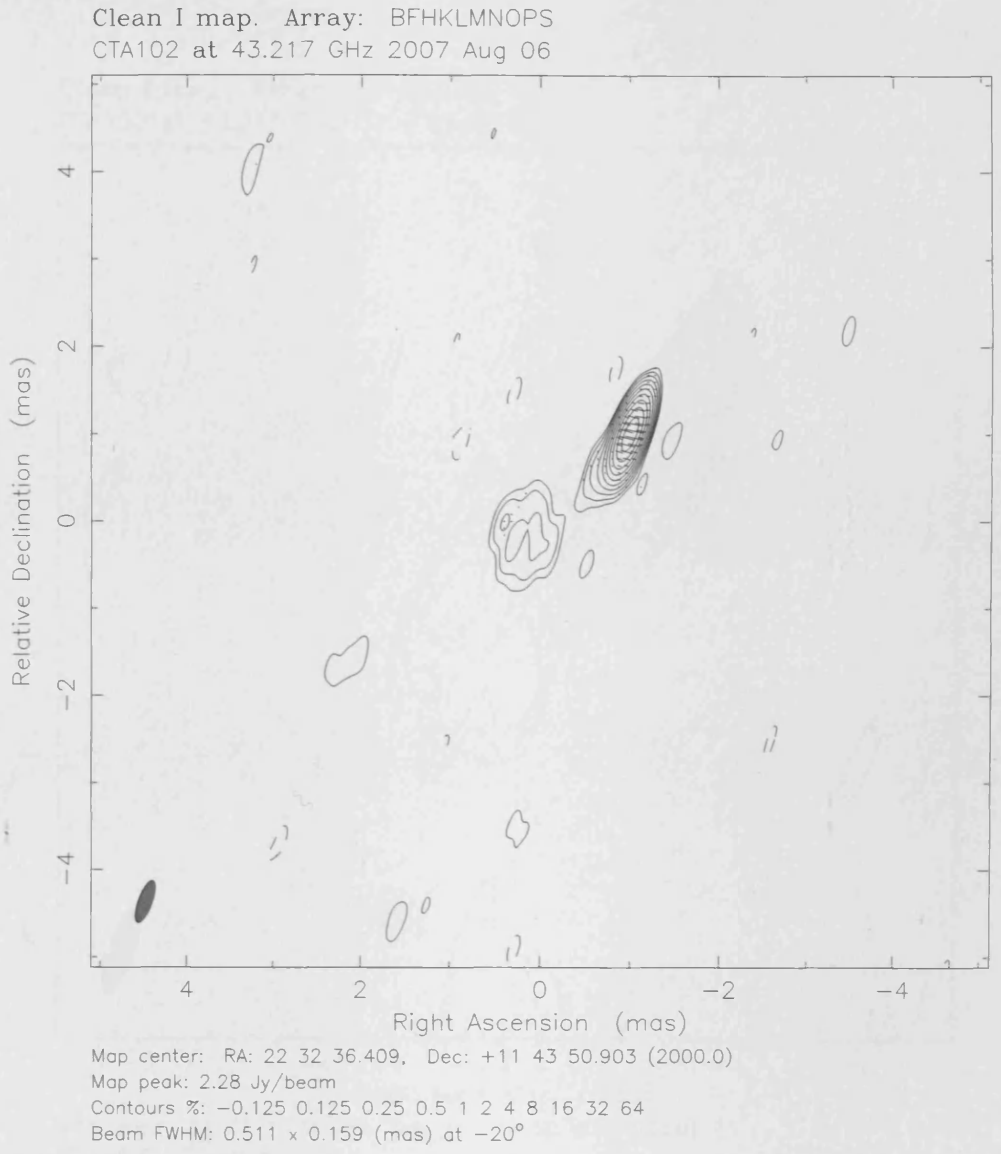

Figure 3.99: August 2007 VLBI Map of CTA102. For polarisation vectors: 1 mas = 8.33×10^{-1} Jy/beam.

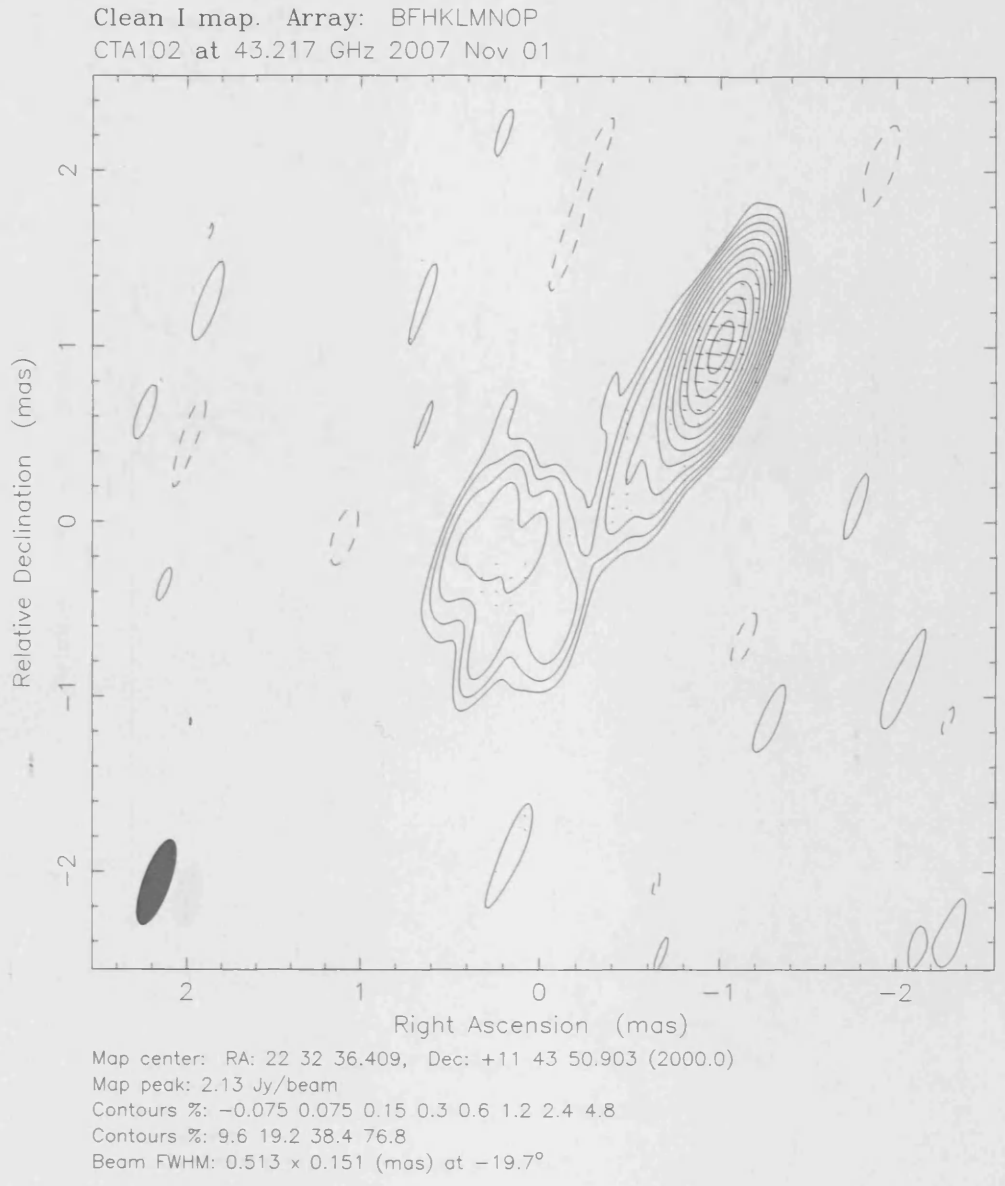

Figure 3.100: November 2007 VLBI Map of CTA102. For polarisation vectors: 1 mas = $6.25 \text{x} 10^{-1}$ Jy/beam.

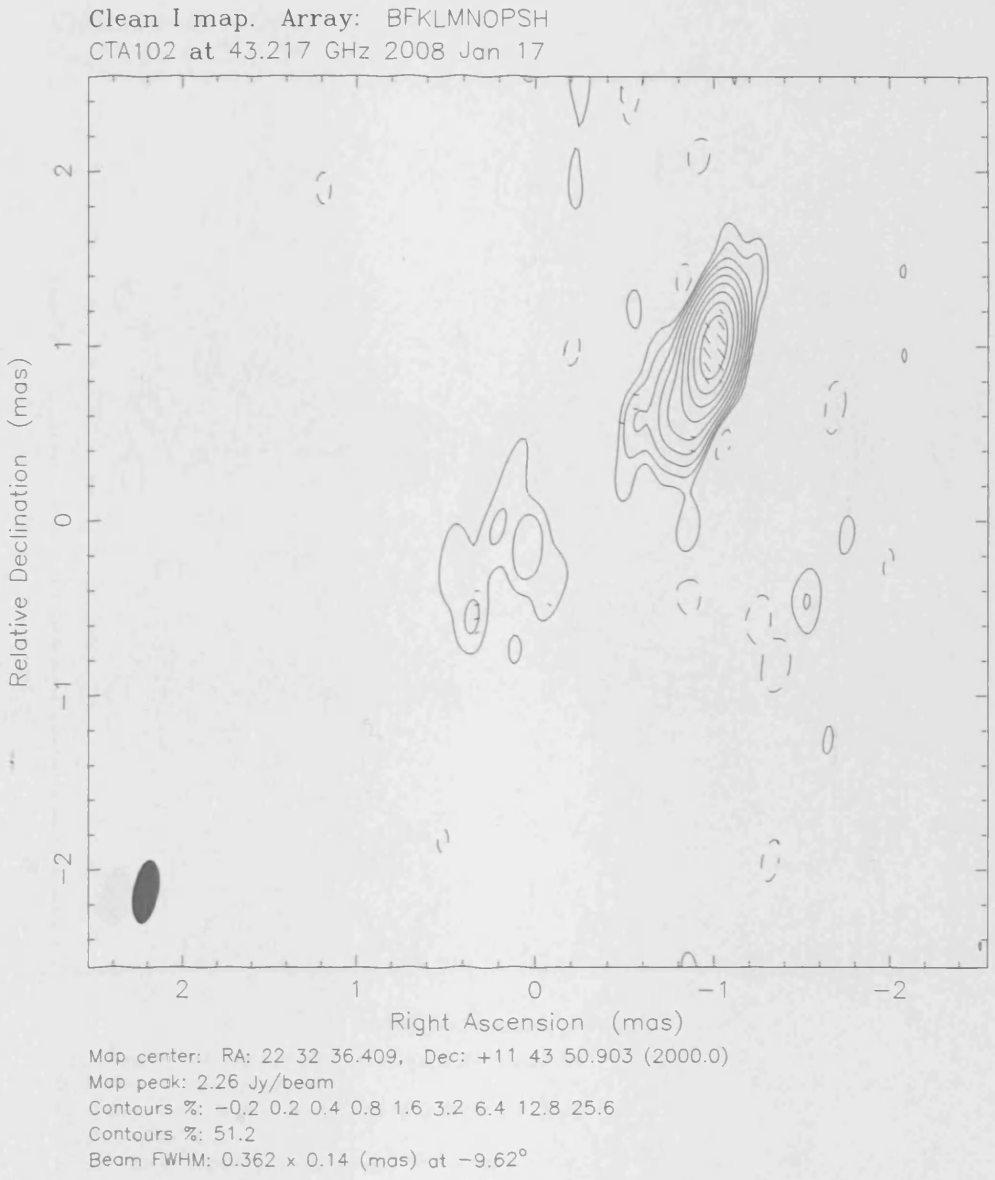

Figure 3.101: January 2008 VLBI Map of CTA102. For polarisation vectors: 1 mas = 5.00×10^{-1} Jy/beam.

OJ287

As can be seen below the VLBI images for this source, the peak flux for this source is higher in November 2007 and January 2008 than it is in August 2007. There appears to be less in the way of extended emission in the January 2008 epoch compared to the others. The maps of polarised intensity show a significantly polarised core in each of the epochs, with some rotation of the position angle of polarisation.

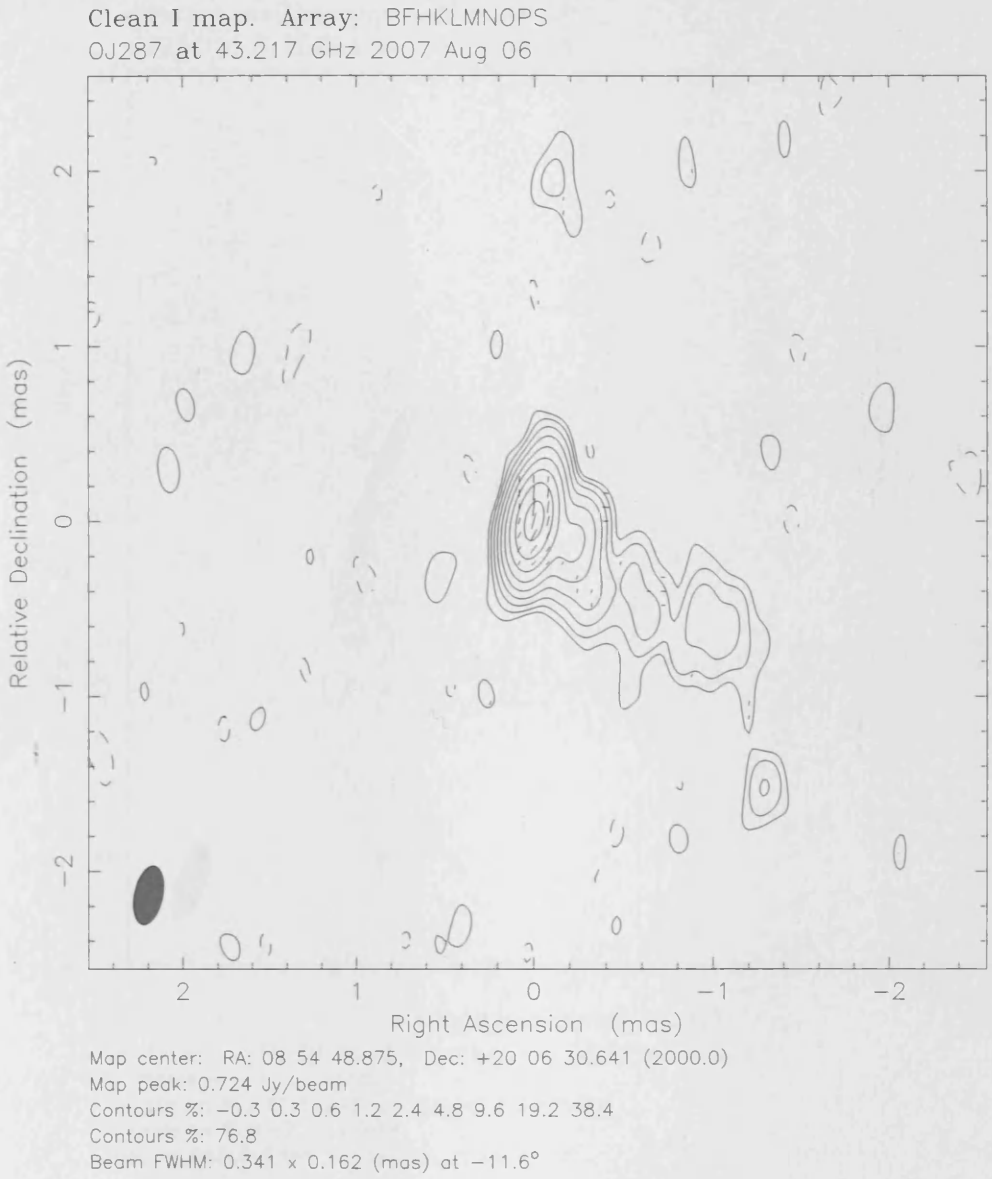

Figure 3.102: August 2007 VLBI Map of OJ287. For polarisation vectors: 1 mas = 5.00×10^{-1} Jy/beam.

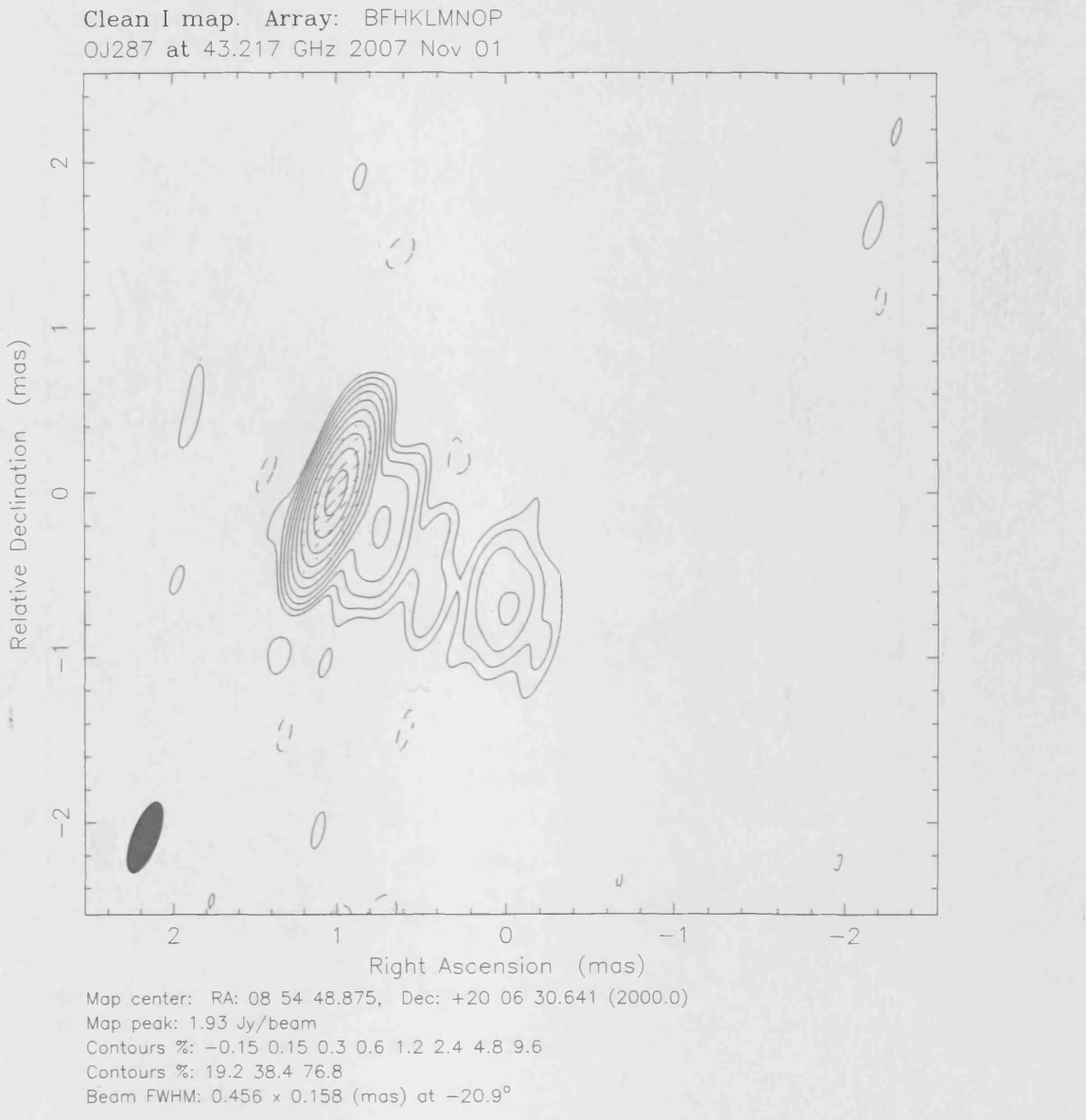

Figure 3.103: November 2007 VLBI Map of OJ287. For polarisation vectors: 1 mas = 1.92×10^0 Jy/beam.

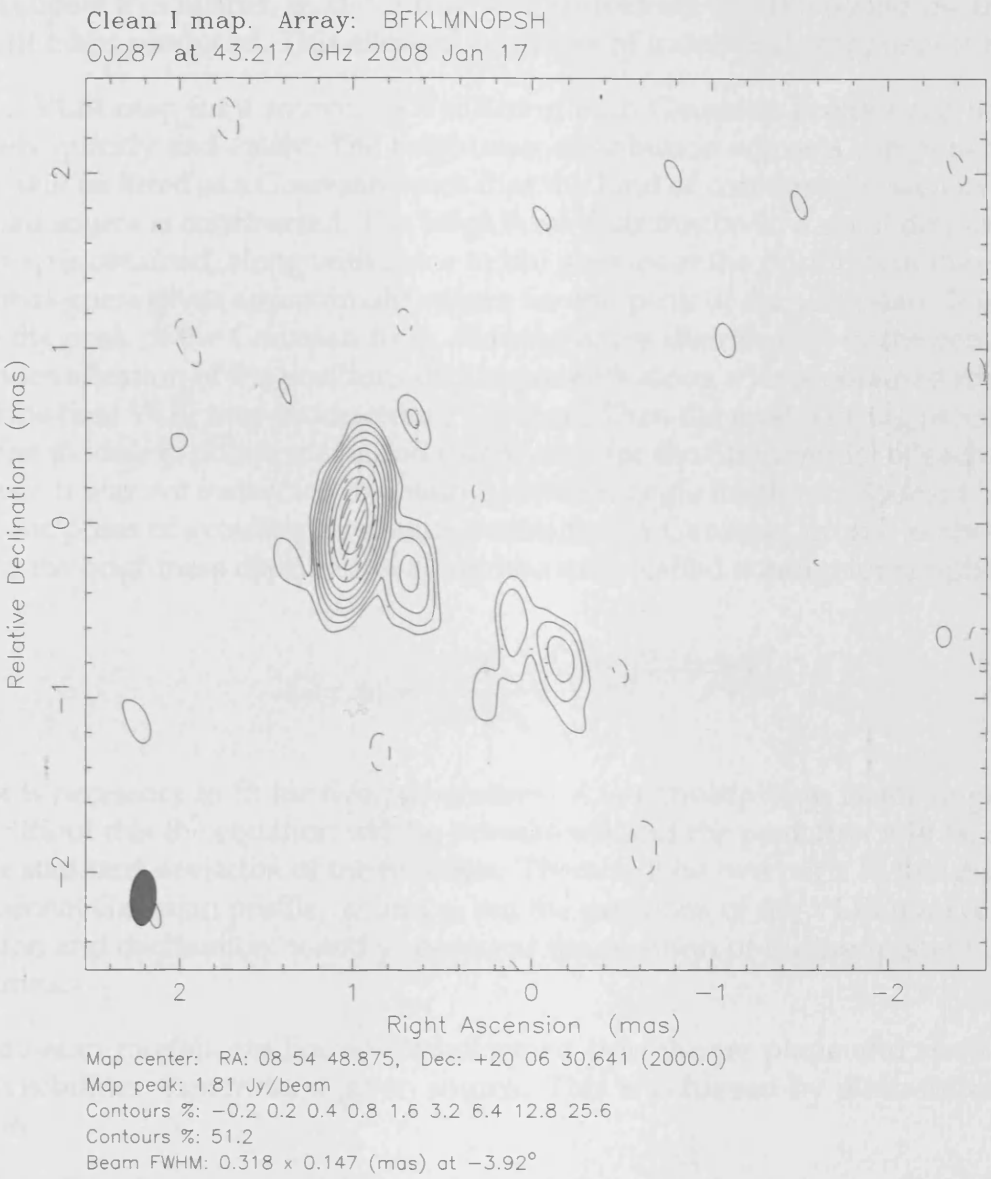

Figure 3.104: January 2008 VLBI Map of OJ287. For polarisation vectors: 1 mas = 5.00×10^{-1} Jy/beam.

3.4 Component Positions and Kinematics

During the map-making process, 3C273 yielded some interesting results. Its jet trajectories across multiple epochs indicated spiral structures. A good example of this from the above results section can be seen in Figure 3.81. Similar trajectories could be seen in maps of 3C345. For example see Figure 3.87 above.

To investigate this further, model fitting was performed in AIPS (using the task jmfit) on the VLBI maps produced. This allowed positions of individual components to be found.

Given a VLBI map for a source, model fitting with Gaussian profiles can be performed relatively quickly and easily. The brightness distribution across a component in any direction will be fitted as a Gaussian, such that the kind of contour plot seen in a VLBI map of a point source is constructed. The brightness distribution in a small defined area of the VLBI map is obtained, along with some initial guesses at the positions of the components. The initial guess gives approximate values for the peak of the Gaussian. It is possible to obtain the peak of the Gaussian from the brightness distribution of the component. An initial identification of the positions of components along a jet is obtained from examination of the final VLBI map produced for a source. Then the model fitting procedure will fit Gaussian models to obtain major and minor axes for the fitted model of each component. However, it was not instructed to obtain a position angle for the component in most cases for the purposes of avoiding erroneous model fits. A Gaussian profile as shown below is fitted to the brightness distribution along two axes (called x and y for simplicity here):

$$G(x,y) = \frac{A}{2\pi\sigma_x\sigma_y} e^{-\left[\frac{(x-x_0)^2}{2\sigma_x^2}+\frac{(y-y_0)^2}{2\sigma_y^2}\right]} \tag{3.1}$$

Thus it is necessary to fit for five parameters. A is a multiplying factor to give the peak flux (without this the equation will be normalised and the peak flux will be unity). Here σ is the standard deviation of the function. There will be two parts to this due to the two dimensional Gaussian profile. x_0 and y_0 are the positions of the VLBI map centre in right ascension and declination. x and y represent the position of the component centre in the same units.

The Gaussian models are Fourier transformed into the uv plane and need to be fitted to the visibilities therein for a given source. This is achieved by minimisation of the χ^2 function.

The peak of the Gaussian model gives the peak flux of the component. The full width half maximum (FWHM) of the Gaussian models yields the axes of an ellipse, hence defining the component's size. Each fitted component should have a blue cross indicating its major and minor axes.

3.5 Jet Model Fitting Results

The tables in this section give information on individual components that were model fitted. The main purpose of this was to pinpoint their locations. This was achieved quantitatively via X and Y offsets. It should be noted that these were with respect to the bright-

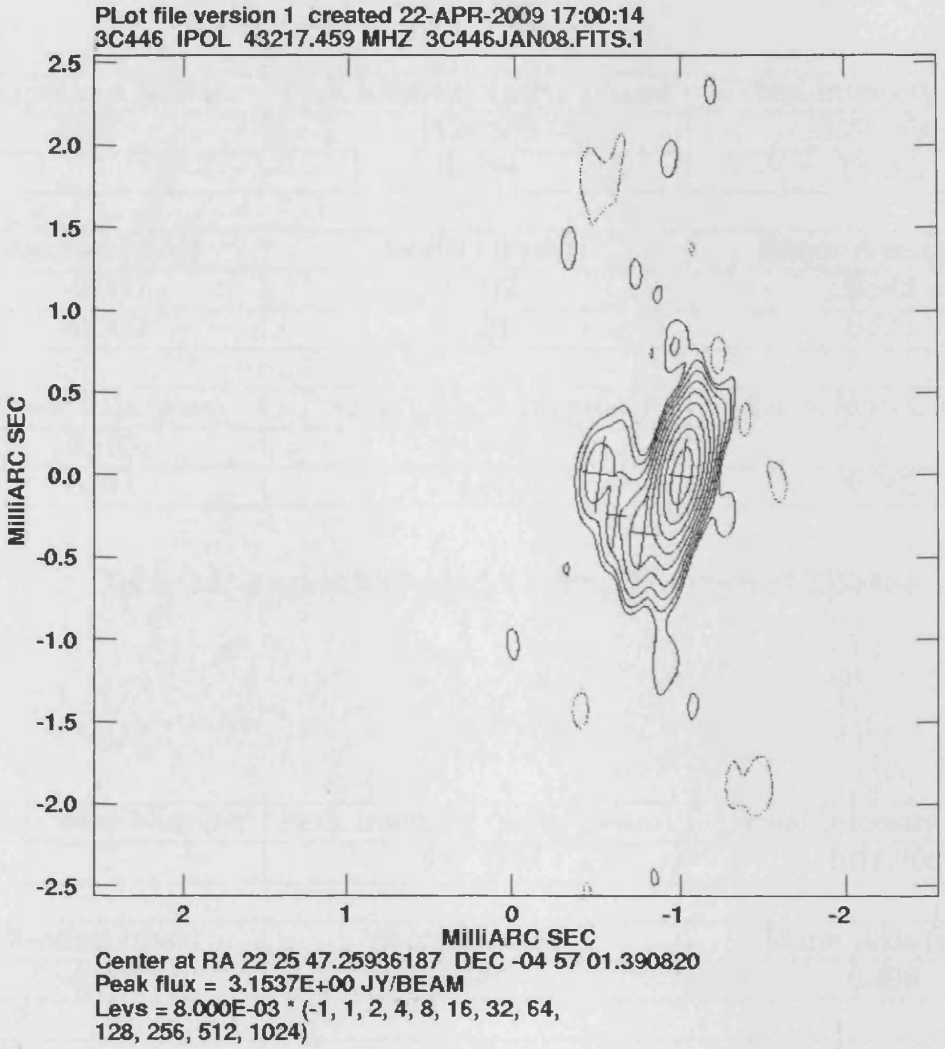

Figure 3.105: Model fitted components

est point on the VLBI map (usually the core). The results are based upon the VLBI maps that were made by the author in August 2007, November 2007 and January 2008.

Component Number	Peak Intensity (mJy/ beam)	Total Intensity (mJy)
C	1126.588	1270.856
1	10.794	15.190

X-offset (mas)	Y-offset (mas)	Major Axis (mas)
-0.006	-0.002	0.343
-0.300	0.701	0.331

Minor Axis (mas)	Position Angle (degrees)	Distance from Core (mas)
0.163	174.802	-
0.211	174.802	0.762

Table 3.1: August 2007 Model Fitting Results for 0235+164

Component Number	Peak Intensity (mJy/ beam)	Total Intensity (mJy)
C	987.179	1016.700

X-offset (mas)	Y-offset (mas)	Major Axis (mas)
-0.001	-0.003	0.490

Minor Axis (mas)	Position Angle (degrees)	Distance from Core (mas)
0.167	162.563	-

Table 3.2: November 2007 Model Fitting Results for 0235+164

Component Number	Peak Intensity (mJy/ beam)	Total Intensity (mJy)
C	516.314	547.727

X-offset (mas)	Y-offset (mas)	Major Axis (mas)
-0.008	0.021	0.405

Minor Axis (mas)	Position Angle (degrees)	Distance from Core (mas)
0.167	170.124	-

Table 3.3: January 2008 Model Fitting Results for 0235+164

Component Number	Peak Intensity (mJy/ beam)	Total Intensity (mJy)
C	777.018	892.852
1	52.183	87.832
2	18.737	31.134
3	12.131	20.914

X-offset (mas)	Y-offset (mas)	Major Axis (mas)
-0.990	-0.508	0.386
-0.579	-0.466	0.406
-0.130	-0.403	0.443
0.636	-0.024	0.459

Minor Axis (mas)	Position Angle (degrees)	Distance from Core (mas)
0.180	171.854	-
0.250	171.854	0.413
0.226	171.854	0.866
0.226	171.854	1.697

Table 3.4: August 2007 Model Fitting Results for 0336-019

Component Number	Peak Intensity (mJy/ beam)	Total Intensity (mJy)
C	902.359	1315.941
1N	41.426	90.814
1	19.451	23.706
2N	12.287	15.225
2	15.518	21.169

X-offset (mas)	Y-offset (mas)	Major Axis (mas)
-0.977	-0.492	0.650
-0.600	-0.498	0.697
-0.181	-0.335	0.669
0.059	-0.343	0.681
0.751	-0.003	0.794

Minor Axis (mas)	Position Angle (degrees)	Distance from Core (mas)
0.235	161.741	-
0.330	161.741	0.377
0.191	161.741	0.811
0.191	161.741	1.047
0.180	161.741	1.796

Table 3.5: November 2007 Model Fitting Results for 0336-019

Component Number	Peak Intensity (mJy/ beam)	Total Intensity (mJy)
C	626.704	913.402
3N	20.556	26.876
1	18.529	18.395
2	11.545	20.593

X-offset (mas)	Y-offset (mas)	Major Axis (mas)
-1.008	-0.485	0.463
-0.685	-0.254	0.477
0.084	-0.011	0.442
0.903	-0.006	0.468

Minor Axis (mas)	Position Angle (degrees)	Distance from Core (mas)
0.265	171.945	-
0.231	171.945	0.397
0.189	171.945	1.190
0.321	171.945	1.970

Table 3.6: January 2008 Model Fitting Results for 0336-019

Component Number	Peak Intensity (mJy/ beam)	Total Intensity (mJy)
C	2058.460	3790.033
1	70.056	163.476

X-offset (mas)	Y-offset (mas)	Major Axis (mas)
-0.028	1.011	0.383
-0.173	0.617	0.385

Minor Axis (mas)	Position Angle (degrees)	Distance from Core (mas)
0.260	173.362	-
0.328	173.362	0.420

Table 3.7: August 2007 Model Fitting Results for 0420-014

Component Number	Peak Intensity (mJy/ beam)	Total Intensity (mJy)
C	2181.534	3901.952
1	28.882	39.915

X-offset (mas)	Y-offset (mas)	Major Axis (mas)
0.015	1.002	0.680
-0.307	0.559	0.798

Minor Axis (mas)	Position Angle (degrees)	Distance from Core (mas)
0.262	161.838	-
0.173	161.838	0.548

Table 3.8: November 2007 Model Fitting Results for 0420-014

Component Number	Peak Intensity (mJy/ beam)	Total Intensity (mJy)
C	1460.125	2935.081
1	128.456	221.427
2	33.358	40.015

X-offset (mas)	Y-offset (mas)	Major Axis (mas)
0.004	0.986	0.408
0.149	0.517	0.420
0.568	0.050	0.378

Minor Axis (mas)	Position Angle (degrees)	Distance from Core (mas)
0.282	174.392	-
0.235	174.392	0.491
0.182	174.392	1.093

Table 3.9: January 2008 Model Fitting Results for 0420-014

Component Number	Peak Intensity (mJy/ beam)	Total Intensity (mJy)
C	3132.337	3471.243
1	205.630	713.964

X-offset (mas)	Y-offset (mas)	Major Axis (mas)
-1.001	-0.503	0.327
-0.557	-0.381	0.479

Minor Axis (mas)	Position Angle (degrees)	Distance from Core (mas)
0.156	178.900	-
0.334	178.900	0.460

Table 3.10: August 2007 Model Fitting Results for 0528+134

Component Number	Peak Intensity (mJy/ beam)	Total Intensity (mJy)
C	3190.585	3878.737
1	206.056	528.676

X-offset (mas)	Y-offset (mas)	Major Axis (mas)
-0.004	-0.988	0.508
0.448	-0.851	0.612

Minor Axis (mas)	Position Angle (degrees)	Distance from Core (mas)
0.193	161.520	-
0.339	161.520	0.472

Table 3.11: November 2007 Model Fitting Results for 0528+134

Component Number	Peak Intensity (mJy/ beam)	Total Intensity (mJy)
C	1693.313	2385.399
1	120.777	253.823

X-offset (mas)	Y-offset (mas)	Major Axis (mas)
0.005	-0.996	0.339
0.499	-0.864	0.436

Minor Axis (mas)	Position Angle (degrees)	Distance from Core (mas)
0.214	175.155	-
0.248	175.155	0.511

Table 3.12: January 2008 Model Fitting Results for 0528+134

Component Number	Peak Intensity (mJy/ beam)	Total Intensity (mJy)
C	1015.865	1081.621
1	11.594	12.369

X-offset (mas)	Y-offset (mas)	Major Axis (mas)
0.003	0.005	0.243
0.122	0.561	0.259

Minor Axis (mas)	Position Angle (degrees)	Distance from Core (mas)
0.164	2.949	-
0.154	2.950	0.569

Table 3.13: August 2007 Model Fitting Results for 0716+714

Component Number	Peak Intensity (mJy/ beam)	Total Intensity (mJy)
C	2617.567	2709.854
1	9.105	8.140

X-offset (mas)	Y-offset (mas)	Major Axis (mas)
0.000	-0.997	0.265
0.256	0.009	0.261

Minor Axis (mas)	Position Angle (degrees)	Distance from Core (mas)
0.172	168.821	-
0.151	168.821	1.038

Table 3.14: November 2007 Model Fitting Results for 0716+714

Component Number	Peak Intensity (mJy/ beam)	Total Intensity (mJy)
C	738.073	815.395
1N	7.487	11.869

X-offset (mas)	Y-offset (mas)	Major Axis (mas)
0.003	-0.996	0.277
0.387	-0.138	0.293

Minor Axis (mas)	Position Angle (degrees)	Distance from Core (mas)
0.179	13.866	-
0.243	13.867	0.940

Table 3.15: January 2008 Model Fitting Results for 0716+714

Component Number	Peak Intensity (mJy/ beam)	Total Intensity (mJy)
C	309.874	311.500
1	44.617	64.791

X-offset (mas)	Y-offset (mas)	Major Axis (mas)
-0.957	-0.958	1.435
0.354	0.826	1.992

Minor Axis (mas)	Position Angle (degrees)	Distance from Core (mas)
0.937	8.563	-
0.975	8.563	2.214

Table 3.16: November 2007 Model Fitting Results for 0735+178

Component Number	Peak Intensity (mJy/ beam)	Total Intensity (mJy)
C	1345.961	1441.057
2	9.623	14.950

X-offset (mas)	Y-offset (mas)	Major Axis (mas)
-0.004	0.000	0.299
0.445	-0.021	0.335

Minor Axis (mas)	Position Angle (degrees)	Distance from Core (mas)
0.160	0.172	-
0.207	0.172	0.449

Table 3.17: August 2007 Model Fitting Results for 0827+243

Component Number	Peak Intensity (mJy/ beam)	Total Intensity (mJy)
C	843.162	1144.904

X-offset (mas)	Y-offset (mas)	Major Axis (mas)
-0.463	-0.015	0.483

Minor Axis (mas)	Position Angle (degrees)	Distance from Core (mas)
0.215	160.753	-

Table 3.18: November 2007 Model Fitting Results for 0827+243

Component Number	Peak Intensity (mJy/ beam)	Total Intensity (mJy)
C	570.509	1066.574
1N	25.429	25.197
1	14.659	13.687

X-offset (mas)	Y-offset (mas)	Major Axis (mas)
-0.496	0.000	0.376
-0.196	0.039	0.332
-0.032	-0.432	0.326

Minor Axis (mas)	Position Angle (degrees)	Distance from Core (mas)
0.253	176.042	-
0.152	176.042	0.303
0.146	176.042	0.634

Table 3.19: January 2008 Model Fitting Results for 0827+243

Component Number	Peak Intensity (mJy/ beam)	Total Intensity (mJy)
C	343.948	369.582

X-offset (mas)	Y-offset (mas)	Major Axis (mas)
-0.983	-0.993	1.191

Minor Axis (mas)	Position Angle (degrees)	Distance from Core (mas)
0.456	58.531	-

Table 3.20: August 2007 Model Fitting Results for 0829+046

Component Number	Peak Intensity (mJy/ beam)	Total Intensity (mJy)
C	271.543	276.214
1	7.965	6.259

X-offset (mas)	Y-offset (mas)	Major Axis (mas)
-1.015	-1.035	1.260
1.150	-0.108	1.134

Minor Axis (mas)	Position Angle (degrees)	Distance from Core (mas)
0.484	59.901	-
0.416	59.901	2.355

Table 3.21: November 2007 Model Fitting Results for 0829+046

Component Number	Peak Intensity (mJy/ beam)	Total Intensity (mJy)
C	828.803	1058.504
1	7.211	9.548
2	8.494	9.042
3	8.219	9.941
4	8.241	15.011
5	6.792	8.527

X-offset (mas)	Y-offset (mas)	Major Axis (mas)
0.006	0.000	0.243
-0.599	-0.644	0.265
-0.711	-0.832	0.198
-0.941	-1.227	0.206
-1.251	-1.529	0.262
-1.720	-2.150	0.228

Minor Axis (mas)	Position Angle (degrees)	Distance from Core (mas)
0.183	15.064	-
0.174	15.064	0.884
0.187	105.064	1.098
0.205	105.064	1.550
0.242	105.064	1.979
0.191	105.064	2.757

Table 3.22: August 2007 Model Fitting Results for 0836+710

Component Number	Peak Intensity (mJy/ beam)	Total Intensity (mJy)
C	940.679	1075.990
1N	51.757	85.283
2N	6.849	8.087
3N	5.461	5.407
4N	7.094	8.630
5N	8.528	29.925
6N	4.893	16.205

X-offset (mas)	Y-offset (mas)	Major Axis (mas)
1.001	1.005	0.244
0.911	0.815	0.275
0.623	0.795	0.356
0.105	0.352	0.203
0.320	0.101	0.262
-0.120	-0.397	0.392
-0.936	-1.516	0.721

Minor Axis (mas)	Position Angle (degrees)	Distance from Core (mas)
0.191	158.331	-
0.245	158.331	0.210
0.136	158.331	0.432
0.199	68.331	1.109
0.190	158.331	1.132
0.366	68.331	1.795
0.188	158.331	3.179

Table 3.23: November 2007 Model Fitting Results for 0836+710

Component Number	Peak Intensity (mJy/ beam)	Total Intensity (mJy)
C	745.352	836.931
1N	7.290	7.050
5N	5.553	29.105

X-offset (mas)	Y-offset (mas)	Major Axis (mas)
0.999	1.000	0.266
0.738	0.583	0.263
-0.133	-0.352	0.516

Minor Axis (mas)	Position Angle (degrees)	Distance from Core (mas)
0.191	1.948	-
0.166	1.948	0.492
0.459	91.948	1.763

Table 3.24: January 2008 Model Fitting Results for 0836+710

Component Number	Peak Intensity (mJy/ beam)	Total Intensity (mJy)
C	898.992	940.012
1	38.009	96.074

X-offset (mas)	Y-offset (mas)	Major Axis (mas)
-0.003	-0.005	0.212
-0.180	0.389	0.356

Minor Axis (mas)	Position Angle (degrees)	Distance from Core (mas)
0.173	170.524	-
0.250	170.524	0.432

Table 3.25: August 2007 Model Fitting Results for 0954+658

Component Number	Peak Intensity (mJy/ beam)	Total Intensity (mJy)
C	1115.779	1156.734
1N	70.392	81.390
1	38.956	61.488

X-offset (mas)	Y-offset (mas)	Major Axis (mas)
0.000	-0.003	0.276
-0.100	0.282	0.274
-0.252	0.492	0.293

Minor Axis (mas)	Position Angle (degrees)	Distance from Core (mas)
0.181	168.092	-
0.203	168.092	0.302
0.259	168.092	0.555

Table 3.26: November 2007 Model Fitting Results for 0954+658

Component Number	Peak Intensity (mJy/ beam)	Total Intensity (mJy)
C	478.542	500.748
2N	93.973	108.272
1N	60.367	83.320
1	5.533	10.260
3N	5.713	6.110
4N	5.548	4.863

X-offset (mas)	Y-offset (mas)	Major Axis (mas)
-0.002	0.034	0.303
-0.064	0.259	0.309
-0.211	0.502	0.302
-0.510	0.846	0.376
-0.975	1.207	0.276
-1.023	2.056	0.263

Minor Axis (mas)	Position Angle (degrees)	Distance from Core (mas)
0.190	179.915	-
0.205	179.915	0.233
0.251	179.915	0.513
0.271	179.915	0.958
0.213	179.915	1.524
0.183	179.915	2.265

Table 3.27: January 2008 Model Fitting Results for 0954+658

Component Number	Peak Intensity (mJy/ beam)	Total Intensity (mJy)
C	588.087	719.445
1	100.848	146.089
2	72.394	122.777

X-offset (mas)	Y-offset (mas)	Major Axis (mas)
-1.987	0.008	0.572
-1.508	0.021	0.595
-1.250	0.133	0.683

Minor Axis (mas)	Position Angle (degrees)	Distance from Core (mas)
0.273	172.367	-
0.311	172.367	0.479
0.317	172.367	0.748

Table 3.28: August 2007 Model Fitting Results for 1127-145

Component Number	Peak Intensity (mJy/ beam)	Total Intensity (mJy)
C	589.126	630.831
1N	255.268	373.426
2N	10.729	12.312

X-offset (mas)	Y-offset (mas)	Major Axis (mas)
-1.097	-0.037	0.851
-0.600	0.024	0.896
3.800	0.212	0.912

Minor Axis (mas)	Position Angle (degrees)	Distance from Core (mas)
0.533	9.812	-
0.691	9.812	0.501
0.533	9.812	4.903

Table 3.29: November 2007 Model Fitting Results for 1127-145

Component Number	Peak Intensity (mJy/ beam)	Total Intensity (mJy)
C	424.373	562.564
1	103.087	136.030
2	36.673	60.167

X-offset (mas)	Y-offset (mas)	Major Axis (mas)
-0.987	-0.052	1.452
-0.372	-0.036	1.477
-0.042	0.379	1.558

Minor Axis (mas)	Position Angle (degrees)	Distance from Core (mas)
0.316	161.716	-
0.309	161.716	0.615
0.365	161.716	1.039

Table 3.30: January 2008 Model Fitting Results for 1127-145

Component Number	Peak Intensity (mJy/ beam)	Total Intensity (mJy)
C	337.377	356.058
1	11.371	15.055

X-offset (mas)	Y-offset (mas)	Major Axis (mas)
0.002	0.000	0.415
0.140	0.539	0.503

Minor Axis (mas)	Position Angle (degrees)	Distance from Core (mas)
0.195	157.609	-
0.202	157.609	0.556

Table 3.31: August 2007 Model Fitting Results for 1156+295

Component Number	Peak Intensity (mJy/ beam)	Total Intensity (mJy)
C	631.903	661.334
1N	6.574	7.552

X-offset (mas)	Y-offset (mas)	Major Axis (mas)
0.000	-1.003	0.451
0.306	-0.528	0.445

Minor Axis (mas)	Position Angle (degrees)	Distance from Core (mas)
0.173	161.021	-
0.192	161.021	0.565

Table 3.32: November 2007 Model Fitting Results for 1156+295

Component Number	Peak Intensity (mJy/ beam)	Total Intensity (mJy)
C	794.347	809.470
2N	56.367	83.593
3N	7.438	10.692

X-offset (mas)	Y-offset (mas)	Major Axis (mas)
-0.007	-0.984	0.318
-0.043	-0.701	0.382
-0.268	-0.178	0.309

Minor Axis (mas)	Position Angle (degrees)	Distance from Core (mas)
0.168	176.453	-
0.204	176.453	0.285
0.244	176.453	0.847

Table 3.33: January 2008 Model Fitting Results for 1156+295

Component Number	Peak Intensity (mJy/ beam)	Total Intensity (mJy)
C	208.637	219.926

X-offset (mas)	Y-offset (mas)	Major Axis (mas)
-1.695	-0.003	1.561

Minor Axis (mas)	Position Angle (degrees)	Distance from Core (mas)
1.347	43.171	-

Table 3.34: January 2008 Model Fitting Results for 1219+285

Component Number	Peak Intensity (mJy/ beam)	Total Intensity (mJy)
C	341.655	354.748

X-offset (mas)	Y-offset (mas)	Major Axis (mas)
0.000	0.007	0.876

Minor Axis (mas)	Position Angle (degrees)	Distance from Core (mas)
0.264	172.159	-

Table 3.35: January 2008 Model Fitting Results for 1222+216

Component Number	Peak Intensity (mJy/ beam)	Total Intensity (mJy)
C	299.675	335.837
1	17.273	29.288
2	8.111	10.485

X-offset (mas)	Y-offset (mas)	Major Axis (mas)
0.016	0.034	0.606
-0.425	0.073	0.616
-0.762	-0.016	0.578

Minor Axis (mas)	Position Angle (degrees)	Distance from Core (mas)
0.302	162.314	-
0.450	162.314	0.443
0.365	162.314	0.780

Table 3.36: August 2007 Model Fitting Results for 1406-076

Component Number	Peak Intensity (mJy/ beam)	Total Intensity (mJy)
C	369.184	387.636
1	26.928	38.780

X-offset (mas)	Y-offset (mas)	Major Axis (mas)
-0.001	0.016	0.634
-0.547	0.001	0.681

Minor Axis (mas)	Position Angle (degrees)	Distance from Core (mas)
0.412	178.263	-
0.527	178.263	0.546

Table 3.37: November 2007 Model Fitting Results for 1406-076

Component Number	Peak Intensity (mJy/ beam)	Total Intensity (mJy)
C	343.280	380.280

X-offset (mas)	Y-offset (mas)	Major Axis (mas)
0.010	-0.013	1.672

Minor Axis (mas)	Position Angle (degrees)	Distance from Core (mas)
0.544	38.168	-

Table 3.38: January 2008 Model Fitting Results for 1406-076

Component Number	Peak Intensity (mJy/ beam)	Total Intensity (mJy)
C	1263.800	1310.070
1	52.317	69.251
2	14.143	14.668

X-offset (mas)	Y-offset (mas)	Major Axis (mas)
0.006	-1.007	0.477
-0.193	-0.810	0.614
-0.759	0.655	0.552

Minor Axis (mas)	Position Angle (degrees)	Distance from Core (mas)
0.152	166.424	-
0.151	166.424	0.280
0.132	166.424	1.830

Table 3.39: August 2007 Model Fitting Results for 1510-089

Component Number	Peak Intensity (mJy/ beam)	Total Intensity (mJy)
C	780.685	964.481
2	13.840	13.906
1N	7.445	10.594

X-offset (mas)	Y-offset (mas)	Major Axis (mas)
1.000	-1.014	0.688
-0.248	1.055	0.670
-0.590	1.557	0.728

Minor Axis (mas)	Position Angle (degrees)	Distance from Core (mas)
0.185	161.709	-
0.155	161.709	2.416
0.202	161.709	3.023

Table 3.40: November 2007 Model Fitting Results for 1510-089

Component Number	Peak Intensity (mJy/ beam)	Total Intensity (mJy)
C	661.240	750.810
2N	221.981	306.451

X-offset (mas)	Y-offset (mas)	Major Axis (mas)
1.009	-1.023	0.454
0.787	-0.729	0.459

Minor Axis (mas)	Position Angle (degrees)	Distance from Core (mas)
0.154	171.368	-
0.185	171.368	0.368

Table 3.41: January 2008 Model Fitting Results for 1510-089

Component Number	Peak Intensity (mJy/ beam)	Total Intensity (mJy)
C	666.631	1130.607
1	17.017	29.725
2	32.612	85.193
3	19.060	51.894

X-offset (mas)	Y-offset (mas)	Major Axis (mas)
-0.506	1.510	0.392
-0.075	1.286	0.516
-0.286	1.071	0.391
-0.086	0.640	0.544

Minor Axis (mas)	Position Angle (degrees)	Distance from Core (mas)
0.233	156.164	-
0.182	156.164	0.486
0.360	66.164	0.491
0.269	156.164	0.966

Table 3.42: August 2007 Model Fitting Results for 1611+343

Component Number	Peak Intensity (mJy/ beam)	Total Intensity (mJy)
C	619.734	1048.231
1	23.393	70.619
2	41.336	61.457
1N	8.769	43.931

X-offset (mas)	Y-offset (mas)	Major Axis (mas)
-0.994	2.005	0.464
-0.599	1.172	0.551
-0.586	1.699	0.440
-0.027	-1.124	0.932

Minor Axis (mas)	Position Angle (degrees)	Distance from Core (mas)
0.248	159.104	-
0.373	159.104	0.922
0.230	159.104	0.510
0.366	159.104	3.275

Table 3.43: November 2007 Model Fitting Results for 1611+343

Component Number	Peak Intensity (mJy/ beam)	Total Intensity (mJy)
C	532.881	829.239
1	48.883	80.412
2	35.109	53.207
3	3.813	4.222
1N	6.702	29.651

X-offset (mas)	Y-offset (mas)	Major Axis (mas)
-0.994	1.996	0.431
-0.578	1.631	0.482
-0.539	1.217	0.437
-0.309	0.780	0.403
0.100	-1.156	0.568

Minor Axis (mas)	Position Angle (degrees)	Distance from Core (mas)
0.237	171.229	-
0.224	171.229	0.553
0.227	171.229	0.902
0.180	171.229	1.396
0.511	171.229	3.336

Table 3.44: January 2008 Model Fitting Results for 1611+343

Component Number	Peak Intensity (mJy/ beam)	Total Intensity (mJy)
C	576.850	864.634

X-offset (mas)	Y-offset (mas)	Major Axis (mas)
0.513	0.017	0.916

Minor Axis (mas)	Position Angle (degrees)	Distance from Core (mas)
0.214	166.619	-

Table 3.45: August 2007 Model Fitting Results for 1622-297

Component Number	Peak Intensity (mJy/ beam)	Total Intensity (mJy)
C	876.359	988.843
1	102.714	155.117

X-offset (mas)	Y-offset (mas)	Major Axis (mas)
1.042	-0.043	1.235
0.671	0.188	1.459

Minor Axis (mas)	Position Angle (degrees)	Distance from Core (mas)
0.464	4.814	-
0.526	4.814	0.437

Table 3.46: November 2007 Model Fitting Results for 1622-297

Component Number	Peak Intensity (mJy/ beam)	Total Intensity (mJy)
C	504.016	946.648
1N	33.731	32.366
2N	32.757	27.902

X-offset (mas)	Y-offset (mas)	Major Axis (mas)
0.995	-0.099	1.332
0.406	0.000	1.276
0.204	-0.502	1.237

Minor Axis (mas)	Position Angle (degrees)	Distance from Core (mas)
0.260	165.320	-
0.139	165.320	0.597
0.127	165.320	0.888

Table 3.47: January 2008 Model Fitting Results for 1622-297

Component Number	Peak Intensity (mJy/ beam)	Total Intensity (mJy)
C	1357.269	1448.027
1	96.060	203.379

X-offset (mas)	Y-offset (mas)	Major Axis (mas)
1.506	-0.005	0.273
1.345	0.165	0.421

Minor Axis (mas)	Position Angle (degrees)	Distance from Core (mas)
0.158	157.389	-
0.202	157.389	0.234

Table 3.48: August 2007 Model Fitting Results for 1633+382

Component Number	Peak Intensity (mJy/ beam)	Total Intensity (mJy)
C	1440.231	1734.830

X-offset (mas)	Y-offset (mas)	Major Axis (mas)
2.000	-0.002	0.372

Minor Axis (mas)	Position Angle (degrees)	Distance from Core (mas)
0.165	151.444	-

Table 3.49: November 2007 Model Fitting Results for 1633+382

Component Number	Peak Intensity (mJy/ beam)	Total Intensity (mJy)
C	1439.893	1935.226
1	26.991	53.291
1N	7.912	15.661

X-offset (mas)	Y-offset (mas)	Major Axis (mas)
1.995	-0.005	0.325
1.655	0.248	0.285
1.497	0.001	0.315

Minor Axis (mas)	Position Angle (degrees)	Distance from Core (mas)
0.162	161.260	-
0.270	161.260	0.424
0.245	71.260	0.498

Table 3.50: January 2008 Model Fitting Results for 1633+382

Component Number	Peak Intensity (mJy/ beam)	Total Intensity (mJy)
C	1443.401	1539.236
1	14.770	18.697
2	79.772	248.862
3	9.813	21.273
4	16.541	52.479
5	13.554	27.019

X-offset (mas)	Y-offset (mas)	Major Axis (mas)
0.011	-1.019	0.712
0.210	-0.336	0.898
-0.184	0.357	0.996
0.271	0.596	0.791
0.589	0.615	1.075
0.311	1.480	0.843

Minor Axis (mas)	Position Angle (degrees)	Distance from Core (mas)
0.158	162.116	-
0.149	162.116	0.711
0.331	162.117	1.390
0.290	162.117	1.636
0.312	162.117	1.733
0.250	162.117	2.517

Table 3.51: August 2007 Model Fitting Results for 1730-130

Component Number	Peak Intensity (mJy/ beam)	Total Intensity (mJy)
C	2044.439	2172.011
2	76.713	264.211
3	10.562	64.872
4	5.229	6.853
5	13.218	28.397

X-offset (mas)	Y-offset (mas)	Major Axis (mas)
-0.499	-1.503	0.684
-0.697	-0.024	0.998
-0.258	0.382	0.935
0.163	0.290	0.821
-0.191	0.762	1.004

Minor Axis (mas)	Position Angle (degrees)	Distance from Core (mas)
0.157	163.274	-
0.348	163.274	1.492
0.663	163.274	1.900
0.161	163.274	1.911
0.216	163.274	2.286

Table 3.52: November 2007 Model Fitting Results for 1730-130

Component Number	Peak Intensity (mJy/ beam)	Total Intensity (mJy)
C	1968.236	2179.044
2	41.839	106.672
4	10.325	12.811
1N	21.370	61.926
5	13.465	36.640

X-offset (mas)	Y-offset (mas)	Major Axis (mas)
-0.504	-1.495	0.465
-0.753	0.040	0.526
-0.190	0.130	0.397
-0.617	0.263	0.692
-0.510	0.435	0.626

Minor Axis (mas)	Position Angle (degrees)	Distance from Core (mas)
0.142	171.390	-
0.290	171.390	1.555
0.187	171.390	1.655
0.250	171.390	1.762
0.260	171.390	1.930

Table 3.53: January 2008 Model Fitting Results for 1730-130

Component Number	Peak Intensity (mJy/ beam)	Total Intensity (mJy)
C	1755.915	2425.218
1	1165.824	2609.047
2	1127.360	1444.032
3	277.332	406.803
4	70.574	178.565
5	59.875	129.046
6	24.826	145.604
7	16.631	35.625
8	21.801	32.479

X-offset (mas)	Y-offset (mas)	Major Axis (mas)
-1.044	-0.013	0.285
-0.926	0.007	0.304
-0.620	0.030	0.279
-0.501	0.192	0.247
-0.151	0.318	0.347
-0.068	0.387	0.301
0.993	0.819	0.503
1.205	1.035	0.371
1.481	1.055	0.319

Minor Axis (mas)	Position Angle (degrees)	Distance from Core (mas)
0.195	176.324	-
0.295	86.324	0.120
0.184	176.324	0.426
0.239	86.324	0.580
0.293	86.324	0.952
0.287	86.324	1.055
0.468	86.324	2.200
0.232	176.324	2.481
0.187	176.324	2.742

Table 3.54: August 2007 Model Fitting Results for 3C111

Component Number	Peak Intensity (mJy/ beam)	Total Intensity (mJy)
C	877.012	2118.874
1	3454.587	5987.830
2	1662.198	2878.507
3	944.674	2406.925
4	58.429	73.505

X-offset (mas)	Y-offset (mas)	Major Axis (mas)
-1.197	-0.516	0.375
-1.014	-0.495	0.341
-0.717	-0.439	0.373
-0.492	-0.367	0.375
0.037	-0.154	0.411

Minor Axis (mas)	Position Angle (degrees)	Distance from Core (mas)
0.347	160.485	-
0.274	160.485	0.184
0.250	160.485	0.486
0.366	160.485	0.721
0.165	160.485	1.286

Table 3.55: November 2007 Model Fitting Results for 3C111

Component Number	Peak Intensity (mJy/ beam)	Total Intensity (mJy)
C	1364.433	1306.194
1N	709.777	724.844
1	1238.341	2197.399
2	657.717	1231.856
3	233.059	555.569
2N	59.389	112.235

X-offset (mas)	Y-offset (mas)	Major Axis (mas)
-1.022	-0.502	0.272
-0.904	-0.467	0.300
-0.738	-0.372	0.354
-0.451	-0.426	0.343
-0.300	-0.361	0.402
-0.020	-0.038	0.313

Minor Axis (mas)	Position Angle (degrees)	Distance from Core (mas)
0.159	177.017	-
0.154	177.017	0.123
0.226	177.017	0.312
0.246	177.017	0.576
0.267	177.017	0.736
0.272	177.017	1.104

Table 3.56: January 2008 Model Fitting Results for 3C111

Component Number	Peak Intensity (mJy/ beam)	Total Intensity (mJy)
C	432.464	771.804
1	3307.423	4371.612
2	2314.439	4563.629
3	102.599	209.735
4N	127.699	140.818
4	652.912	1489.329
5	42.985	56.024
6	125.562	140.292
7	108.338	162.475
8	98.723	203.905
9	130.976	267.918
10	22.315	13.035
11	50.691	74.389
12	81.999	173.959

X-offset (mas)	Y-offset (mas)	Major Axis (mas)
4.175	4.315	0.411
4.004	4.011	0.401
3.806	3.663	0.413
3.444	3.516	0.475
3.422	3.113	0.556
3.073	3.042	0.437
2.663	2.237	0.395
2.516	2.172	0.431
2.424	1.770	0.418
2.188	1.698	0.522
2.079	1.483	0.493
1.833	1.643	0.298
1.586	1.411	0.388
0.345	0.043	0.454

Minor Axis (mas)	Position Angle (degrees)	Distance from Core (mas)
0.277	172.602	-
0.211	172.602	0.349
0.305	172.602	0.749
0.275	172.602	1.083
0.127	172.602	1.418
0.333	172.602	1.684
0.211	172.602	2.570
0.166	172.602	2.710
0.230	172.602	3.089
0.253	172.602	3.286
0.266	172.602	3.523
0.125	172.602	3.553
0.242	172.602	3.891
0.299	172.602	5.737

Table 3.57: August 2007 Model Fitting Results for 3C273

Component Number	Peak Intensity (mJy/ beam)	Total Intensity (mJy)
C	888.065	1109.427
1	2360.570	2309.006
2	3161.322	7555.528
3	368.870	718.646
4	788.825	1737.978
5	135.991	316.277
6	195.188	374.092
7	233.475	675.976
9	206.849	343.027
11	109.502	150.879
12	83.090	183.588

X-offset (mas)	Y-offset (mas)	Major Axis (mas)
2.358	2.583	0.641
2.249	2.335	0.641
1.978	1.941	0.668
1.686	1.574	0.667
1.210	1.223	0.689
0.671	0.277	0.882
0.534	0.113	0.747
0.611	-0.097	1.126
0.312	-0.254	0.611
-0.144	-0.316	0.699
-1.467	-1.799	0.763

Minor Axis (mas)	Position Angle (degrees)	Distance from Core (mas)
0.214	164.457	-
0.167	162.012	0.271
0.393	170.381	0.746
0.321	161.588	1.212
0.351	154.904	1.780
0.290	161.673	2.857
0.282	161.673	3.070
0.282	161.673	3.199
0.298	161.673	3.498
0.217	161.673	3.829
0.318	161.673	5.817

Table 3.58: November 2007 Model Fitting Results for 3C273

Component Number	Peak Intensity (mJy/ beam)	Total Intensity (mJy)
C	3244.532	4231.999
1	1360.091	1870.658
2	2293.487	6548.979
3	293.571	247.088
1N	145.420	267.105
4	342.563	1064.469
2N	165.607	388.211
5	244.081	263.356
9	111.500	138.918
11	199.435	308.250
3N	77.370	59.489

X-offset (mas)	Y-offset (mas)	Major Axis (mas)
1.995	2.005	0.437
1.917	1.760	0.448
1.541	1.325	0.445
1.242	1.206	0.341
0.778	1.070	0.439
0.649	0.573	0.555
0.924	0.229	0.469
0.171	-0.403	0.373
0.144	-0.851	0.386
-0.072	-0.817	0.472
-0.127	-1.177	0.313

Minor Axis (mas)	Position Angle (degrees)	Distance from Core (mas)
0.180	178.645	-
0.185	178.645	0.257
0.387	178.645	0.818
0.149	178.645	1.098
0.252	178.645	1.535
0.337	178.645	1.965
0.301	178.645	2.074
0.174	178.645	3.021
0.194	178.645	3.403
0.197	178.645	3.498
0.148	178.645	3.825

Table 3.59: January 2008 Model Fitting Results for 3C273

Component Number	Peak Intensity (mJy/ beam)	Total Intensity (mJy)
C	6853.069	7420.189
1	658.842	1207.532
2	314.633	421.853
3	56.506	284.149
4	86.032	192.728
5	28.142	45.270

X-offset (mas)	Y-offset (mas)	Major Axis (mas)
0.000	-0.003	0.384
-0.268	-0.184	0.415
-0.494	-0.282	0.398
-0.754	-0.438	0.624
-0.852	-1.144	0.457
-1.093	-1.169	0.412

Minor Axis (mas)	Position Angle (degrees)	Distance from Core (mas)
0.161	170.652	-
0.252	170.652	0.323
0.193	170.652	0.567
0.461	170.652	0.870
0.281	170.652	1.424
0.223	170.652	1.598

Table 3.60: August 2007 Model Fitting Results for 3C279

Component Number	Peak Intensity (Jy/ beam)	Total Intensity (Jy)
C	10.583	12.451
1	0.390	1.054
2	0.060	0.136
3	0.078	0.094
4	0.086	0.164

X-offset (mas)	Y-offset (mas)	Major Axis (mas)
1.004	0.984	0.628
0.618	0.740	0.686
0.307	0.517	0.770
0.052	0.227	0.579
-0.010	-0.242	0.766

Minor Axis (mas)	Position Angle (degrees)	Distance from Core (mas)
0.191	161.132	-
0.402	161.132	0.457
0.301	161.132	0.839
0.213	161.132	1.216
0.254	161.132	1.591

Table 3.61: November 2007 Model Fitting Results for 3C279

Component Number	Peak Intensity (mJy/ beam)	Total Intensity (mJy)
C	7751.245	7928.726
1	239.684	361.427
2	60.516	59.266
1N	48.417	93.559
3	28.874	37.341
4	28.124	41.175

X-offset (mas)	Y-offset (mas)	Major Axis (mas)
1.002	0.989	0.422
0.612	0.656	0.488
0.064	0.601	0.379
0.048	0.308	0.493
-0.102	-0.022	0.463
-0.325	-0.370	0.462

Minor Axis (mas)	Position Angle (degrees)	Distance from Core (mas)
0.162	172.982	-
0.206	172.982	0.513
0.172	172.982	1.015
0.261	172.982	1.172
0.186	172.982	1.497
0.211	172.982	1.899

Table 3.62: January 2008 Model Fitting Results for 3C279

Component Number	Peak Intensity (mJy/ beam)	Total Intensity (mJy)
C	1149.454	1801.498
1N	475.856	640.093
1A	43.059	55.399
1B	23.041	31.594
1*	13.060	18.822
2*	18.736	20.529
3*	15.125	20.561
4*	16.207	39.604
5*	12.043	19.936
6*	14.485	22.829

X-offset (mas)	Y-offset (mas)	Major Axis (mas)
2.045	0.000	0.296
1.890	0.014	0.256
1.631	-0.013	0.248
1.385	0.082	0.271
0.639	-0.012	0.280
-0.760	-0.417	0.261
-0.999	-0.175	0.315
-1.192	-0.055	0.351
-1.399	-0.019	0.284
-2.025	-0.159	0.340

Minor Axis (mas)	Position Angle (degrees)	Distance from Core (mas)
0.252	63.903	-
0.250	63.903	0.156
0.247	63.903	0.414
0.241	153.903	0.665
0.245	153.903	1.406
0.199	153.903	2.836
0.205	153.903	3.049
0.331	63.903	3.237
0.277	153.903	3.444
0.220	153.903	4.073

Table 3.63: August 2007 Model Fitting Results for 3C345

Component Number	Peak Intensity (mJy/ beam)	Total Intensity (mJy)
C	1158.130	2240.894
1N	50.379	95.843
1A	34.088	46.693
1B	15.807	38.265
1N*	9.939	18.272
2N*	7.933	14.524
3N*	8.523	9.124
4N*	11.102	21.263
5N*	6.945	7.895
6N*	19.028	133.363
1N**	9.015	7.458
4*	21.215	27.939
5*	21.040	42.515
7N*	8.105	9.080
6*	17.131	21.789
8N*	14.194	10.748

X-offset (mas)	Y-offset (mas)	Major Axis (mas)
1.959	-0.007	0.338
1.577	-0.041	0.364
1.279	0.051	0.361
0.905	-0.039	0.463
0.698	-0.028	0.379
0.586	-0.023	0.318
0.164	-0.317	0.364
-0.142	0.030	0.572
-0.279	-0.201	0.356
-0.884	-0.250	0.902
-1.146	-0.610	0.340
-1.327	0.039	0.367
-1.580	0.015	0.457
-2.092	-0.097	0.372
-2.202	-0.307	0.368
-2.409	-0.308	0.290

Minor Axis (mas)	Position Angle (degrees)	Distance from Core (mas)
0.273	150.663	-
0.249	150.663	0.384
0.181	150.663	0.682
0.249	150.663	1.054
0.231	150.663	1.261
0.274	60.663	1.373
0.140	150.663	1.822
0.160	150.663	2.101
0.152	150.663	2.246
0.370	150.663	2.853
0.116	150.663	3.163
0.171	150.663	3.286
0.211	150.663	3.539
0.144	150.663	4.052
0.165	150.663	4.172
0.125	150.663	4.378

Table 3.64: November 2007 Model Fitting Results for 3C345

Component Number	Peak Intensity (mJy/ beam)	Total Intensity (mJy)
C	697.252	1142.608
2N	278.929	529.414
1N	67.663	103.288
1A	16.918	38.335
1B	17.189	48.875
1N*	6.218	12.394
2N*	4.708	3.962
3N*	6.769	8.395
2N**	6.726	5.585
4N*	11.556	13.747
6N*	8.525	51.462
3N**	10.395	12.986
6N**	16.883	59.429
4N**	5.937	7.616
6*	5.667	11.963
8N*	4.382	12.462
5N**	5.907	10.593

X-offset (mas)	Y-offset (mas)	Major Axis (mas)
2.044	-0.002	0.255
1.866	-0.011	0.293
1.594	-0.044	0.322
1.319	-0.106	0.384
0.827	-0.003	0.337
0.358	-0.044	0.369
0.059	-0.081	0.222
-0.324	-0.406	0.286
-0.385	-0.043	0.242
-0.488	-0.219	0.255
-0.935	-0.123	0.608
-1.098	-0.497	0.276
-1.528	-0.096	0.384
-1.814	-0.521	0.243
-2.113	-0.326	0.388
-2.212	-0.393	0.337
-2.321	-0.026	0.374

Minor Axis (mas)	Position Angle (degrees)	Distance from Core (mas)
0.247	60.990	-
0.250	60.991	0.178
0.183	150.991	0.452
0.228	150.991	0.732
0.325	150.991	1.217
0.208	150.991	1.687
0.146	150.991	1.987
0.167	150.991	2.402
0.132	150.991	2.429
0.180	150.991	2.541
0.383	150.991	2.981
0.175	150.991	3.181
0.353	150.991	3.573
0.204	150.991	3.893
0.210	150.991	4.170
0.326	60.991	4.274
0.185	150.991	4.365

Table 3.65: January 2008 Model Fitting Results for 3C345. It was noted that 6N** could be a merger of 4* and 5*.

Component Number	Peak Intensity (Jy/ beam)	Total Intensity (Jy)
C	3.374	3.747
2	0.346	0.612
3	0.092	0.169
4	0.022	0.032

X-offset (mas)	Y-offset (mas)	Major Axis (mas)
-0.007	0.009	0.540
0.216	-0.292	0.559
0.468	-0.065	0.588
0.744	0.233	0.544

Minor Axis (mas)	Position Angle (degrees)	Distance from Core (mas)
0.166	162.364	-
0.255	162.364	0.375
0.253	162.364	0.481
0.218	162.364	0.784

Table 3.66: August 2007 Model Fitting Results for 3C446

Component Number	Peak Intensity (mJy/ beam)	Total Intensity (mJy)
C	4475.096	5148.767
3	102.525	320.905

X-offset (mas)	Y-offset (mas)	Major Axis (mas)
-1.005	-0.004	0.643
-0.530	-0.073	0.723

Minor Axis (mas)	Position Angle (degrees)	Distance from Core (mas)
0.168	162.094	-
0.406	162.094	0.480

Table 3.67: November 2007 Model Fitting Results for 3C446

Component Number	Peak Intensity (Jy/ beam)	Total Intensity (Jy)
C	3.115	4.145
1N	0.236	0.338
2	0.051	0.058
3	0.051	0.101

X-offset (mas)	Y-offset (mas)	Major Axis (mas)
-1.001	-0.006	0.456
-0.774	-0.355	0.453
-0.610	-0.245	0.446
-0.512	0.005	0.469

Minor Axis (mas)	Position Angle (degrees)	Distance from Core (mas)
0.147	172.808	-
0.160	172.808	0.416
0.128	172.808	0.458
0.215	172.808	0.489

Table 3.68: January 2008 Model Fitting Results for 3C446

Component Number	Peak Intensity (mJy/ beam)	Total Intensity (mJy)
C	5788.138	6214.187
1	55.216	92.498
2	31.458	28.896
3	59.759	77.008
4	135.428	251.917
5	130.169	220.675

X-offset (mas)	Y-offset (mas)	Major Axis (mas)
0.000	-0.001	0.453
-0.523	0.011	0.468
-0.684	-0.092	0.542
-0.861	-0.162	0.430
-1.059	-0.056	0.517
-1.331	-0.123	0.518

Minor Axis (mas)	Position Angle (degrees)	Distance from Core (mas)
0.162	161.159	-
0.246	161.159	0.523
0.116	161.159	0.690
0.205	161.159	0.876
0.247	161.159	1.060
0.224	161.159	1.337

Table 3.69: August 2007 Model Fitting Results for 3C454.3

Component Number	Peak Intensity (mJy/ beam)	Total Intensity (mJy)
C	7043.168	8225.572
1N	87.241	187.603
2N	47.820	139.710
3N	56.814	108.901
1	61.754	105.065
2	76.346	197.483
3	86.384	231.696
4	66.882	56.168

X-offset (mas)	Y-offset (mas)	Major Axis (mas)
1.001	-0.002	0.498
0.699	0.001	0.620
0.448	-0.043	0.598
0.319	0.004	0.565
0.054	-0.030	0.603
-0.103	-0.083	0.664
-0.323	-0.124	0.638
-0.456	-0.122	0.491

Minor Axis (mas)	Position Angle (degrees)	Distance from Core (mas)
0.173	159.927	-
0.256	159.927	0.302
0.361	159.927	0.555
0.250	159.927	0.682
0.209	159.927	0.947
0.288	159.927	1.107
0.310	159.927	1.330
0.126	159.927	1.462

Table 3.70: November 2007 Model Fitting Results for 3C454.3

Component Number	Peak Intensity (Jy/ beam)	Total Intensity (Jy)
C	6.509	9.227
2N	0.029	0.034
3N	0.035	0.045
4N	0.035	0.046
1	0.061	0.087
2	0.041	0.045
5N	0.069	0.128

X-offset (mas)	Y-offset (mas)	Major Axis (mas)
1.003	-0.001	0.350
0.425	0.022	0.327
0.215	0.088	0.366
0.051	-0.086	0.332
-0.134	-0.060	0.389
-0.262	-0.214	0.413
-0.478	-0.124	0.437

Minor Axis (mas)	Position Angle (degrees)	Distance from Core (mas)
0.182	170.351	-
0.158	170.351	0.578
0.157	170.351	0.793
0.178	170.351	0.956
0.165	170.351	1.139
0.117	170.351	1.283
0.190	170.351	1.486

Table 3.71: January 2008 Model Fitting Results for 3C454.3

Component Number	Peak Intensity (mJy/ beam)	Total Intensity (mJy)
C	1653.297	1813.256
1	816.091	1019.492
2	10.900	22.873
3	21.264	47.259
4	18.345	41.367

X-offset (mas)	Y-offset (mas)	Major Axis (mas)
-0.002	1.016	0.299
-0.067	0.779	0.308
-0.176	0.190	0.427
-0.266	-0.244	0.402
-0.222	-0.635	0.388

Minor Axis (mas)	Position Angle (degrees)	Distance from Core (mas)
0.166	153.097	-
0.183	153.097	0.246
0.222	153.097	0.844
0.249	153.097	1.287
0.262	153.097	1.666

Table 3.72: August 2007 Model Fitting Results for BL Lac

Component Number	Peak Intensity (mJy/ beam)	Total Intensity (mJy)
C	1988.922	2654.300
1	967.341	1247.954
2	22.643	39.510
3	61.033	103.633
1N	26.828	44.841

X-offset (mas)	Y-offset (mas)	Major Axis (mas)
0.002	1.544	0.309
-0.059	1.326	0.307
-0.129	0.655	0.450
-0.274	0.217	0.345
-0.215	-0.089	0.291

Minor Axis (mas)	Position Angle (degrees)	Distance from Core (mas)
0.187	150.407	-
0.182	150.407	0.226
0.168	150.407	0.899
0.214	150.407	1.355
0.249	150.407	1.647

Table 3.73: November 2007 Model Fitting Results for BL Lac

Component Number	Peak Intensity (mJy/ beam)	Total Intensity (mJy)
C	826.936	1041.085
1	511.087	674.878
2N	15.650	21.299
2	16.598	39.267
3	44.058	130.389
1N	12.584	5.276
3N	14.599	100.112
4N	13.790	19.497
4	8.191	33.250

X-offset (mas)	Y-offset (mas)	Major Axis (mas)
0.019	1.545	0.295
-0.056	1.331	0.322
-0.325	0.932	0.338
-0.149	0.598	0.427
-0.250	0.155	0.411
-0.177	0.001	0.186
-0.339	-0.394	0.779
-0.455	-0.414	0.261
-0.233	-0.793	0.443

Minor Axis (mas)	Position Angle (degrees)	Distance from Core (mas)
0.162	170.458	-
0.156	170.458	0.227
0.153	170.458	0.703
0.210	170.458	0.962
0.273	170.458	1.416
0.086	170.458	1.556
0.334	80.458	1.972
0.206	170.458	2.016
0.348	170.458	2.352

Table 3.74: January 2008 Model Fitting Results for BL Lac

Component Number	Peak Intensity (mJy/ beam)	Total Intensity (mJy)
C	2285.934	2371.013
1	20.963	30.647
2	13.213	81.266
3	15.434	43.700
4	8.883	6.383

X-offset (mas)	Y-offset (mas)	Major Axis (mas)
-0.999	1.000	0.514
-0.678	0.604	0.547
0.048	-0.165	1.017
0.279	-0.203	0.722
0.414	0.018	0.397

Minor Axis (mas)	Position Angle (degrees)	Distance from Core (mas)
0.163	160.026	-
0.216	160.026	0.510
0.490	160.026	1.566
0.317	160.026	1.755
0.146	160.026	1.721

Table 3.75: August 2007 Model Fitting Results for CTA102

Component Number	Peak Intensity (mJy/ beam)	Total Intensity (mJy)
C	2127.356	2354.508
1	13.240	73.118
2	12.481	38.351
3	18.978	31.008
4	24.379	43.275
2N	12.749	24.539

X-offset (mas)	Y-offset (mas)	Major Axis (mas)
-0.999	0.999	0.518
-0.537	0.374	1.709
-0.085	-0.511	0.620
0.060	-0.145	0.619
0.238	-0.049	0.608
0.266	-0.597	0.814

Minor Axis (mas)	Position Angle (degrees)	Distance from Core (mas)
0.166	160.325	-
0.251	160.325	0.777
0.385	160.325	1.765
0.205	160.325	1.559
0.227	160.325	1.621
0.184	160.325	2.037

Table 3.76: November 2007 Model Fitting Results for CTA102

Component Number	Peak Intensity (mJy/ beam)	Total Intensity (mJy)
C	2254.695	2461.374
1	19.741	22.779
3	16.081	22.913
4	10.270	18.076
2N	10.652	14.324

X-offset (mas)	Y-offset (mas)	Major Axis (mas)
-0.997	0.993	0.379
-0.575	0.568	0.390
0.042	-0.155	0.419
0.206	-0.049	0.511
0.350	-0.550	0.414

Minor Axis (mas)	Position Angle (degrees)	Distance from Core (mas)
0.146	170.384	-
0.150	170.384	0.599
0.172	170.384	1.548
0.174	170.384	1.592
0.164	170.384	2.048

Table 3.77: January 2008 Model Fitting Results for CTA102

Component Number	Peak Intensity (mJy/ beam)	Total Intensity (mJy)
C	721.338	800.685
1	85.728	114.886
2	19.788	20.400
3	9.373	11.075
4	11.297	15.801
5	11.413	19.411
6	11.670	20.195
7	9.003	9.231

X-offset (mas)	Y-offset (mas)	Major Axis (mas)
-0.002	0.001	0.378
-0.220	-0.131	0.367
-0.326	-0.433	0.300
-0.535	-0.313	0.339
-0.637	-0.565	0.345
-0.913	-0.529	0.507
-1.075	-0.642	0.396
-1.289	-1.530	0.315

Minor Axis (mas)	Position Angle (degrees)	Distance from Core (mas)
0.163	168.358	-
0.202	168.358	0.255
0.190	168.358	0.542
0.193	168.358	0.619
0.224	168.358	0.851
0.186	168.358	1.054
0.242	168.358	1.251
0.180	168.359	2.000

Table 3.78: August 2007 Model Fitting Results for OJ287

Component Number	Peak Intensity (mJy/ beam)	Total Intensity (mJy)
C	1922.219	2108.587
1	50.950	121.482
3	9.221	16.039
4	9.973	14.043
5	14.978	22.291
6	24.141	35.820
1N	6.462	7.476

X-offset (mas)	Y-offset (mas)	Major Axis (mas)
1.001	-0.003	0.499
0.720	-0.209	0.636
0.415	-0.296	0.565
0.445	-0.679	0.509
0.072	-0.507	0.555
-0.030	-0.722	0.488
-0.210	-0.956	0.642

Minor Axis (mas)	Position Angle (degrees)	Distance from Core (mas)
0.158	159.132	-
0.270	159.132	0.348
0.221	159.132	0.655
0.199	159.132	0.875
0.193	159.132	1.057
0.218	159.132	1.257
0.130	159.132	1.541

Table 3.79: November 2007 Model Fitting Results for OJ287

Component Number	Peak Intensity (mJy/ beam)	Total Intensity (mJy)
C	1780.670	2273.510
1	37.208	50.453
5	12.133	19.924
6	21.270	28.165

X-offset (mas)	Y-offset (mas)	Major Axis (mas)
0.997	0.001	0.381
0.673	-0.302	0.380
0.098	-0.584	0.440
-0.162	-0.784	0.334

Minor Axis (mas)	Position Angle (degrees)	Distance from Core (mas)
0.157	176.081	-
0.167	176.081	0.444
0.174	176.081	1.073
0.185	176.081	1.400

Table 3.80: January 2008 Model Fitting Results for OJ287

3.6 Kinematic Plots

This section shows plots for individual components. The plots are based upon model fitting data. This is all given in tables for each of the sources in the previous section. Identified components' separation from (what has been judged to be) the core is plotted against observation date. Some of the sources did not have enough in the way of model fitting data to warrant a kinematic plot. Linear fits to the data have been applied. By simple analysis of the gradients of the linear lines, it was possible to extract velocities of the jets from the component behaviours. The linear fits are weighted by the sizes of the errors on each plot, such as to give a better value of the gradient in each case.

Errors in the positions of the components (ΔR) are calculated via the following formula (Papageorgiou, 2005):

$$\Delta R = \frac{FWHM}{(\frac{S_p}{3\sigma})} \tag{3.2}$$

In this equation, σ is the noise level of the VLBI map, FWHM is the full width at half maximum for the major axis of the fitted Gaussian and S_p is the peak flux of the component.

Given the uncertainty in identifying components across different epochs, it was decided that the FWHM would be taken as the major axis of the model fitted ellipse. This would yield a more conservative estimate of error for the positional uncertainty. The error for the x-offset will equal the error for the y-offset for a given component.

Errors were previously calculated from an expression in Reynolds (2002). In most cases the errors were found to give uncertainties in component positions that appeared too small.

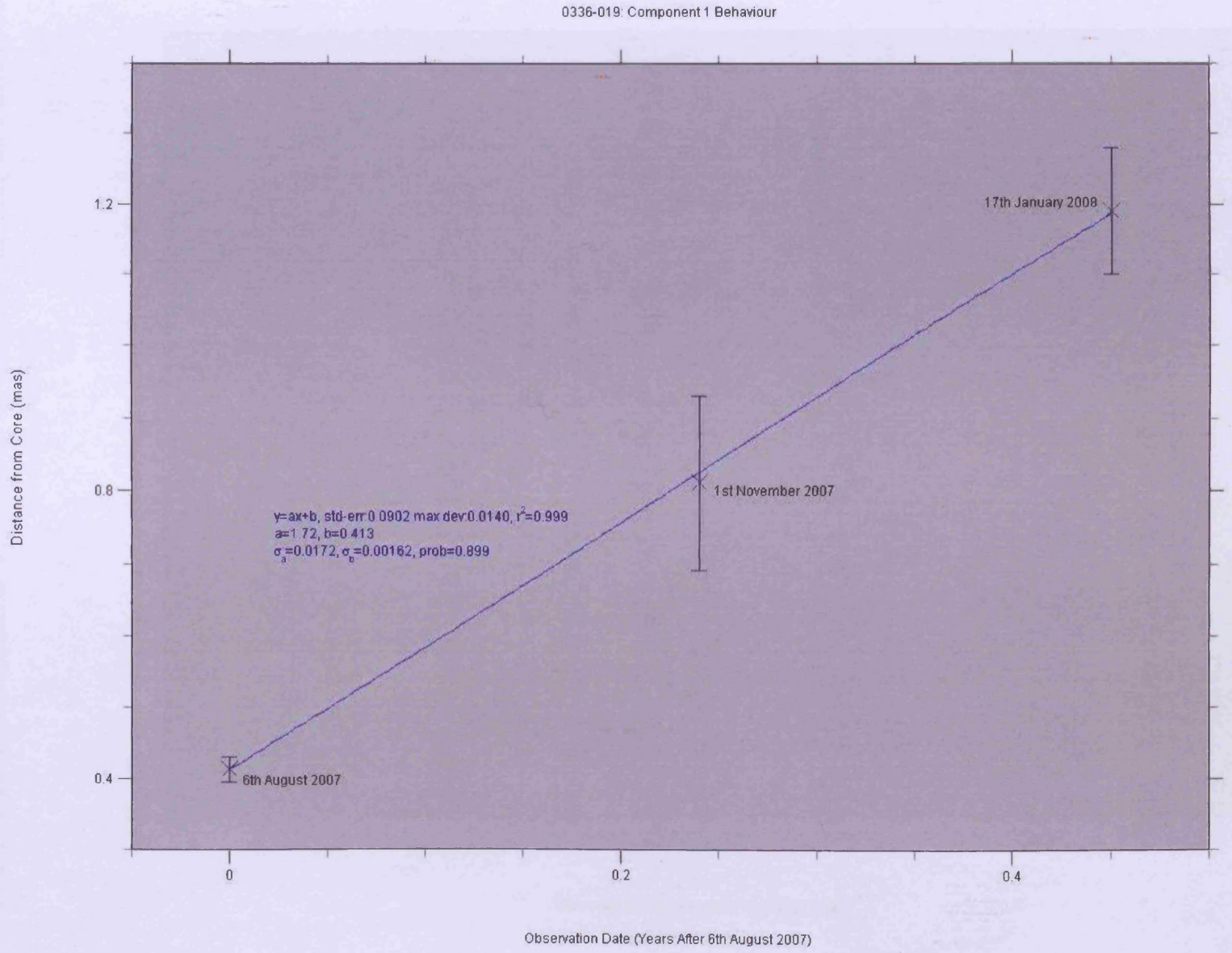
0336-019: Component 1 Behaviour
Distance from Core (mas)
1.2
0.8
0.4
0
0.2
0.4
Observation Date (Years After 6th August 2007)
17th January 2008
1st November 2007
6th August 2007
y=ax+b, std-err 0.0902 max dev 0.0140, r²=0.999
a=1.72, b=0.413
σa=0.0172, σb=0.00162, prob=0.899

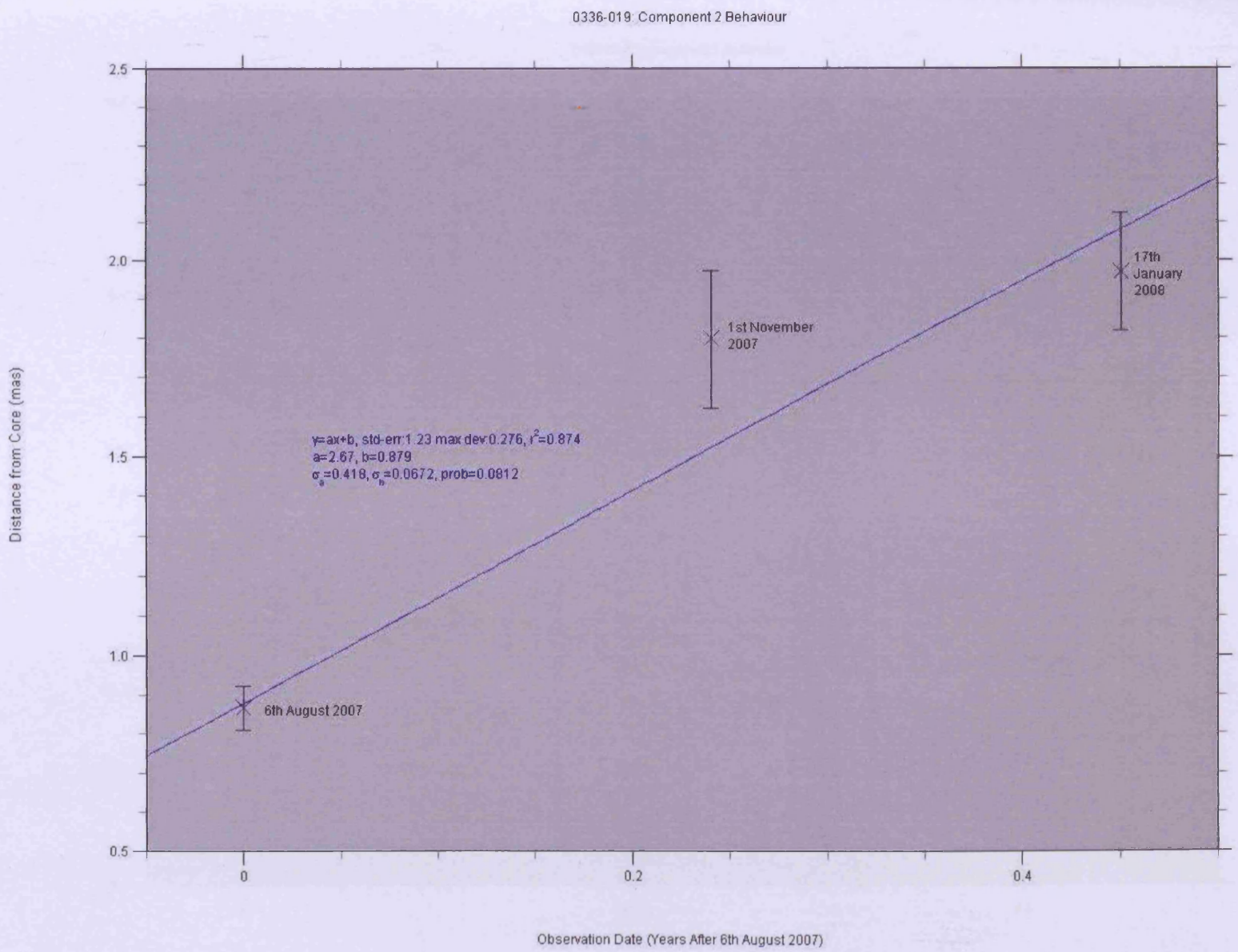
0336-019: Component 2 Behaviour
Distance from Core (mas)
Observation Date (Years After 6th August 2007)
2.5
2.0
1.5
1.0
0.5
0
0.2
0.4
y=ax+b, std-err:1.23 max dev:0.276, r²=0.874
a=2.67, b=0.879
σa=0.418, σb=0.0672, prob=0.0812
6th August 2007
1st November 2007
17th January 2008

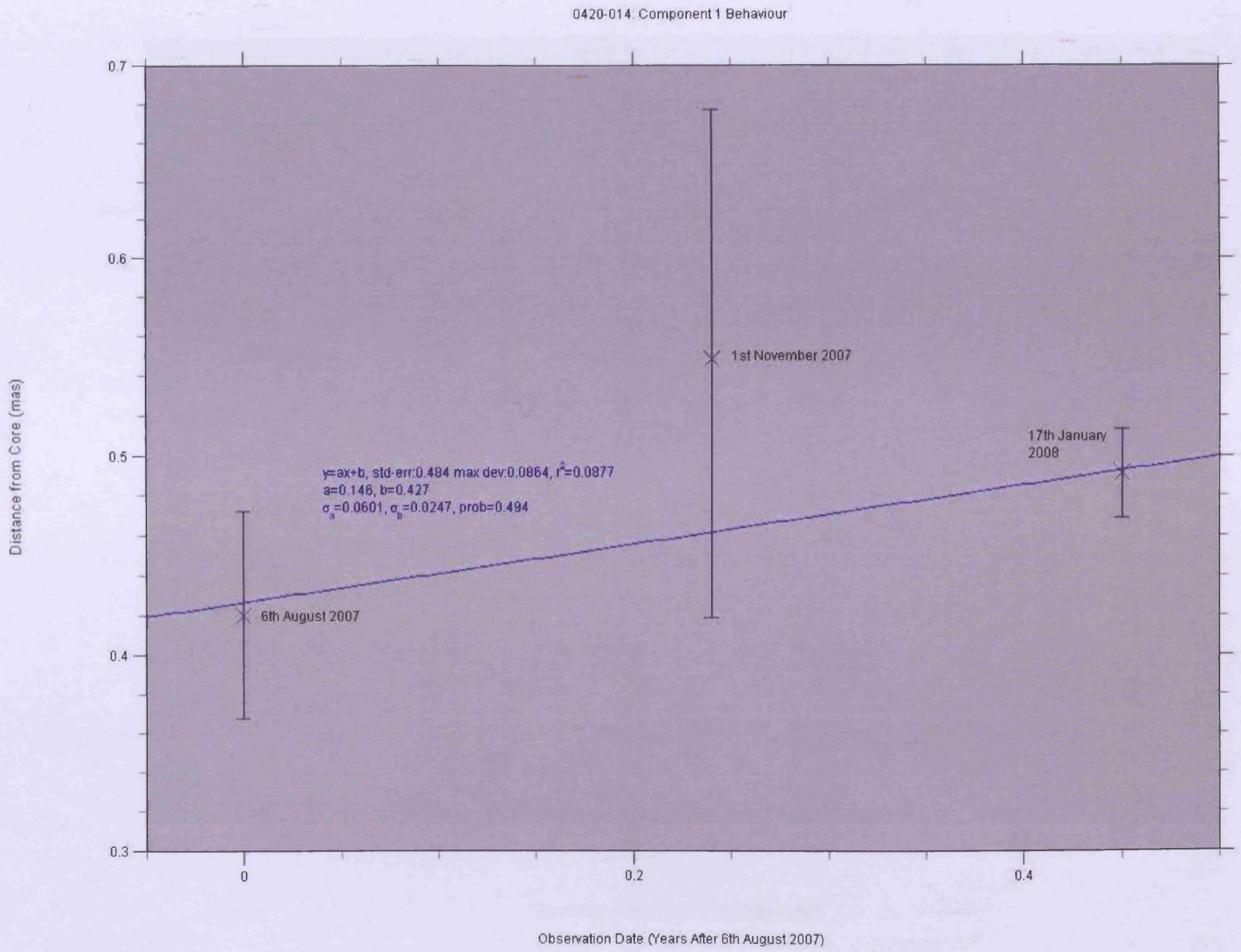
0420-014: Component 1 Behaviour
0.7
0.6
0.5
0.4
0.3
0
0.2
0.4
Distance from Core (mas)
Observation Date (Years After 6th August 2007)
1st November 2007
17th January 2008
6th August 2007
y=ax+b, std-err:0.484 max dev:0.0864, r²=0.0877
a=0.146, b=0.427
σa=0.0601, σb=0.0247, prob=0.494

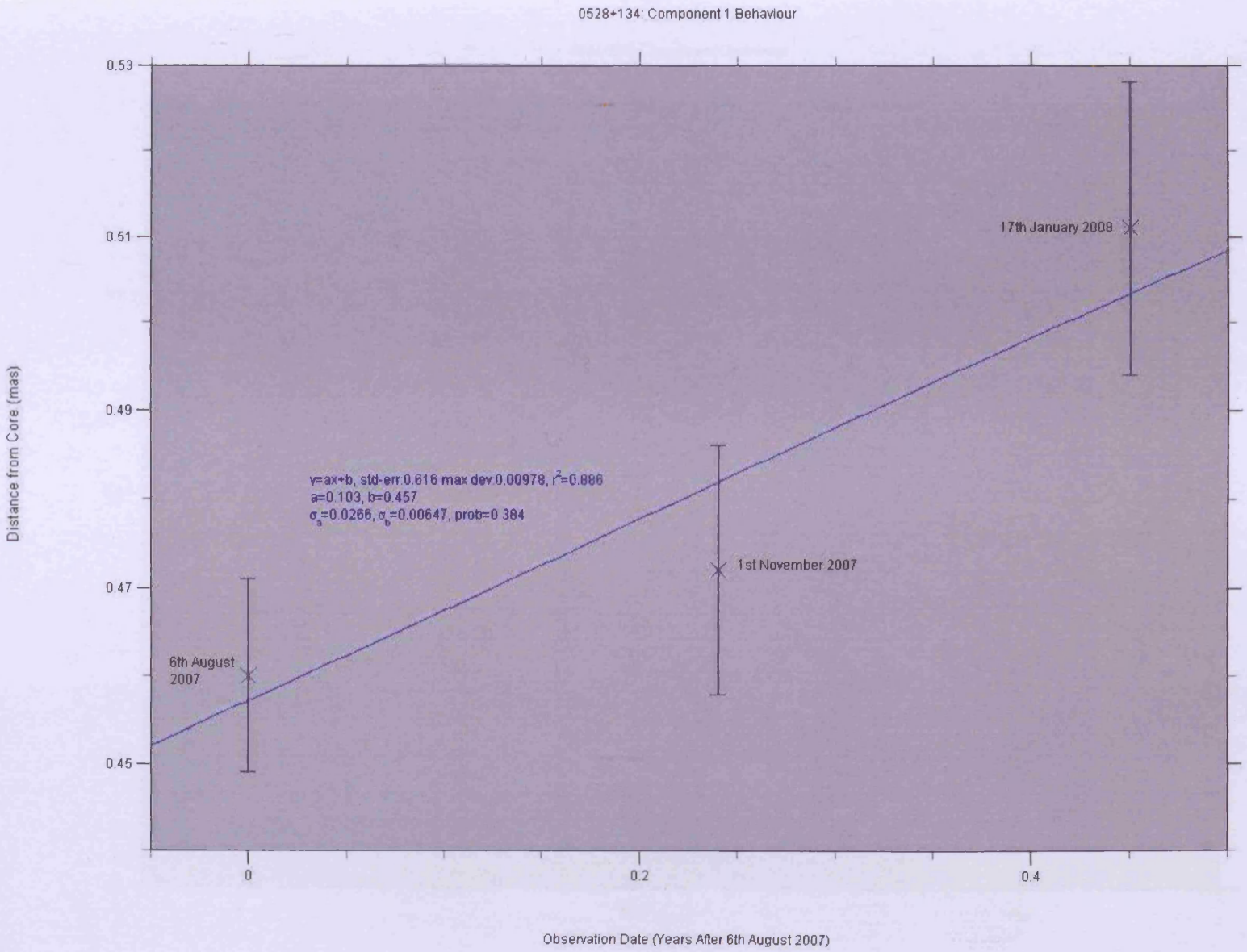
0528+134: Component 1 Behaviour
0.53
0.51
0.49
0.47
0.45
Distance from Core (mas)
y=ax+b, std-err 0.616 max dev 0.00978, r²=0.886
a=0.103, b=0.457
σa=0.0266, σb=0.00647, prob=0.384
17th January 2008
1st November 2007
6th August 2007
0
0.2
0.4
Observation Date (Years After 6th August 2007)

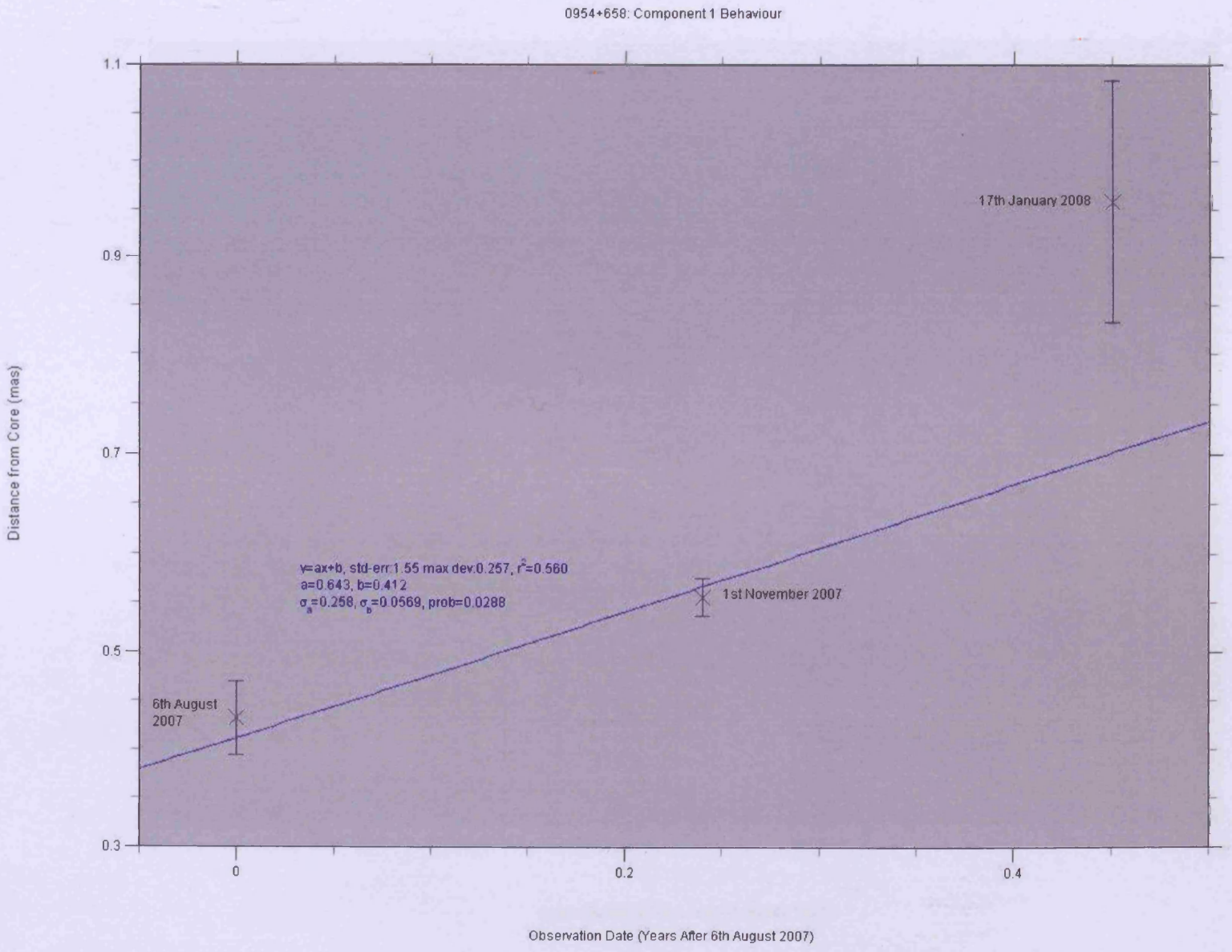
0954+658: Component 1 Behaviour
Distance from Core (mas)
1.1
0.9
0.7
0.5
0.3
0
0.2
0.4
Observation Date (Years After 6th August 2007)
17th January 2008
1st November 2007
6th August 2007
v=ax+b, std-err:1.55 max dev:0.257, r²=0.560
a=0.643, b=0.412
σa=0.258, σb=0.0569, prob=0.0288

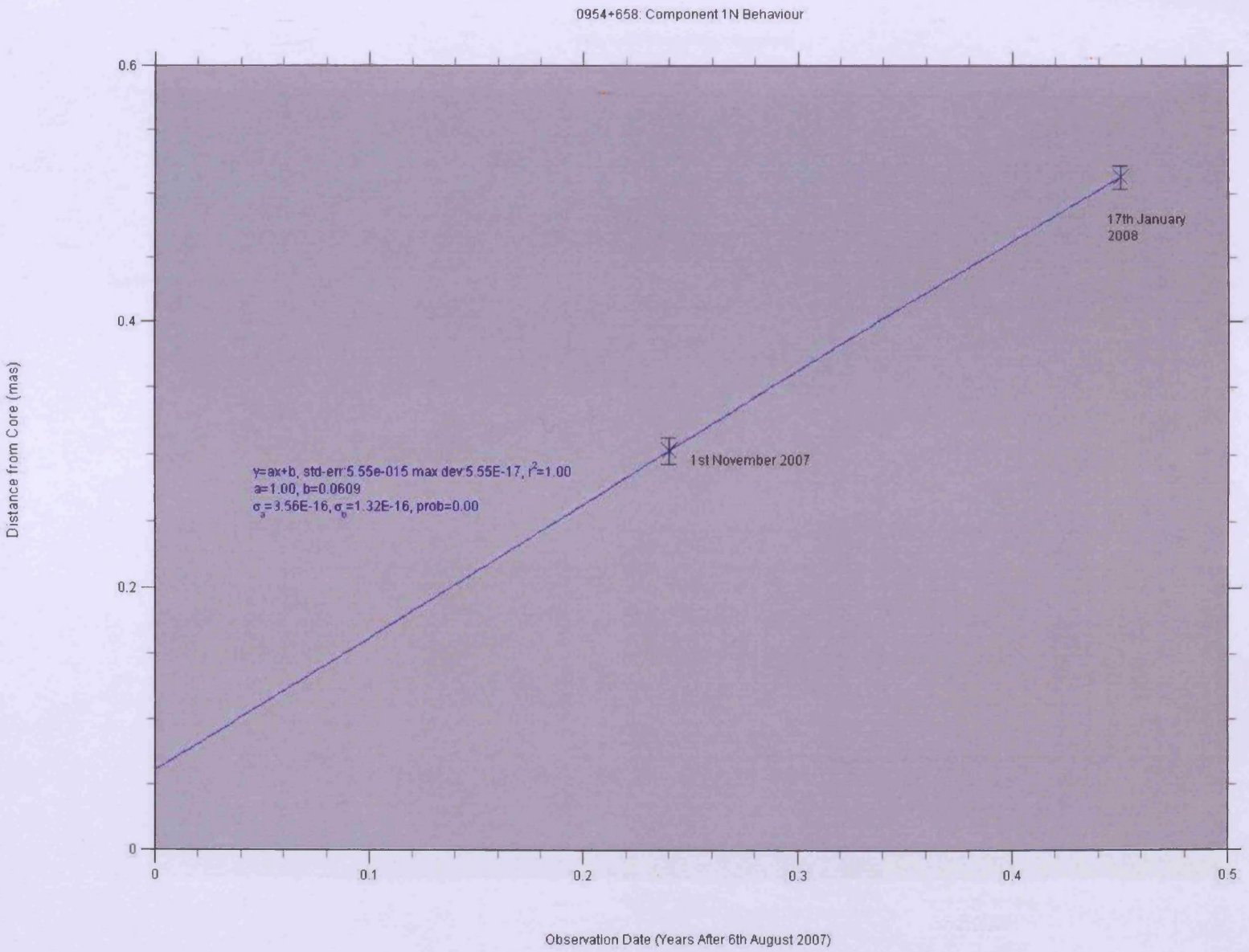
0954+658: Component 1N Behaviour
Distance from Core (mas)
Observation Date (Years After 6th August 2007)
0.6
0.4
0.2
0
0
0.1
0.2
0.3
0.4
0.5
17th January 2008
1st November 2007
y=ax+b, std-err:5.55e-015 max dev:5.55E-17, r²=1.00
a=1.00, b=0.0609
σa=3.56E-16, σb=1.32E-16, prob=0.00

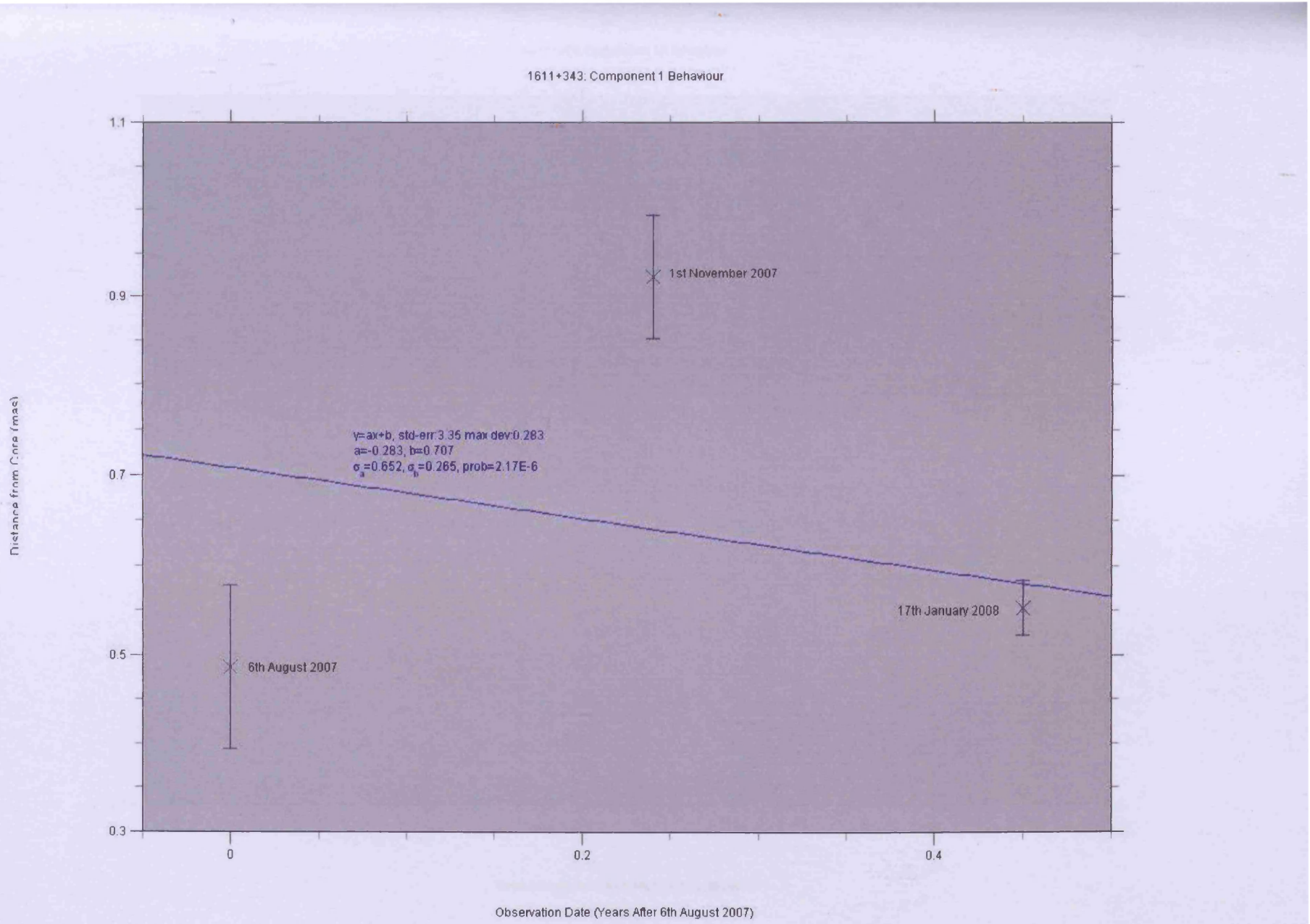
1611+343: Component 1 Behaviour
1.1
0.9
0.7
0.5
0.3
0
0.2
0.4
1st November 2007
y=ax+b, std-err:3.35 max dev:0.283
a=-0.283, b=0.707
σa=0.652, σb=0.265, prob=2.17E-6
17th January 2008
6th August 2007
Observation Date (Years After 6th August 2007)

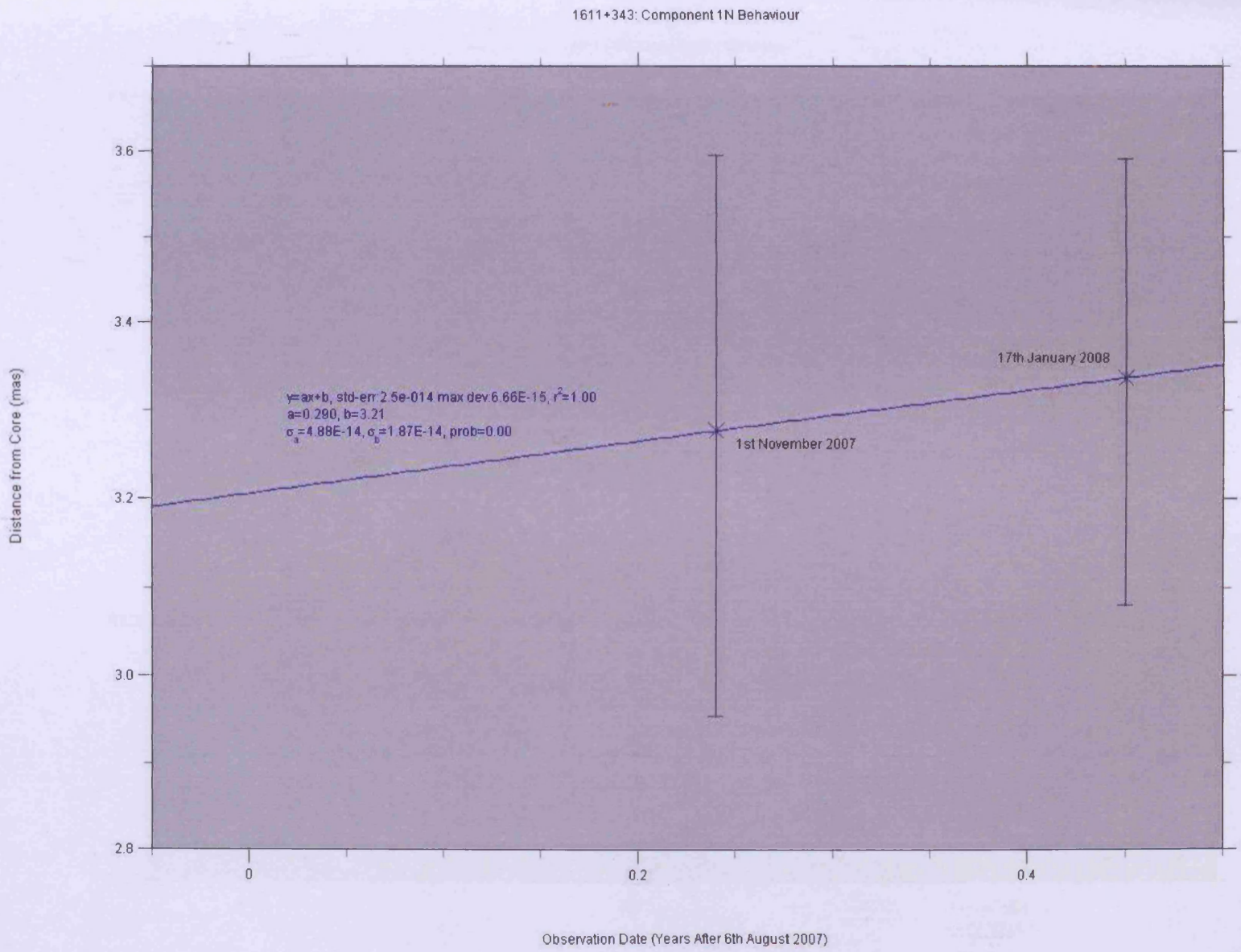
1611+343: Component 1N Behaviour
Distance from Core (mas)
3.6
3.4
3.2
3.0
2.8
0
0.2
0.4
Observation Date (Years After 6th August 2007)
y=ax+b, std-err 2.5e-014 max dev 6.66E-15, r²=1.00
a=0.290, b=3.21
σa=4.88E-14, σb=1.87E-14, prob=0.00
1st November 2007
17th January 2008

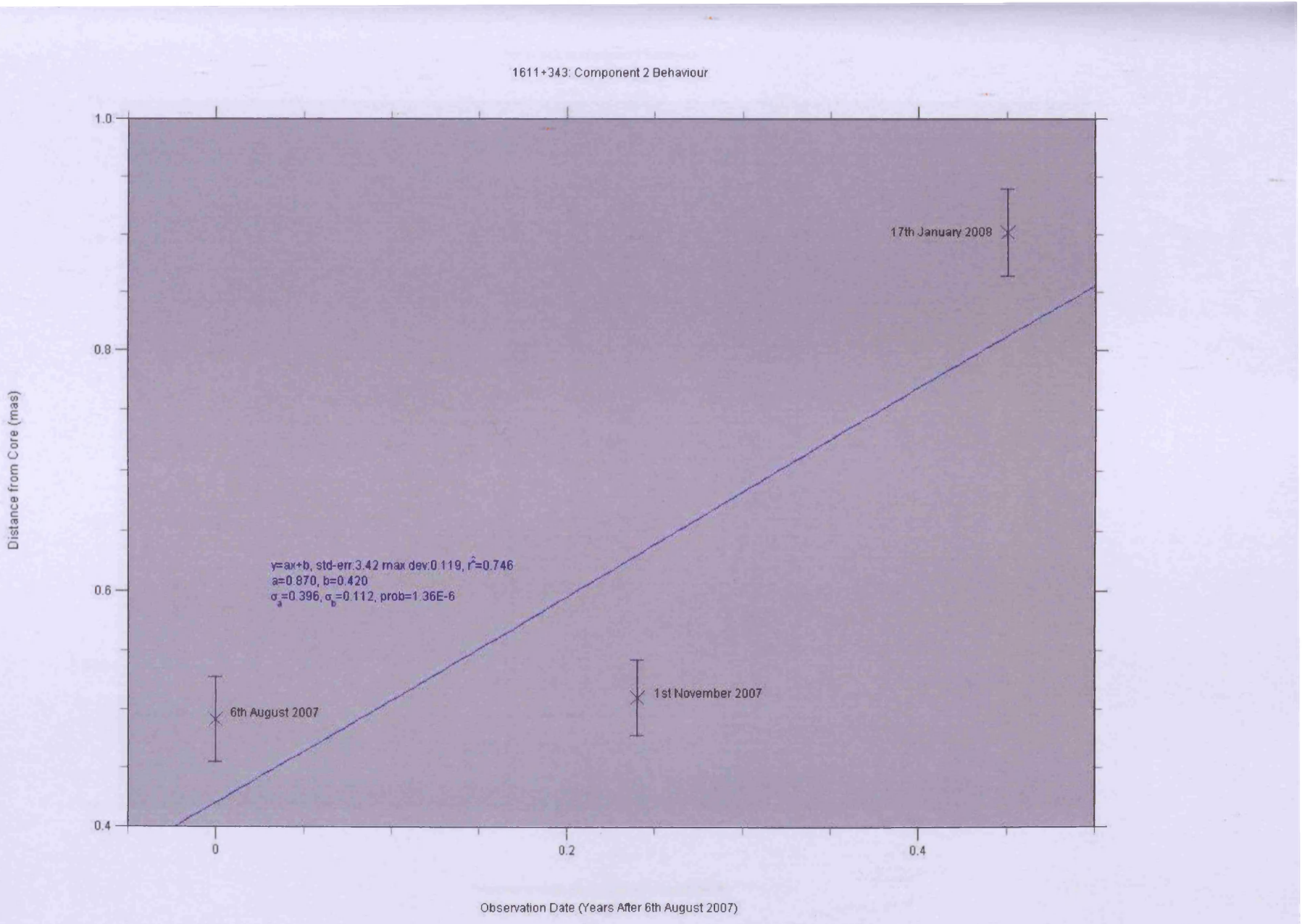
1611+343: Component 2 Behaviour
1.0
0.8
0.6
0.4
0
0.2
0.4
Distance from Core (mas)
Observation Date (Years After 6th August 2007)
17th January 2008
1st November 2007
6th August 2007
y=ax+b, std-err:3.42 max dev:0.119, r̂=0.746
a=0.870, b=0.420
σa=0.396, σb=0.112, prob=1.36E-6

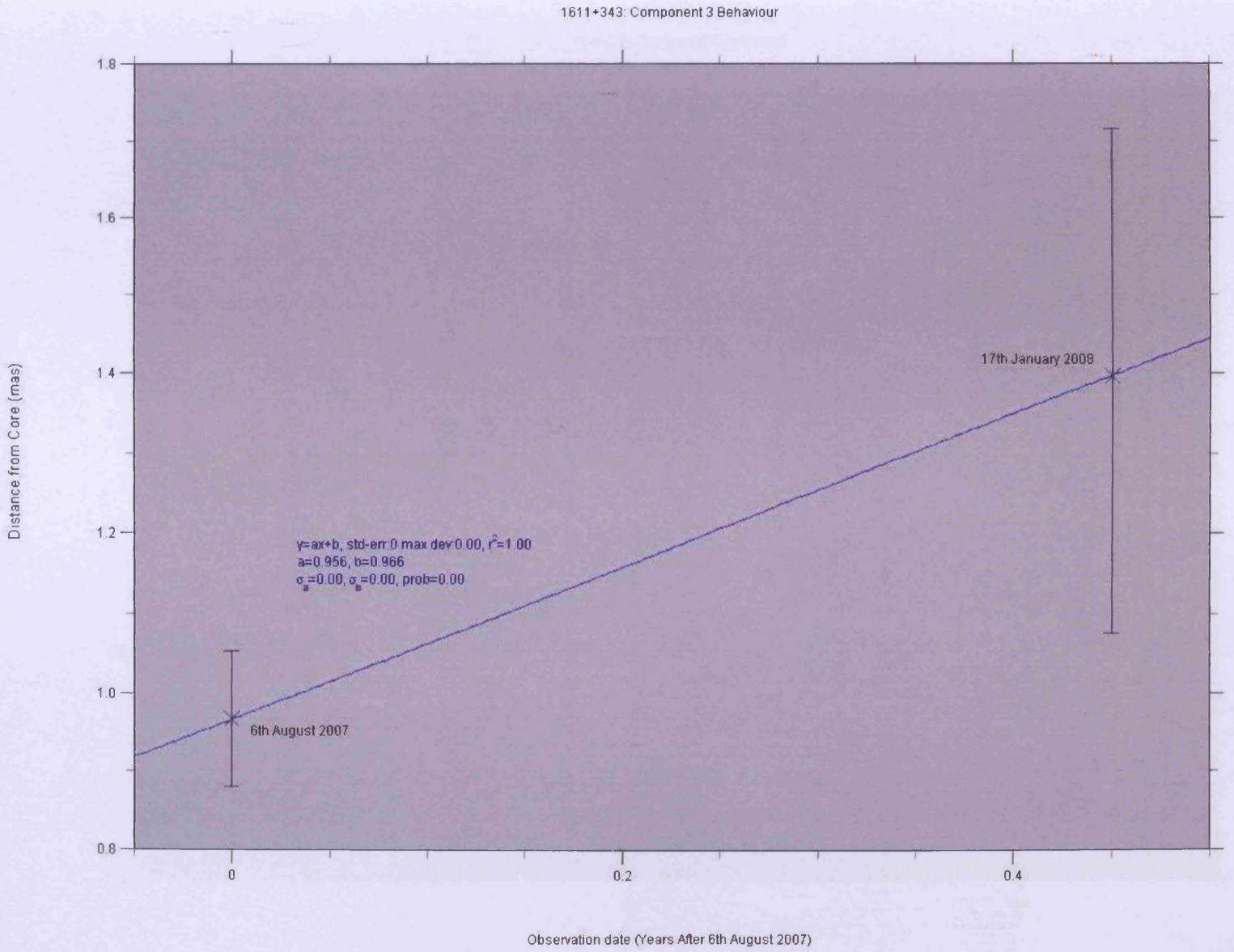
1611+343: Component 3 Behaviour
Distance from Core (mas)
1.8
1.6
1.4
1.2
1.0
0.8
0
0.2
0.4
y=ax+b, std-err 0 max dev 0.00, r²=1.00
a=0.956, b=0.966
σa=0.00, σb=0.00, prob=0.00
17th January 2008
6th August 2007
Observation date (Years After 6th August 2007)

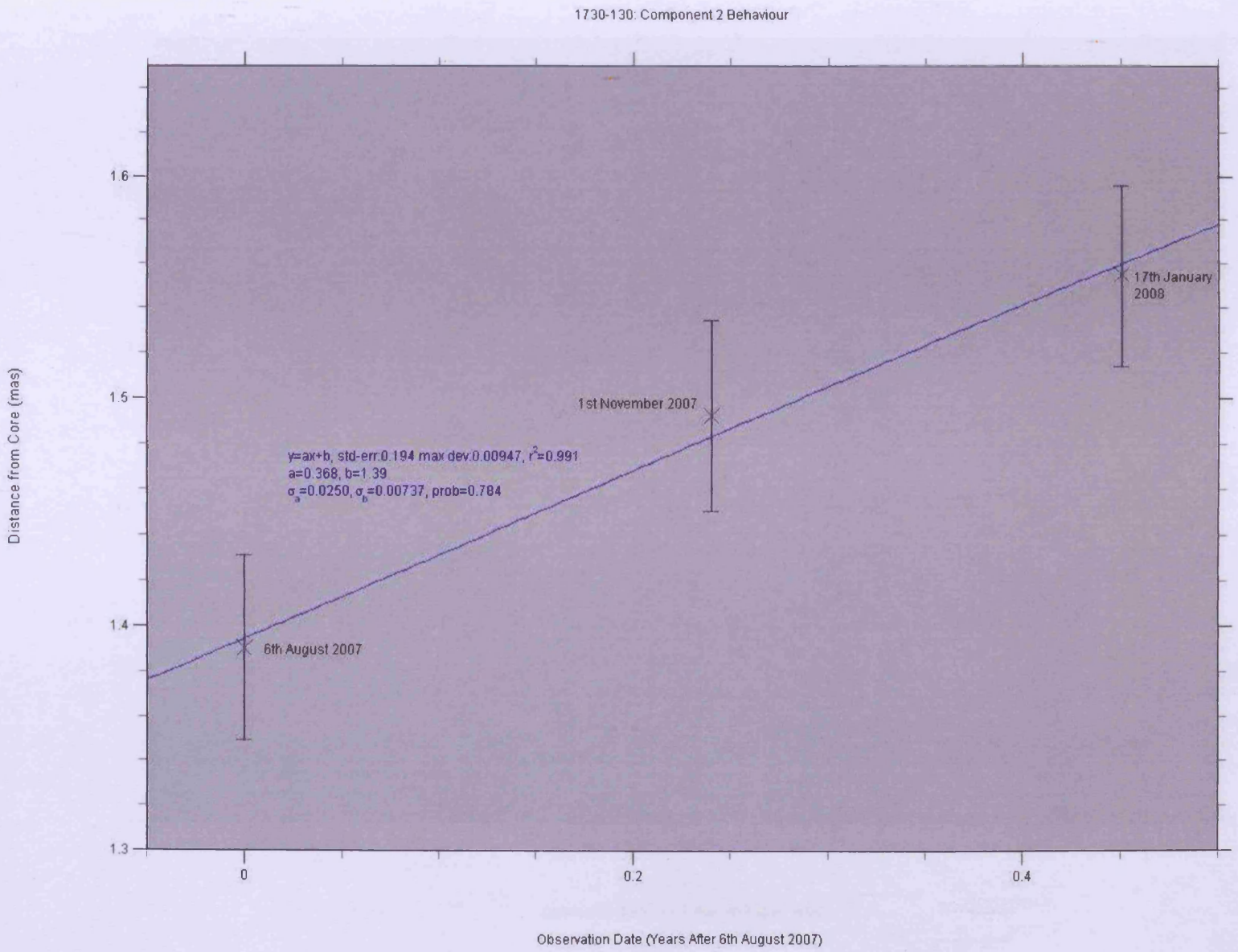
1730-130: Component 2 Behaviour
Distance from Core (mas)
1.6
1.5
1.4
1.3
0
0.2
0.4
Observation Date (Years After 6th August 2007)
y=ax+b, std-err:0.194 max dev:0.00947, r²=0.991
a=0.368, b=1.39
σa=0.0250, σb=0.00737, prob=0.784
6th August 2007
1st November 2007
17th January 2008

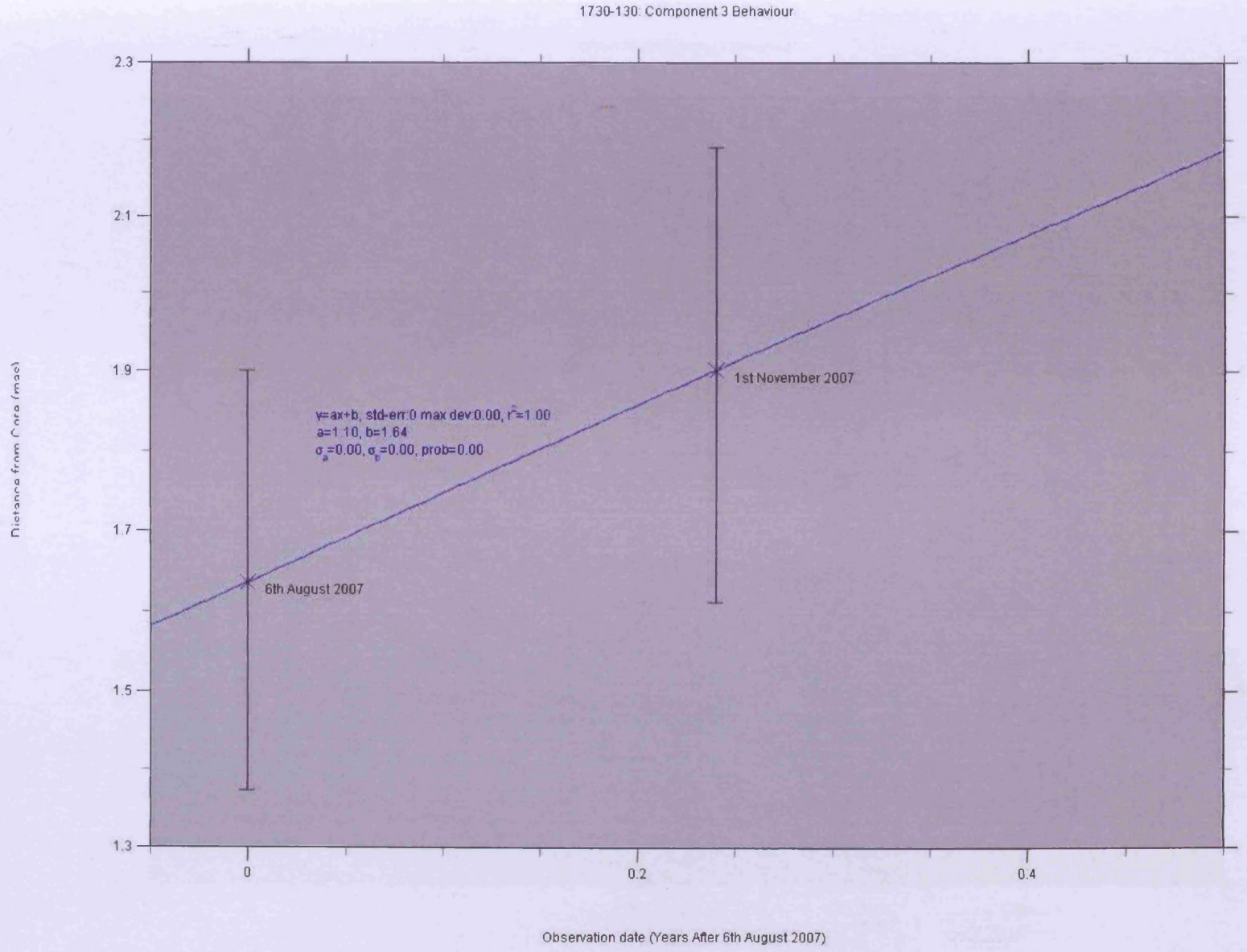
1730-130: Component 3 Behaviour
2.3
2.1
1.9
1.7
1.5
1.3
0
0.2
0.4
y=ax+b, std-err:0 max dev:0.00, r²=1.00
a=1.10, b=1.64
σa=0.00, σb=0.00, prob=0.00
1st November 2007
6th August 2007
Observation date (Years After 6th August 2007)

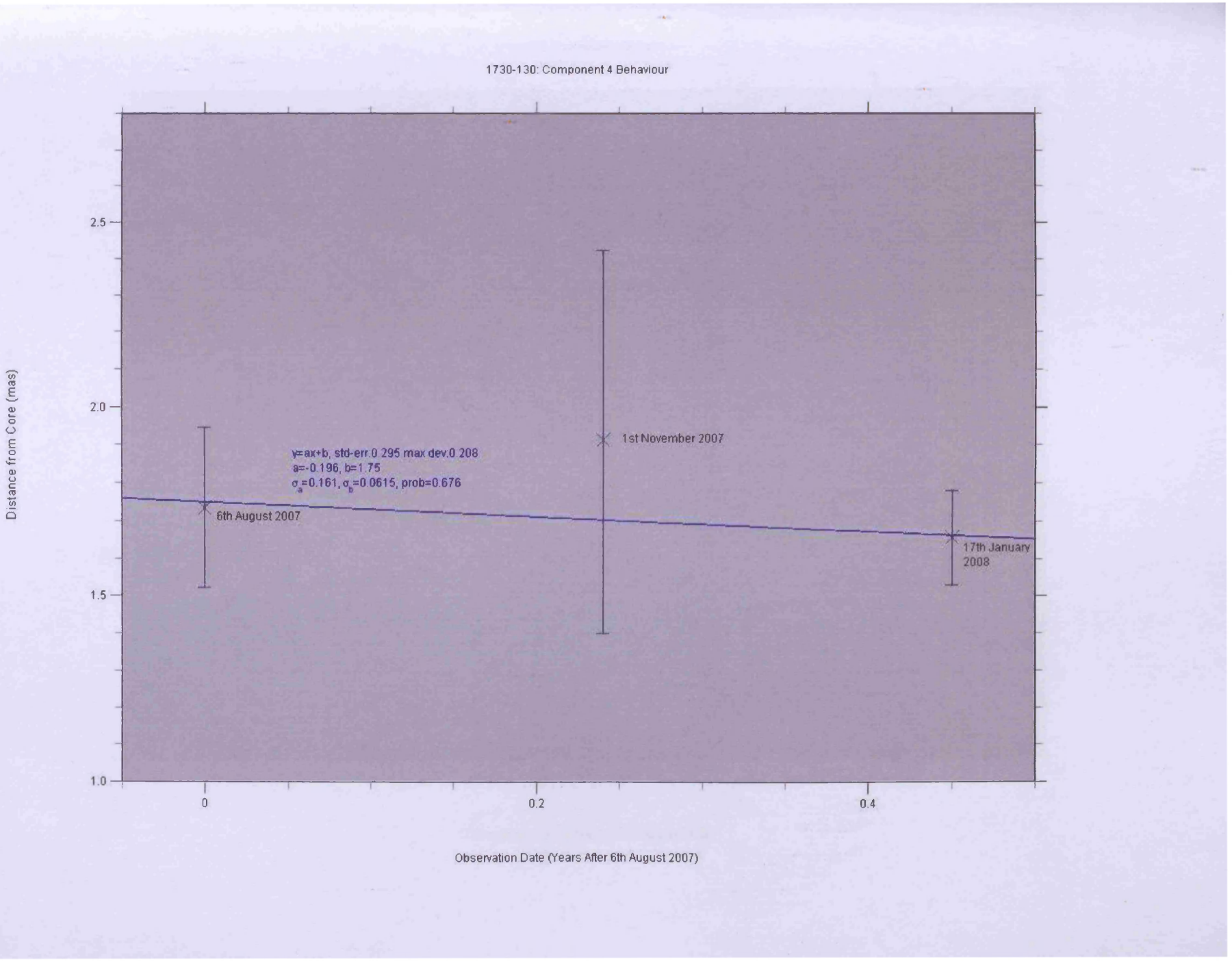
1730-130: Component 4 Behaviour
Distance from Core (mas)
2.5
2.0
1.5
1.0
0
0.2
0.4
y=ax+b, std-err.0.295 max dev.0.208
a=-0.196, b=1.75
σa=0.161, σb=0.0615, prob=0.676
6th August 2007
1st November 2007
17th January 2008
Observation Date (Years After 6th August 2007)

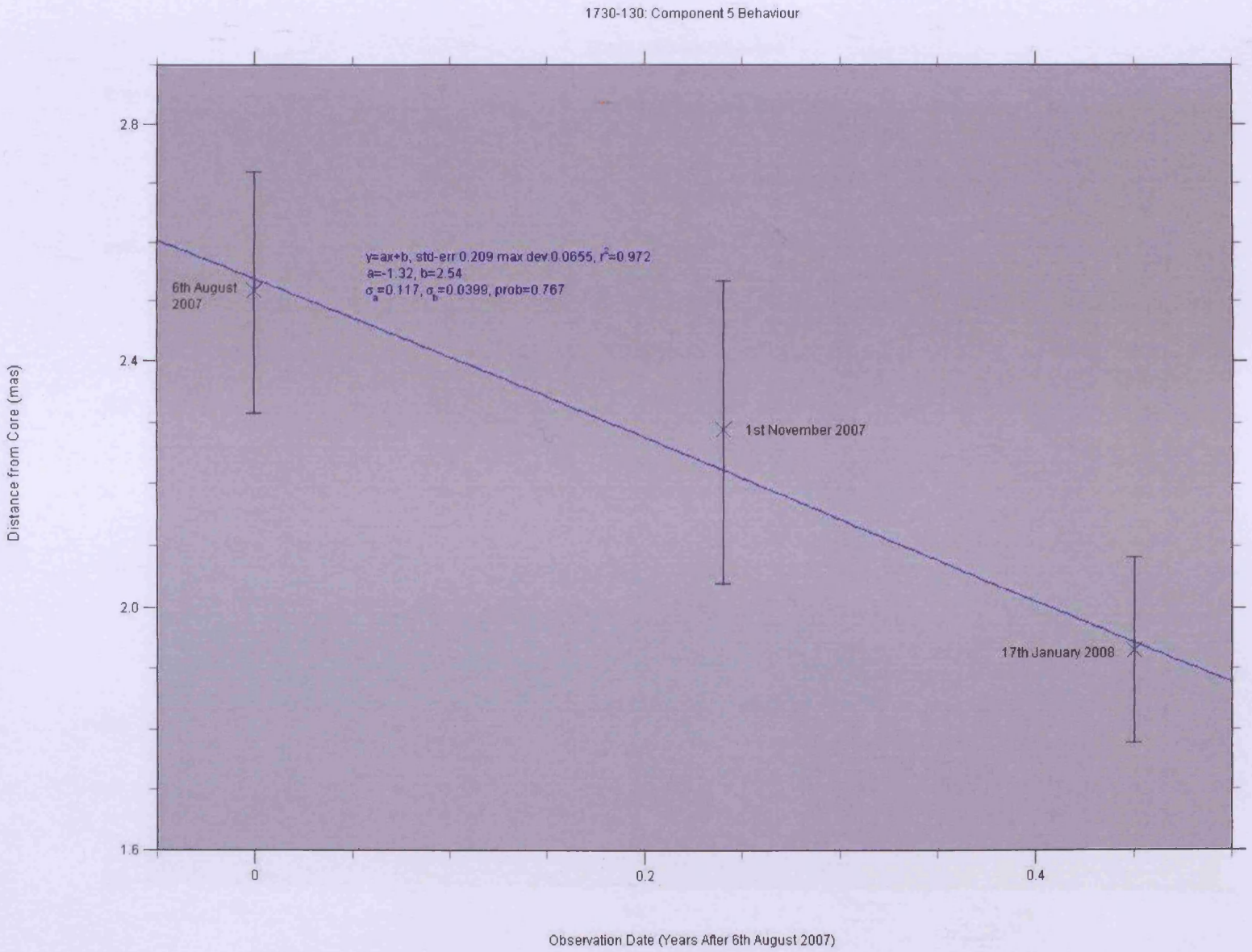
1730-130: Component 5 Behaviour
Distance from Core (mas)
2.8
2.4
2.0
1.6
0
0.2
0.4
Observation Date (Years After 6th August 2007)
y=ax+b, std-err 0.209 max dev.0.0655, r²=0.972
a=-1.32, b=2.54
σa=0.117, σb=0.0399, prob=0.767
6th August 2007
1st November 2007
17th January 2008

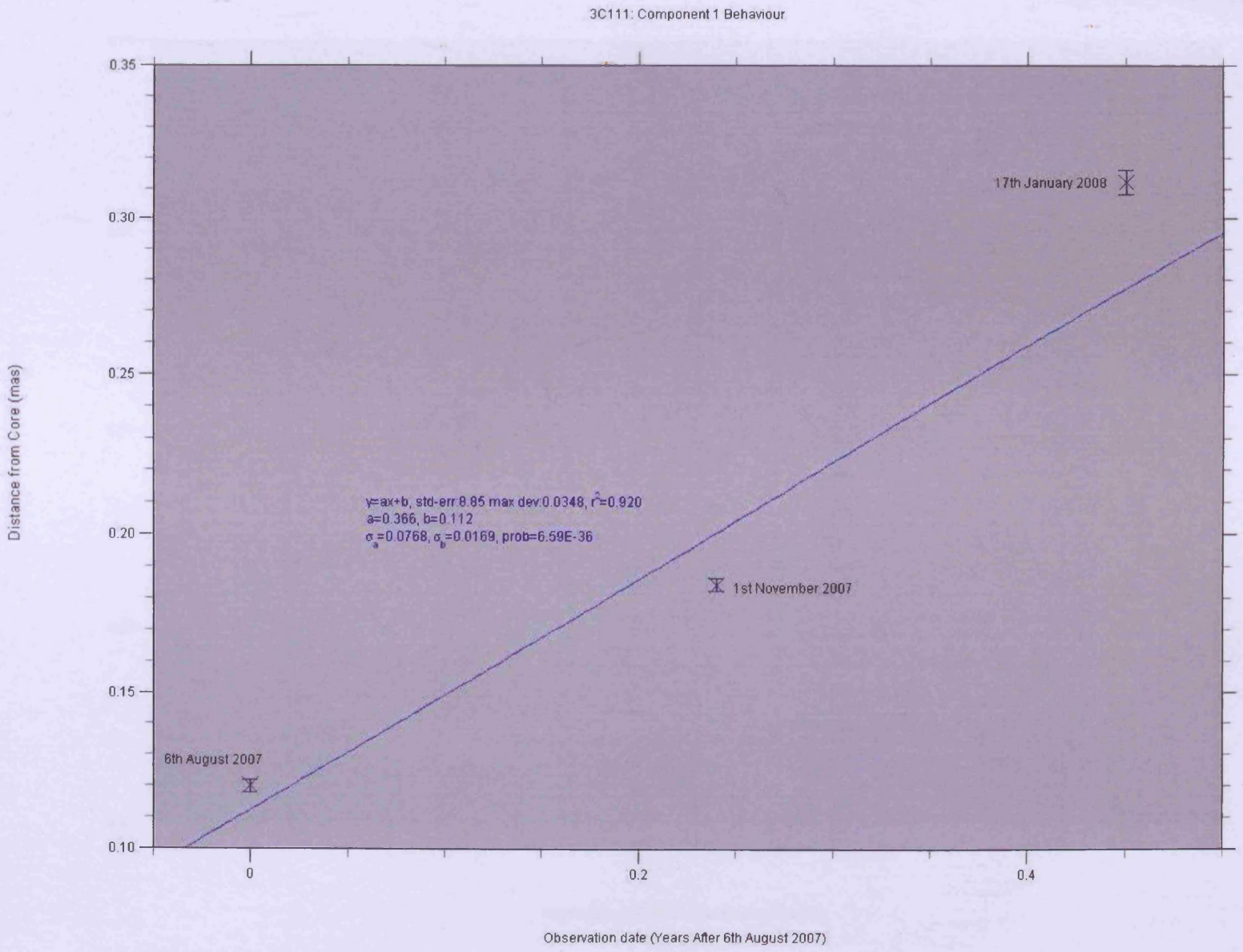
3C111: Component 1 Behaviour
Distance from Core (mas)
0.35
0.30
0.25
0.20
0.15
0.10
0
0.2
0.4
Observation date (Years After 6th August 2007)
y=ax+b, std-err:8.85 max dev:0.0348, r²=0.920
a=0.366, b=0.112
σa=0.0768, σb=0.0169, prob=6.59E-36
17th January 2008
1st November 2007
6th August 2007

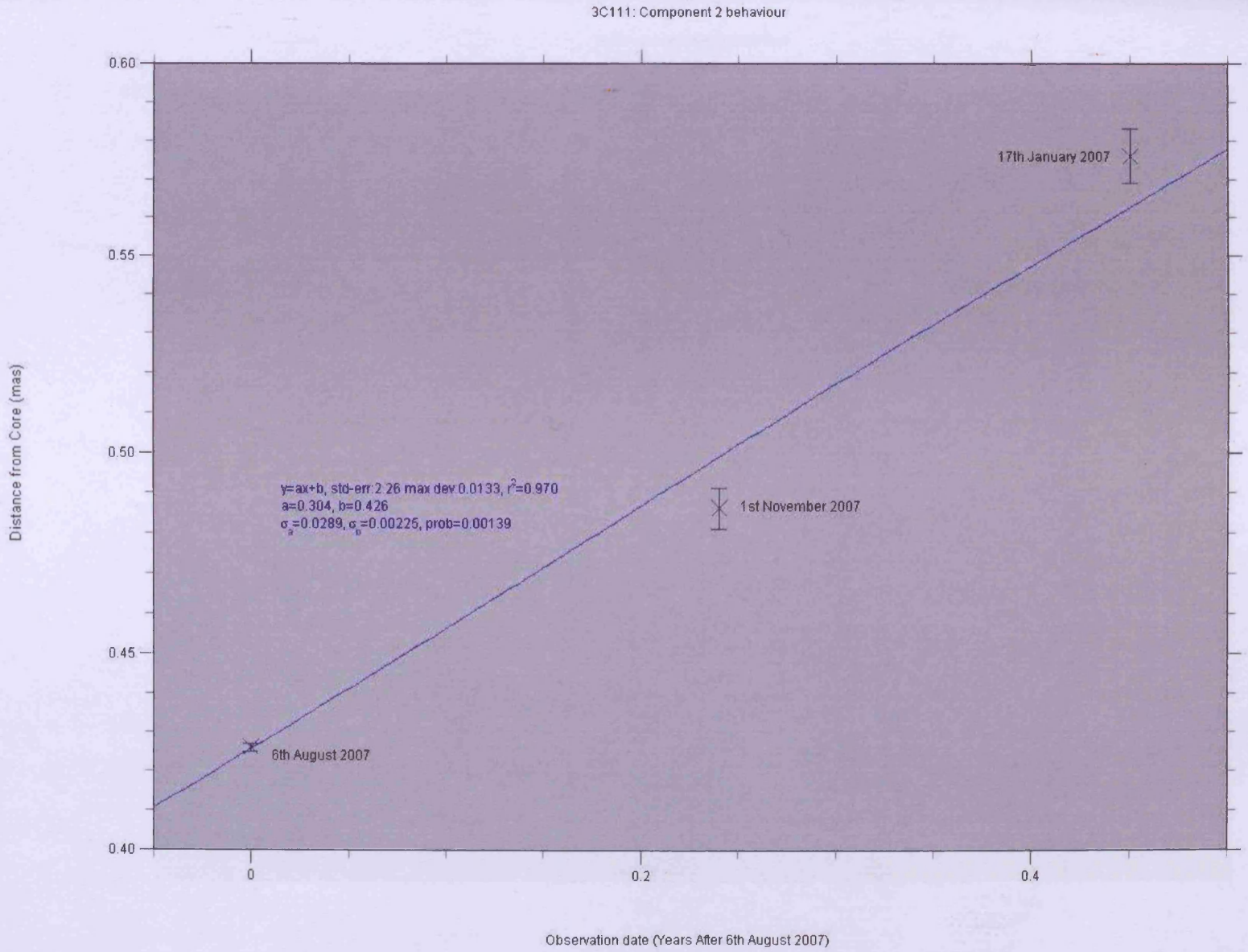
3C111: Component 2 behaviour
0.60
0.55
0.50
0.45
0.40
0
0.2
0.4
Distance from Core (mas)
Observation date (Years After 6th August 2007)
y=ax+b, std-err:2.26 max dev 0.0133, r²=0.970
a=0.304, b=0.426
σa=0.0289, σb=0.00225, prob=0.00139
17th January 2007
1st November 2007
6th August 2007

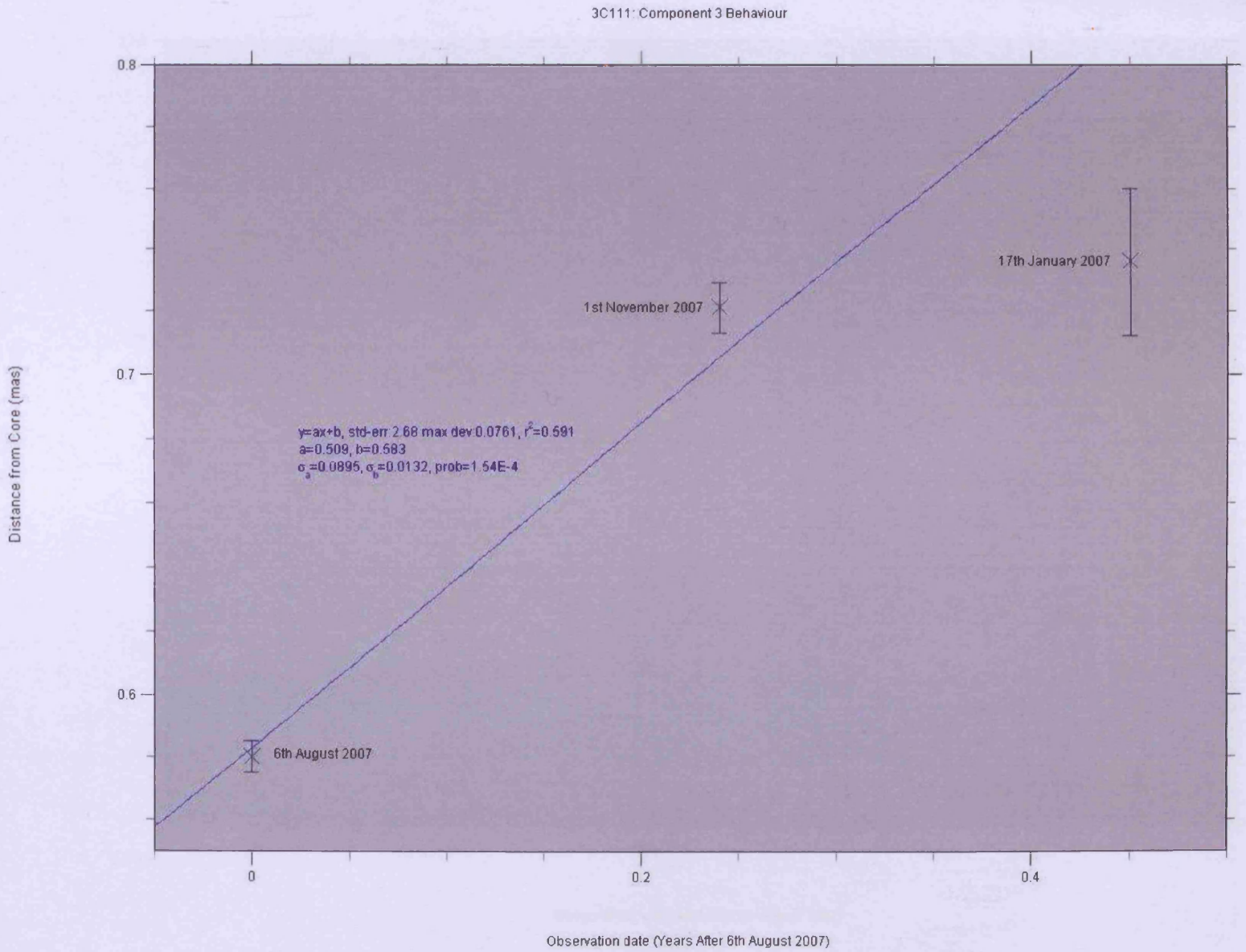
3C111: Component 3 Behaviour
0.8
0.7
0.6
Distance from Core (mas)
y=ax+b, std-err 2.68 max dev 0.0761, r²=0.591
a=0.509, b=0.583
σa=0.0895, σb=0.0132, prob=1.54E-4
1st November 2007
17th January 2007
6th August 2007
0
0.2
0.4
Observation date (Years After 6th August 2007)

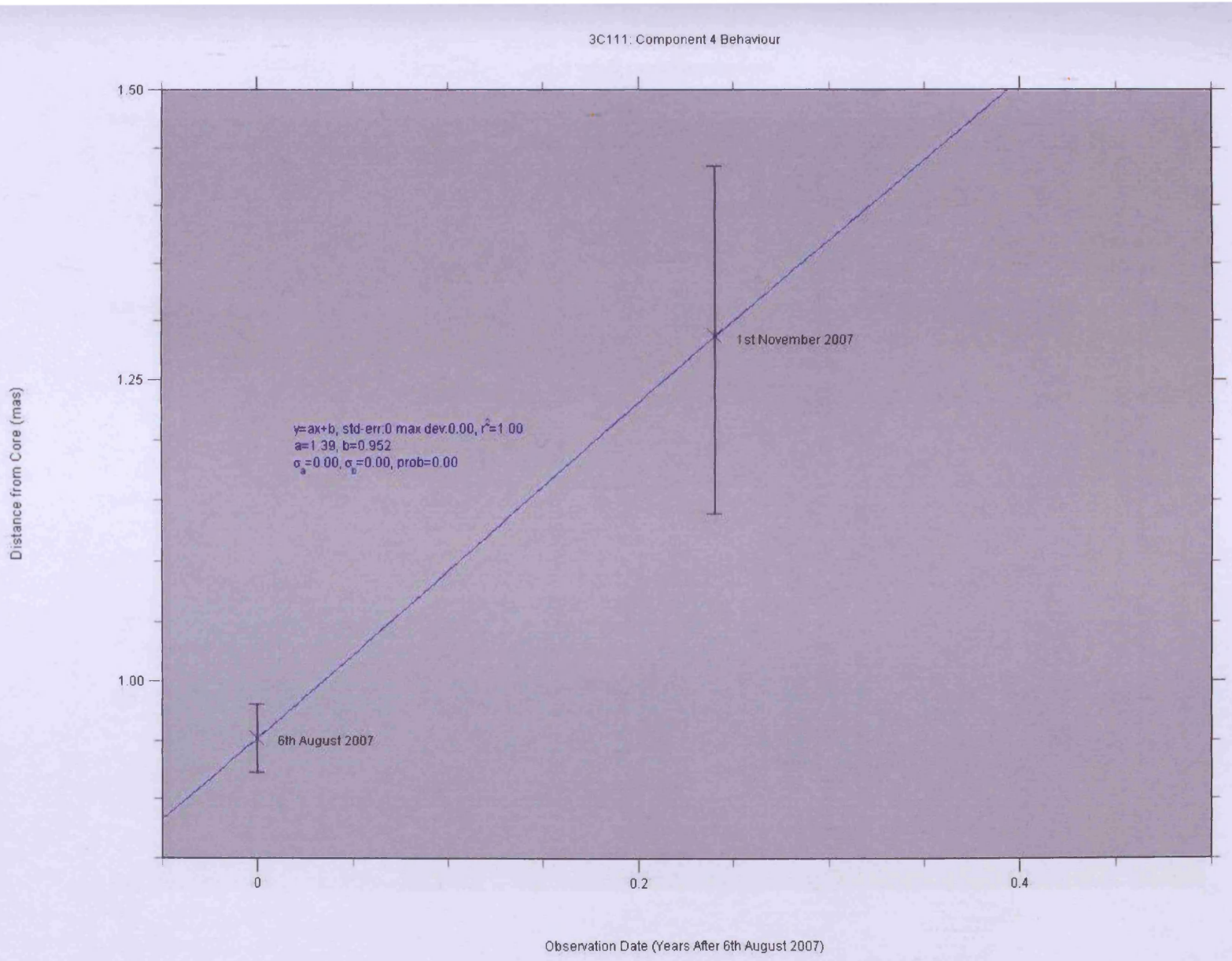
3C111: Component 4 Behaviour
1.50
1.25
1.00
Distance from Core (mas)
y=ax+b, std-err:0 max dev:0.00, r²=1.00
a=1.39, b=0.952
σa=0.00, σb=0.00, prob=0.00
1st November 2007
6th August 2007
0
0.2
0.4
Observation Date (Years After 6th August 2007)

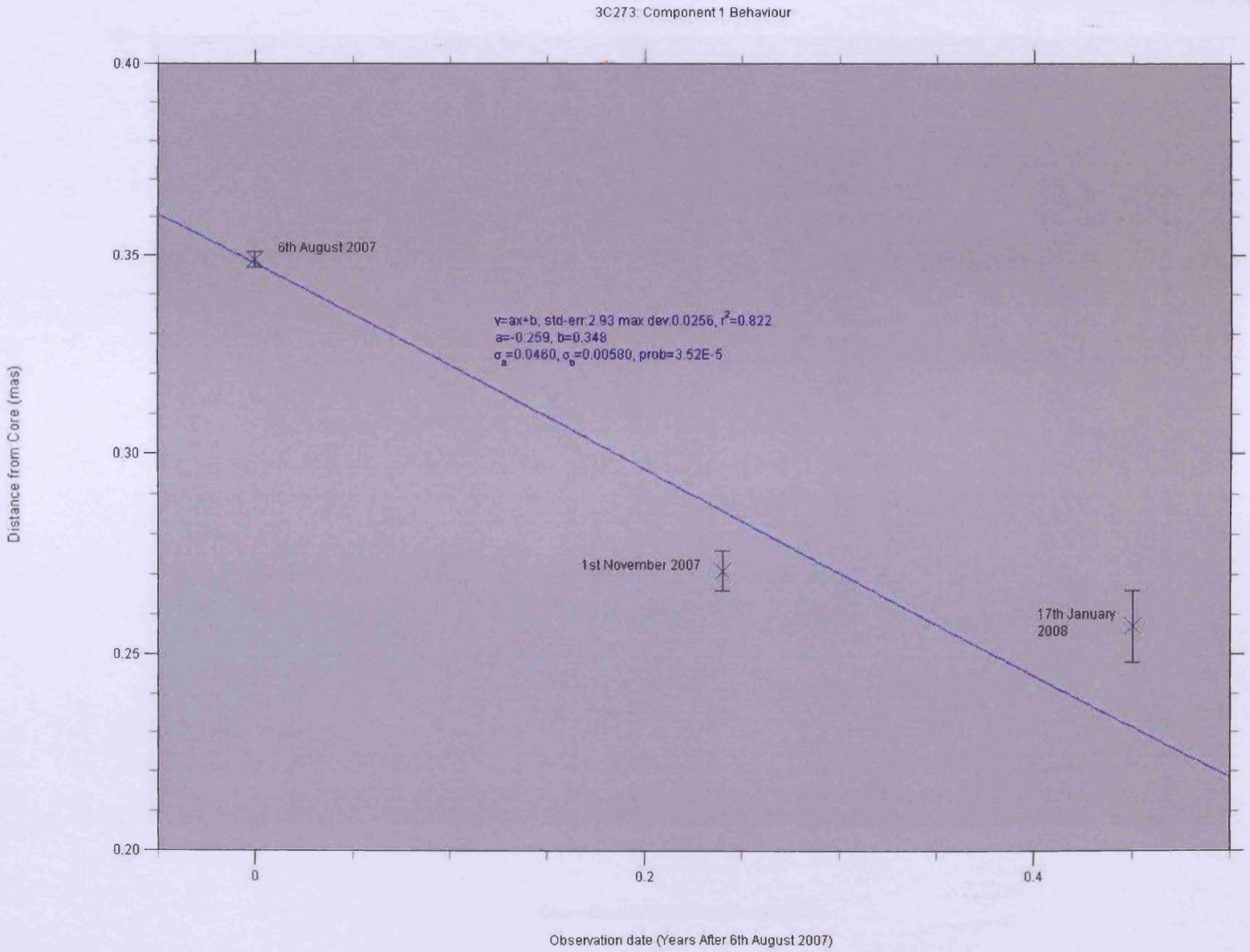
3C273: Component 1 Behaviour
0.40
0.35
0.30
0.25
0.20
Distance from Core (mas)
6th August 2007
v=ax+b, std-err:2.93 max dev:0.0256, r²=0.822
a=-0.259, b=0.348
σa=0.0460, σb=0.00580, prob=3.52E-5
1st November 2007
17th January 2008
0
0.2
0.4
Observation date (Years After 6th August 2007)

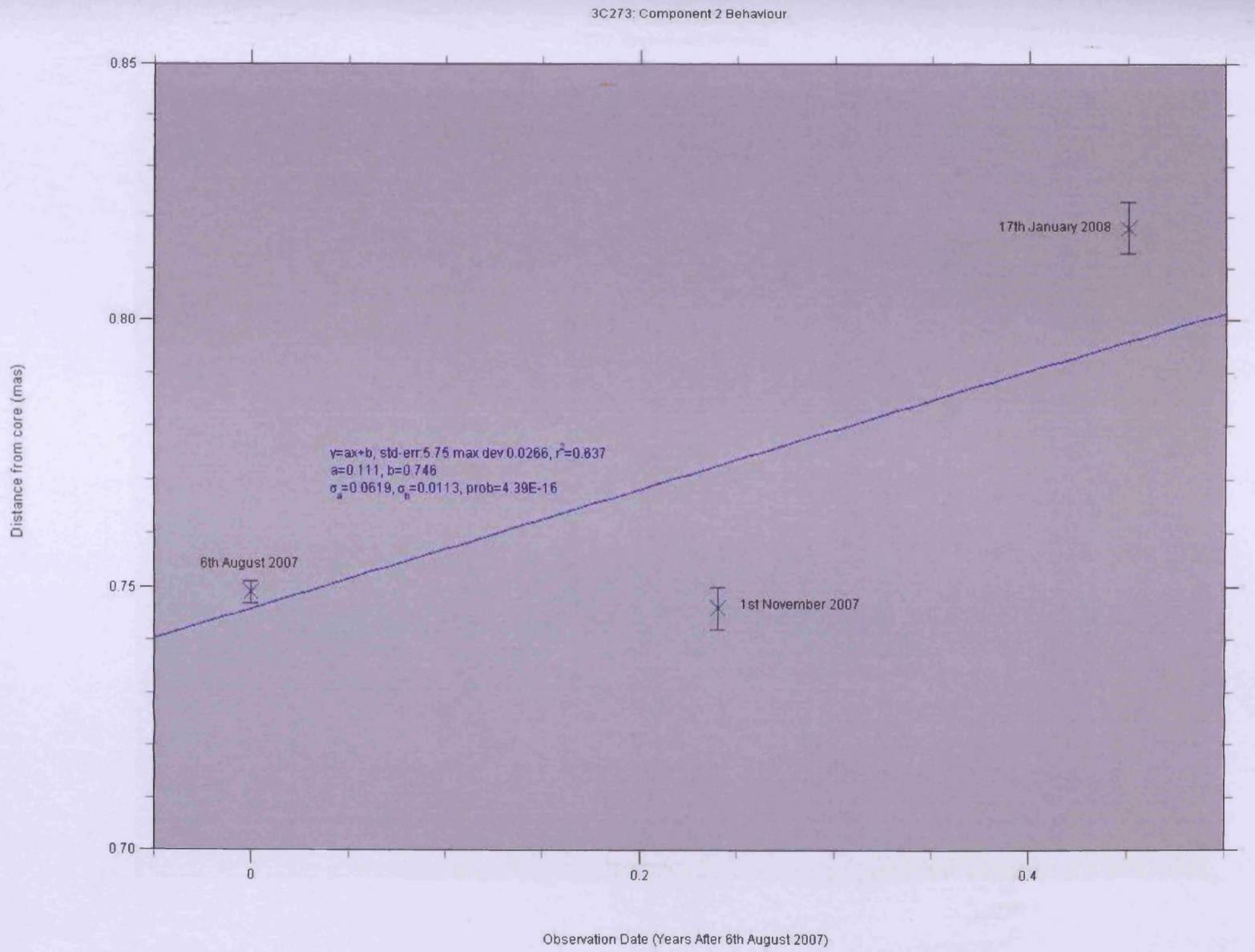
3C273: Component 2 Behaviour
0.85
0.80
0.75
0.70
0
0.2
0.4
Distance from core (mas)
Observation Date (Years After 6th August 2007)
y=ax+b, std-err:5.75 max dev 0.0266, r²=0.837
a=0.111, b=0.746
σa=0.0619, σb=0.0113, prob=4.39E-16
6th August 2007
1st November 2007
17th January 2008

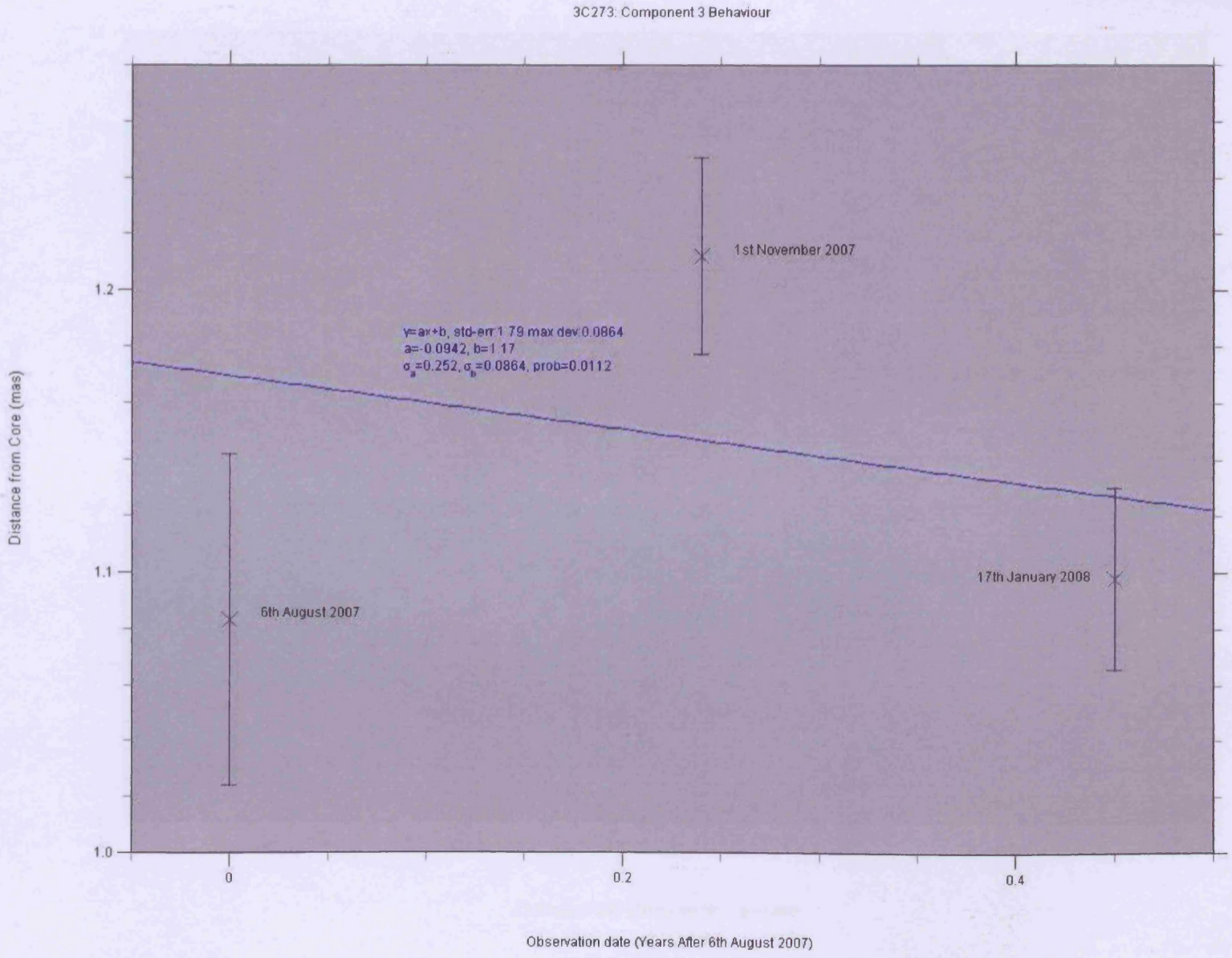
3C273: Component 3 Behaviour
1st November 2007
y=ax+b, std-err 1.79 max dev 0.0864
a=-0.0942, b=1.17
σa=0.252, σb=0.0864, prob=0.0112
6th August 2007
17th January 2008
1.2
1.1
1.0
0
0.2
0.4
Distance from Core (mas)
Observation date (Years After 6th August 2007)

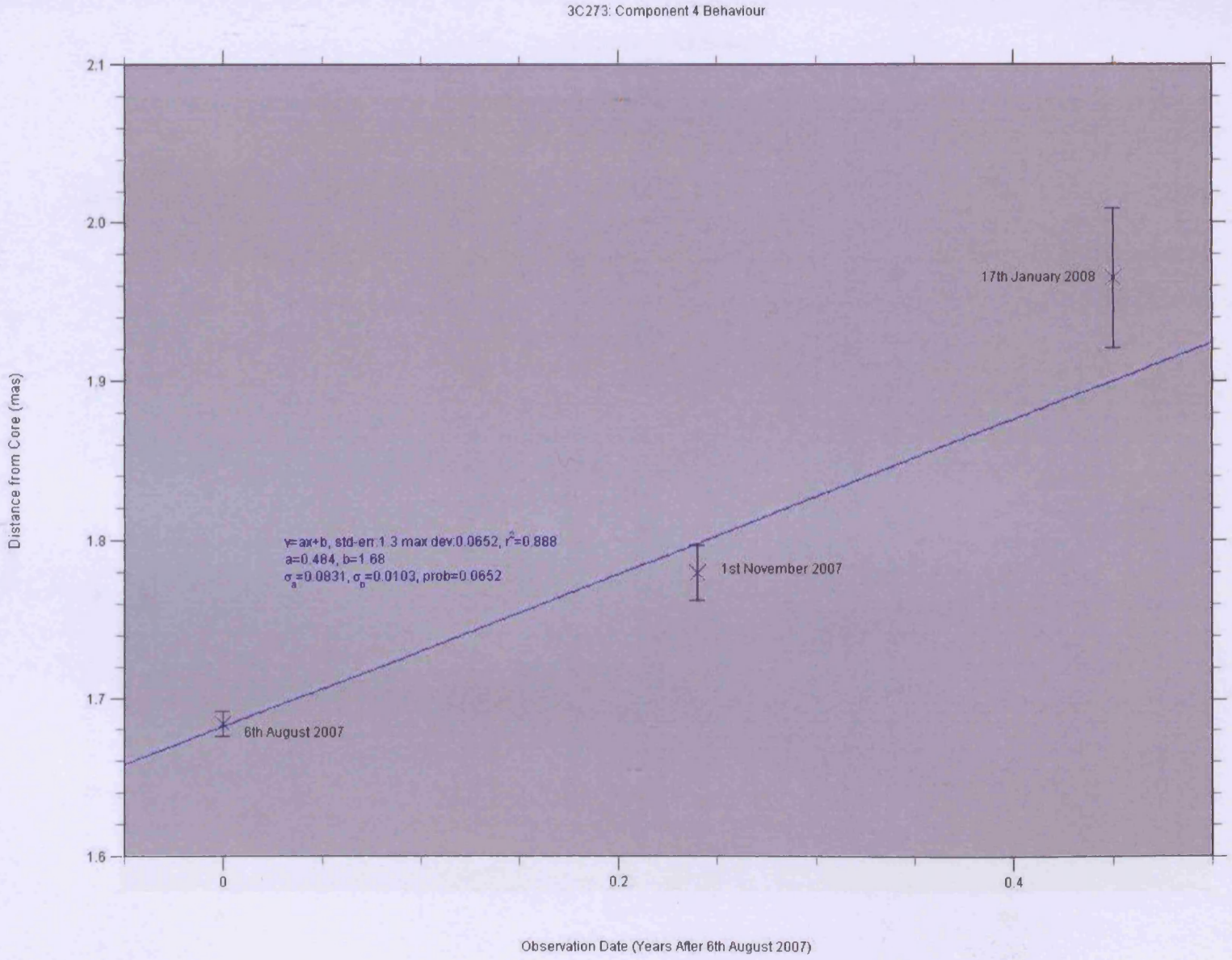
3C273: Component 4 Behaviour
Distance from Core (mas)
2.1
2.0
1.9
1.8
1.7
1.6
0
0.2
0.4
Observation Date (Years After 6th August 2007)
17th January 2008
1st November 2007
6th August 2007
y=ax+b, std-err:1.3 max dev:0.0652, r²=0.888
a=0.484, b=1.68
σa=0.0831, σb=0.0103, prob=0.0652

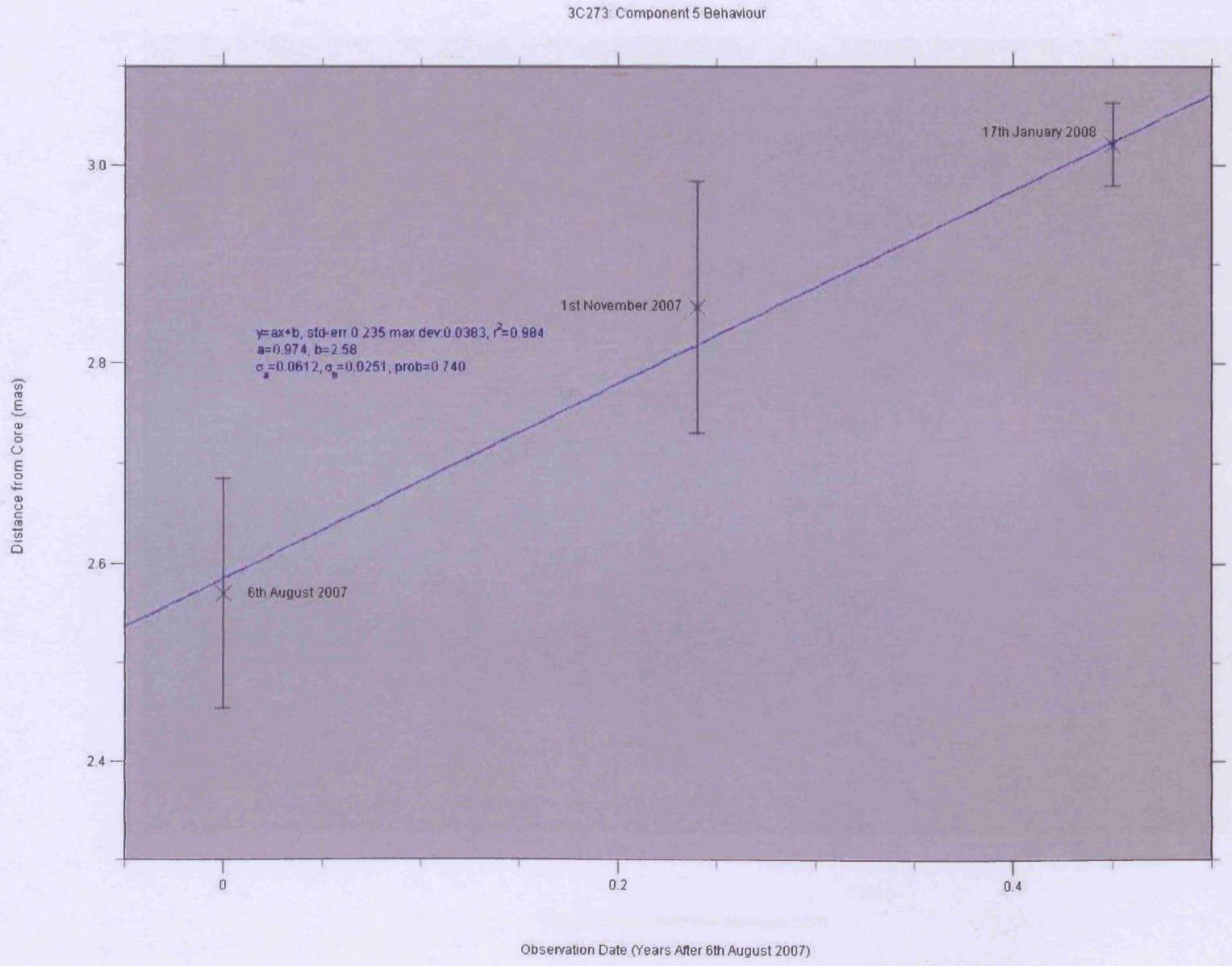
3C273: Component 5 Behaviour
17th January 2008
1st November 2007
6th August 2007
y=ax+b, std-err 0.235 max dev 0.0383, r²=0.984
a=0.974, b=2.58
σa=0.0612, σb=0.0251, prob=0.740
3.0
2.8
2.6
2.4
0
0.2
0.4
Distance from Core (mas)
Observation Date (Years After 6th August 2007)

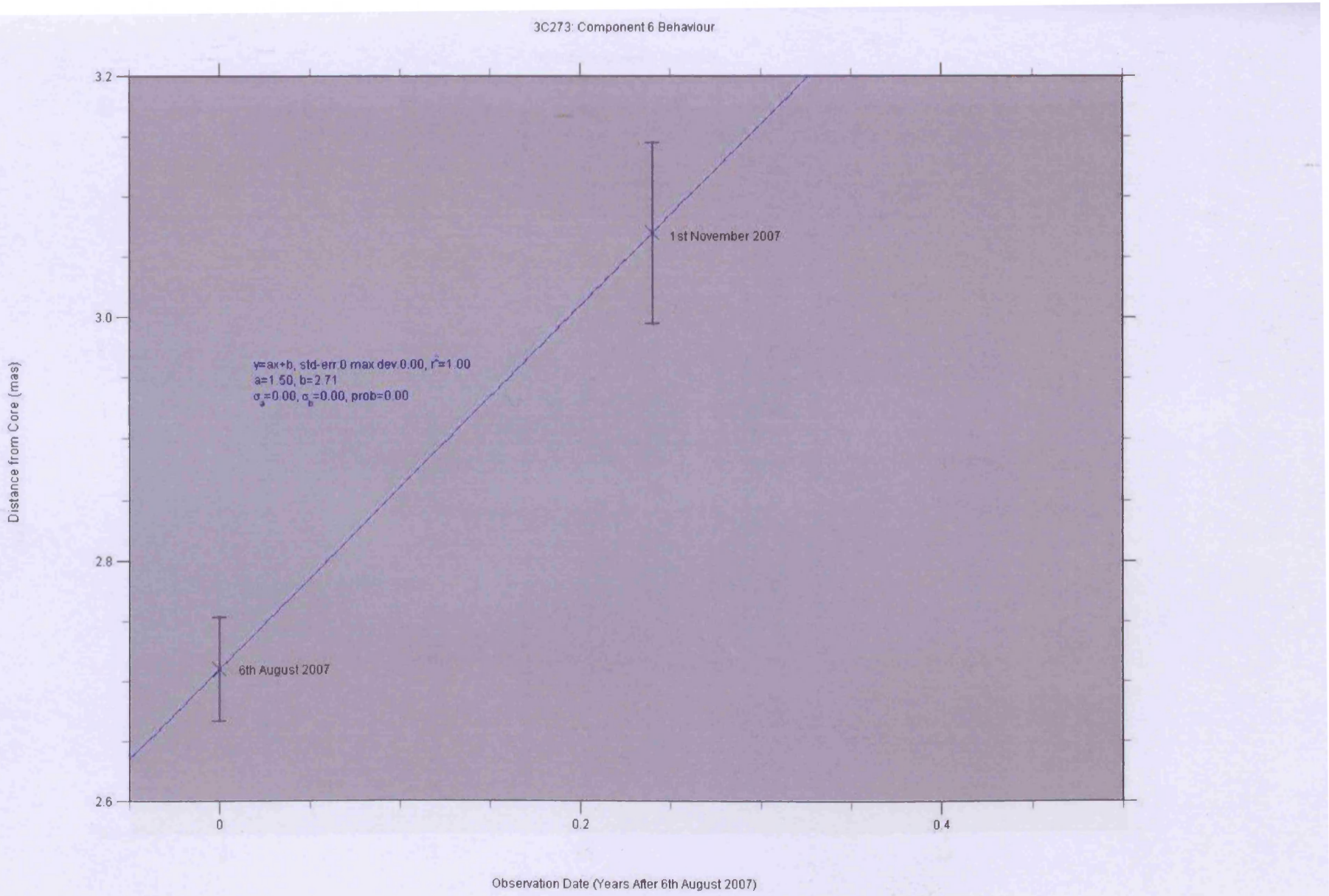
3C273: Component 6 Behaviour
3.2
3.0
2.8
2.6
0
0.2
0.4
Distance from Core (mas)
Observation Date (Years After 6th August 2007)
1st November 2007
6th August 2007
y=ax+b, std-err 0 max dev 0.00, r²=1.00
a=1.50, b=2.71
σa=0.00, σb=0.00, prob=0.00

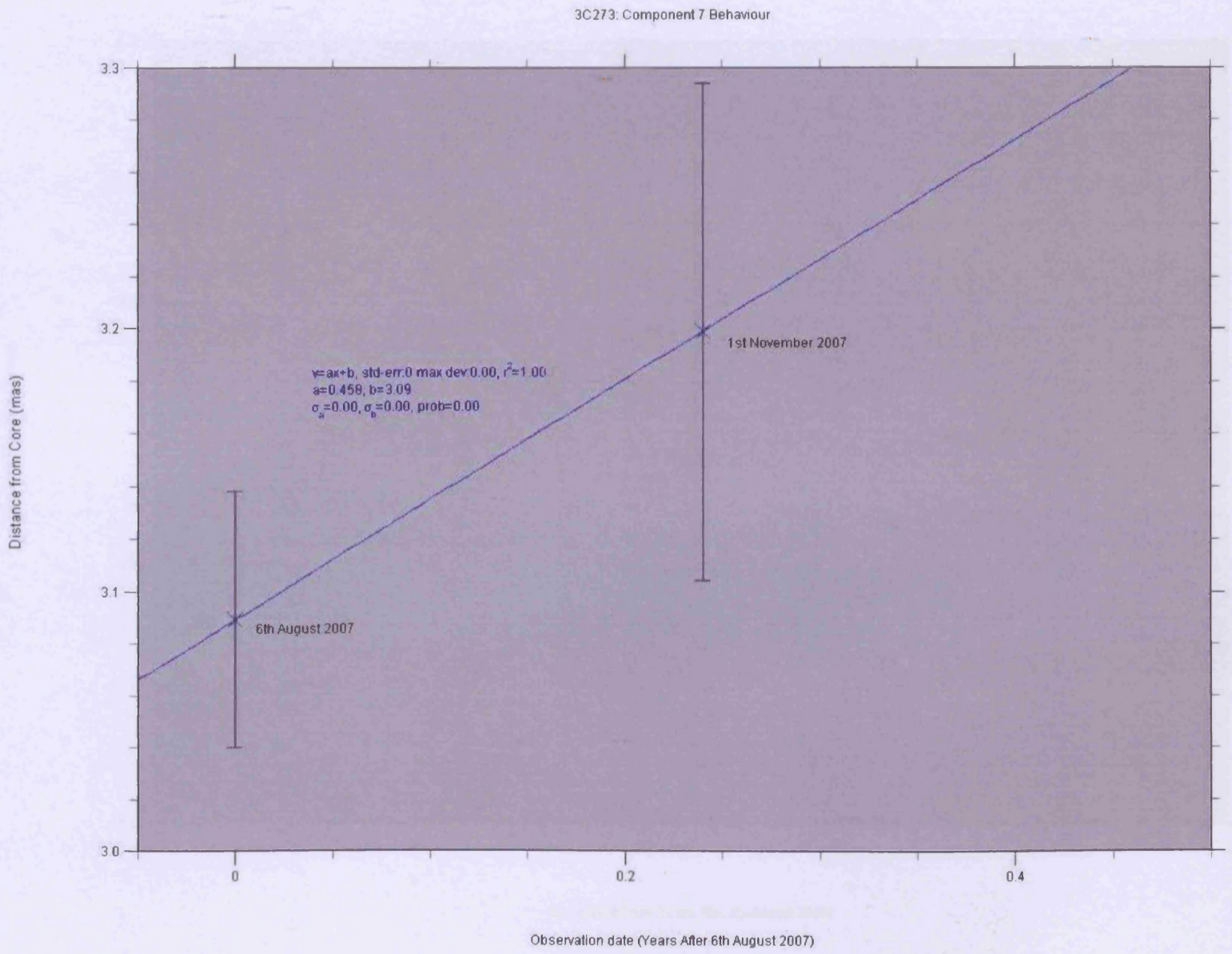
3C273: Component 7 Behaviour
Distance from Core (mas)
Observation date (Years After 6th August 2007)
3.3
3.2
3.1
3.0
0
0.2
0.4
y=ax+b, std-err:0 max dev:0.00, r²=1.00
a=0.458, b=3.09
σa=0.00, σb=0.00, prob=0.00
1st November 2007
6th August 2007

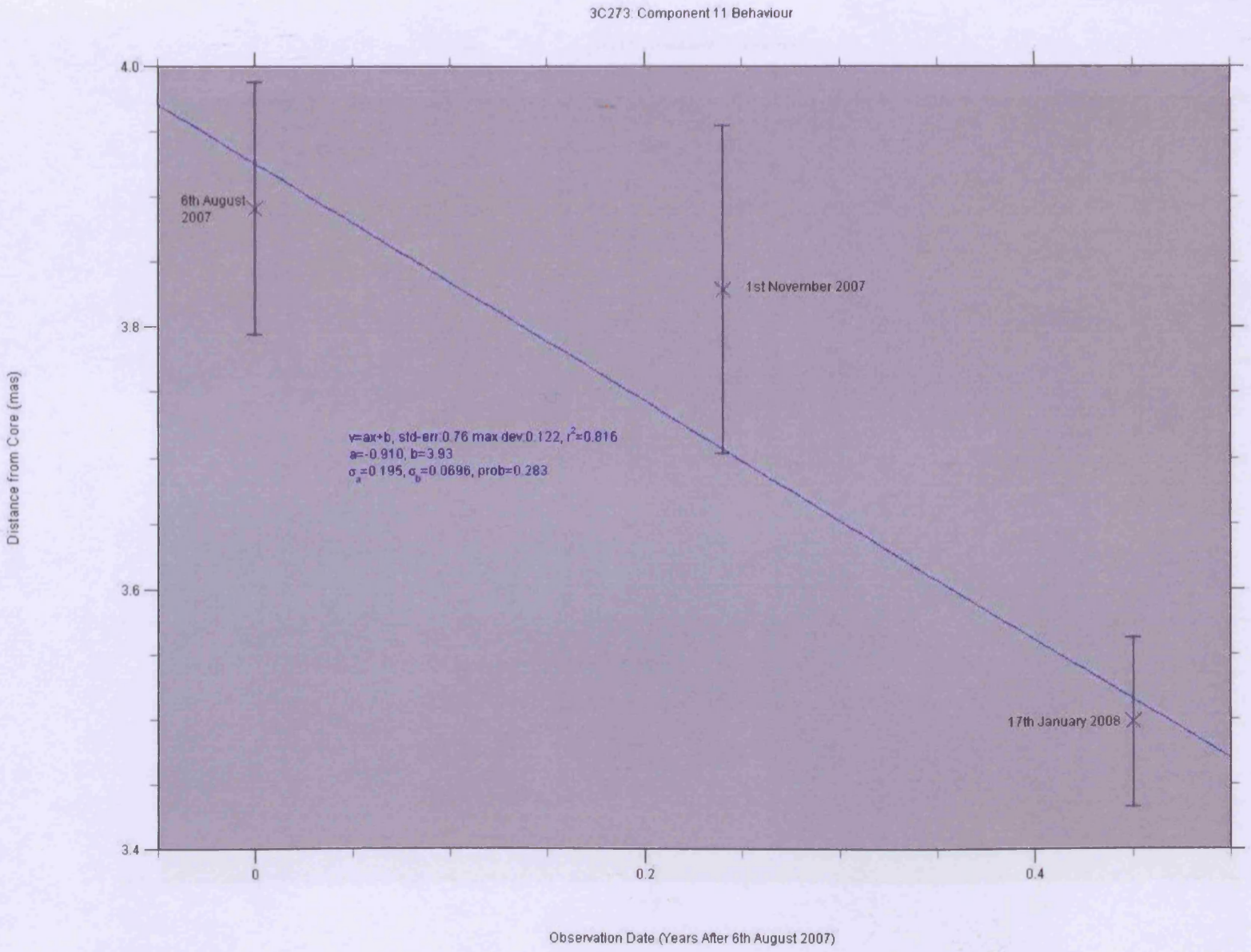
3C273: Component 11 Behaviour
4.0
3.8
3.6
3.4
0
0.2
0.4
6th August 2007
1st November 2007
17th January 2008
v=ax+b, std-err:0.76 max dev:0.122, r²=0.816
a=-0.910, b=3.93
σa=0.195, σb=0.0696, prob=0.283
Distance from Core (mas)
Observation Date (Years After 6th August 2007)

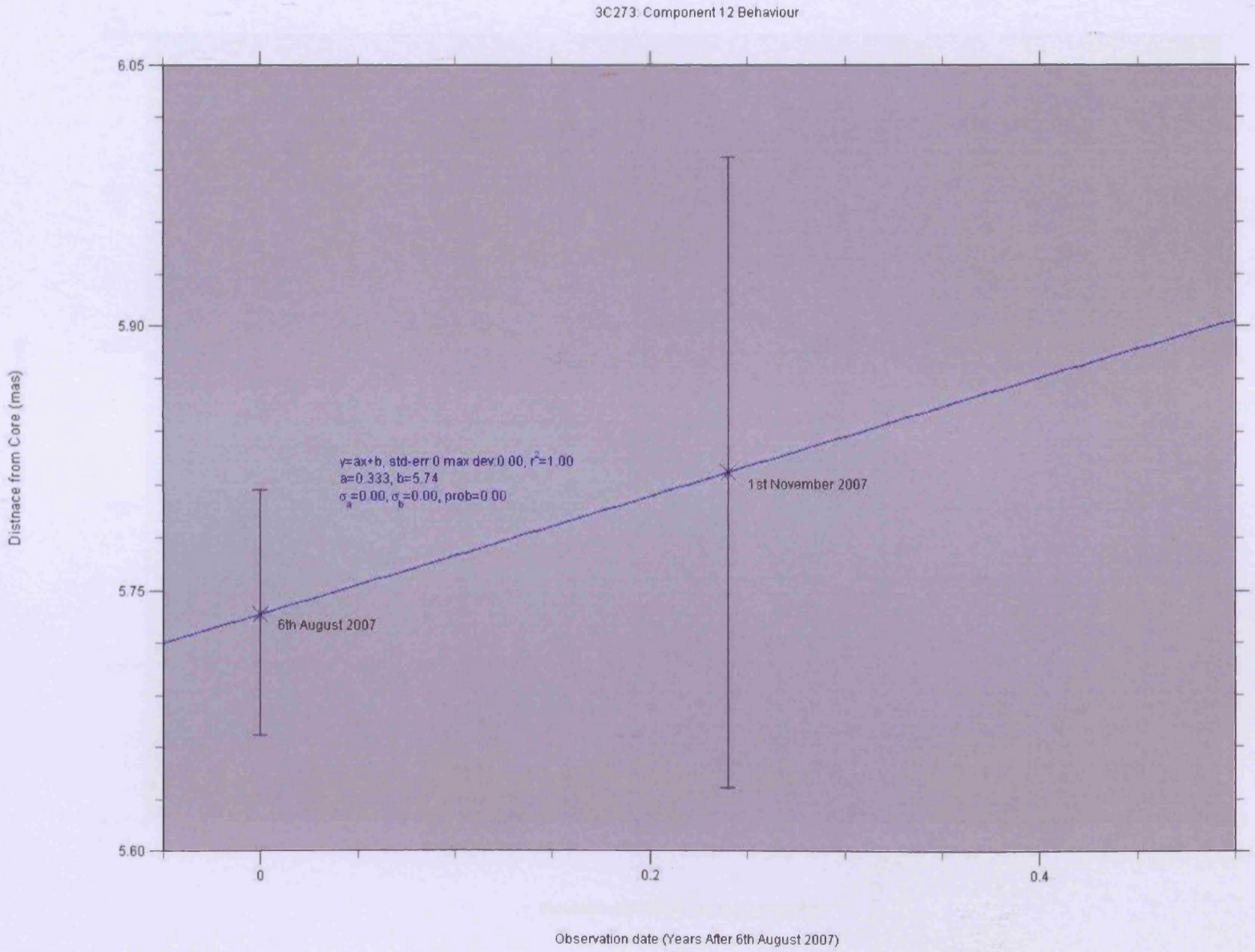
3C273: Component 12 Behaviour
6.05
5.90
5.75
5.60
Distnace from Core (mas)
y=ax+b, std-err 0 max dev 0.00, r²=1.00
a=0.333, b=5.74
σa=0.00, σb=0.00, prob=0.00
6th August 2007
1st November 2007
0
0.2
0.4
Observation date (Years After 6th August 2007)

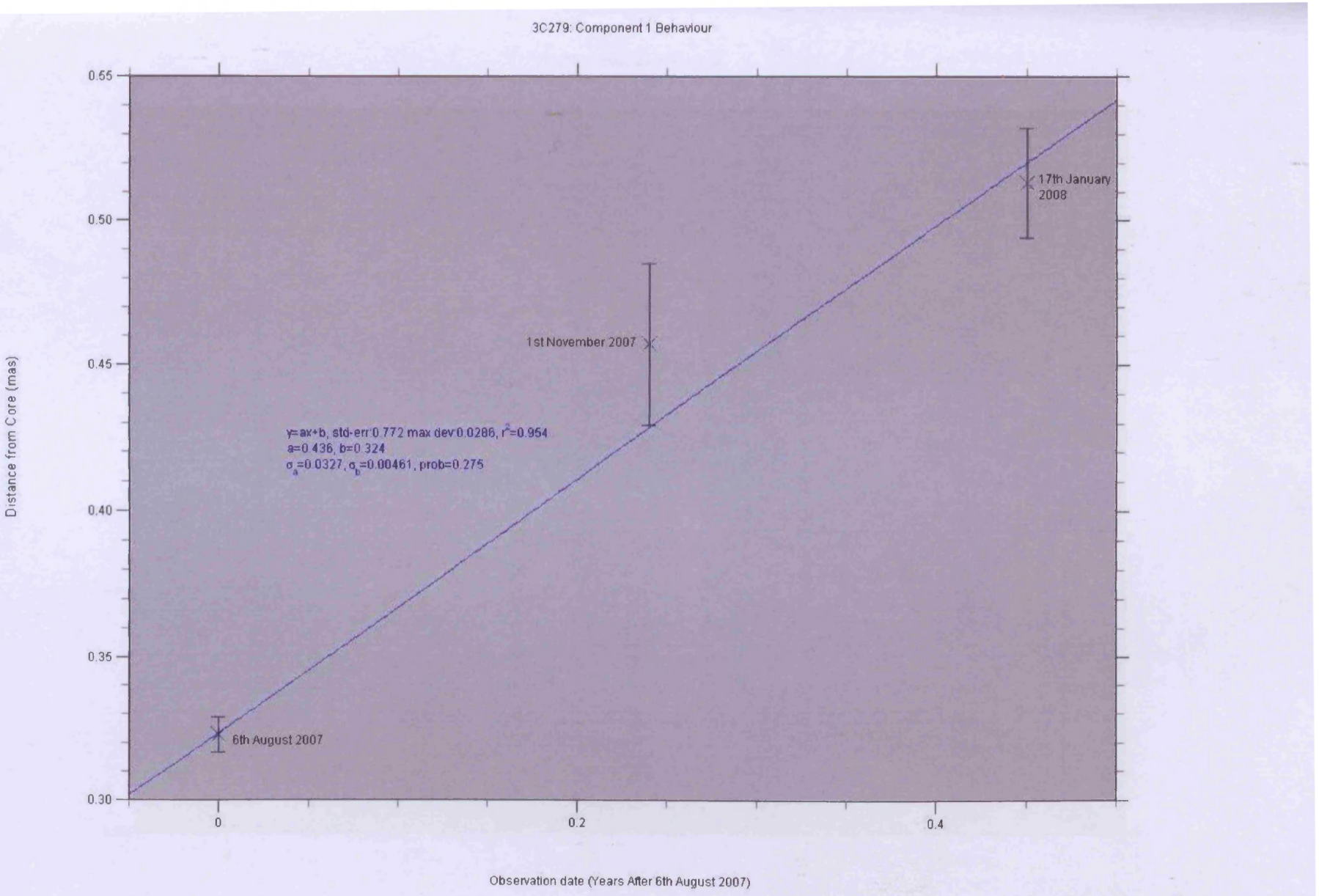
3C279: Component 1 Behaviour
0.55
0.50
0.45
0.40
0.35
0.30
Distance from Core (mas)
0
0.2
0.4
Observation date (Years After 6th August 2007)
17th January 2008
1st November 2007
6th August 2007
y=ax+b, std-err 0.772 max dev 0.0286, r²=0.954
a=0.436, b=0.324
σa=0.0327, σb=0.00461, prob=0.275

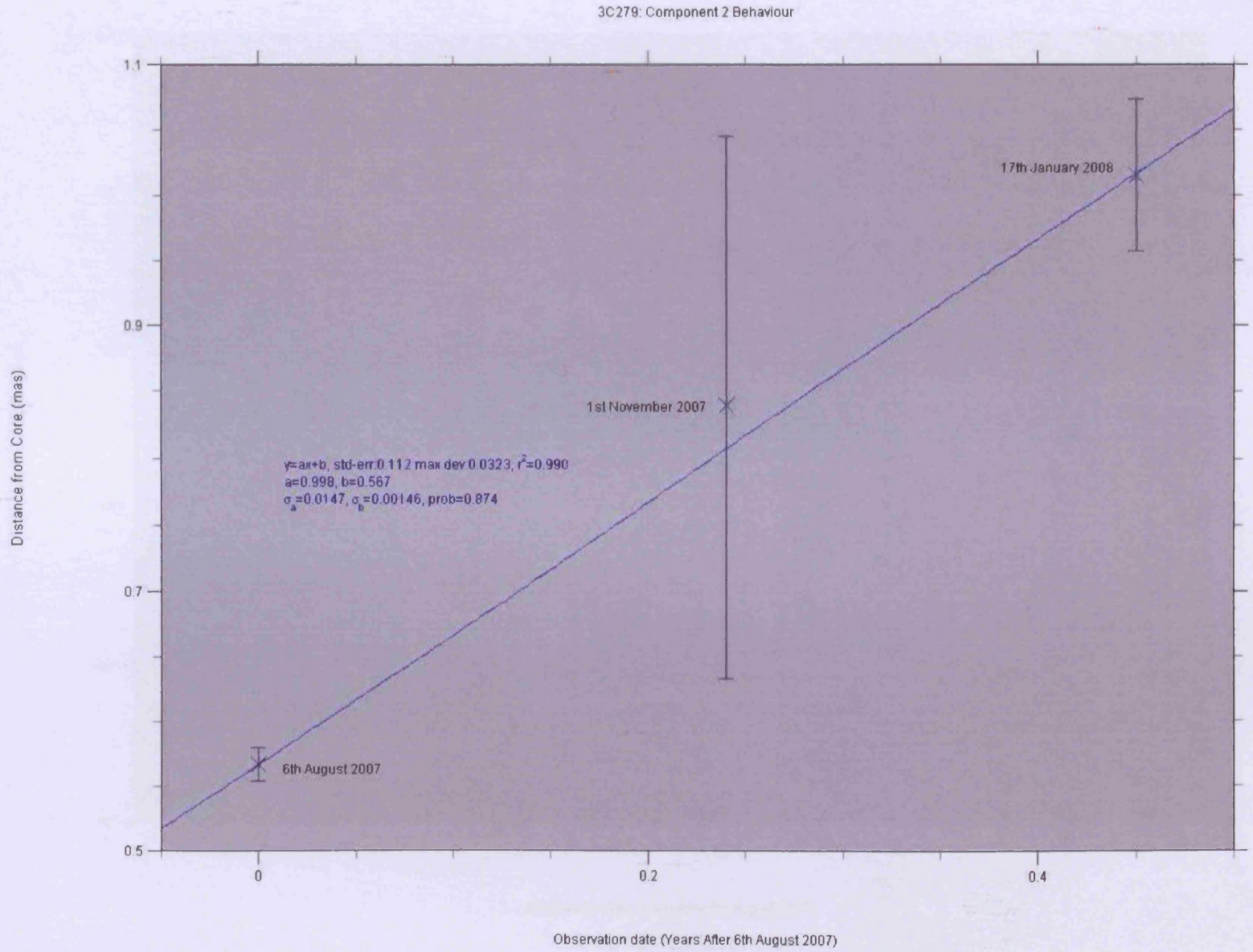
3C279: Component 2 Behaviour
1.1
0.9
0.7
0.5
0
0.2
0.4
Distance from Core (mas)
Observation date (Years After 6th August 2007)
17th January 2008
1st November 2007
6th August 2007
y=ax+b, std-err 0.112 max dev 0.0323, r²=0.990
a=0.998, b=0.567
σa=0.0147, σb=0.00146, prob=0.874

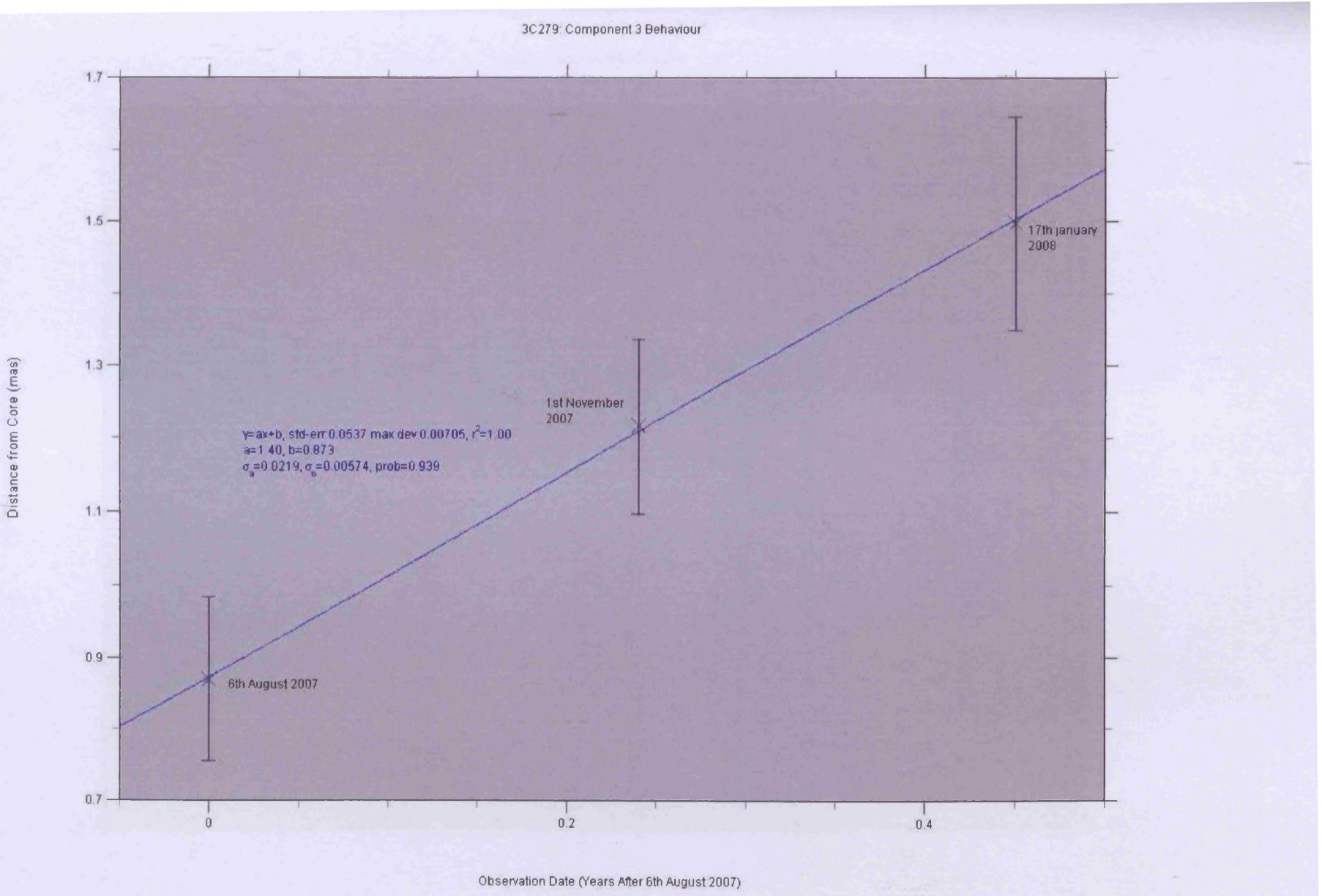
3C279: Component 3 Behaviour
Distance from Core (mas)
1.7
1.5
1.3
1.1
0.9
0.7
0
0.2
0.4
Observation Date (Years After 6th August 2007)
y=ax+b, std-err 0.0537 max dev 0.00705, r²=1.00
a=1.40, b=0.873
σa=0.0219, σb=0.00574, prob=0.939
6th August 2007
1st November 2007
17th january 2008

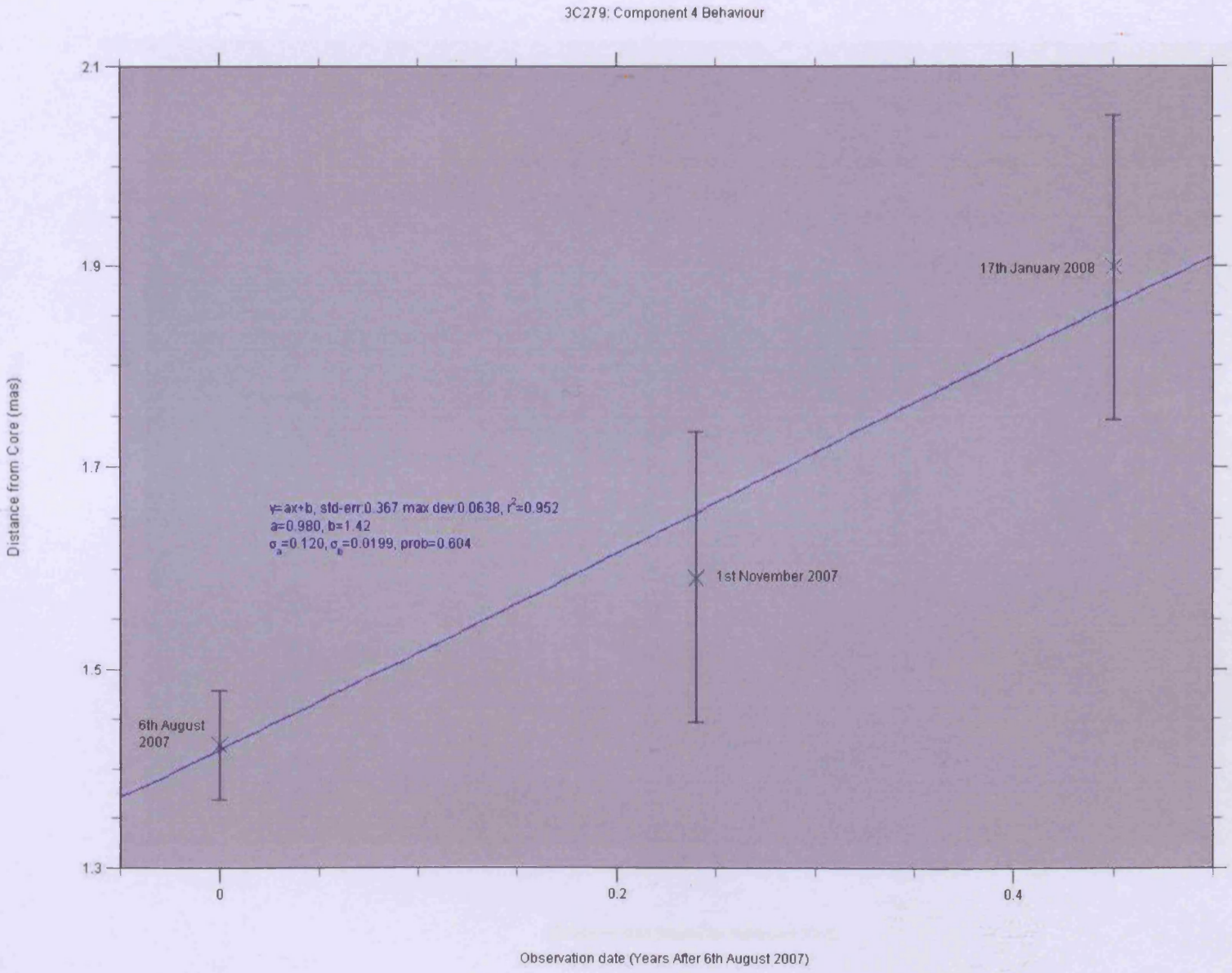
3C279: Component 4 Behaviour
Distance from Core (mas)
2.1
1.9
1.7
1.5
1.3
0
0.2
0.4
Observation date (Years After 6th August 2007)
y=ax+b, std-err 0.367 max dev 0.0638, r²=0.952
a=0.980, b=1.42
σa=0.120, σb=0.0199, prob=0.604
6th August 2007
1st November 2007
17th January 2008

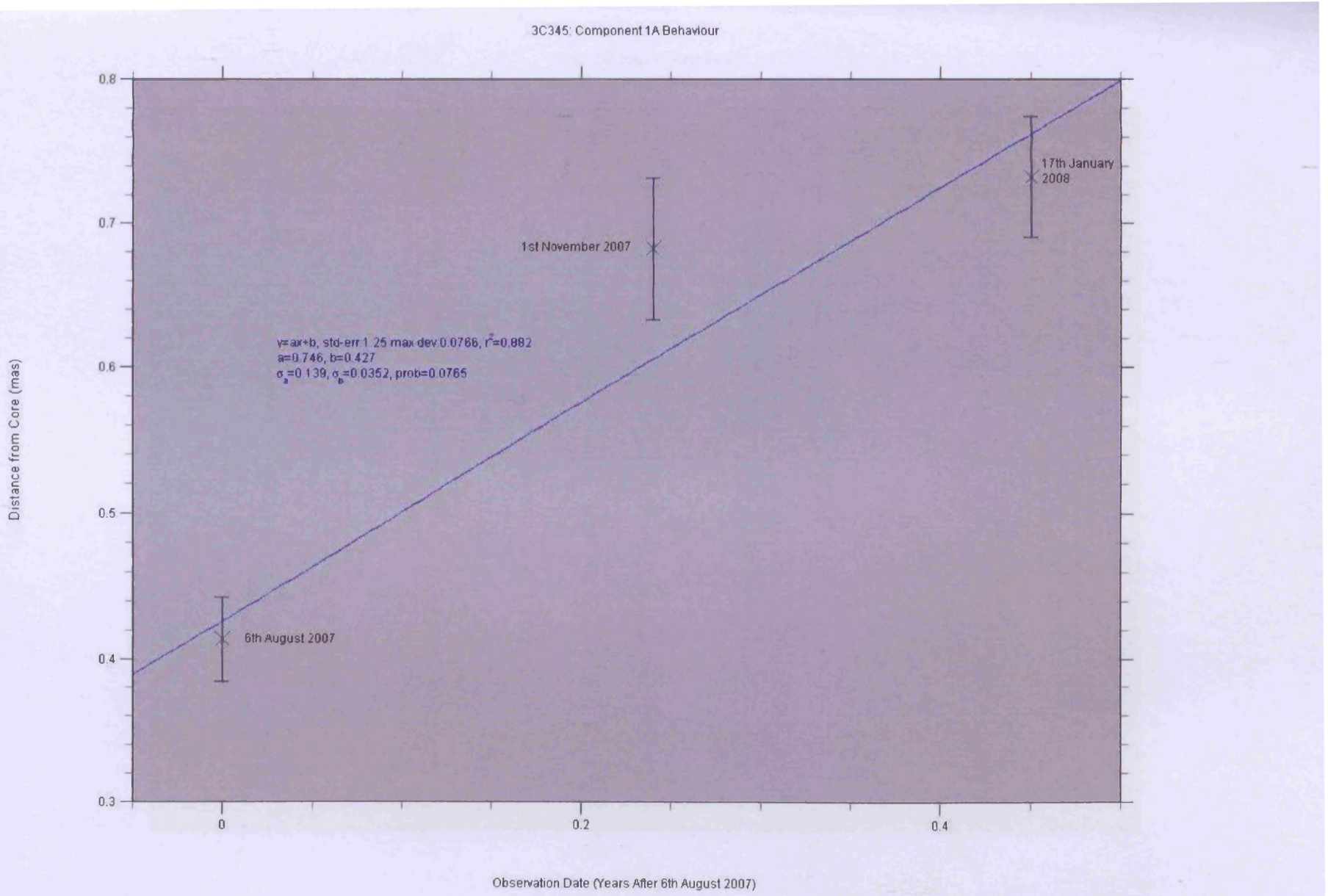
3C345: Component 1A Behaviour
Distance from Core (mas)
Observation Date (Years After 6th August 2007)
0.8
0.7
0.6
0.5
0.4
0.3
0
0.2
0.4
1st November 2007
17th January 2008
6th August 2007
y=ax+b, std-err 1.25 max dev 0.0766, r²=0.882
a=0.746, b=0.427
σa=0.139, σb=0.0352, prob=0.0765

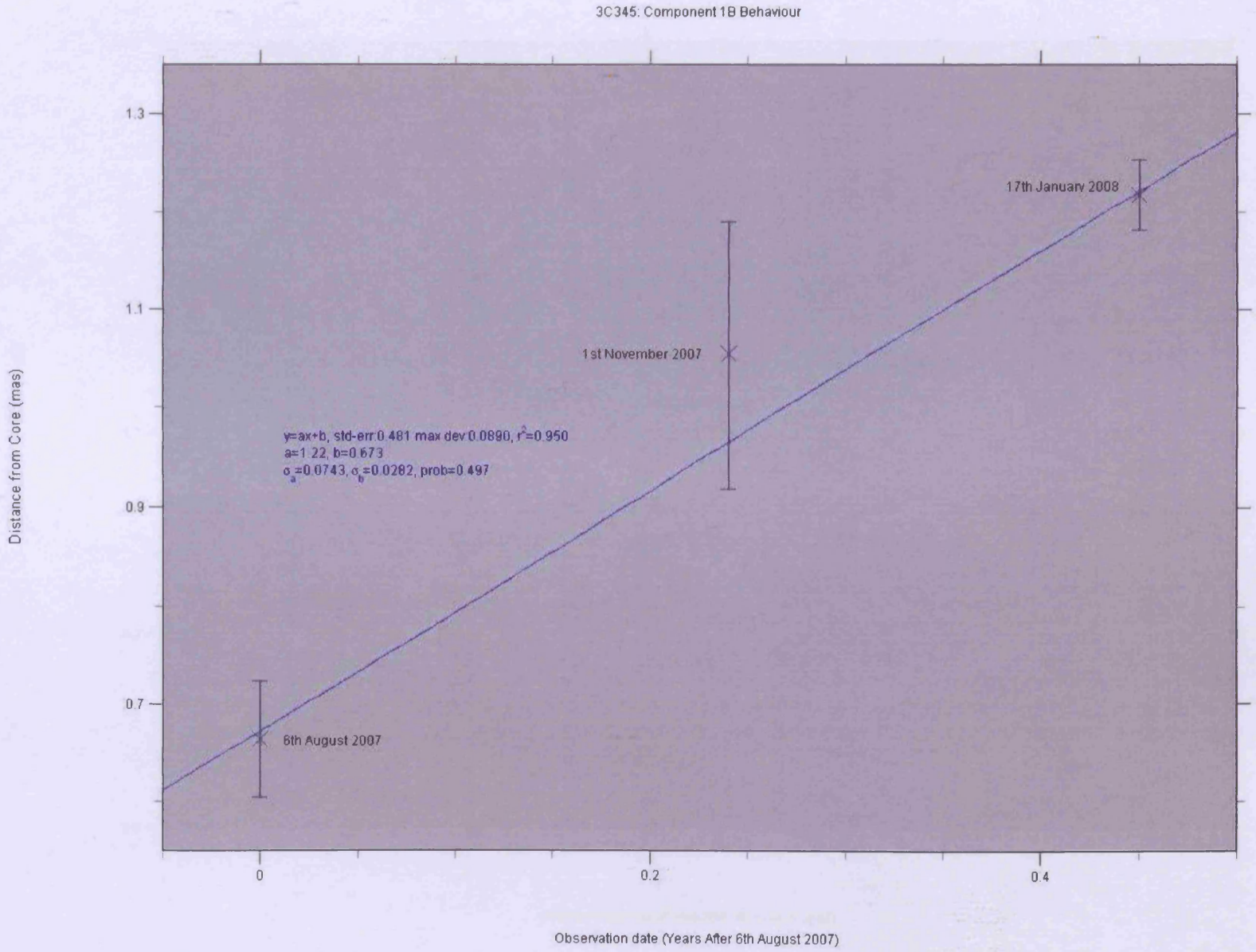
3C345: Component 1B Behaviour
Distance from Core (mas)
1.3
1.1
0.9
0.7
0
0.2
0.4
Observation date (Years After 6th August 2007)
17th January 2008
1st November 2007
6th August 2007
y=ax+b, std-err 0.481 max dev 0.0890, r²=0.950
a=1.22, b=0.673
σa=0.0743, σb=0.0282, prob=0.497

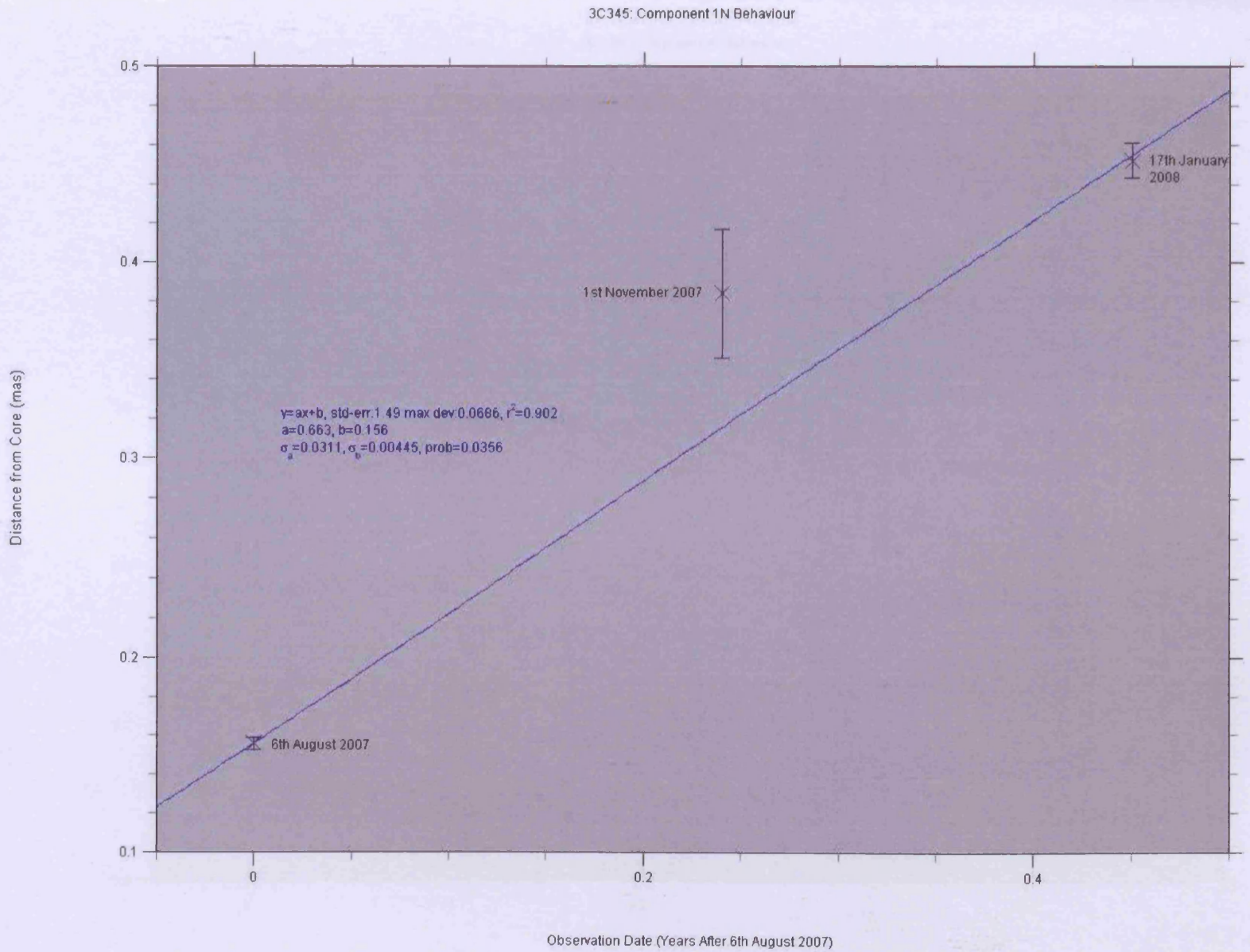
3C345: Component 1N Behaviour
0.5
0.4
0.3
0.2
0.1
0
0.2
0.4
Distance from Core (mas)
Observation Date (Years After 6th August 2007)
17th January 2008
1st November 2007
6th August 2007
y=ax+b, std-err:1.49 max dev:0.0686, r²=0.902
a=0.663, b=0.156
σa=0.0311, σb=0.00445, prob=0.0356

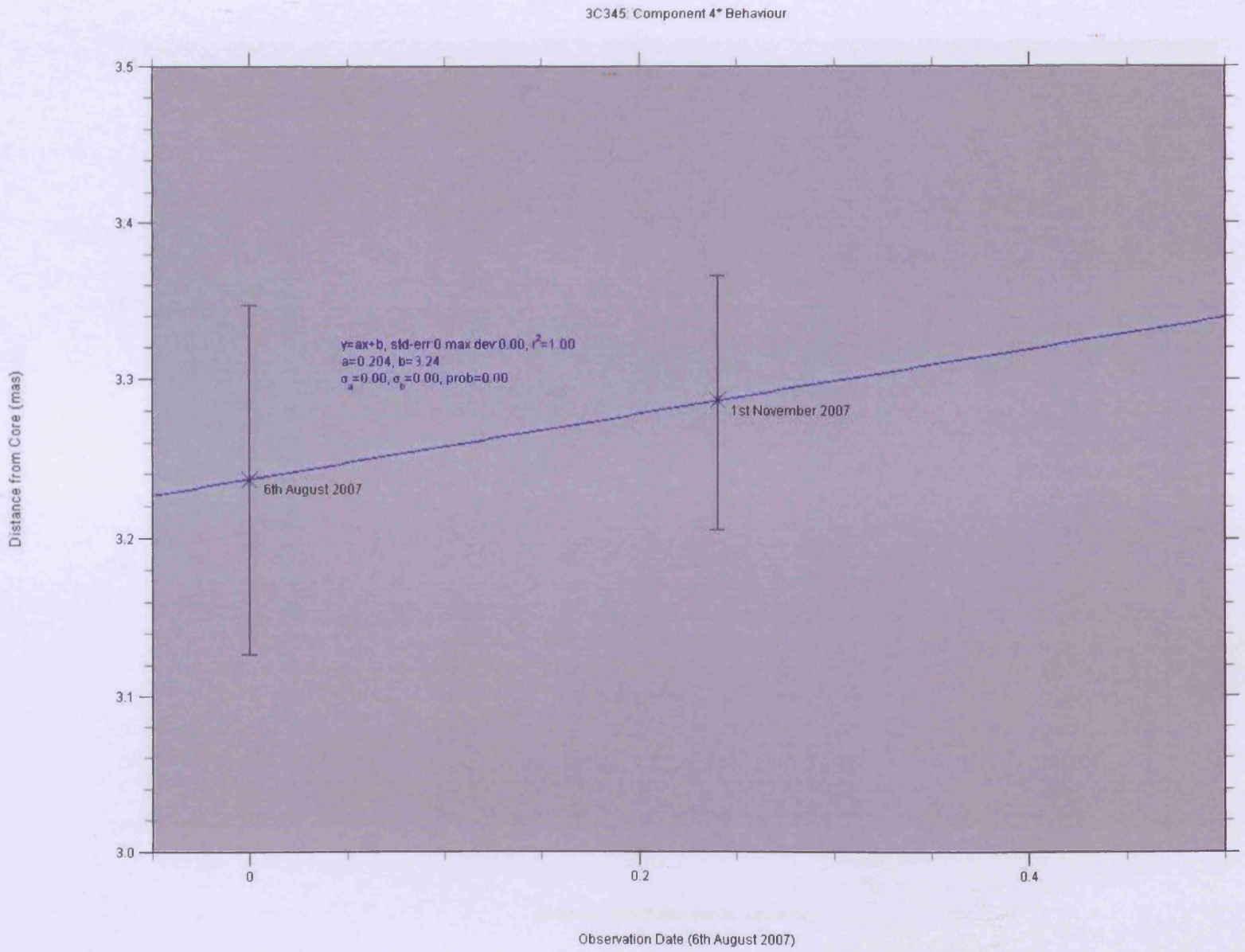
3C345: Component 4* Behaviour
y=ax+b, std-err 0 max dev 0.00, r²=1.00
a=0.204, b=3.24
σa=0.00, σb=0.00, prob=0.00
6th August 2007
1st November 2007
Distance from Core (mas)
Observation Date (6th August 2007)
3.5
3.4
3.3
3.2
3.1
3.0
0
0.2
0.4

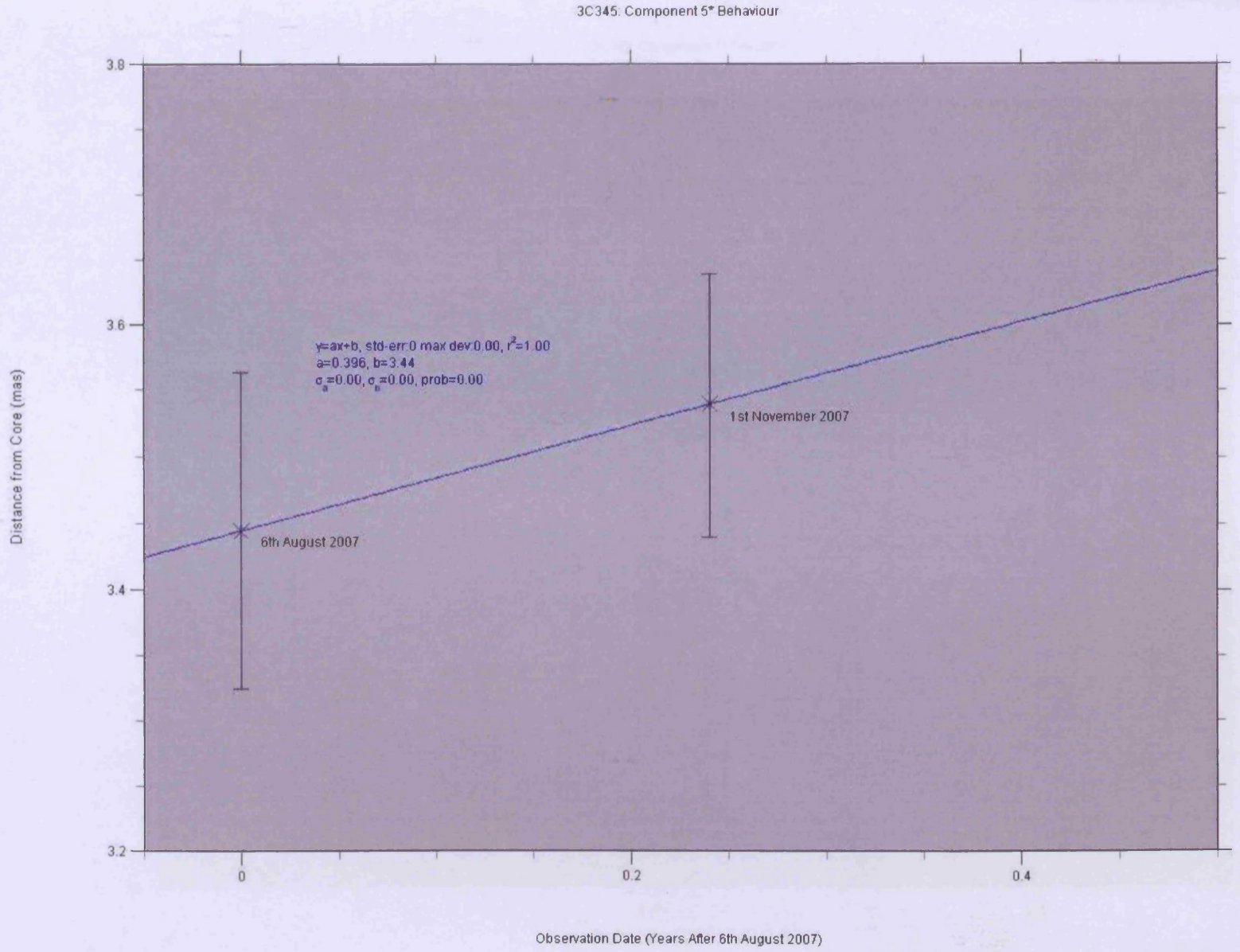
3C345: Component 5* Behaviour
3.8
3.6
3.4
3.2
0
0.2
0.4
Distance from Core (mas)
Observation Date (Years After 6th August 2007)
y=ax+b, std-err:0 max dev:0.00, r²=1.00
a=0.396, b=3.44
σa=0.00, σb=0.00, prob=0.00
6th August 2007
1st November 2007

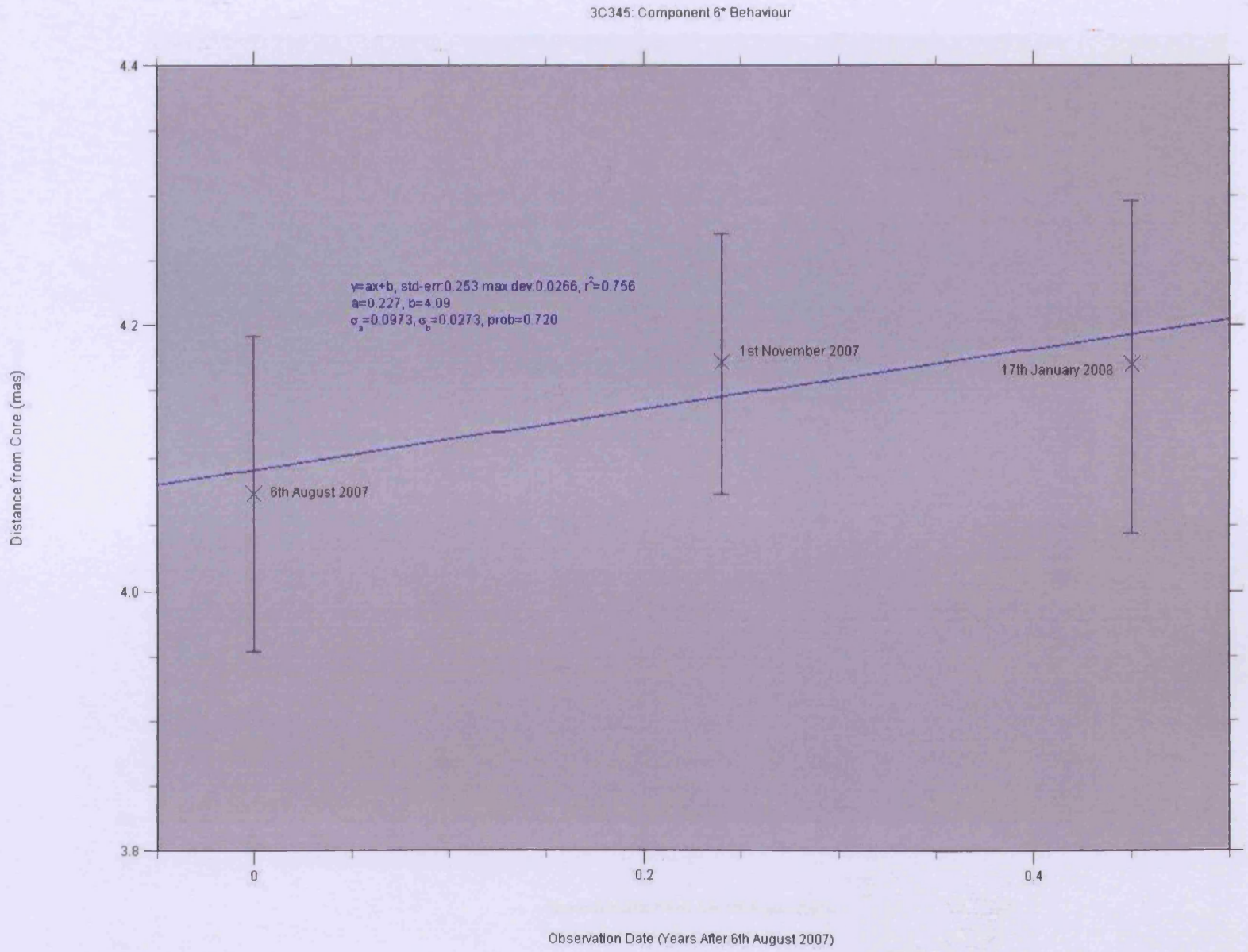
3C345: Component 6* Behaviour
4.4
4.2
4.0
3.8
0
0.2
0.4
Distance from Core (mas)
Observation Date (Years After 6th August 2007)
y=ax+b, std-err:0.253 max dev:0.0266, r²=0.756
a=0.227, b=4.09
σa=0.0973, σb=0.0273, prob=0.720
6th August 2007
1st November 2007
17th January 2008

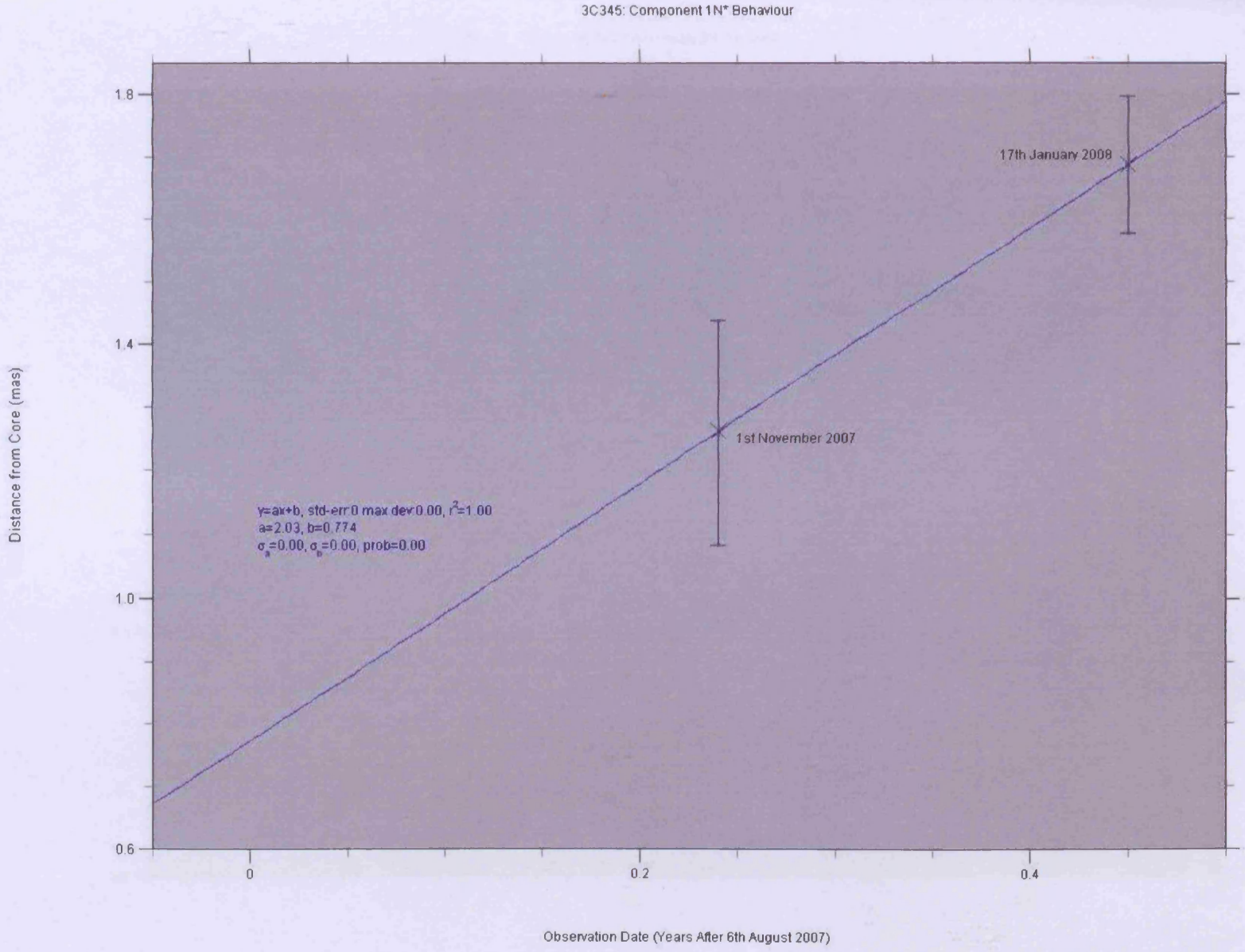
3C345: Component 1N* Behaviour
Distance from Core (mas)
1.8
1.4
1.0
0.6
0
0.2
0.4
17th January 2008
1st November 2007
y=ax+b, std-err:0 max dev:0.00, r²=1.00
a=2.03, b=0.774
σa=0.00, σb=0.00, prob=0.00
Observation Date (Years After 6th August 2007)

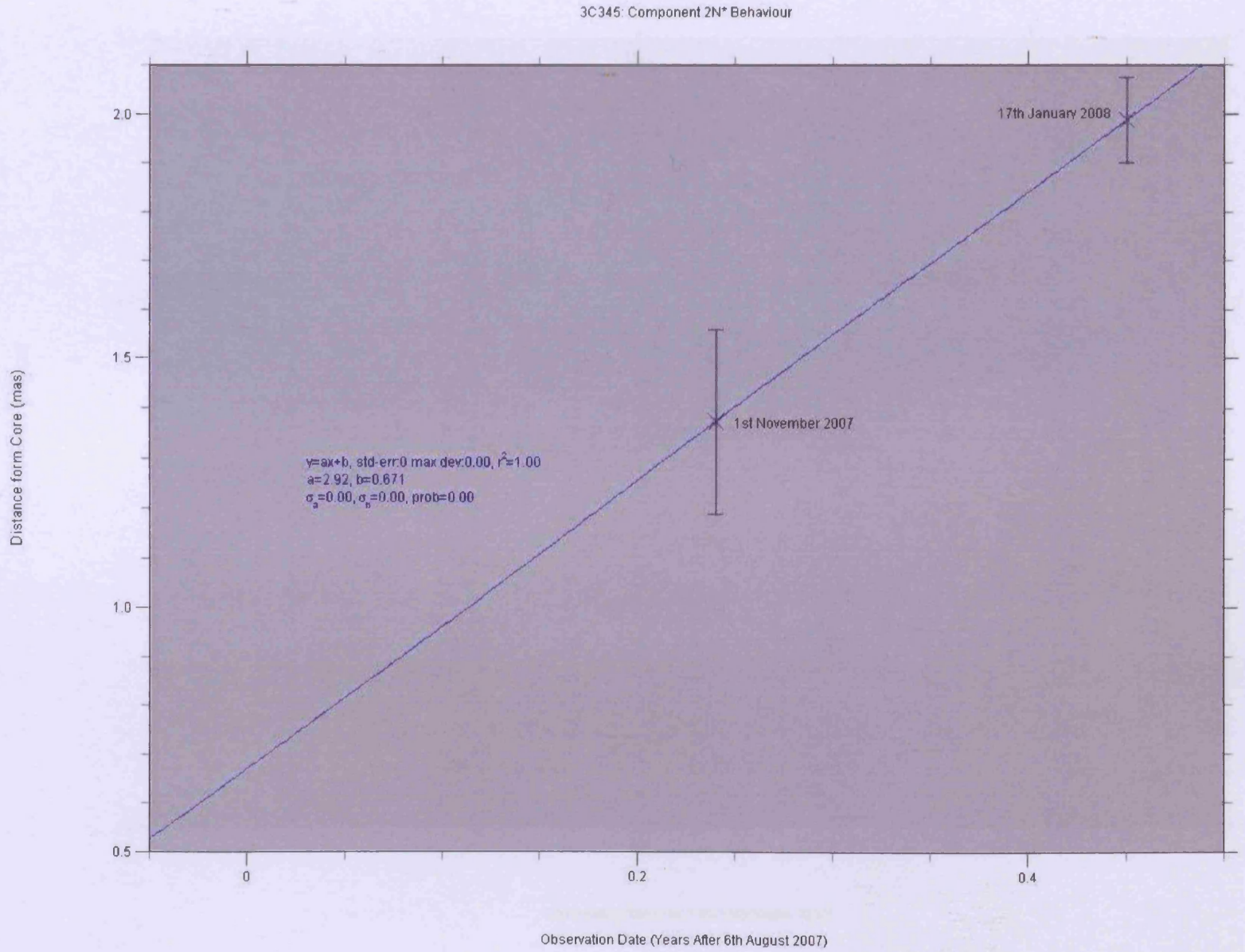
3C345: Component 2N* Behaviour
17th January 2008
1st November 2007
y=ax+b, std-err:0 max dev:0.00, r²=1.00
a=2.92, b=0.671
σa=0.00, σb=0.00, prob=0.00
2.0
1.5
1.0
0.5
0
0.2
0.4
Distance form Core (mas)
Observation Date (Years After 6th August 2007)

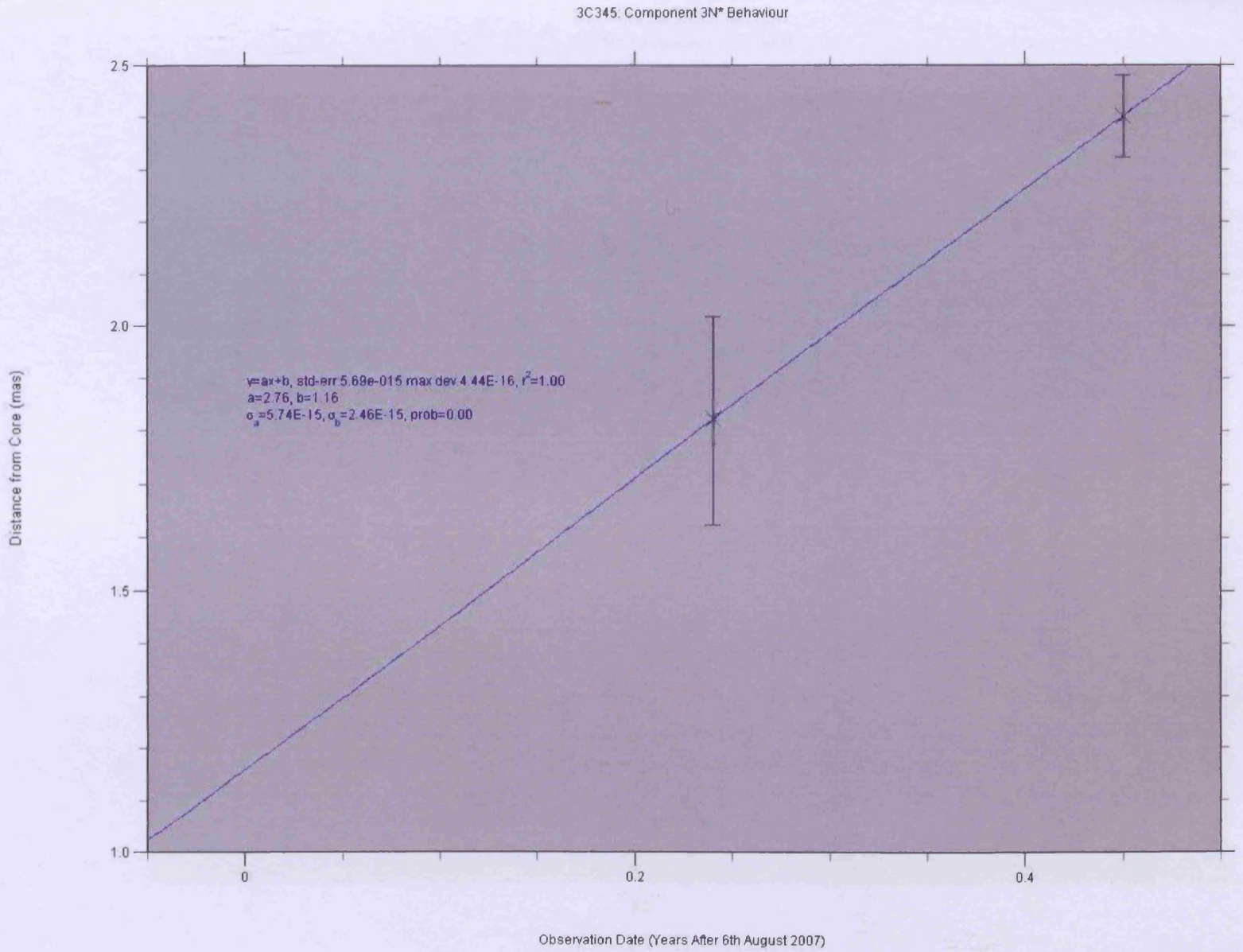
3C345: Component 3N* Behaviour
2.5
2.0
1.5
1.0
0
0.2
0.4
Distance from Core (mas)
Observation Date (Years After 6th August 2007)
y=ax+b, std-err 5.69e-015 max dev 4.44E-16, r²=1.00
a=2.76, b=1.16
σa=5.74E-15, σb=2.46E-15, prob=0.00

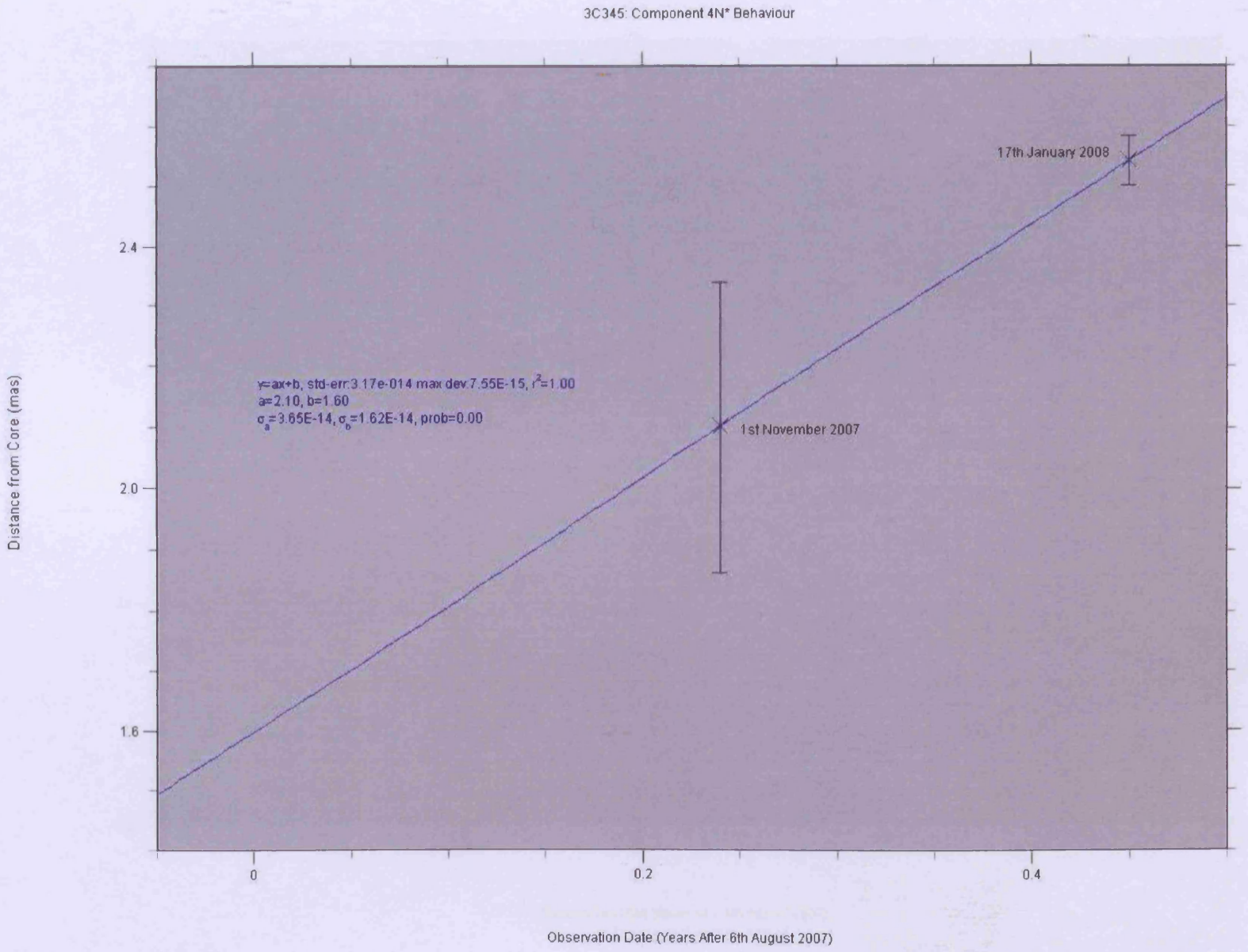
3C345: Component 4N* Behaviour
17th January 2008
1st November 2007
y=ax+b, std-err:3.17e-014 max dev:7.55E-15, r²=1.00
a=2.10, b=1.60
σa=3.65E-14, σb=1.62E-14, prob=0.00
Distance from Core (mas)
2.4
2.0
1.6
0
0.2
0.4
Observation Date (Years After 6th August 2007)

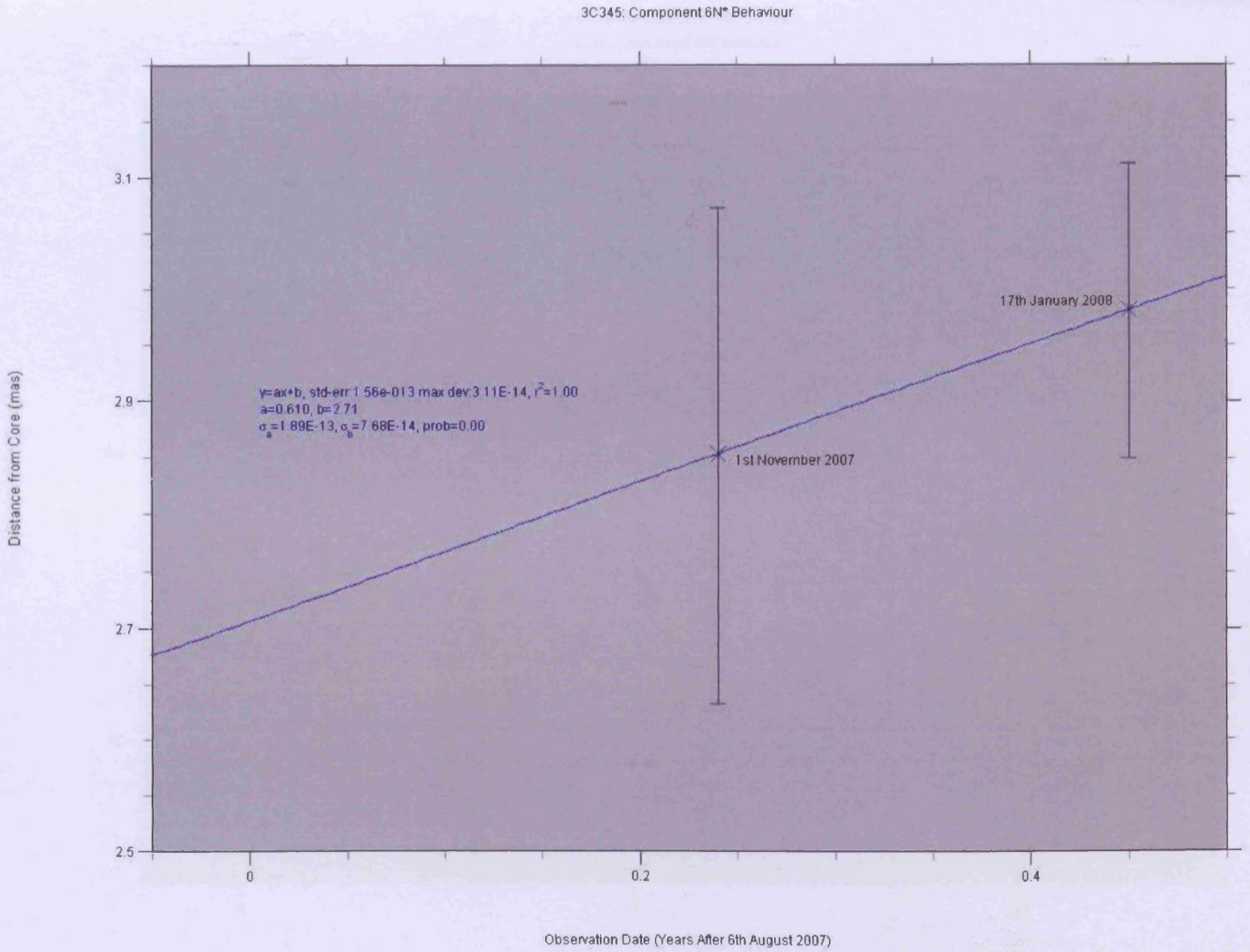
3C345: Component 6N* Behaviour
Distance from Core (mas)
3.1
2.9
2.7
2.5
0
0.2
0.4
Observation Date (Years After 6th August 2007)
y=ax+b, std-err 1.56e-013 max dev 3.11E-14, r²=1.00
a=0.610, b=2.71
σa=1.89E-13, σb=7.68E-14, prob=0.00
1st November 2007
17th January 2008

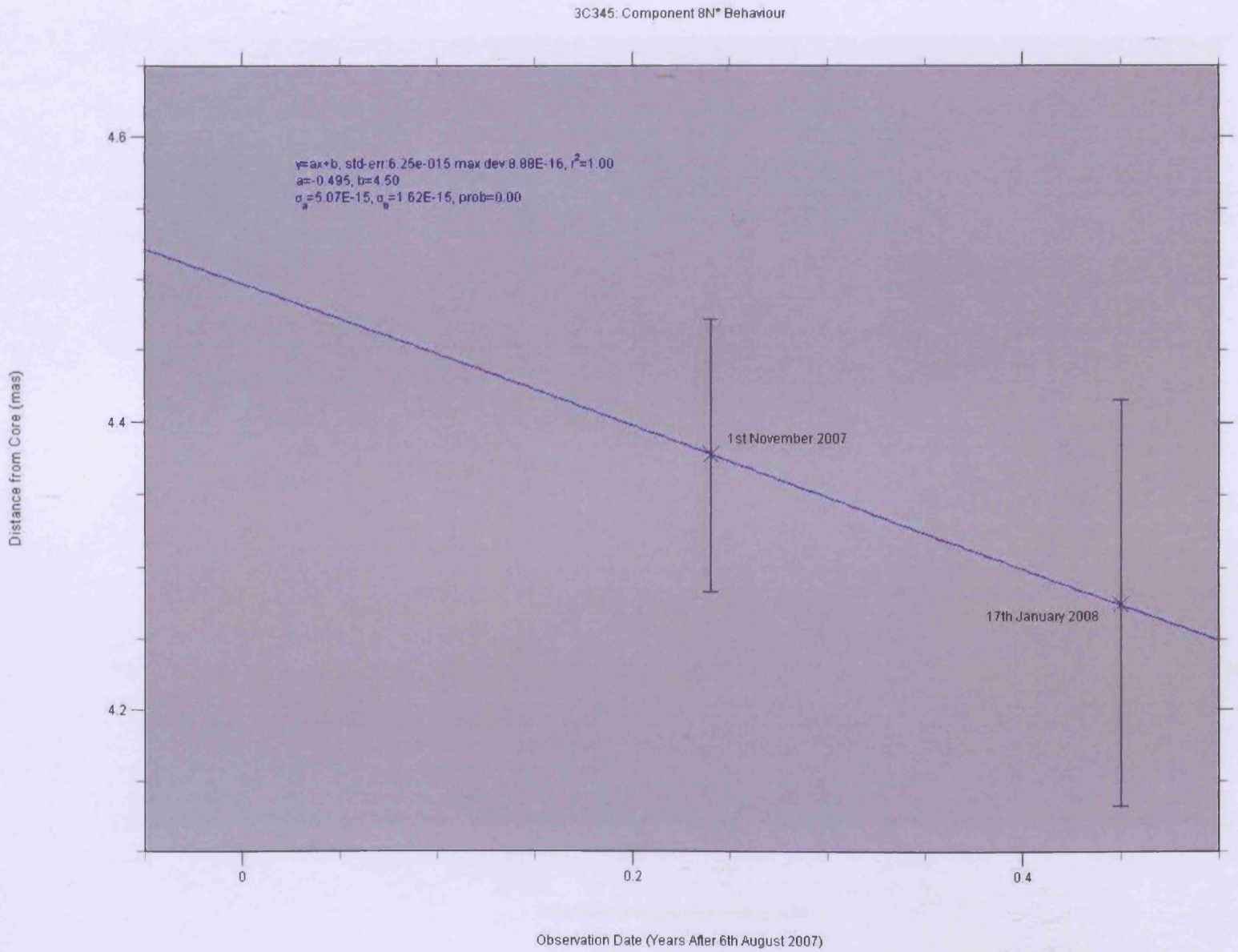
3C345: Component 8N* Behaviour
y=ax+b, std-err:6.25e-015 max dev:8.88E-16, r²=1.00
a=-0.495, b=4.50
σa=5.07E-15, σb=1.62E-15, prob=0.00
1st November 2007
17th January 2008
Distance from Core (mas)
Observation Date (Years After 6th August 2007)
4.6
4.4
4.2
0
0.2
0.4

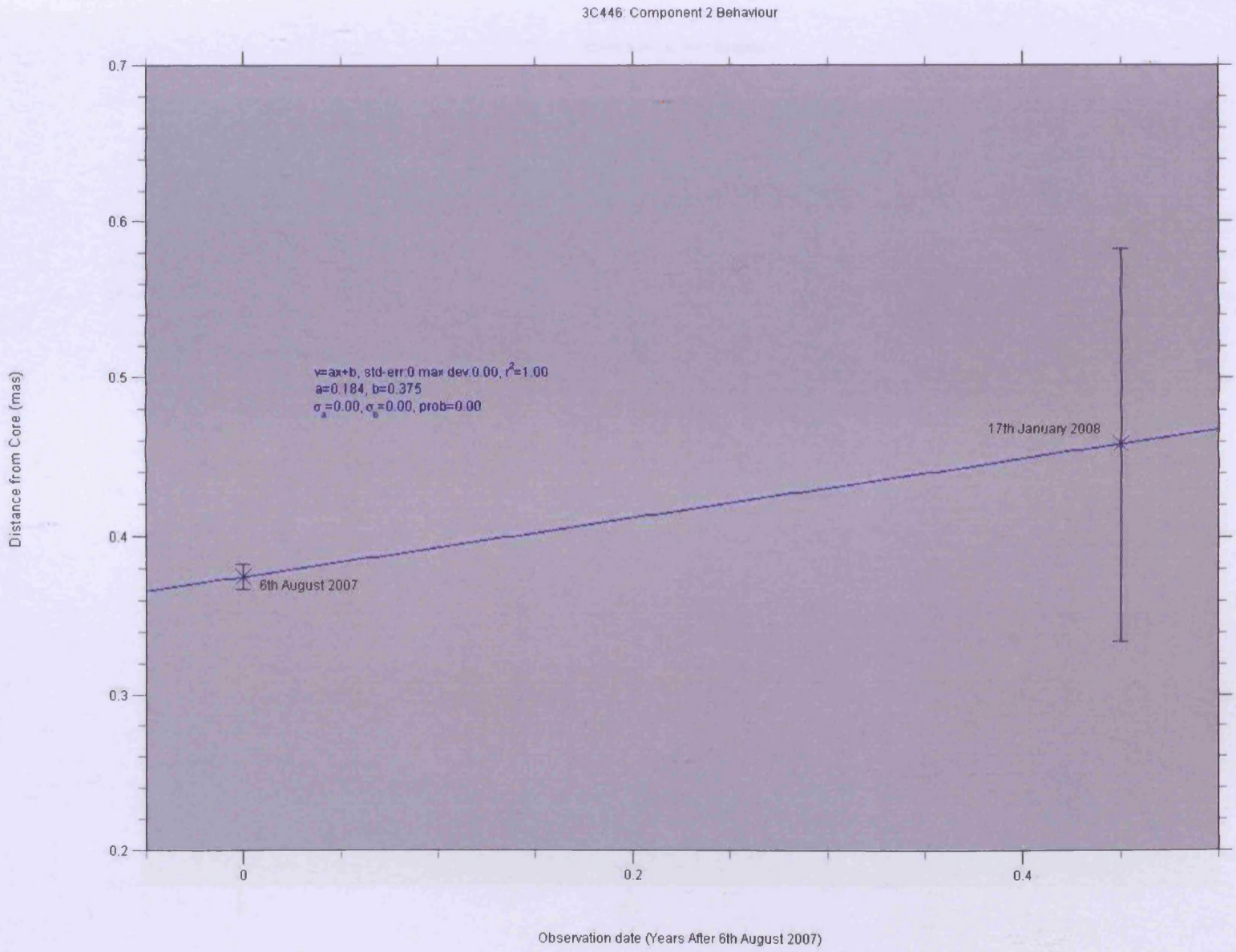
3C446: Component 2 Behaviour
Distance from Core (mas)
Observation date (Years After 6th August 2007)
v=ax+b, std-err:0 max dev:0.00, r²=1.00
a=0.184, b=0.375
σa=0.00, σb=0.00, prob=0.00
6th August 2007
17th January 2008
0.7
0.6
0.5
0.4
0.3
0.2
0
0.2
0.4

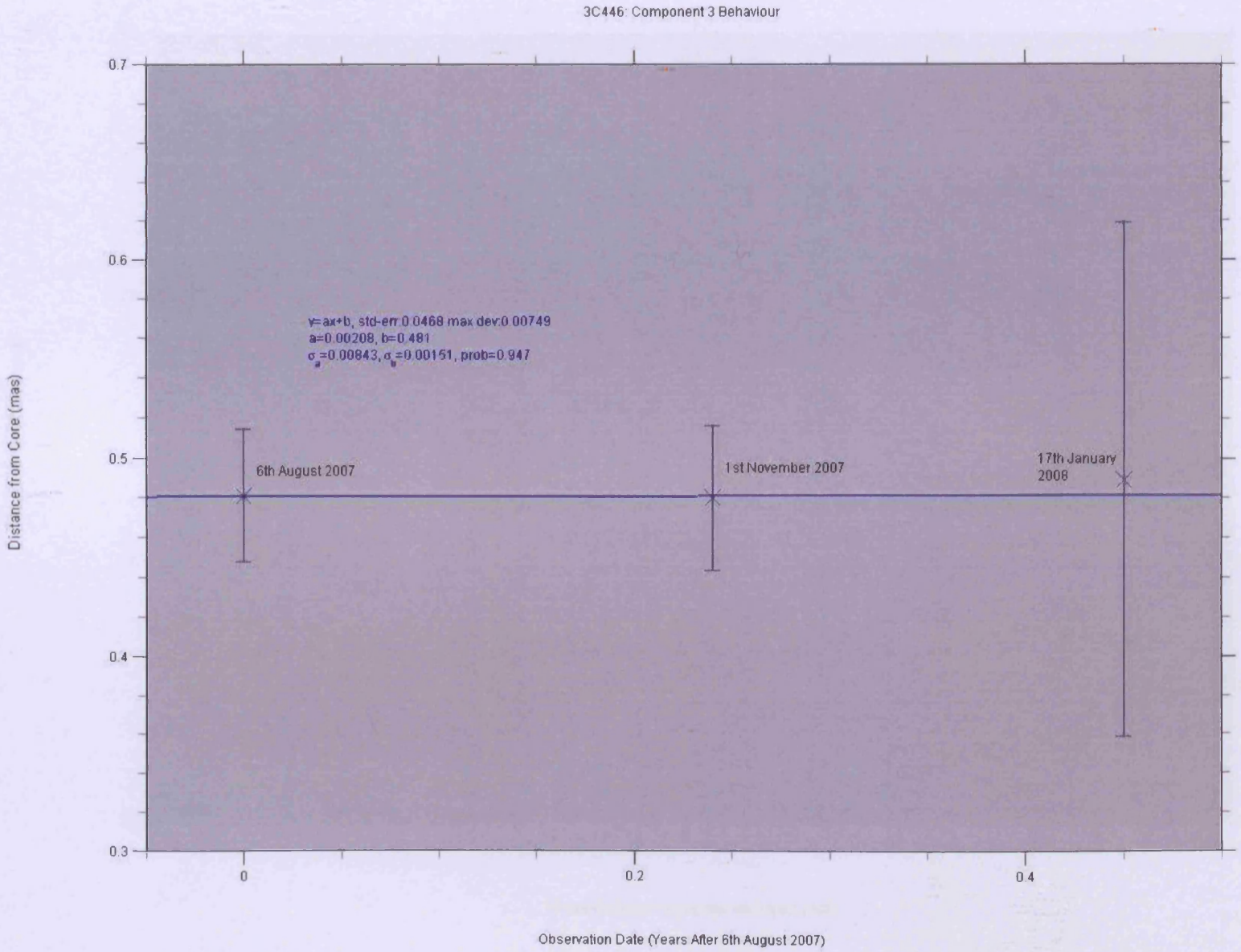
3C446: Component 3 Behaviour
0.7
0.6
0.5
0.4
0.3
Distance from Core (mas)
v=ax+b, std-err:0.0468 max dev:0.00749
a=0.00208, b=0.481
σa=0.00843, σb=0.00151, prob=0.947
6th August 2007
1st November 2007
17th January 2008
0
0.2
0.4
Observation Date (Years After 6th August 2007)

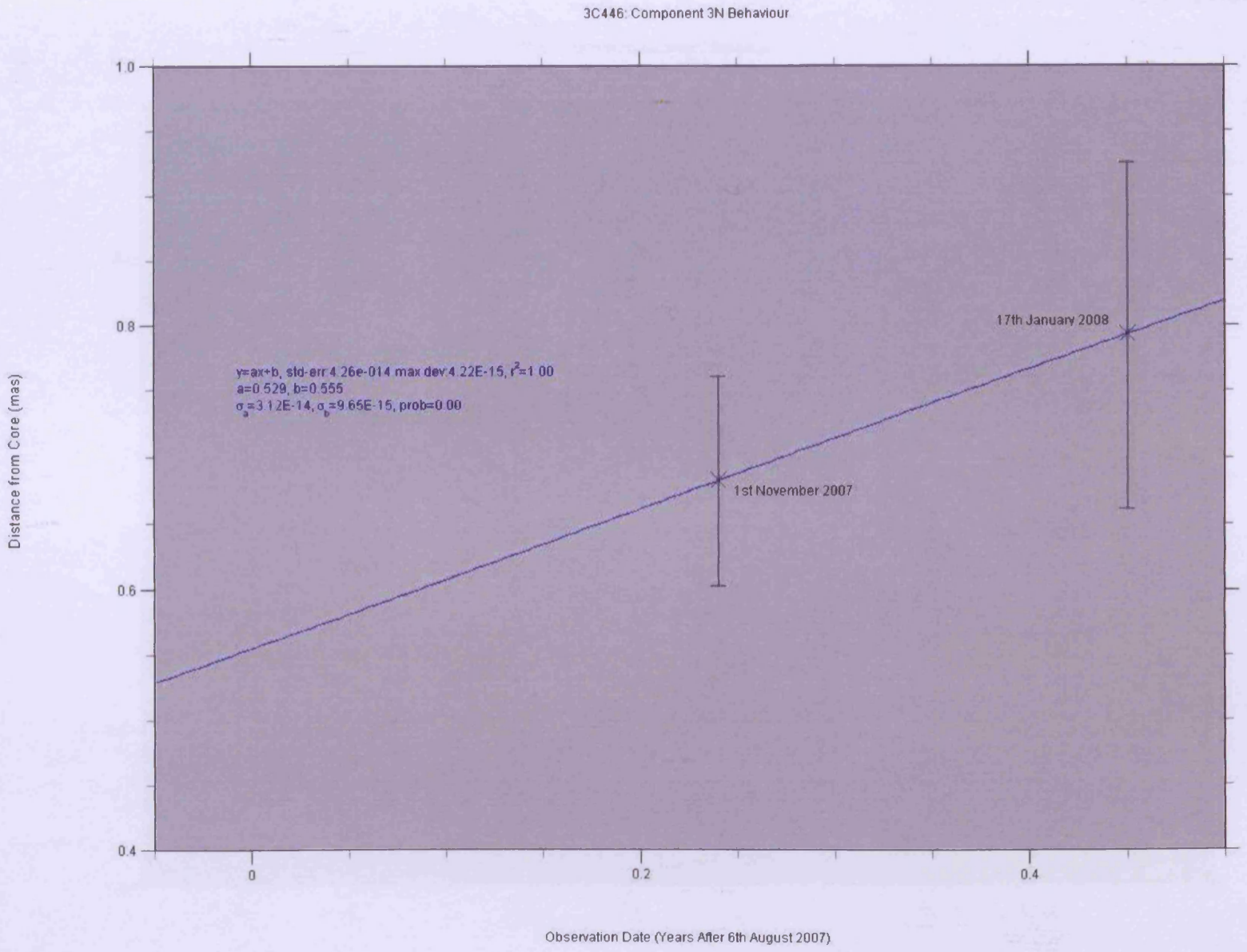
3C446: Component 3N Behaviour
1.0
0.8
0.6
0.4
0
0.2
0.4
Distance from Core (mas)
Observation Date (Years After 6th August 2007)
y=ax+b, std-err 4.26e-014 max dev 4.22E-15, r²=1.00
a=0.529, b=0.555
σa=3.12E-14, σb=9.65E-15, prob=0.00
17th January 2008
1st November 2007

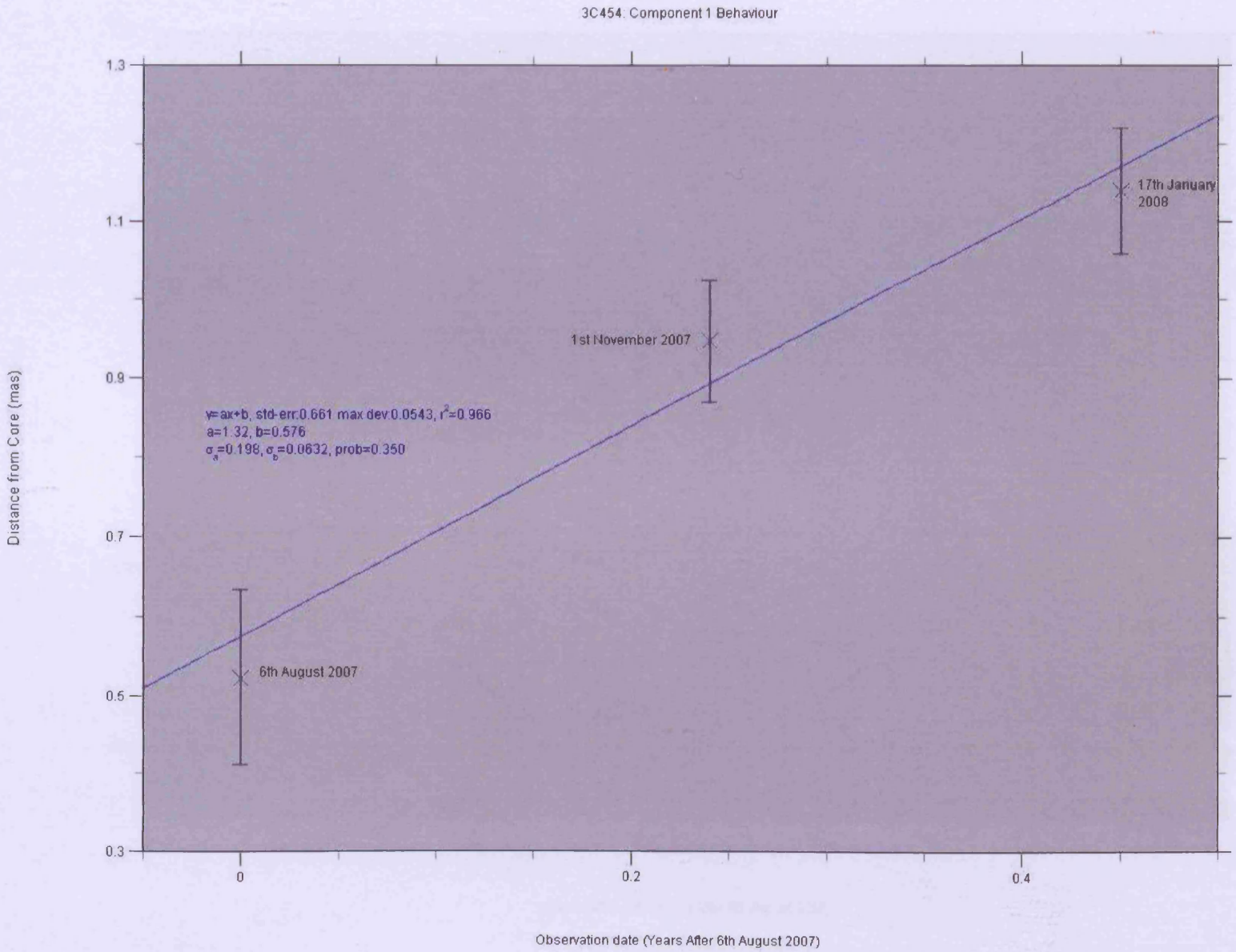
3C454: Component 1 Behaviour
Distance from Core (mas)
Observation date (Years After 6th August 2007)
1.3
1.1
0.9
0.7
0.5
0.3
0
0.2
0.4
y=ax+b, std-err:0.661 max dev:0.0543, r²=0.966
a=1.32, b=0.576
σa=0.198, σb=0.0632, prob=0.350
6th August 2007
1st November 2007
17th January 2008

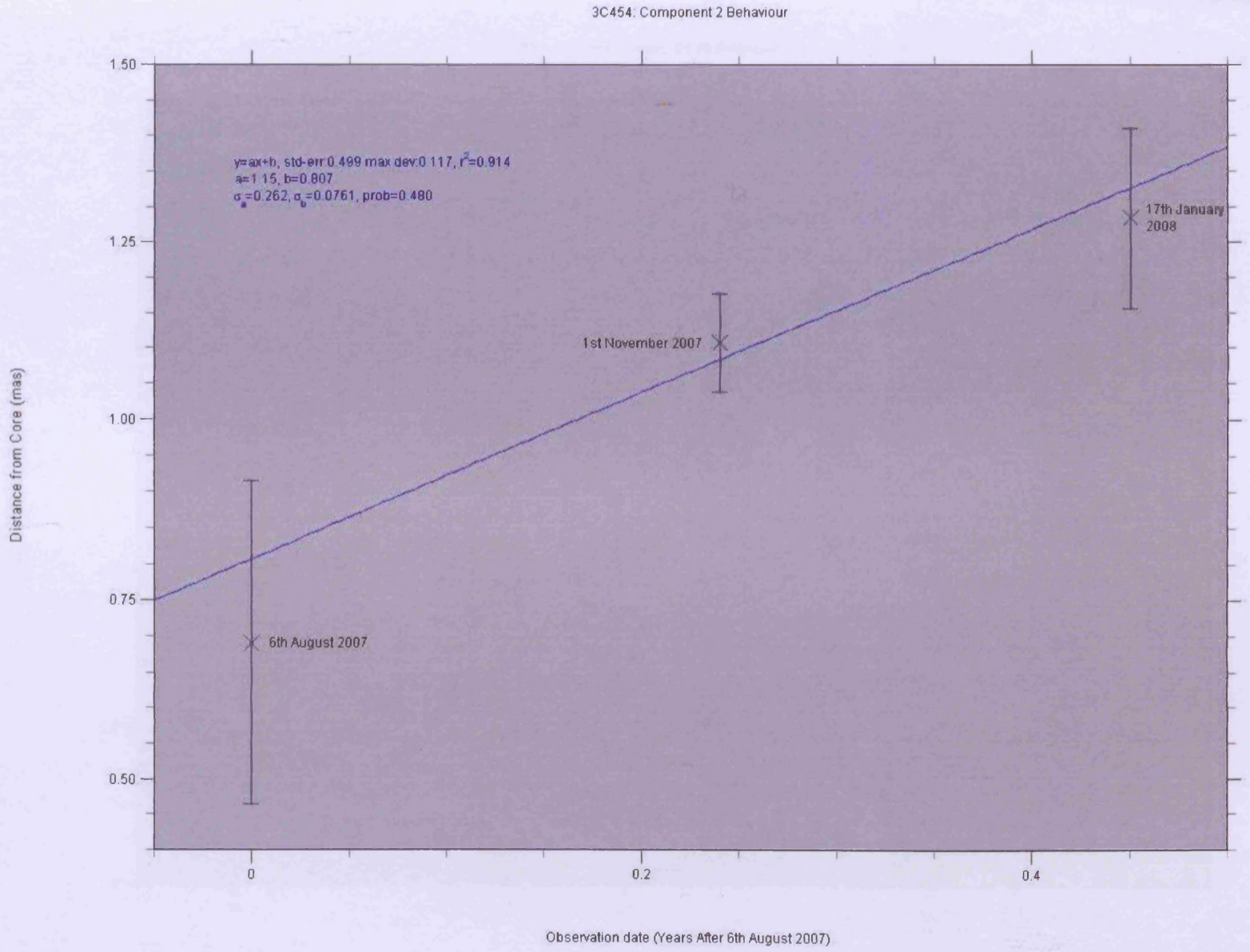
3C454: Component 2 Behaviour
y=ax+b, std-err 0.499 max dev:0.117, r²=0.914
a=1.15, b=0.807
σa=0.262, σb=0.0761, prob=0.480
1st November 2007
17th January 2008
6th August 2007
Distance from Core (mas)
1.50
1.25
1.00
0.75
0.50
0
0.2
0.4
Observation date (Years After 6th August 2007)

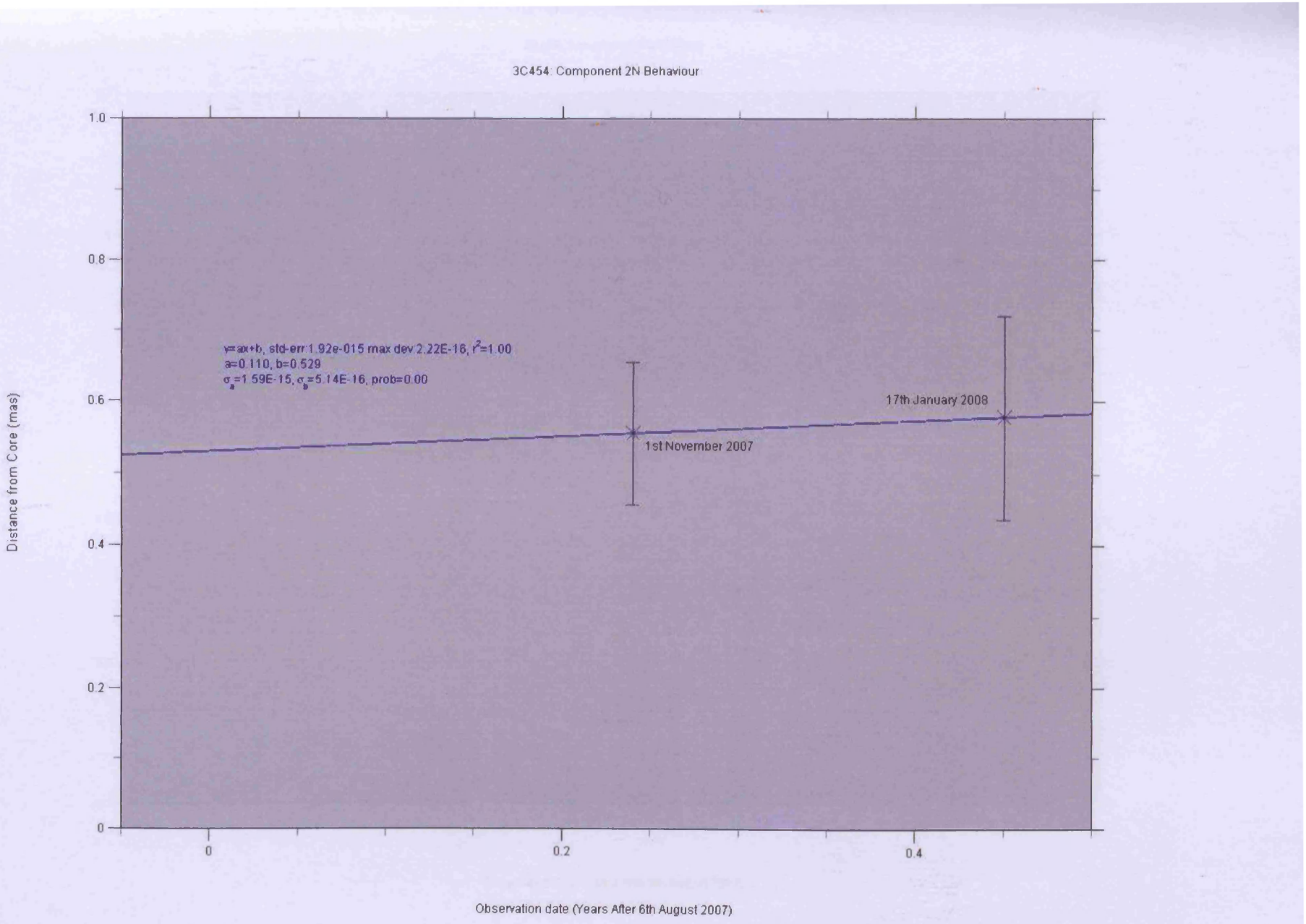
3C454: Component 2N Behaviour
y=ax+b, std-err:1.92e-015 max dev 2.22E-16, r²=1.00
a=0.110, b=0.529
σa=1.59E-15, σb=5.14E-16, prob=0.00
17th January 2008
1st November 2007
Distance from Core (mas)
Observation date (Years After 6th August 2007)
1.0
0.8
0.6
0.4
0.2
0
0
0.2
0.4

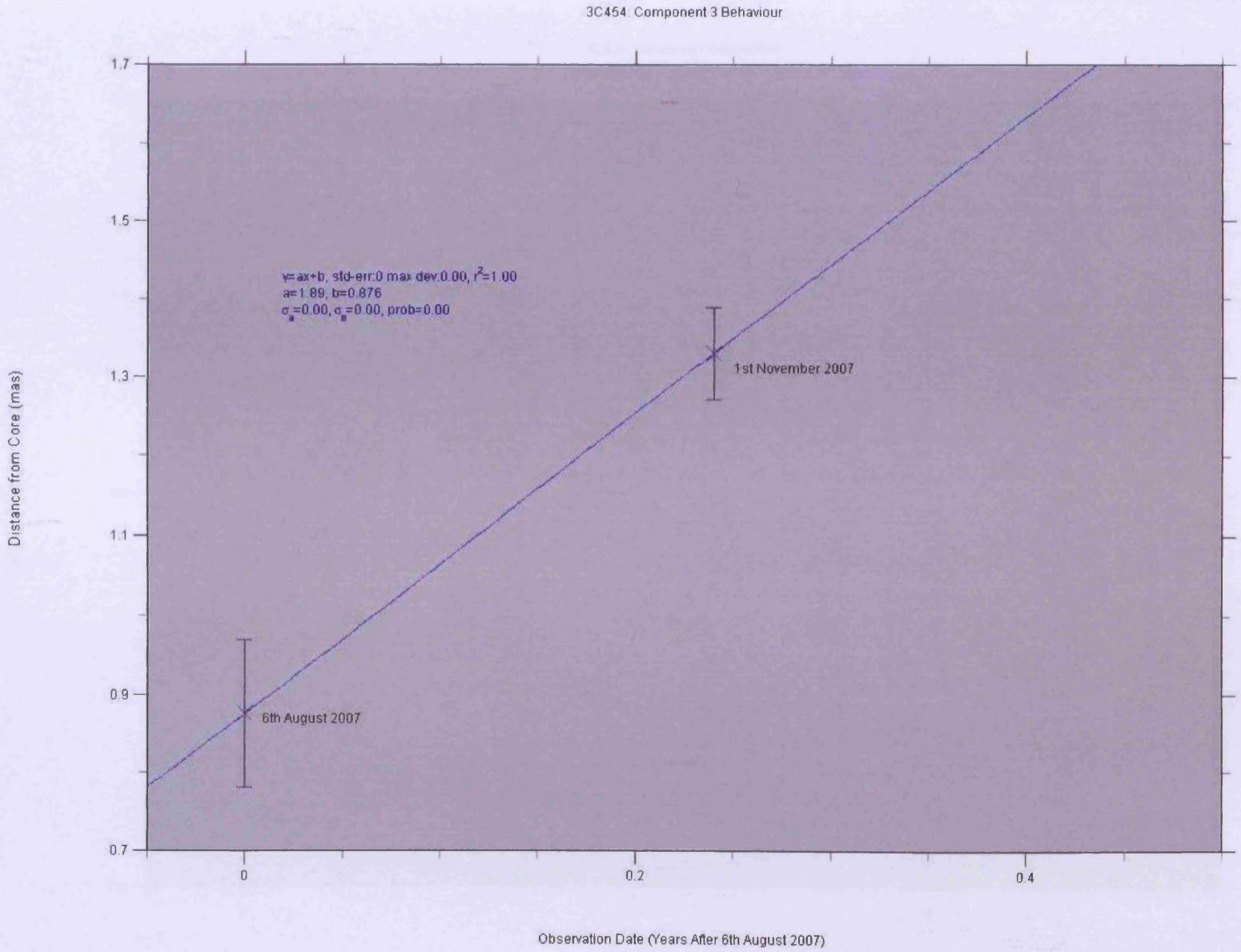
3C454: Component 3 Behaviour
y=ax+b, std-err:0 max dev:0.00, r²=1.00
a=1.89, b=0.876
σa=0.00, σb=0.00, prob=0.00
1st November 2007
6th August 2007
Distance from Core (mas)
Observation Date (Years After 6th August 2007)
1.7
1.5
1.3
1.1
0.9
0.7
0
0.2
0.4

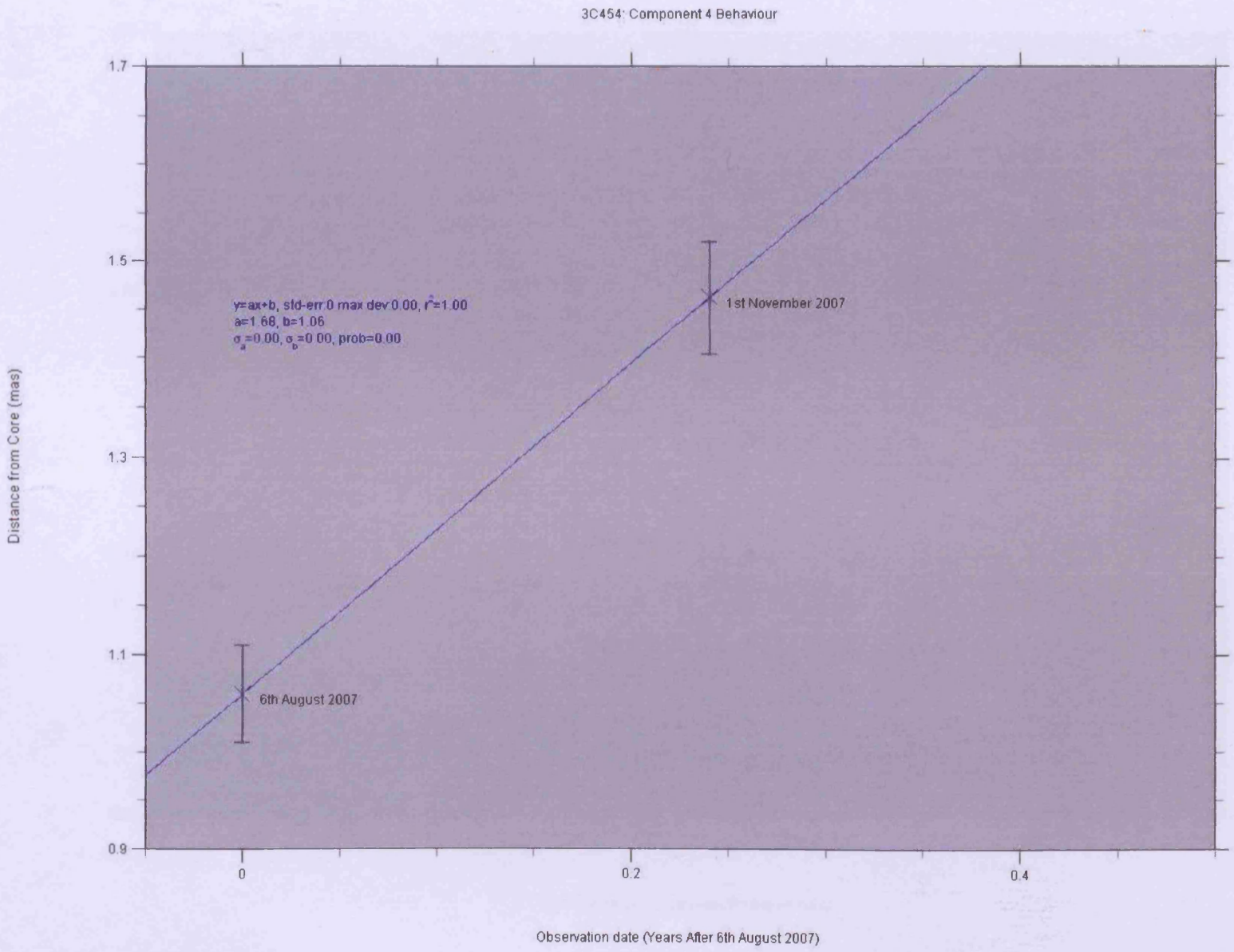
3C454: Component 4 Behaviour
1.7
1.5
1.3
1.1
0.9
0
0.2
0.4
y=ax+b, std-err 0 max dev 0.00, r²=1.00
a=1.68, b=1.06
σa=0.00, σb=0.00, prob=0.00
1st November 2007
6th August 2007
Distance from Core (mas)
Observation date (Years After 6th August 2007)

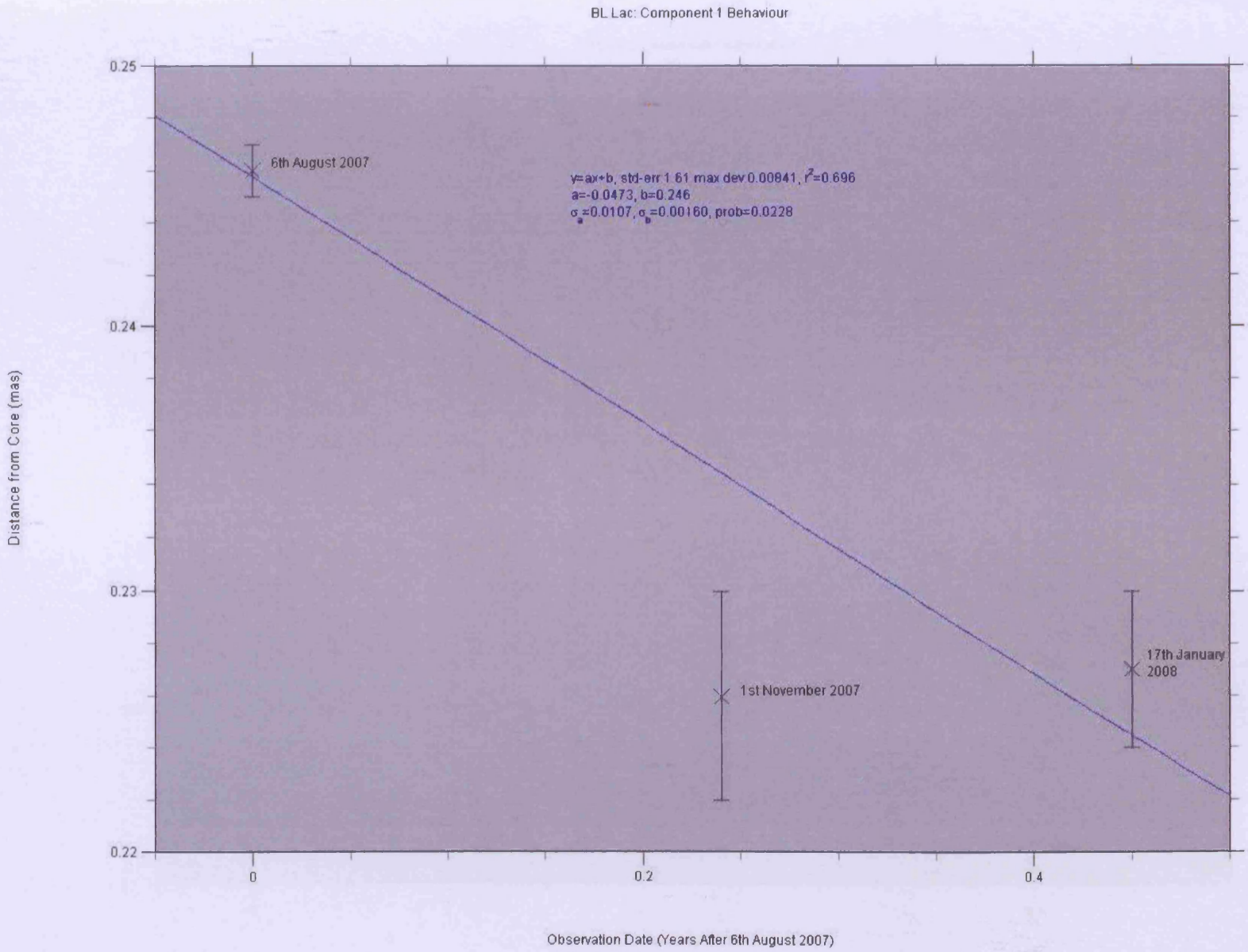
BL Lac: Component 1 Behaviour
0.25
0.24
0.23
0.22
0
0.2
0.4
Distance from Core (mas)
Observation Date (Years After 6th August 2007)
6th August 2007
y=ax+b, std-err 1.61 max dev 0.00841, r²=0.696
a=-0.0473, b=0.246
σa=0.0107, σb=0.00160, prob=0.0228
1st November 2007
17th January 2008

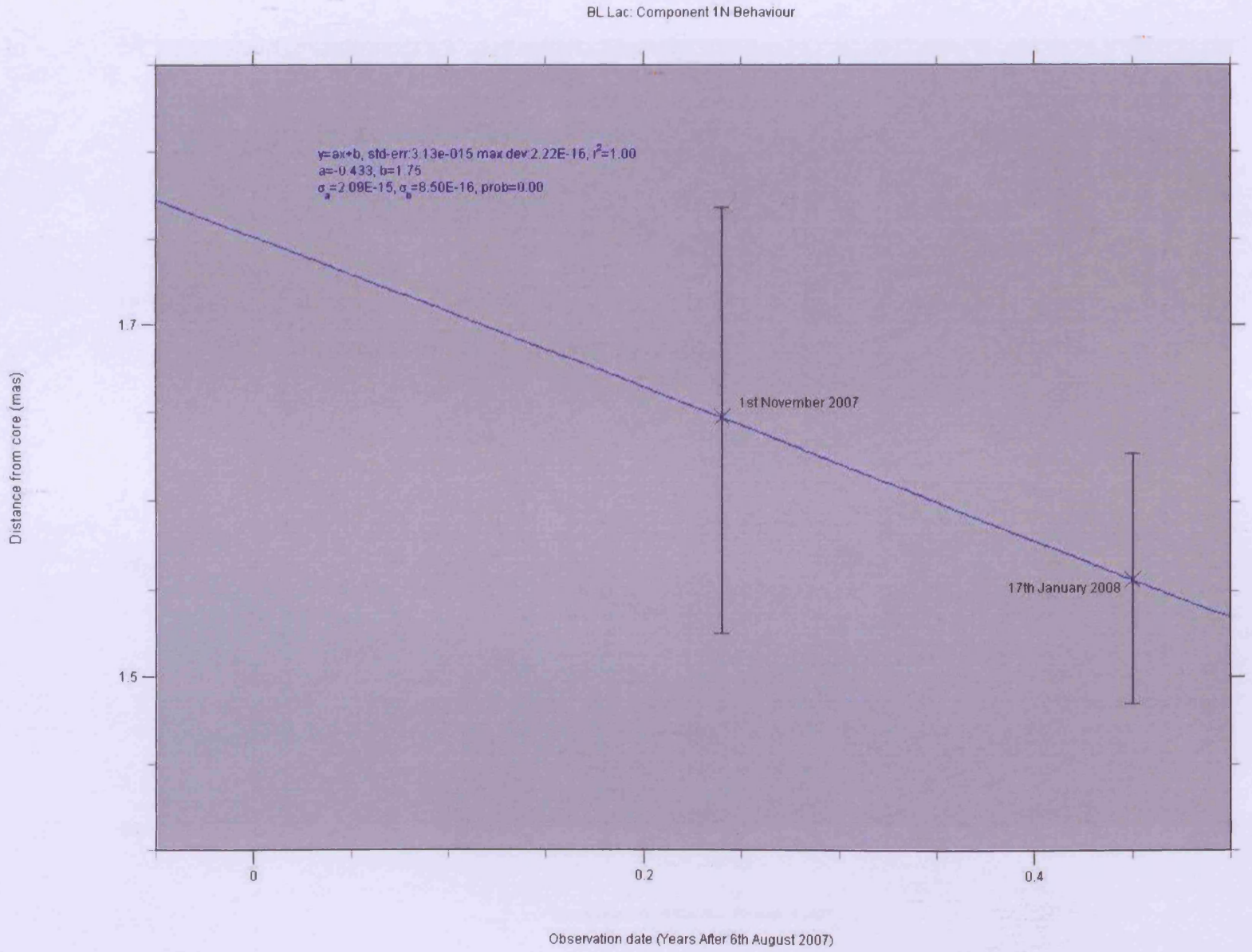
BL Lac: Component 1N Behaviour
y=ax+b, std-err:3.13e-015 max dev:2.22E-16, r²=1.00
a=-0.433, b=1.75
σa=2.09E-15, σb=8.50E-16, prob=0.00
1st November 2007
17th January 2008
1.7
1.5
0
0.2
0.4
Distance from core (mas)
Observation date (Years After 6th August 2007)

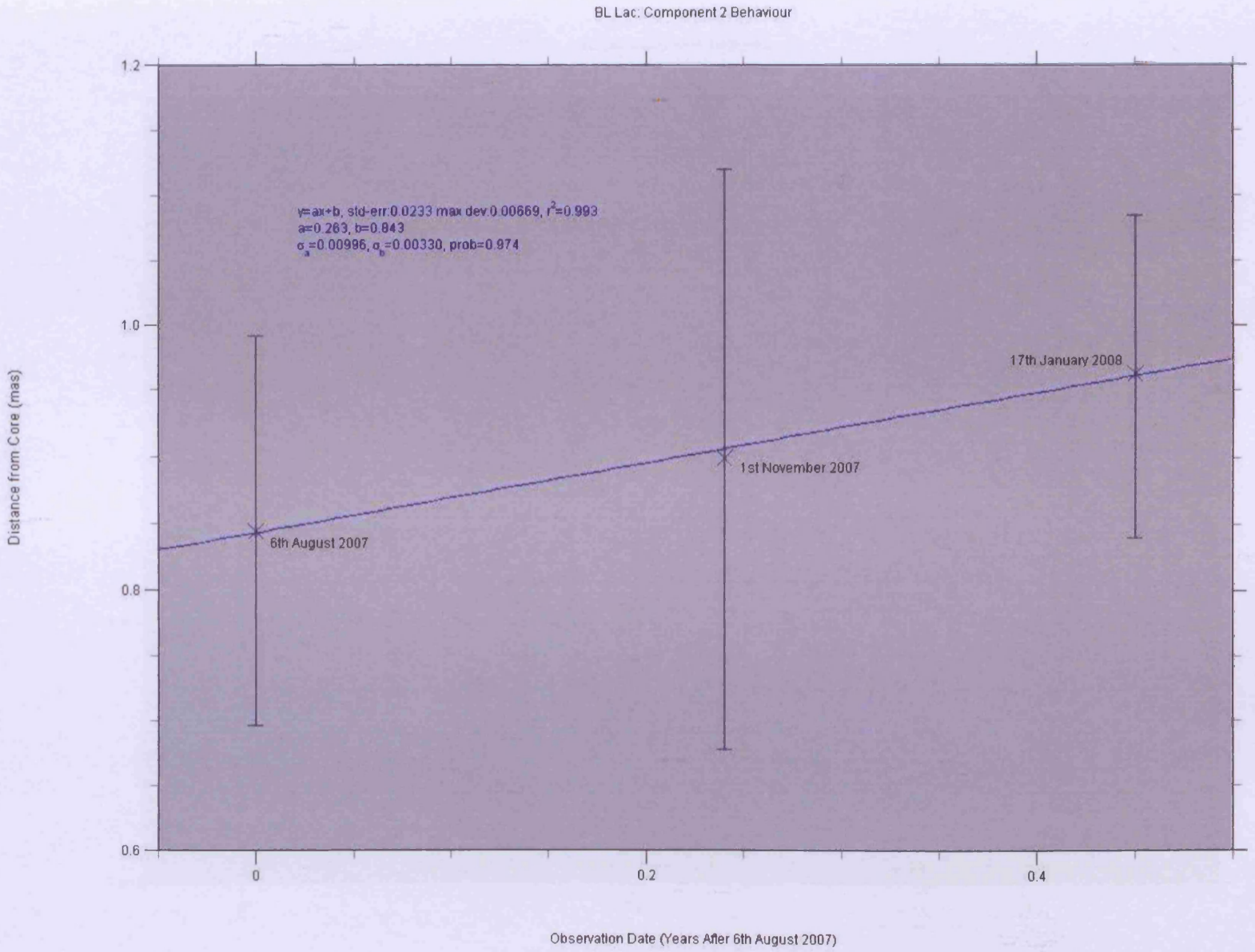
BL Lac: Component 2 Behaviour
y=ax+b, std-err:0.0233 max dev:0.00669, r²=0.993
a=0.263, b=0.843
σa=0.00996, σb=0.00330, prob=0.974
17th January 2008
1st November 2007
6th August 2007
Distance from Core (mas)
Observation Date (Years After 6th August 2007)
1.2
1.0
0.8
0.6
0
0.2
0.4

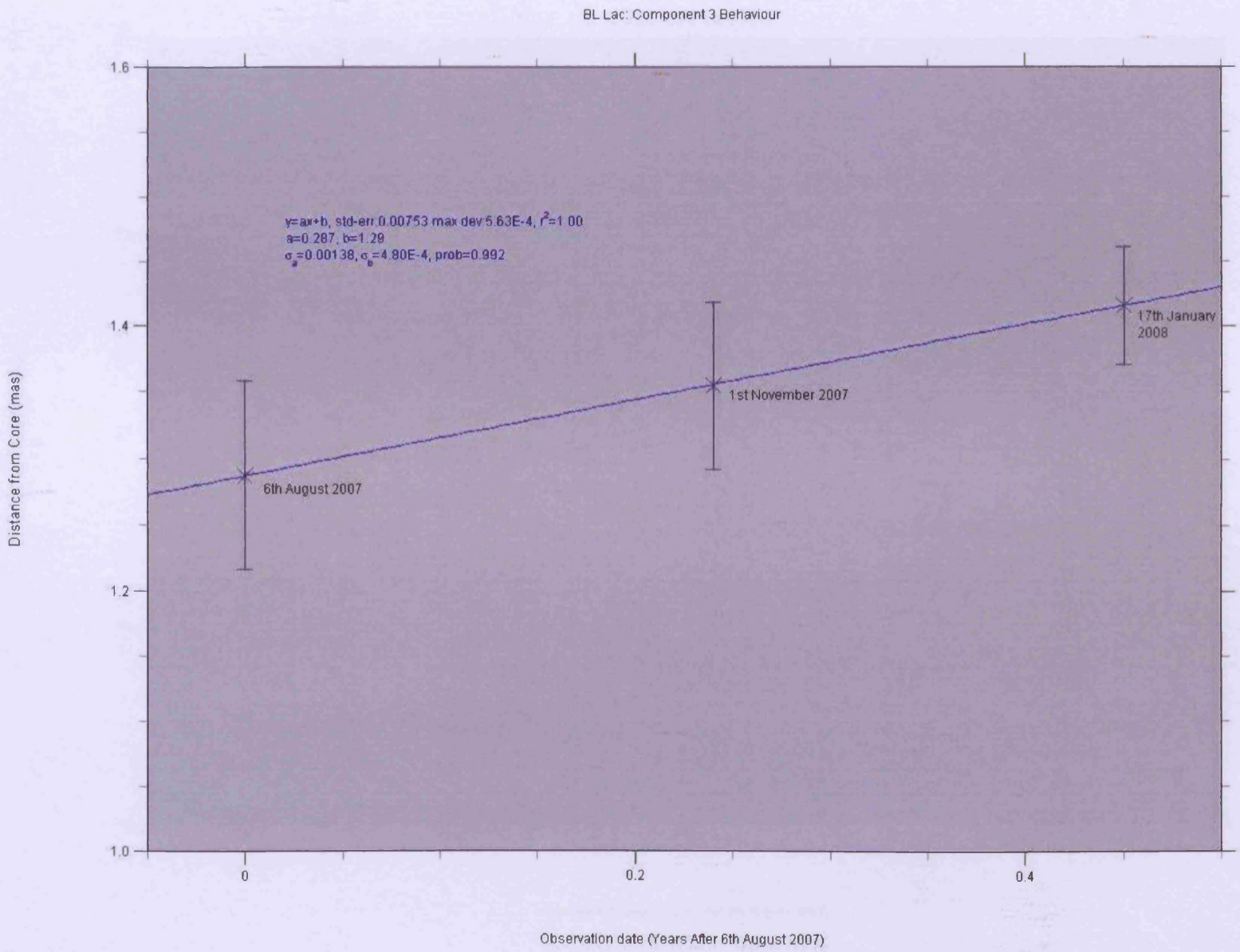
BL Lac: Component 3 Behaviour
y=ax+b, std-err 0.00753 max dev 5.63E-4, r²=1.00
a=0.287, b=1.29
σa=0.00138, σb=4.80E-4, prob=0.992
6th August 2007
1st November 2007
17th January 2008
Distance from Core (mas)
Observation date (Years After 6th August 2007)
1.6
1.4
1.2
1.0
0
0.2
0.4

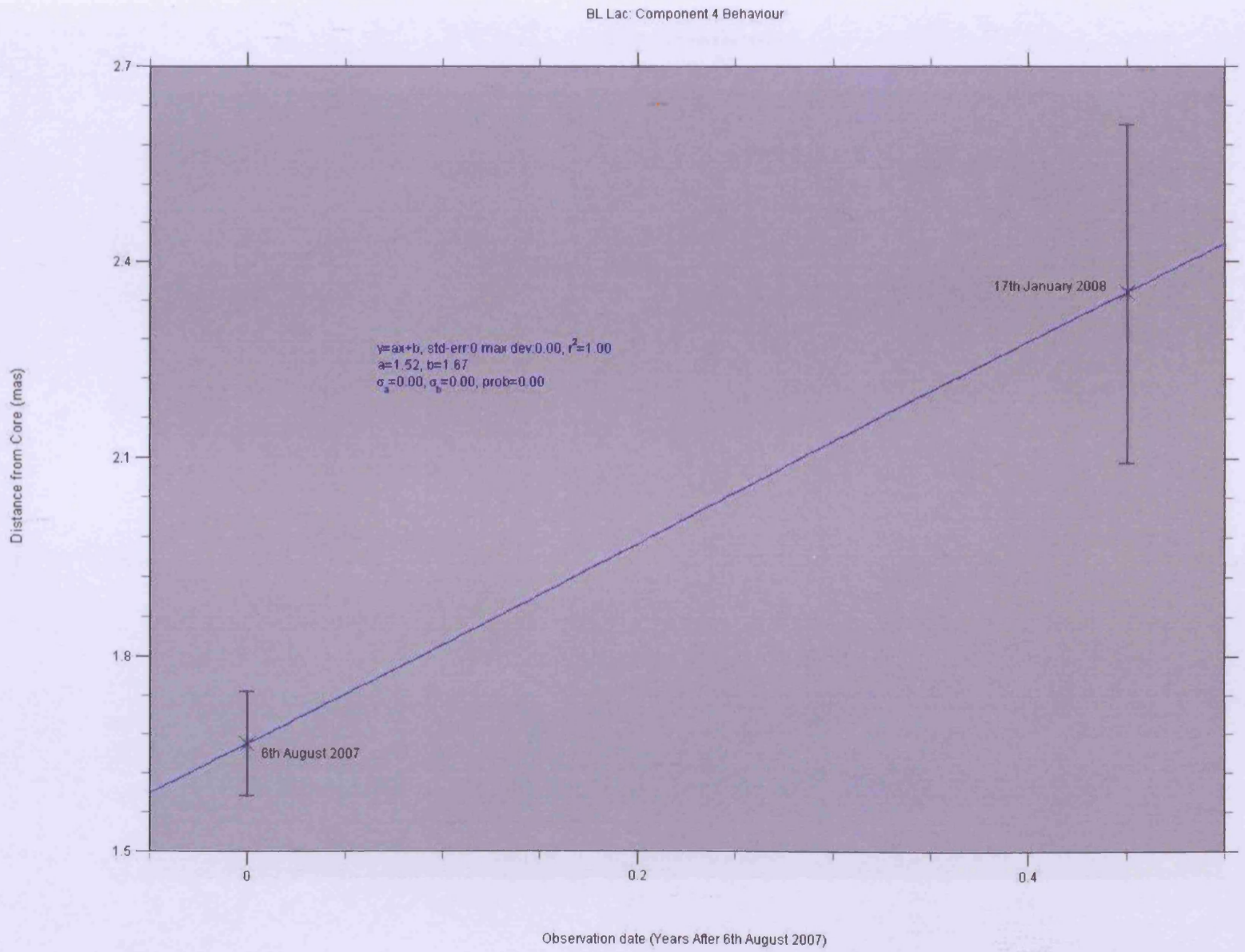
BL Lac: Component 4 Behaviour
Distance from Core (mas)
2.7
2.4
2.1
1.8
1.5
0
0.2
0.4
Observation date (Years After 6th August 2007)
y=ax+b, std-err:0 max dev:0.00, r²=1.00
a=1.52, b=1.67
σa=0.00, σb=0.00, prob=0.00
17th January 2008
6th August 2007

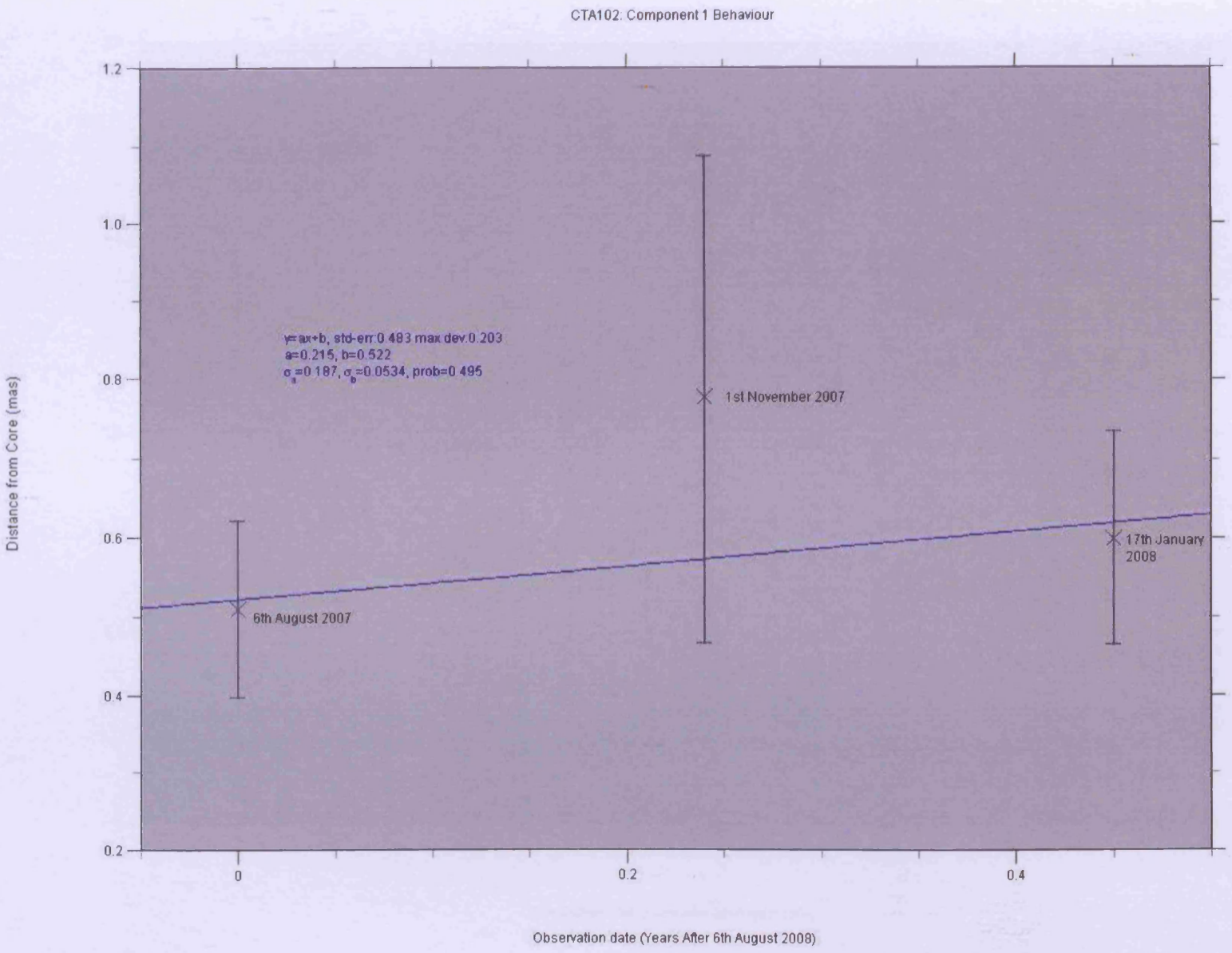
CTA102: Component 1 Behaviour
Distance from Core (mas)
1.2
1.0
0.8
0.6
0.4
0.2
y=ax+b, std-err:0.483 max dev:0.203
a=0.215, b=0.522
σa=0.187, σb=0.0534, prob=0.495
1st November 2007
6th August 2007
17th January 2008
0
0.2
0.4
Observation date (Years After 6th August 2008)

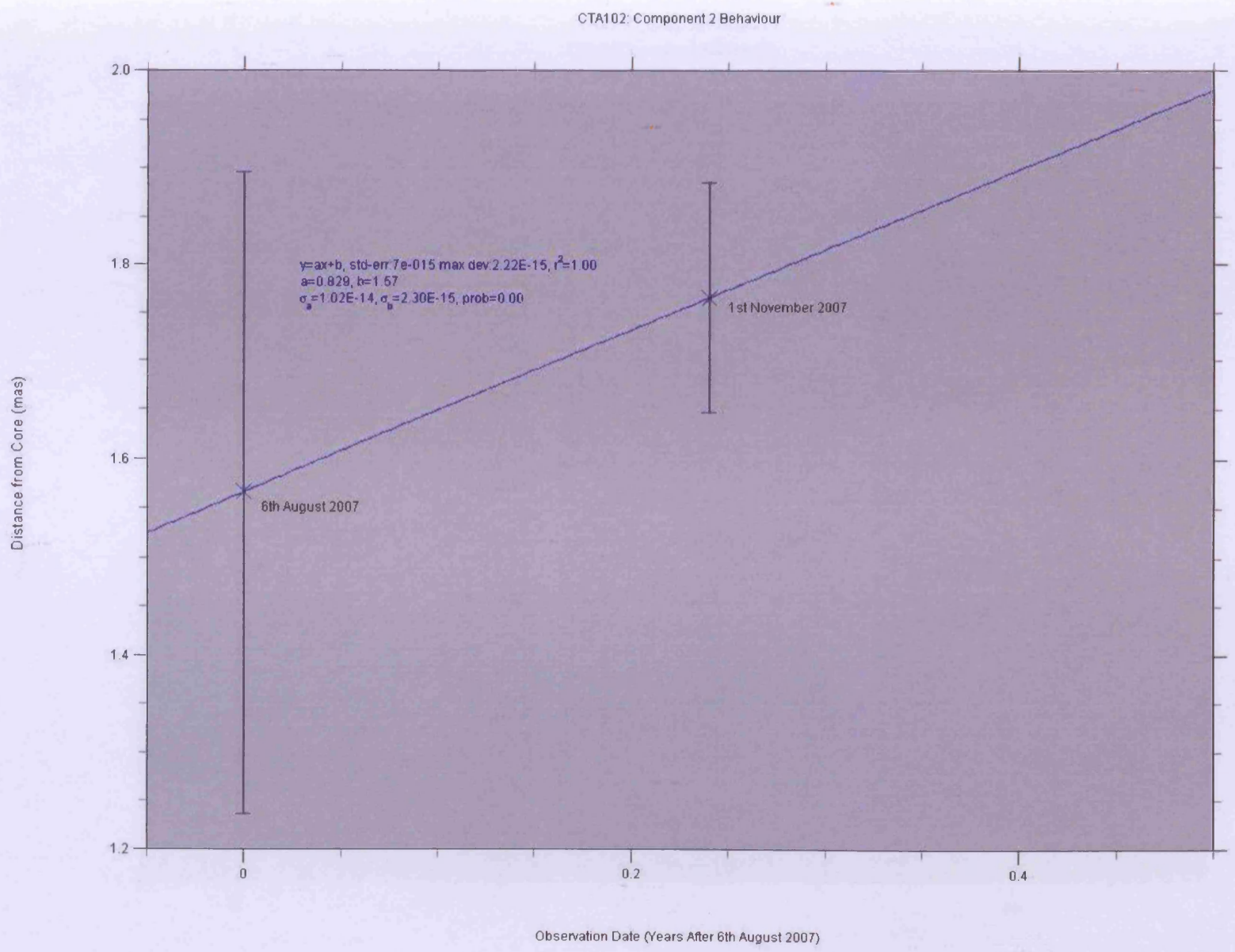
CTA102: Component 2 Behaviour
y=ax+b, std-err:7e-015 max dev:2.22E-15, r²=1.00
a=0.829, b=1.57
σa=1.02E-14, σb=2.30E-15, prob=0.00
6th August 2007
1st November 2007
Distance from Core (mas)
Observation Date (Years After 6th August 2007)
2.0
1.8
1.6
1.4
1.2
0
0.2
0.4

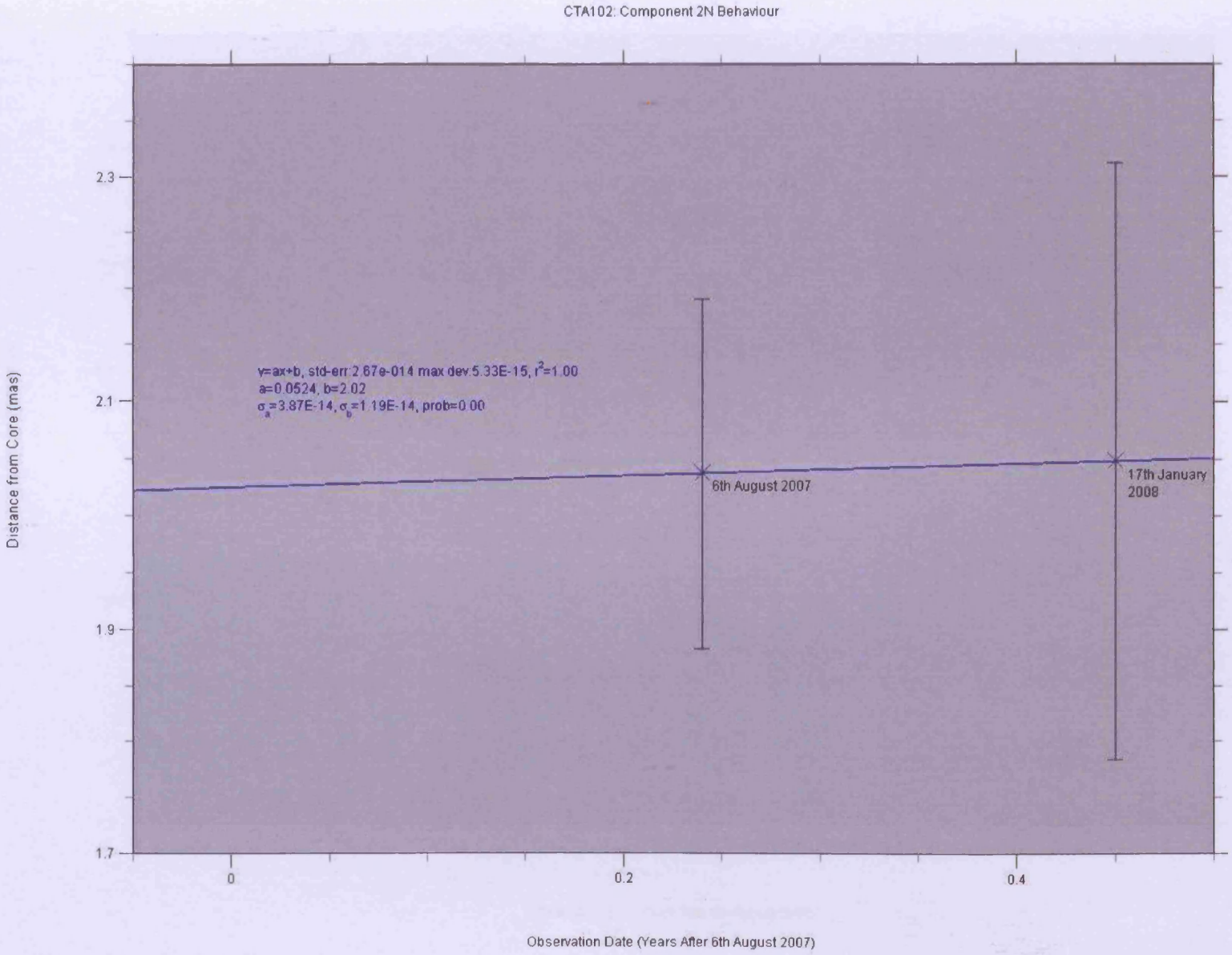
CTA102: Component 2N Behaviour
Distance from Core (mas)
2.3
2.1
1.9
1.7
0
0.2
0.4
Observation Date (Years After 6th August 2007)
y=ax+b, std-err:2.67e-014 max dev:5.33E-15, r²=1.00
a=0.0524, b=2.02
σa=3.87E-14, σb=1.19E-14, prob=0.00
6th August 2007
17th January 2008

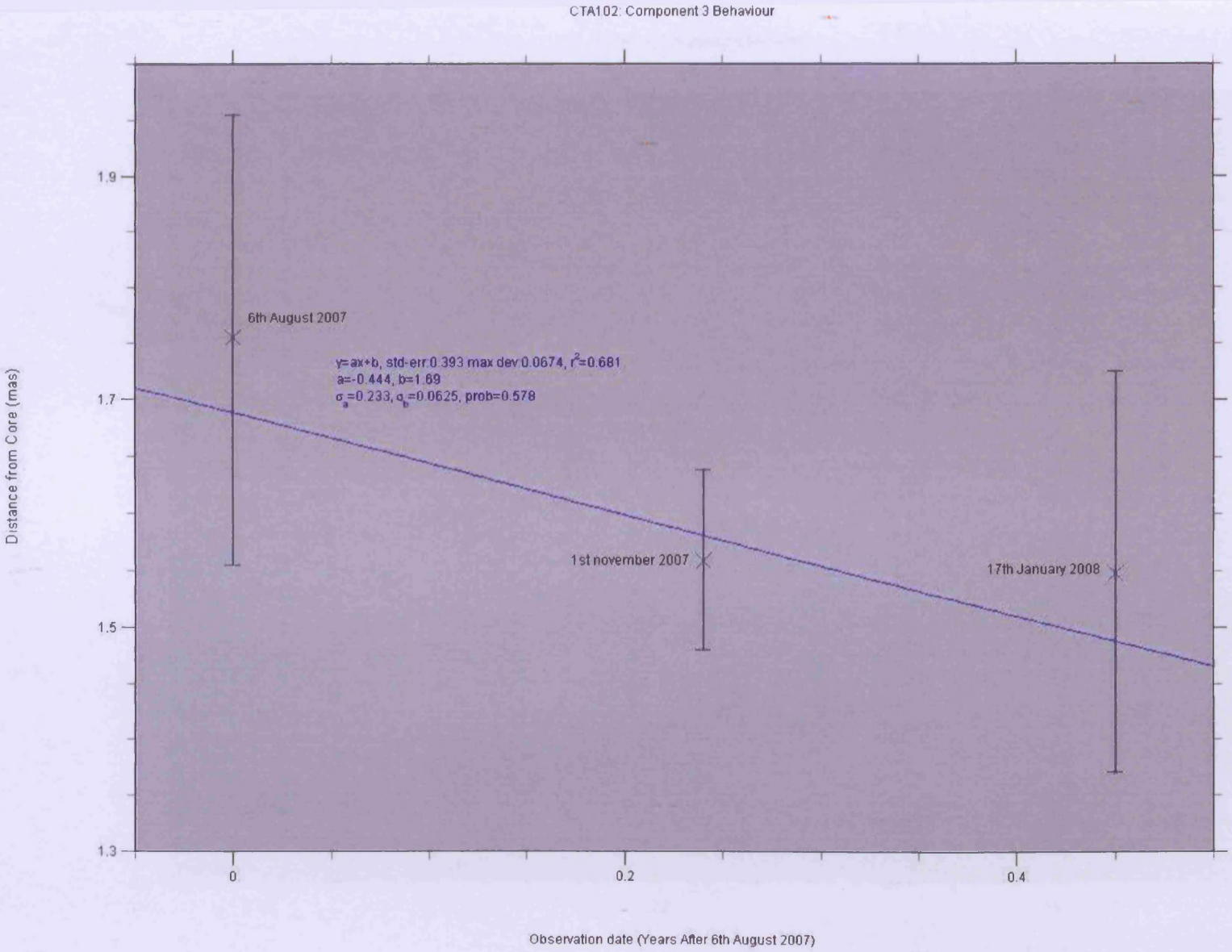
CTA102: Component 3 Behaviour
1.9
1.7
1.5
1.3
Distance from Core (mas)
6th August 2007
y=ax+b, std-err 0.393 max dev 0.0674, r²=0.681
a=-0.444, b=1.69
σa=0.233, σb=0.0625, prob=0.578
1st november 2007
17th January 2008
0
0.2
0.4
Observation date (Years After 6th August 2007)

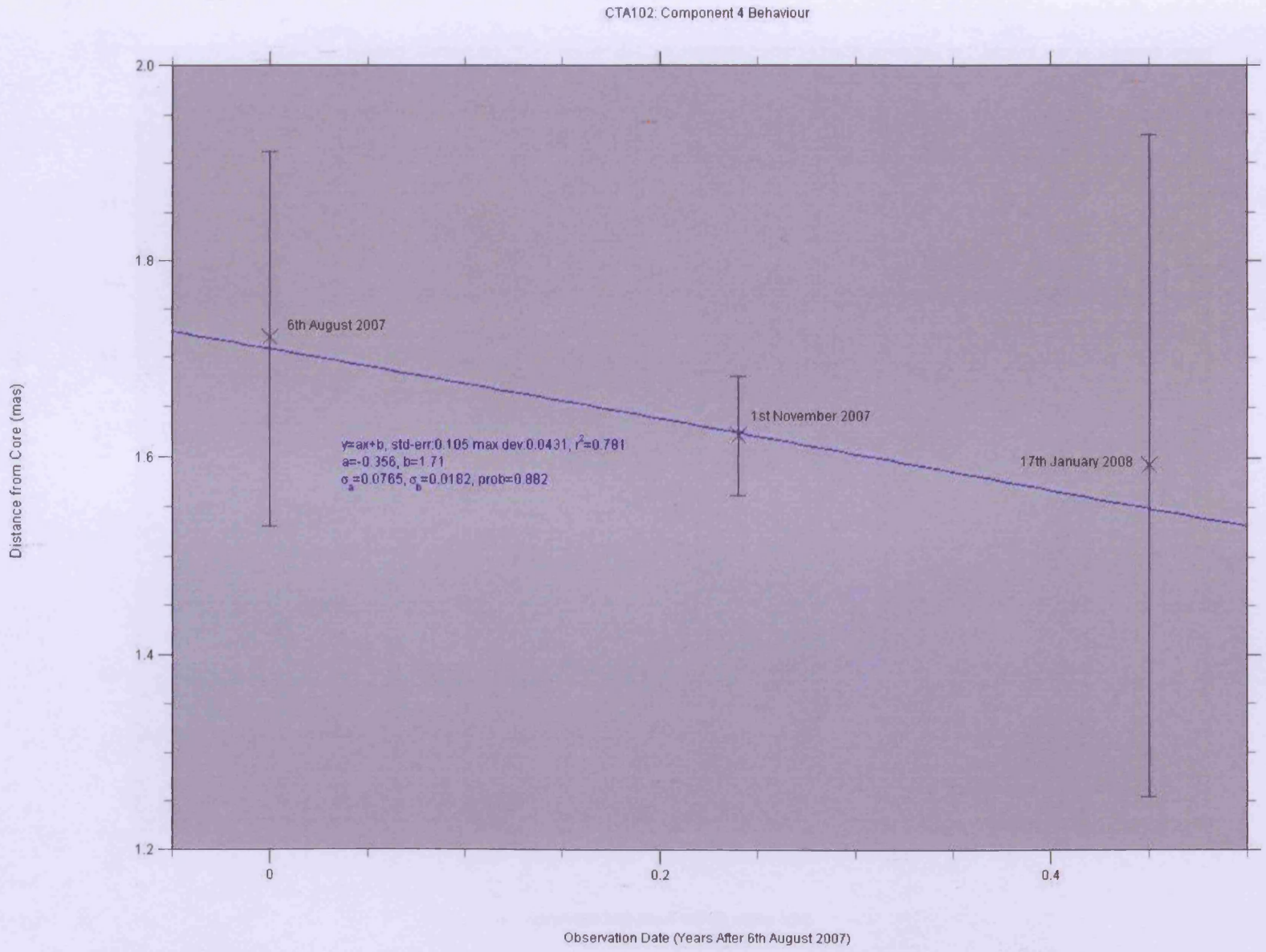
CTA102: Component 4 Behaviour
2.0
1.8
1.6
1.4
1.2
Distance from Core (mas)
6th August 2007
1st November 2007
17th January 2008
y=ax+b, std-err:0.105 max dev:0.0431, r²=0.781
a=-0.356, b=1.71
σa=0.0765, σb=0.0182, prob=0.882
0
0.2
0.4
Observation Date (Years After 6th August 2007)

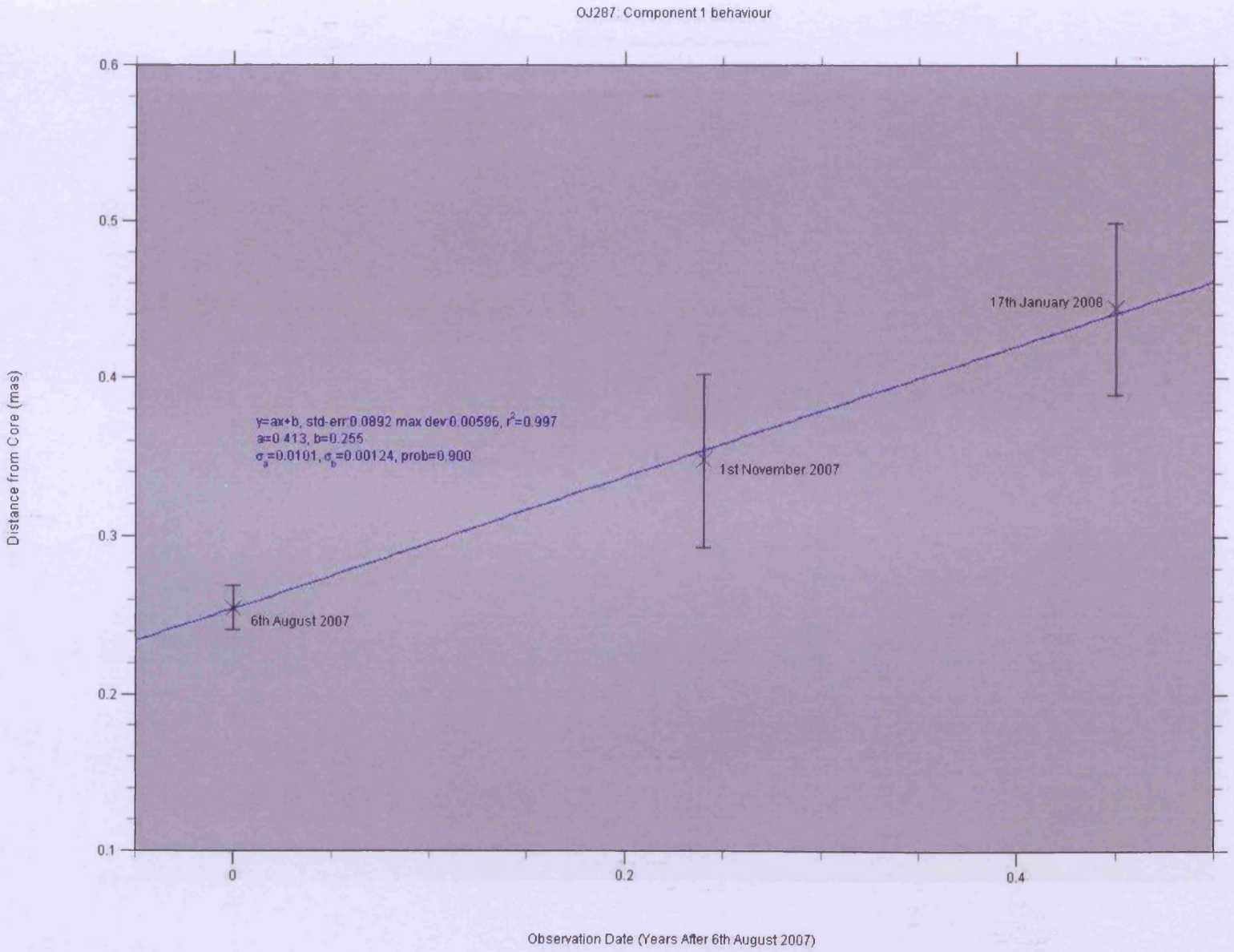
OJ287: Component 1 behaviour
Distance from Core (mas)
Observation Date (Years After 6th August 2007)
0.6
0.5
0.4
0.3
0.2
0.1
0
0.2
0.4
y=ax+b, std-err:0.0892 max dev:0.00596, r²=0.997
a=0.413, b=0.255
σa=0.0101, σb=0.00124, prob=0.900
6th August 2007
1st November 2007
17th January 2008

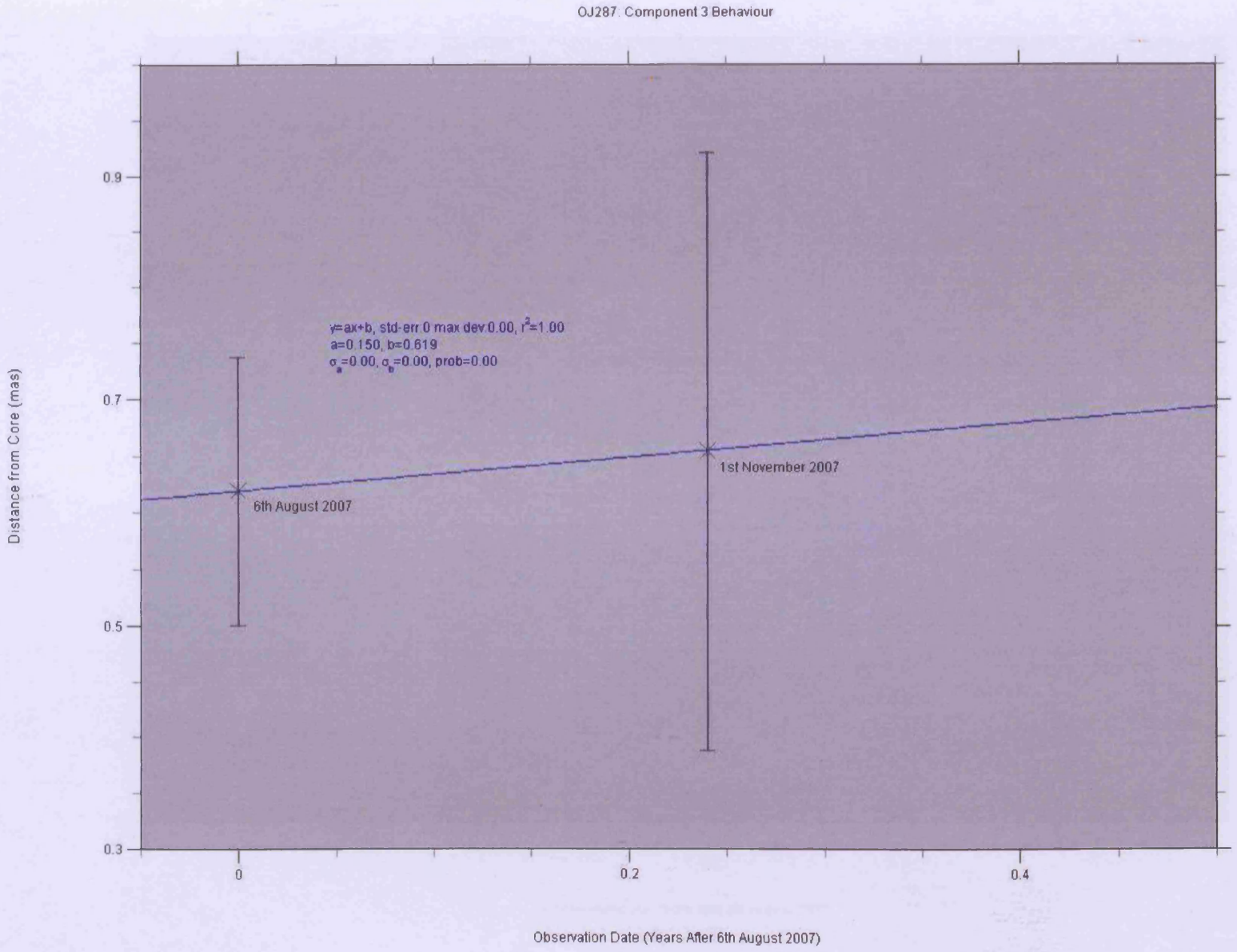
OJ287: Component 3 Behaviour
y=ax+b, std-err 0 max dev 0.00, r²=1.00
a=0.150, b=0.619
σa=0.00, σb=0.00, prob=0.00
6th August 2007
1st November 2007
Distance from Core (mas)
0.9
0.7
0.5
0.3
0
0.2
0.4
Observation Date (Years After 6th August 2007)

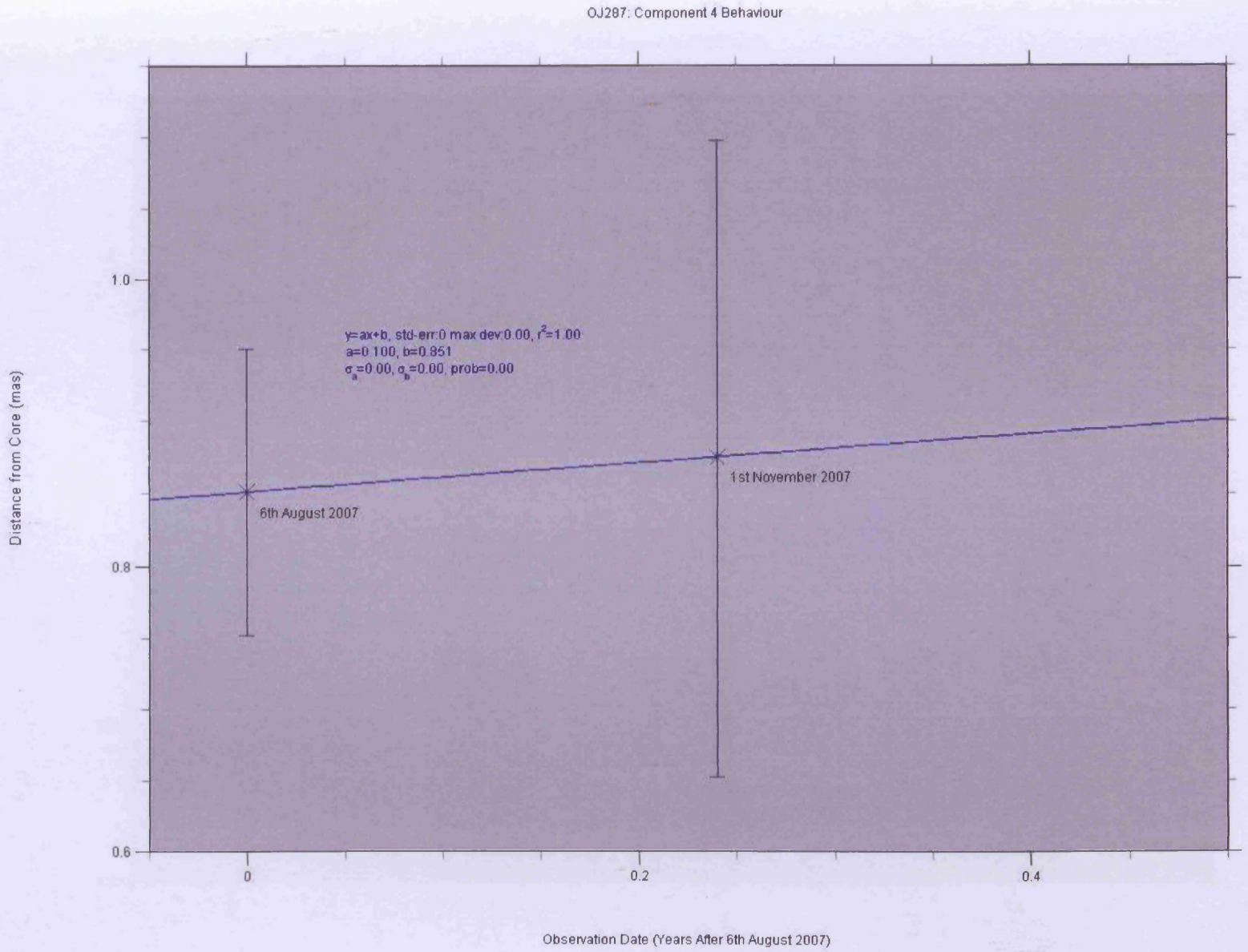
OJ287: Component 4 Behaviour
y=ax+b, std-err:0 max dev:0.00, r²=1.00
a=0.100, b=0.851
σa=0.00, σb=0.00, prob=0.00
6th August 2007
1st November 2007
Distance from Core (mas)
1.0
0.8
0.6
0
0.2
0.4
Observation Date (Years After 6th August 2007)

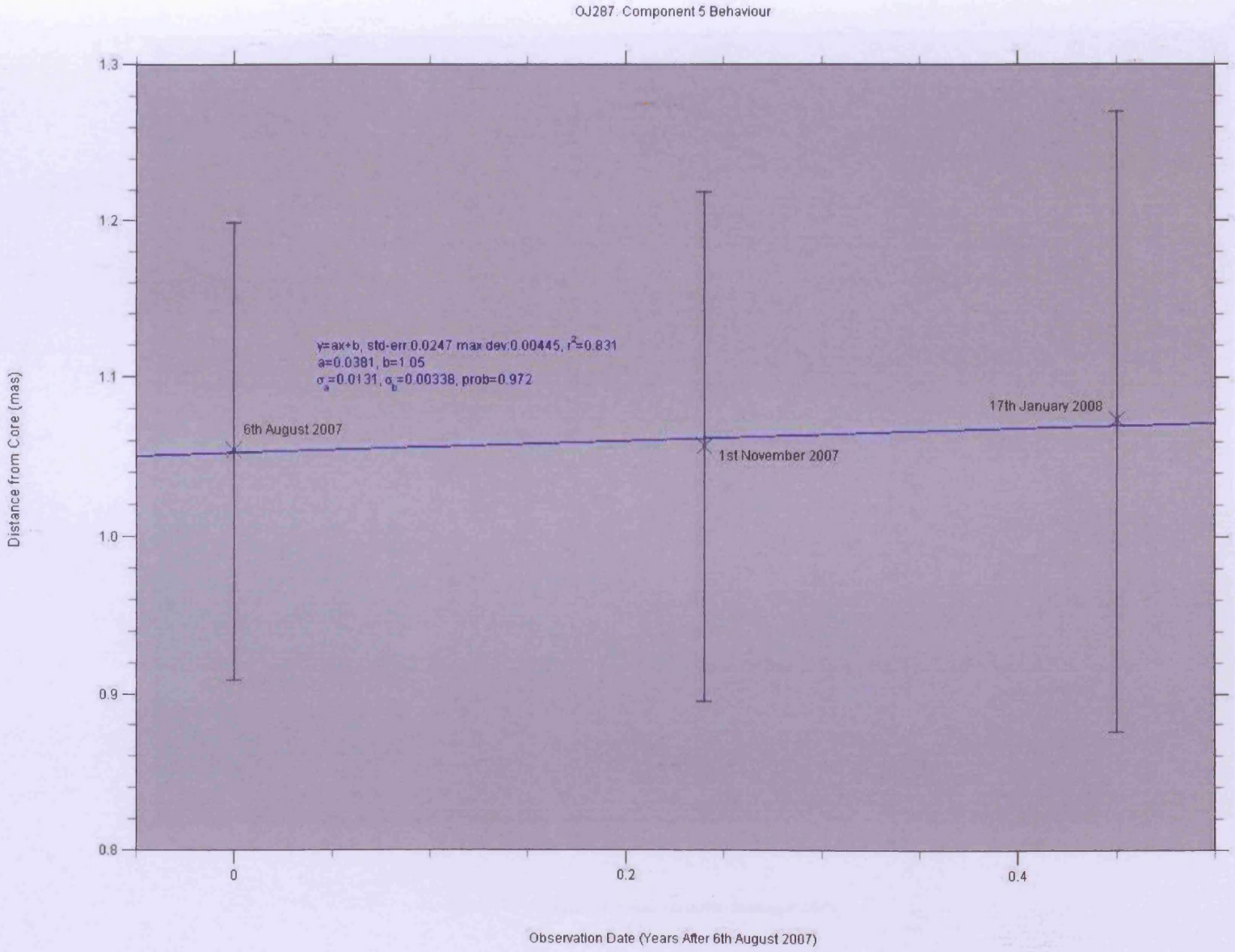
OJ287: Component 5 Behaviour
y=ax+b, std-err:0.0247 max dev:0.00445, r²=0.831
a=0.0381, b=1.05
σa=0.0131, σb=0.00338, prob=0.972
6th August 2007
1st November 2007
17th January 2008
Distance from Core (mas)
Observation Date (Years After 6th August 2007)
1.3
1.2
1.1
1.0
0.9
0.8
0
0.2
0.4

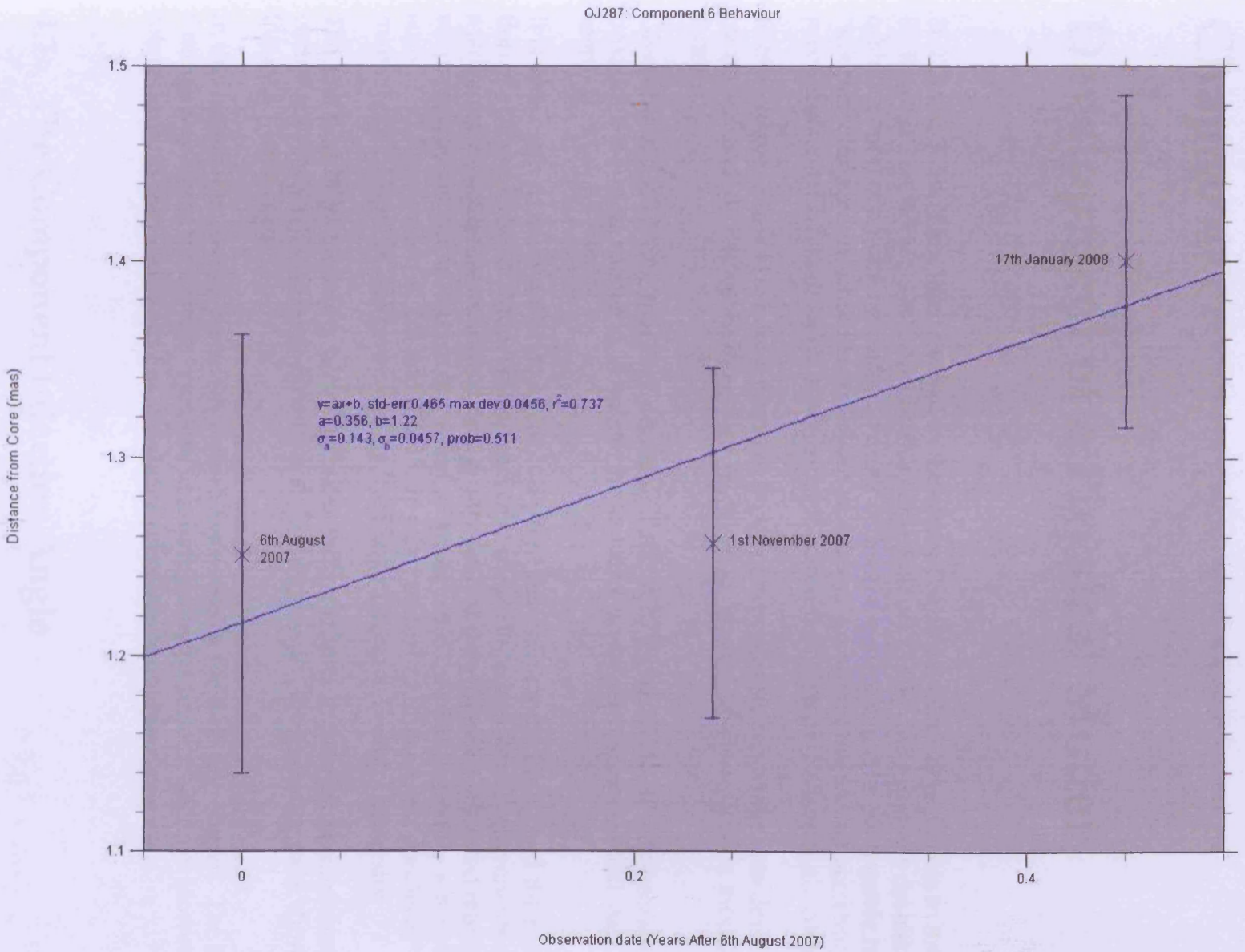
OJ287: Component 6 Behaviour
1.5
1.4
1.3
1.2
1.1
0
0.2
0.4
Distance from Core (mas)
Observation date (Years After 6th August 2007)
y=ax+b, std-err 0.465 max dev 0.0456, r²=0.737
a=0.356, b=1.22
σa=0.143, σb=0.0457, prob=0.511
6th August 2007
1st November 2007
17th January 2008

Chapter 4

Development of a Physical Model

3C273 and 3C345 have been studied in the context of binary black hole models in the past by Kaastra and Roos (1992) and Lobanov and Roland (2005). Such models describe the orbital motion of a black hole around another. Such a system could be responsible for the 'wiggles' observed in some Blazar jets on pc-scales. An alternative is that accretion disc precession could be an intrinsic property of the accretion system (Zensus et al., 2006).

In this chapter I describe how a physical model for helical jet behaviour was developed by myself and A. Papageorgiou, from whom a great deal of input on this model was received.

Given the model fitting that was performed for 3C273 and 3C345, it was necessary to produce a physical model to simulate the helical/ spiral jet trajectories that had been seen.

It is important to make a distinction at this point between model fitting and the production of a physical model. Model fitting serves to make fits to individual components along a jet in order to pinpoint their locations. A physical model will utilise a limited number of set parameters in order to trace out spiral jet trajectories that will hopefully reflect those seen in VLBI maps for 3C273 and 3C345. It was possible to utilise extra epochs of VLBI maps for 3C273 and 3C345 generated by the Blazar Group at Boston University.

The first part of jet modeling was to construct a conic helix in three dimensions using a vector approach with classical kinematics. To begin with, the reference axes shown in Figure 4.1 were used.

In this framework, the jet precesses around the z-axis in the direction shown. The angle θ remains constant for a single component moving along a linear trajectory. However, θ rotates around the z-axis with $\hat{I}$ as the vector precesses about the z-axis itself.

4.1 The Component Injection Angle

It was assumed at this stage that there was a constant injection of components into the jet. The injection angle (unit) vector is denoted as $\hat{I}$. It has components of $\bar{I}_x$, $\bar{I}_y$ and $\bar{I}_z$.

Considering a view along the z-axis, it is possible to define another new vector, $\bar{I}_{xy}$. It

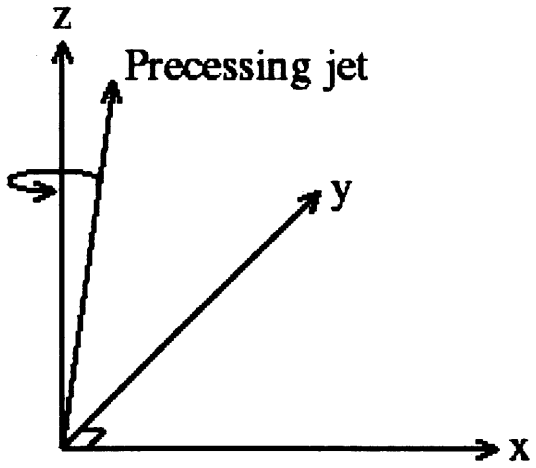

Figure 4.1: Definition of Reference Axes

may be considered as the projection of $\hat{I}$ onto the x-y plane.

Here, the angle ϕ is defined as the angle between $\bar{I}_{xy}$ and the x-axis, in the x-y plane. From Figure 4.3 it is possible to deduce the relation between ϕ and the two components of $\bar{I}_{xy}$:

$$tan\phi = \frac{\mid \bar{I}_y \mid}{\mid \bar{I}_x \mid} \tag{4.1}$$

Looking at $\bar{I}_{xy}$ and $\hat{I}$ together, it can be seen that $\mid \bar{I}_{xy} \mid = sin\theta$ because $\mid \hat{I} \mid = 1$ as can be seen in Figure 4.4.

It is possible to establish another key expression given the equation for a circle of radius, r with x-y reference axes ($x^2 + y^2 = r^2$) as shown in Figure 4.3.

$$\begin{aligned} \mid \bar{I}_x \mid^2 + \mid \bar{I}_y \mid^2 &= \mid \bar{I}_{xy}^2 \mid \\ &= sin^2\theta \text{ because } \mid \bar{I}_{xy} \mid = sin(\theta) \text{ as stated above.} \end{aligned} \tag{4.2}$$

$$\mid \bar{I}_y \mid^2 = \mid \bar{I}_{xy} \mid \tag{4.3}$$

The following equation follows from the definition of $\bar{I}$:

$$\mid \bar{I}_z \mid = cos\theta \tag{4.4}$$

It is now necessary to look at how ϕ changes as $\hat{I}$ precesses. ϕ as a function of time is required. If the time for one rotation of $\hat{I}$ around the z-axis is a period denoted as P, it is possible to arrive at the following expression:

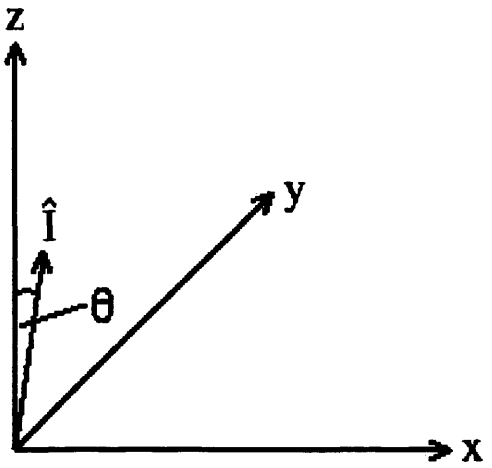

Figure 4.2: The Injection Vector

$$\phi(t) = \frac{2\pi t}{P} \tag{4.5}$$

Taking ϕ to be an angle in radians, it can be seen that this equation is dimensionally correct. Now it is possible to define each of the components of $\hat{I}$ in terms of the parameters introduced so far. Firstly:

$$tan\phi = tan\left(\frac{2\pi t}{P}\right) = \frac{|\,\bar{I}_y\,|}{|\,\bar{I}_x\,|} \tag{4.6}$$

Rearranging:

$$|\,\bar{I}_y\,| = tan\left(\frac{2\pi t}{P}\right)|\,\bar{I}_x\,| \tag{4.7}$$

Squaring this equation and substituting into Equation 4.2 the following expression is obtained once $|\,\bar{I}_x\,|$ is factored out:

$$|\,\bar{I}_x\,|^2 = \frac{sin^2\theta}{1 + tan^2\left(\frac{2\pi t}{P}\right)} \tag{4.8}$$

Using the identities $tan(\frac{2\pi t}{P}) = \frac{sin(\frac{2\pi t}{P})}{cos(\frac{2\pi t}{P})}$ and $sin^2(\frac{2\pi t}{P}) + cos^2(\frac{2\pi t}{P}) = 1$ it is possible to finish with a relatively simple expression for $|\,\bar{I}_x\,|$:

$$|\,\bar{I}_x\,| = sin\theta cos\left(\frac{2\pi t}{P}\right) \tag{4.9}$$

Now substituting this into Equation 4.7 it is possible to arrive at a similar equation for $|\,\bar{I}_y\,|$:

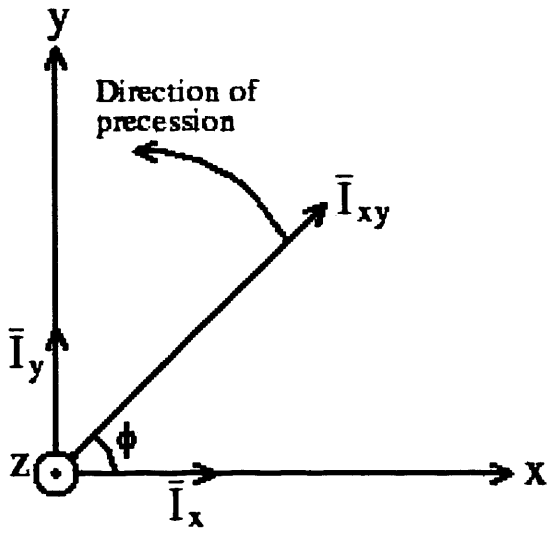

Figure 4.3: Definition of $\bar{I}_{xy}$

$$\mid \bar{I}_y \mid = sin\theta sin\left(\frac{2\pi t}{P}\right) \tag{4.10}$$

Thus, it is now possible to show each of the components of the magnitude of $\hat{I}$:

$$\mid \hat{I} \mid = (sin\theta cos\left(\frac{2\pi t}{P}\right), sin\theta sin\left(\frac{2\pi t}{P}\right), cos\theta) = 1 \tag{4.11}$$

Therefore:

$$\hat{I} = (sin\theta cos\left(\frac{2\pi t}{P}\right)\hat{I}_x, sin\theta sin\left(\frac{2\pi t}{P}\right)\hat{I}_y, (cos\theta)\hat{I}_z) \tag{4.12}$$

It should be appreciated that $\bar{I}_x$ and $\bar{I}_y$ may be positive or negative depending on the progression of the precessing vector $\bar{I}$.

4.2 Component Injection Velocity

If it is assumed that jet components follow linear paths, then the component velocity can be expressed simply as a vector.

$$\bar{u} = u_0\hat{I} \tag{4.13}$$

u_0 here is the injection velocity for a new component entering the jet. It is a free parameter and is to be set as a constant. In this equation, $\hat{I}$ essentially provides directional information and u_0 gives the magnitude of the velocity.

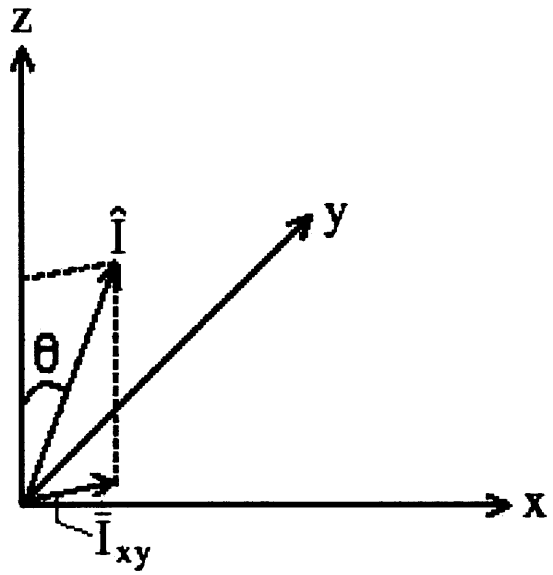

Figure 4.4: The Injection Vector and its projection onto the x-y plane

By showing $\hat{I}$ in its fully expanded form, it is possible to express $\bar{u}$ as follows:

$$\bar{u} = u_0(sin\theta cos\left(\frac{2\pi t}{P}\right)\hat{I}_x, sin\theta sin\left(\frac{2\pi t}{P}\right)\hat{I}_y, (cos\theta)\hat{I}_z) \tag{4.14}$$

4.3 Component Displacements

Using simple classical kinematics, that is $s = ut$, it is possible to construct a straightforward expression for a single component. The component is given an initial velocity of $\bar{u}(t_0)$, which allows it to move from $\bar{s}(t_0)$ to $\bar{s}(t_1)$. The equation is the following:

$$\bar{s}(t_1) = \bar{u}(t_0)[t_1 - t_0] \tag{4.15}$$

Substituting for $\bar{u}(t_0)$ and expanding $\hat{I}$ with $t = t_0$:

$$\bar{s}(t_1) = u_0(sin\theta cos\left(\frac{2\pi t}{P}\right)\hat{I}_x, sin\theta sin\left(\frac{2\pi t}{P}\right)\hat{I}_y, cos\theta\hat{I}_z)[t_1 - t_0] \tag{4.16}$$

Or in a more compact form:

$$\bar{s}(t_1) = u_0\hat{I}(\theta, t_0, P)[t_1 - t_0] \tag{4.17}$$

Therefore, this equation gives the displacement of a single component. The time t_1 is the current injection time or the time of observation, set equal to zero. It is the time at which the new components are injected into the jet flow. The time t_0 is the time at which an already separated component was introduced into the jet in the past. The parameters to

be set to explore possible jet trajectories (all structures that trace out a conic helix) are u_0, θ, t_0 and P.

4.4 Plotting Component Displacements

Figure 4.5 shows a portion of the expected jet trajectory from the model as it is up to this point.

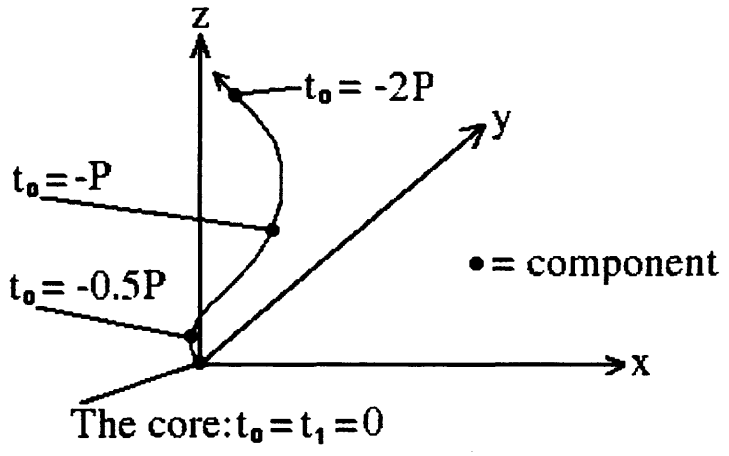

Figure 4.5: Expected trajectory for the jet model, showing components injected into the jet at different times

The core is located at the origin of Figure 4.5. Each component could be linked to the core via a straight line to show its individual kinematic motion. The curved line that is shown serves only to link up the components, such that a structure resembling a conic helix begins to take shape.

Components that are more separated from the core were injected into the jet flow further into the past. This demonstrates that as component displacement increases, t_0 becomes more negative.

Therefore, in the previous equation for a component well separated from the core, $t_1 = 0$ and t_0 is negative. Thus $t_1 - t_0$ will be positive. But $\hat{I}(\theta, t_0, P)$ should also be considered. t_0 is negative as has already been stated.

4.5 Vector Transformation from Three Dimensions to Two

The model thus far has made a conic helix structure in three dimensions. However, the view that is taken of jets is a projection into two dimensions (onto the sky). These same two dimensions are shown when viewing a VLBI map.

It is necessary to introduce a new vector and two new angles. Figure 4.6 shows all of the new elements that have been added to the modeling.

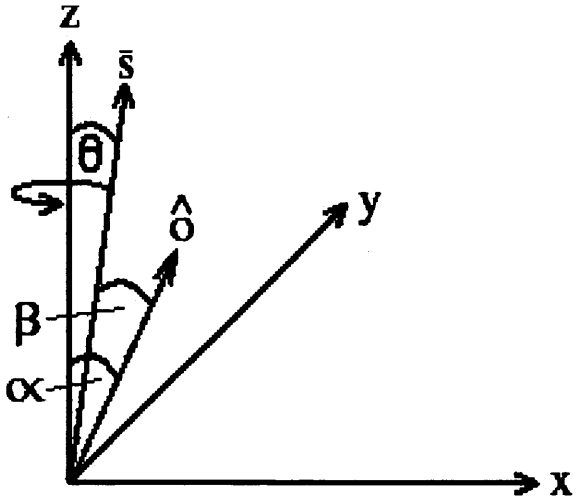

Figure 4.6: How the new elements of the model fit together with respect to the reference axes

$\bar{s}$ precesses around the z-axis over time. However, it is possible to define a unit vector, $\hat{o}$ that is directed towards the observer. In Figure 4.6 $\hat{o}$ is shown at an angle of β with respect to $\bar{s}$. β should be a small angle, to simulate the situation in the case of Blazars, where the jet is observed to be at a relatively small angle to the line of sight. Since $\hat{o}$ is fixed at a known angle and $\bar{s}$ is a precessing vector, β will vary in time when considering multiple components along a jet. For a single component, β remains constant because individual components are assumed to travel along linear trajectories for the purposes of this model.

For clarity, the following is a concise summary of the angles present in Figure 4.6:

α The angle between the observer (unit) vector, $\hat{o}$ and the z-axis.

β The angle between the observer vector, $\hat{o}$ and the precessing $\bar{s}$ vector.

θ The angle between the precessing $\bar{s}$ vector and the z-axis. It is also the angle between the injection (unit) vector, $\hat{I}$ and the z-axis.

The three dimensional jet trajectories resulting from the model so far can be projected onto a two dimensional plane, which is the sky for the observer. At this point, a diagram may be shown to illustrate this transformation more clearly. In Figure 4.7, the shaded region indicates the sky that is visible to the observer. A representation of a possible jet trajectory in three dimensions is shown precessing around the z-axis. Following the direction of the observer vector, $\hat{o}$ it is possible to trace out a view of the jet on the sky, from the perspective of the observer.

Using scalar product notation it is possible to express the following two equations:

$$\hat{o} \cdot \bar{s_z} = \mid \bar{s_z} \mid cos\alpha \tag{4.18}$$

$$\hat{o} \cdot \bar{s} = \mid \bar{s} \mid cos\beta \tag{4.19}$$

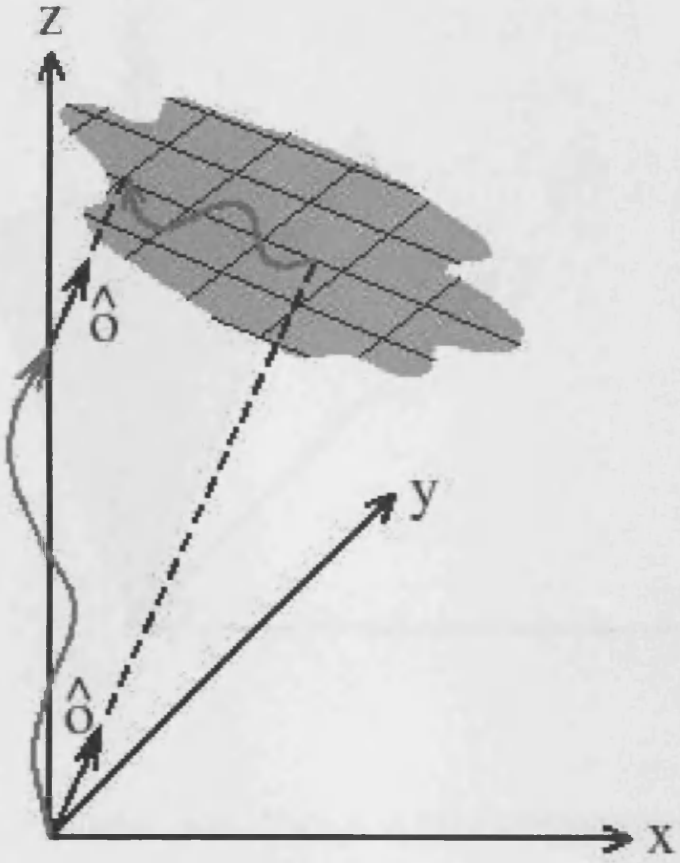

Figure 4.7: Illustrating how a 3D jet trajectory is transformed onto a 2D plane (the sky)

But at this point, the angle β is unknown and will change as $\bar{s}$ precesses. It will be shown that β can be expressed using terms that have been established already. However, it is necessary to simplify the analysis by looking for symmetries that arise due to how the model has been set up so far.

Figure 4.8 shows two cones that represent all possible $\hat{o}$ and $\bar{s}$ vectors (given set values of the angles α and θ respectively). The observer vector $\hat{o}$ is fixed but $\bar{s}$ will precess in time. Two observers may view the same $\bar{s}$ vector differently, but with time the vector will rotate. The two observers *will* therefore have the same view of the vector but at different times.

There is a conic symmetry that allows placement of the $\hat{o}$ vector in the x-z plane such that $\bar{o}_y = 0$.

It is possible to write that:

$$\bar{s}_{||\hat{o}} = \mid \bar{s}_{||\hat{o}} \mid \hat{o} \tag{4.20}$$

Also, the following expression can be shown:

$$\hat{o} \cdot \bar{s} = \mid \hat{o} \mid\mid \bar{s} \mid cos\beta \tag{4.21}$$

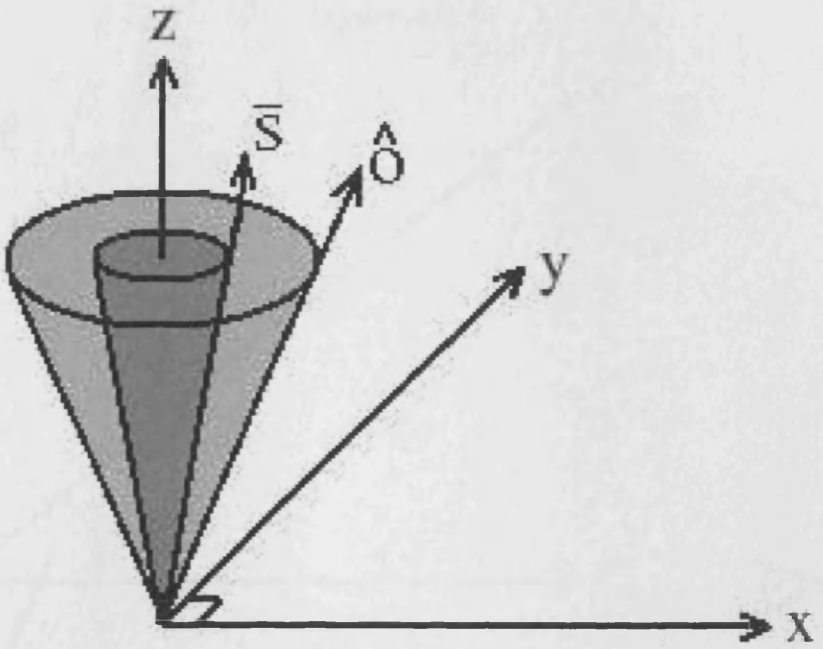

Figure 4.8: Simplification of the model via symmetries

At this point, more definition of β is required using the components of the previous scalar product. Therefore:

$$| \bar{o}_x || \bar{s}_x | + | \bar{o}_y || \bar{s}_y | + | \bar{o}_z || \bar{s}_z |=| \bar{s} | cos\beta \tag{4.22}$$

Since $\bar{o_y} = 0$ it is possible to cancel a term here and write:

$$cos\beta = \frac{| \bar{o}_x || \bar{s}_x | + | \bar{o}_z || \bar{s}_z |}{| \bar{s} |} \tag{4.23}$$

From the simple figure showing $\bar{s}$ and $\hat{o}$:

$$| \bar{s}_{||\hat{o}} |=| \bar{s} | cos\beta \tag{4.24}$$

Multiplying through by $\hat{o}$ and using $\bar{s}_{||\hat{o}} =| \bar{s}_{||\bar{o}} | \hat{o}$ it can be shown that $\bar{s}_{||\hat{o}} =| \bar{s} | (cos\beta)\hat{o}$.

Similarly, it can be shown that $\bar{s}_{\perp\hat{o}} =| \bar{s} | (sin\beta)\hat{o}$. Now substituting for $cos\beta$ and canceling terms:

$$\bar{s}_{||\hat{o}} = \hat{o}(| \bar{o_x} || \bar{s_x} | + | \bar{o_z} || \bar{s_z} |) \tag{4.25}$$

Looking at parallel and perpendicular components of $\bar{s}$, vector addition allows that:

$$\bar{s}_{\perp\hat{o}} =| \bar{s} | -[\hat{o}(| \bar{o_x} || \bar{s_x} | + | \bar{o_z} || \bar{s_z} |)] \tag{4.26}$$

Figure 4.9:

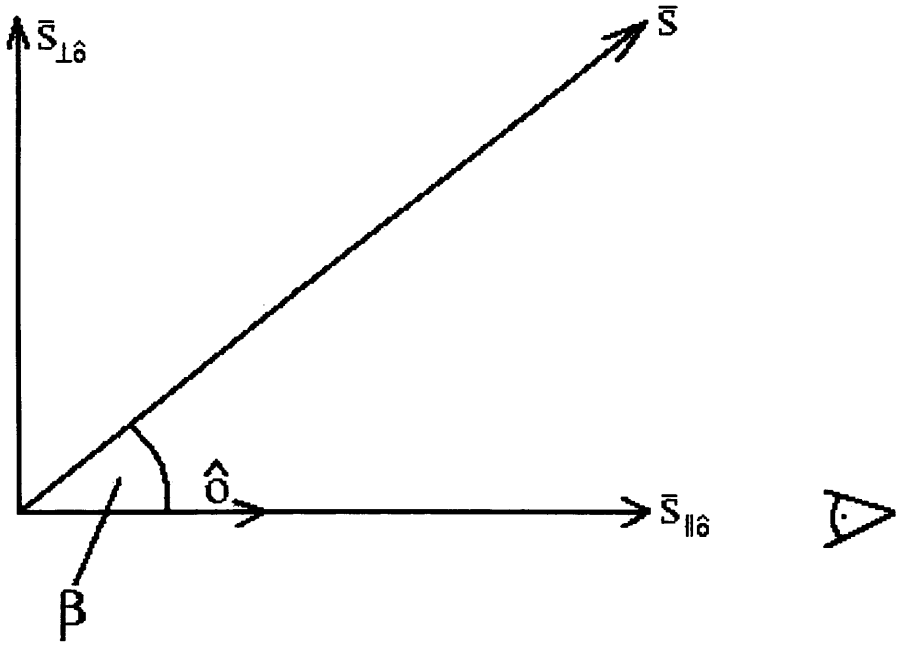

4.6 Obtaining 2D map or sky coordinates

The x, y and z axes have now been defined along with the observer vector $\hat{o}$. Now allow $\bar{s}$ to have sky coordinates such as $\bar{s}(X, Y, Z)$. In making map plots, only two of these dimensions shall be required.

$\hat{o}$ lies in the x-z plane so to simplify the analysis it is possible to rotate axes such that z is parallel to Z and $\hat{o}$. In doing this, y is unaffected and runs parallel to Y. x now rotates to become a new axis X. The diagram that features the observer's sky also shows the new axes.

It is now possible to define $\bar{s}$ in terms of map or sky coordinates: $\bar{s}(X, Y = y, \hat{o} = Z)$. $\bar{s}(Y) = \bar{s}(y)$ but $\bar{s}(X)$ and $\bar{s}(\hat{o})$ need to be defined. It is now possible to add the new axes to the x-z plane.

$\mid \bar{s}_x \mid = \mid \bar{s} \mid sin\theta$ and $\mid \bar{s}_z \mid = \mid \bar{s} \mid cos\theta$. The precession of $\bar{s}$ is such that $\mid \bar{s}_z \mid$ is always positive.

Consider projections of $\bar{s}_x$ and $\bar{s}_z$ onto the X-axis and term these projections $\bar{s}_{xX}$ and $\bar{s}_{zX}$.

Rotation of the axes is such that the angle between the x and X axes is the angle α. It can be seen that $\bar{s}_{zX} = \bar{s}_z sin\alpha$ and $\bar{s}_{xX} = \bar{s}_x cos\alpha$.

It is now possible to express the components of $\bar{s}$ in terms of the map or sky coordinates mentioned above.

$\bar{s}_X$ shall be considered first. Note that $\mid \bar{s}_{xX} \mid$ runs along the positive X axis but $\mid \bar{s}_{zX} \mid$ runs along negative X. Therefore:

Figure 4.10:

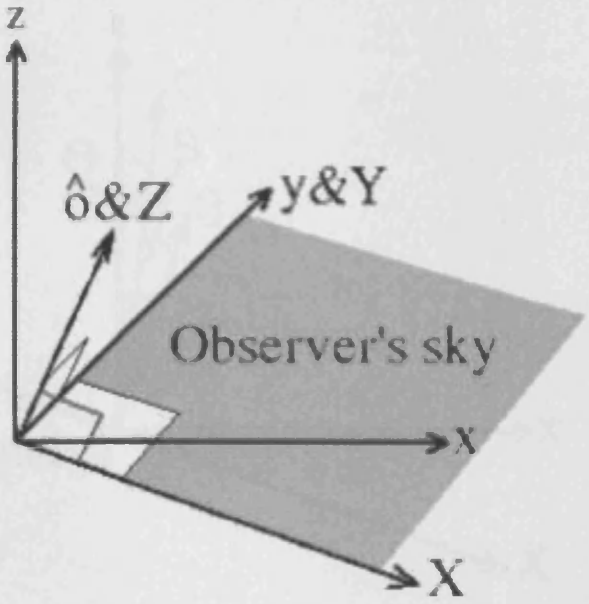

$$| \bar{s}_X | = | \bar{s}_{xX} | - | \bar{s}_{zX} | = | \bar{s}_x | cos\alpha - | \bar{s}_z | sin\alpha \tag{4.27}$$

In this equation in the first instance, the negative component along the X-axis has subtracted from the positive component.

$\bar{s}_Y$ is a simple case with $| \bar{s}_Y | = | \bar{s}_y |$ such that $\bar{s}_Y = | \bar{s}_y | \hat{Y}$.

Finally, $\bar{s}_{\hat{o}}$ needs some definition.

$$| \bar{s}_{\hat{o}} | = | \bar{s} | cos\beta = | \bar{s} | \frac{| \bar{o_x} || \bar{s_x} | + | \bar{o_z} || \bar{s_z} |}{| \bar{s} |} = | \bar{o_x} || \bar{s_x} | + | \bar{o_z} || \bar{s_z} | \tag{4.28}$$

Here, the earlier definition in Equation 4.23 has been used to remove β (time dependent) and replace it with parameters that may be set in the model.

Now it remains to define $\bar{s}_{\hat{o}}$ in terms of angles and components of $s(x, y, z)$ only.

By simple trigonometry it can be seen that $| \bar{o}_x | = sin\alpha$ and $| \bar{o}_z | = cos\alpha$ because $| \hat{o} | = 1$. Therefore:

$$| \bar{s}_{\hat{o}} | = | \bar{s}_x | sin\alpha + | \bar{s}_z | cos\alpha \tag{4.29}$$

It is now possible to arrive at the final expression for this model ($\bar{s}(X, Y)$ may be taken from this for plotting):

$$\bar{s}(X, Y, \hat{o}) = [(| \bar{s}_x | cos\alpha - | \bar{s}_z | sin\alpha)X, | \bar{s}_y | Y, (| \bar{s}_x | sin\alpha + | \bar{s}_z | cos\alpha)\hat{o}] \tag{4.30}$$

and therefore,

Figure 4.11:

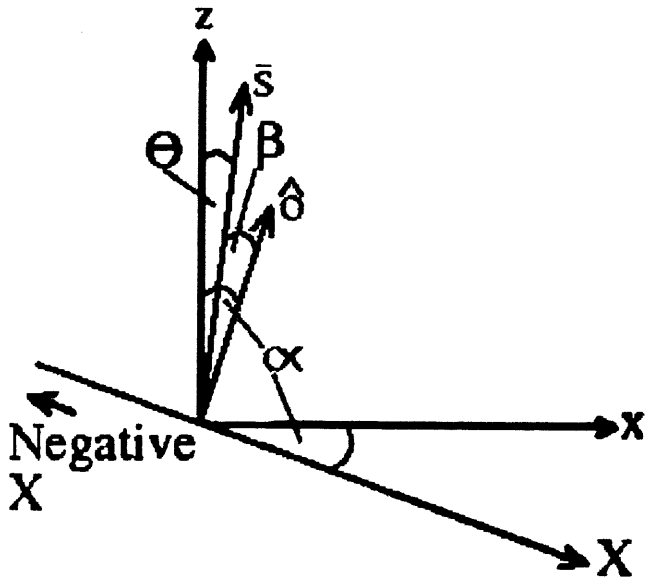

$$| \bar{s}(X,Y,\hat{o}) | = [(| \bar{s}_x | cos\alpha - | \bar{s}_z | sin\alpha), | \bar{s}_y |, (| \bar{s}_x | sin\alpha + | \bar{s}_z | cos\alpha)] \qquad (4.31)$$

Figure 4.12:

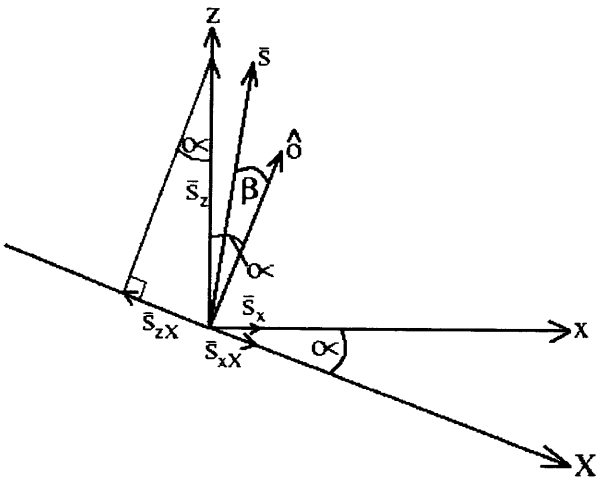

Figure 4.13:

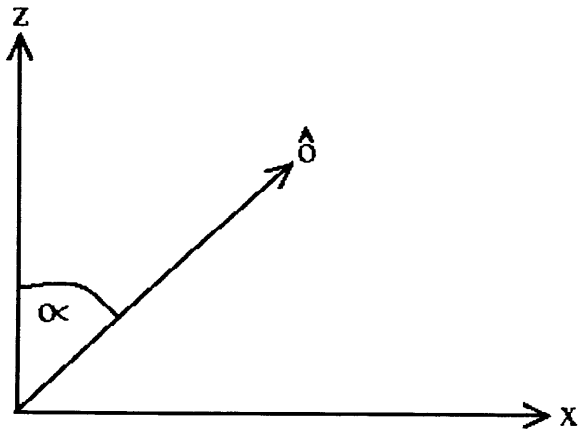

Chapter 5

Application of the Physical Model to Results

It was possible to plot out trajectories described by the physical model using the Mathcad computer program. In addition to this I utilised the Levenberg-Marquardt algorithm or LMA to fit the trajectories to my model fitted component positions. The LMA is a very useful curve fitting algorithm that can minimise a function over a space of parameters. The algorithm was first published by Kenneth Levenberg, while working at the Frankford Army Arsenal. It was rediscovered by Donald Marquardt who worked as a statistician at DuPont, an American Chemical Company. See Levenberg (1944) as well as Marquardt (1963) for further information.

Values for the observer angle α for 3C273 and 3C345 have been previously reported (Jorstad et al., 2005) as 6.1 and 2.7 degrees respectively. To simplify matters, these values were incorporated as fixed parameters.

Weighted averages of the Lorentz factor for the sources were also presented in Jorstad et al. (2005). These were 10.6 and 18.7 for 3C273 and 3C345 respectively. From these values it was possible to calculate velocities that could serve as u_0 for the two sources. It is assumed that components are injected, and propagate down the jets at a constant velocity. The calculated velocities were 0.996c for 3C273 and 0.999c for 3C345.

It is worth describing the methods employed in deriving some of the parameters in Jorstad et al. (2005). The Lorentz factors and viewing angles in this work were solutions of a system that combined two equations (one for the apparent speed of the knots studied and the other for their Doppler factors) for a knot having a measured apparent speed and a variability Doppler factor derived via the following equation:

$$\delta_{var} = \frac{sD}{c\Delta t_{var}(1+z)} \tag{5.1}$$

Here D is the luminosity distance, s is the angular size of the component and Δt_{var} is the timescale of variability for each superluminal component.

The two equations that were combined are as follows:

$$\beta_{app} = \beta sin\theta_0 (1 - \beta cos\theta_0)^{-1} \tag{5.2}$$

In this case, β is the intrinsic velocity of a component and θ_0 is the angle between the jet trajectory and the line of sight. There is calculation of proper motions for jet components in the work.

$$\delta = [\Gamma(1 - \beta cos\theta_0)]^{-1} \tag{5.3}$$

Where Γ is the Lorentz factor of the knot.

For their work with jet velocities, Jorstad et al. (2005) adopt an inhomogeneous Friedmann-Lemaître-Robertson-Walker cosmology with $\Omega_m = 0.3$, $\Omega_\Lambda = 0.7$ and Hubble constant $H_0 = 70 kms^{-1} Mpc^{-1}$.

Offset subtractions were made to the model fitting results such that the origin of the plots would be the (presumed) core of each jet image.

It was possible to rotate the model fitting results for 3C273 and 3C345 so as to remove angular offsets. The rotation matrix used is shown below. It rotated each of the model fitted coordinates in an anticlockwise direction.

$$\begin{bmatrix} cos\theta & -sin\theta \\ sin\theta & cos\theta \end{bmatrix}$$

In the sections that follow, I plot the component positions either side of the jet axis against time for 3C273 and 3C345. The component of displacement away from the jet core parallel to the jet axis will be assumed to increase at a constant rate.

The graphs indicate the application of the physical model to my model fitted data.

5.1 3C273 Plots

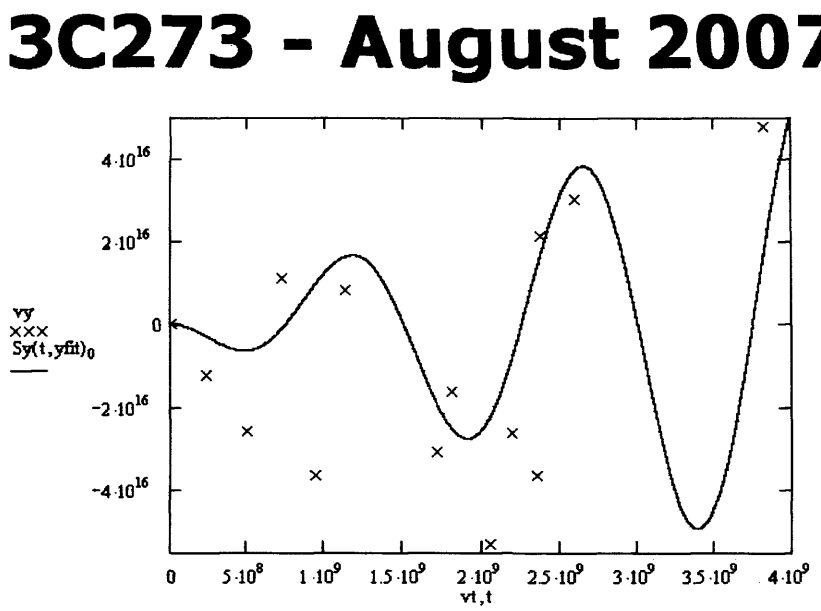

Figure 5.1: 3C273 in August 2007. A graph showing the model fitting results along with a fitted physical model. Parameters obtained from the fitting were $\theta = 2.793°$ and $P = 47.502$ years.

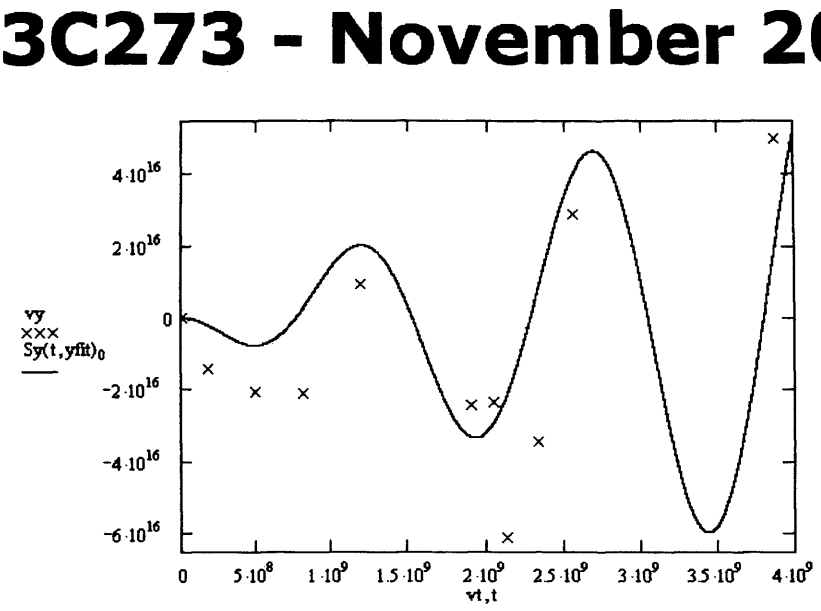

Figure 5.2: 3C273 in November 2007. A graph showing the model fitting results along with a fitted physical model. Parameters obtained from the fitting were $\theta = 3.346°$ and $P = 48.119$ years.

3C273 - January 2008

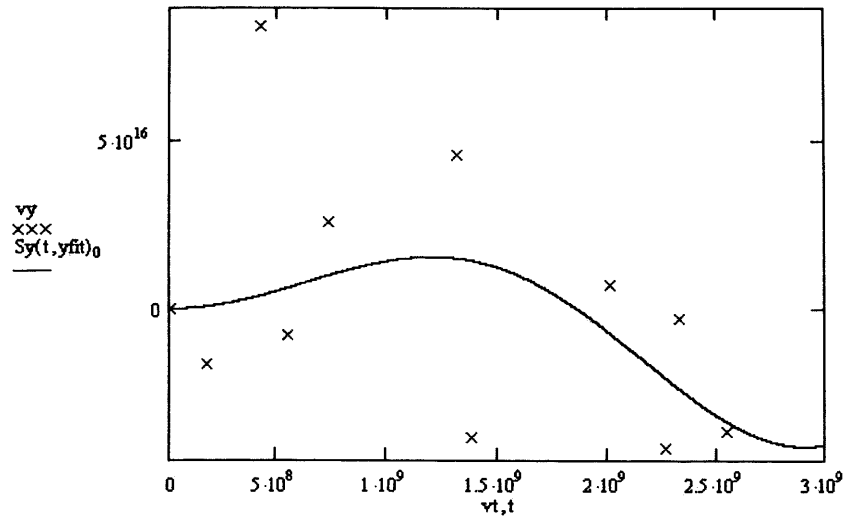

Figure 5.3: 3C273 in January 2008. A graph showing the model fitting results along with a fitted physical model. Parameters obtained from the fitting were $\theta = 2.764°$ and $P = 117.861$ years.

5.2 3C345 Plots

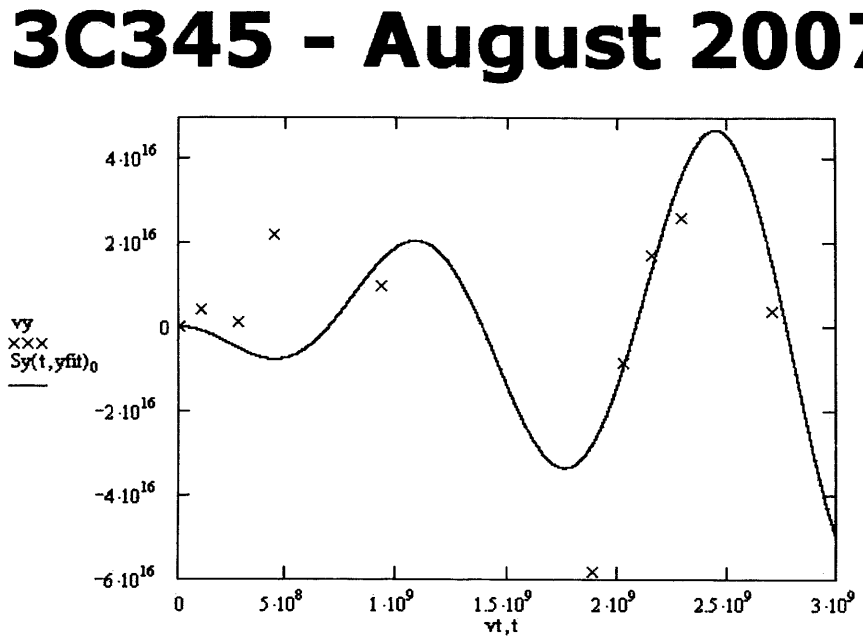

Figure 5.4: 3C345 in August 2007. A graph showing the model fitting results along with a fitted physical model. Parameters obtained from the fitting were $\theta = 3.691°$ and $P = 43.880$ years.

3C345 - November 2007

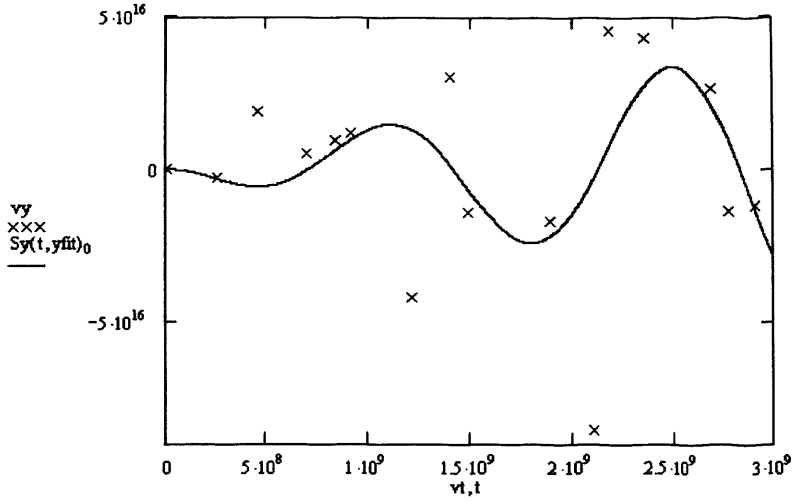

Figure 5.5: 3C345 in November 2007. A graph showing the model fitting results along with a fitted physical model. Parameters obtained from the fitting were $\theta = 2.603°$ and $P = 44.802$ years.

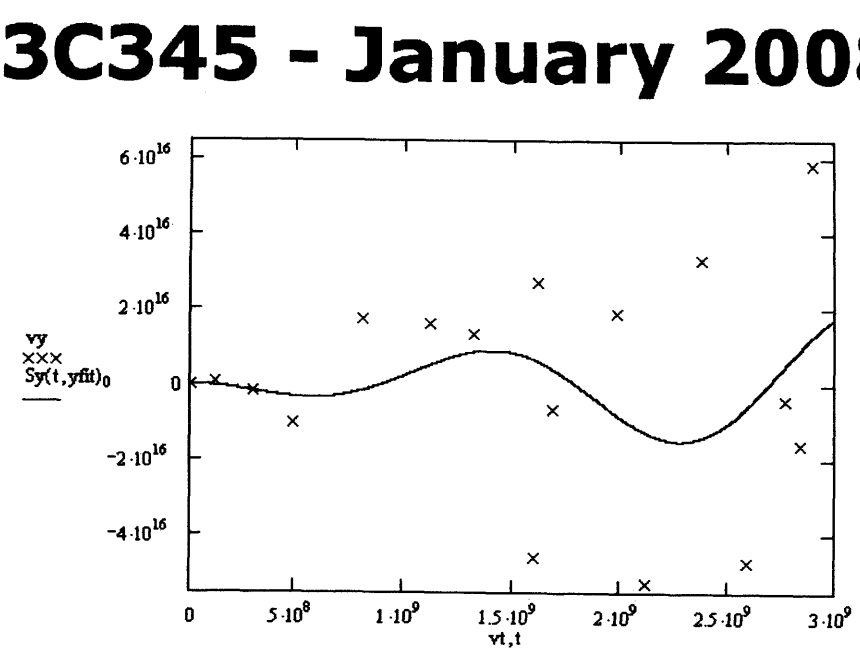

Figure 5.6: 3C345 in January 2008. A graph showing the model fitting results along with a fitted physical model. Parameters obtained from the fitting were $\theta = 1.262°$ and $P = 56.752$ years.

Chapter 6

Principle Results of Kinematic Study

The conclusions here are split into two main parts. These are the calculated jet velocities and the outcomes from the fitting of a physical model to maps generated for 3C273 and 3C345.

6.1 Jet Velocities

It has been possible to calculate jet velocities for 15 Blazar sources. Linear fits were made to the kinematic plots that were generated for selected sources. For many sources, it was not worthwhile making such plots since there was simply not enough data to work with. The final results are shown in tables for each source. Data is sorted in terms of the velocities derived. Jet velocities are shown firstly as proper motions (mas/ yr) and are then converted into apparent superluminal (or subluminal) velocities via the following equation (Cohen, 2009):

$$v = \mu D(1 + z) \tag{6.1}$$

Here v is the apparent velocity and μ is the proper motion of a component. D is the luminosity distance to the source and z is its redshift.

Luminosity distances are incorporated assuming $H_0 = 71 km/s/Mpc$, $\Omega_\Lambda = 0.73$ and $\Omega_m = 0.27$.

The luminosity distances and redshifts of sources were taken from data made publically available on the MOJAVE (2cm VLBI survey) database which may be viewed at www.physics.purdue.edu/astro/MOJAVE. The database is maintained by the MOJAVE team (Lister et al., 2009).

In some cases the proper motion error (and therefore the apparent velocity error) is marked with N/A. Since the errors were the uncertainties in the linear fits to the kinematic plots, this is a reflection of having only two points to fit to for some components.

Component	Internal Proper Motion (mas/ yr)	Apparent Transverse Velocity (c)
1	1.72 ± 0.0172	79.90 ± 0.80
2	2.67 ± 0.4180	124.03 ± 19.42

Table 6.1: Component Kinematics for 0336-019. Maximum jet velocity as quoted from the MOJAVE database: 22.36*c*.

Component	Internal Proper Motion (mas/ yr)	Apparent Transverse Velocity (c)
1	0.146 ± 0.0601	7.16 ± 2.95

Table 6.2: Component Kinematics for 0420-014. Maximum jet velocity as quoted from the MOJAVE database: 7.35*c*.

Component	Internal Proper Motion (mas/ yr)	Apparent Transverse Velocity (c)
1	0.103 ± 0.0266	8.73 ± 2.25

Table 6.3: Component Kinematics for 0528+134. Maximum jet velocity as quoted from the MOJAVE database: 19.20*c*.

Component	Internal Proper Motion (mas/ yr)	Apparent Transverse Velocity (c)
1	0.643 ± 0.258	14.53 ± 5.83
1N	$1.00 \pm$ N/A	$22.59 \pm$ N/A

Table 6.4: Component Kinematics for 0954+658. It was difficult to find a comparison jet velocity for this source. This could be due to its compact structure not allowing observation of many components. Indeed, at lower frequencies 0954+658 would almost certainly appear as a point source.

Component	Internal Proper Motion (mas/ yr)	Apparent Transverse Velocity (c)
1	-0.283 ± 0.652	-18.83 ± 43.39
1N	$0.290 \pm$ N/A	$19.30 \pm$ N/A
2	0.870 ± 0.396	57.89 ± 26.35
3	$0.956 \pm$ N/A	$63.62 \pm$ N/A

Table 6.5: Component Kinematics for 1611+343. Maximum jet velocity as quoted from the MOJAVE database: 14.09*c*.

Component	Internal Proper Motion (mas/ yr)	Apparent Transverse Velocity (c)
5	-1.32 ± 0.117	-64.12 ± 5.68
4	-0.196 ± 0.161	-9.52 ± 7.82
2	0.368 ± 0.0250	17.88 ± 1.21
3	$1.10 \pm$ N/A	$53.44 \pm$ N/A

Table 6.6: Component Kinematics for 1730-130. Maximum jet velocity as quoted from the MOJAVE database: 35.69*c*.

Component	Internal Proper Motion (mas/ yr)	Apparent Transverse Velocity (c)
2	0.304 ± 0.0289	0.99 ± 0.09
1	0.366 ± 0.0768	1.19 ± 0.25
3	0.509 ± 0.0895	1.66 ± 0.29
4	1.39 ± N/A	4.52 ± N/A

Table 6.7: Component Kinematics for 3C111. Maximum jet velocity as quoted from the MOJAVE database: 5.86*c*.

Component	Internal Proper Motion (mas/ yr)	Apparent Transverse Velocity (c)
11	-0.910 ± 0.195	-9.29 ± 1.99
1	-0.259 ± 0.0460	-2.64 ± 0.47
3	-0.0942 ± 0.252	-0.96 ± 2.57
2	0.111 ± 0.0619	1.13 ± 0.63
12	0.333 ± N/A	3.40 ± N/A
7	0.458 ± N/A	4.68 ± N/A
4	0.484 ± 0.0831	4.94 ± 0.85
5	0.974 ± 0.0612	9.95 ± 0.62
6	1.50 ± N/A	15.32 ± N/A

Table 6.8: Component Kinematics for 3C273. Maximum jet velocity as quoted from the MOJAVE database: 13.43*c*.

Component	Internal Proper Motion (mas/ yr)	Apparent Transverse Velocity (c)
1	0.436 ± 0.0327	13.80 ± 1.04
4	0.980 ± 0.120	31.02 ± 3.80
2	0.998 ± 0.0147	31.59 ± 0.47
3	1.40 ± 0.0219	44.32 ± 0.69

Table 6.9: Component Kinematics for 3C279. Maximum jet velocity as quoted from the MOJAVE database: 20.57*c*.

Component	Internal Proper Motion (mas/ yr)	Apparent Transverse Velocity (c)
8N*	-0.495 ± N/A	-17.07 ± N/A
4*	0.204 ± N/A	7.04 ± N/A
6*	0.227 ± 0.0973	7.83 ± 3.36
5*	0.396 ± N/A	13.66 ± N/A
6N*	0.610 ± N/A	21.04 ± N/A
1N	0.663 ± 0.0311	22.87 ± 1.07
1A	0.746 ± 0.139	25.73 ± 4.79
1B	1.22 ± 0.0743	42.08 ± 2.56
1N*	2.03 ± N/A	70.02 ± N/A
4N*	2.10 ± N/A	72.44 ± N/A
3N*	2.76 ± N/A	95.20 ± N/A
2N*	2.92 ± N/A	100.72 ± N/A

Table 6.10: Component Kinematics for 3C345. Maximum jet velocity as quoted from the MOJAVE database: 19.27*c*.

Component	Internal Proper Motion (mas/ yr)	Apparent Transverse Velocity (c)
3	0.00208 ± 0.00843	0.14 ± 0.56
2	0.184 ± N/A	12.28 ± N/A

Table 6.11: Component Kinematics for 3C446. Maximum jet velocity as quoted from the MOJAVE database: 17.34*c*.

Component	Internal Proper Motion (mas/ yr)	Apparent Transverse Velocity (c)
2N	0.110 ± N/A	5.14 ± N/A
3N	0.529 ± N/A	24.73 ± N/A
2	1.15 ± 0.262	53.76 ± 12.25
1	1.32 ± 0.198	61.71 ± 9.26
4	1.68 ± N/A	78.54 ± N/A
3	1.89 ± N/A	88.36 ± N/A

Table 6.12: Component Kinematics for 3C454.3. Maximum jet velocity as quoted from the MOJAVE database: 14.19*c*.

Component	Internal Proper Motion (mas/ yr)	Apparent Transverse Velocity (c)
1N	-0.433 ± N/A	-1.95 ± N/A
1	-0.0473 ± 0.0107	-0.21 ± 0.05
2	0.263 ± 0.00996	1.18 ± 0.04
3	0.287 ± 0.00138	1.29 ± 0.01
4	1.52 ± N/A	6.84 ± N/A

Table 6.13: Component Kinematics for BL Lac. Maximum jet velocity as quoted from the MOJAVE database: 10.57*c*.

Component	Internal Proper Motion (mas/ yr)	Apparent Transverse Velocity (c)
3	-0.444 ± 0.233	-23.96 ± 12.57
4	-0.356 ± 0.0765	-19.21 ± 4.13
2N	0.0524 ± N/A	2.83 ± N/A
1	0.215 ± 0.187	11.60 ± 10.09
2	0.829 ± N/A	44.73 ± N/A

Table 6.14: Component Kinematics for CTA102. Maximum jet velocity as quoted from the MOJAVE database: 15.41*c*.

Component	Internal Proper Motion (mas/ yr)	Apparent Transverse Velocity (c)
5	0.0381 ± 0.0131	0.73 ± 0.25
4	0.100 ± N/A	1.91 ± N/A
3	0.150 ± N/A	2.87 ± N/A
6	0.356 ± 0.143	6.80 ± 2.73
1	0.413 ± 0.0101	7.89 ± 0.19

Table 6.15: Component Kinematics for OJ287. Maximum jet velocity as quoted from the MOJAVE database: 15.17*c*.

Source	θ (degrees)	α (degrees)	$\bar{P}$ (years)	u_0 (c)
3C273	2.968 ± 0.153	6.1	71.161 ± 19.066	0.996
3C345	2.519 ± 0.573	2.7	48.478 ± 3.385	0.999

Table 6.16: Final Parameter Values from the Application of a Physical Model to Model Fitting Data. $\bar{\theta}$ and $\bar{P}$ are average values (standard error included) of θ and P for each source.

6.2 Application of a Physical Model to Model Fitting Results

Table 6.16 gives a summary of the parameters obtained from the physical model application. Values for α and u_0 are taken from, or calculated from work presented by Jorstad et al. (2005).

As a reminder of the definitions for the parameters in this table, θ is essentially the jet half angle, α is the angle between the observer vector and the z-axis, which may be taken to be the jet axis in the physical model that has been derived in this work. P is the period of precession of the central engine (causing non-linear jet structure). Finally, u_0 is the component injection velocity.

Chapter 7

Discussion, Conclusions and Further Work

In studying astrophysical jets, one method of analysis comes from looking at the evolution of flux density and EVPA with time. Such work can yield information on new components that may or may not be in the process of being injected into the jet flow for a source. The observational indications of a new component injection are a significant increase in flux density for the source (due to the added flux of the new component) and a change in EVPA. In the optically thick core, it would be expected that the EVPA would be roughly perpendicular to the jet axis. Study of the Blazar OJ287 by D'Arcangelo et al. (2009) supports such an idea. In this work, a spine-sheath model is proposed for OJ287. In the so-called transition region between the spine and sheath in this model, velocity shear is responsible for the orientation of the core EVPA.

There was some attempt to look at the fluxes of the sources analysed in this work. However, no significant jumps in flux were noted. A more thorough look at the fluxes of the sources analysed may be a worthy avenue of possible further work. This thesis has been concerned more with the kinematics of imaged jet structures.

7.1 Component Velocities

In terms of the component velocities calculated, there are some values that appear to be very large. There are also negative velocities.

The main issue with this analysis is the correct identification of components over several epochs. This difficulty has been pointed out by Jorstad et al. (2001). Misidentification of components could have a large impact on the component velocities that have been derived.

Misidentification of components might well explain some of the component velocities that appear to be far too high. Where possible, it is worth looking at such results again and comparing them to proper motions of components derived from a previous study (Jorstad et al., 2001). This work shall be referred to as J-2001 for the remainder of this section. Comparison with previous results will allow an appreciation of whether or not components in certain sources have reached the velocities quoted in this work.

For 0336-019, J-2001 reports proper motion values of 0.18 and 0.42 mas/ yr. These values are significantly lower than those found in this work. In the case of 1611+343 J-2001 gives component proper motion values of 0.57, 0.49, 0.18 and 0.31 mas/yr. Two of the values derived in this work for the same source are closer to unity in terms of proper motion. This is a notable difference. 1730-130 has 0.28 mas/yr as it's highest value in J-2001. This is much lower than the value of 1.10 mas/ yr that has been found for component 3 in the source. For 3C279, proper motions of around 1 mas/ yr and above have been found in this work. 0.31 mas/yr is the highest value given in J-2001 for this source. 3C454.3 is shown with component proper motions of 0.14, 0.34 and 0.53 mas/yr in J-2001. However, in this work, values approaching 2 mas/yr are found. Finally, for CTA102 in J-2001 there are proper motions for components between 0.2 and 0.4 mas/yr. However, in this work a component proper motion of 0.829 mas/yr has been calculated.

It is not true that every source analysed in this work has proper motions that are questionably large. This seems to rule out any kind of systematic error in the analysis.

Negative velocities might possibly be explained by motion of the (presumed) core at 43 GHz. If a component distance from the core is calculated in one epoch and then the core appears to move downstream such that the distance is reduced, the overall effect would be that the component would appear to be moving toward the core.

7.2 Fitting the Physical Model

The outcomes of the fitting were mixed in terms of success. There are cases where the trajectories plotted do not really reflect the data for a certain source and epoch. However, there is some good agreement. Figure 5.2 demonstrates some reasonable correlation for 3C273. Also, there is a fairly good fit in Figure 5.4.

To perform the application of the physical model more successfully more observed and model fitted components would be helpful for both 3C273 and 3C345. This would give a better impression of how well a model fits the observed component positions.

The limit is the VLBA's ability to resolve components. Observations at higher frequency would be a worthwhile study. It may be found that a component at 43 GHz may be resolved into more than one component at higher frequency.

This work indicates that with more model fitted components, it could be possible to analyse and understand key characteristics of non-linear Blazar jets. The basic method to follow is:

1. Produce VLBI images of a sample of Blazar jets and look for non-linear structures. The sample should be as big as possible to maximise the chances of finding non-linear jets.

2. Model fit as many components as possible in the jets demonstrating non-linear structure.

3. Develop a physical model to simulate the jet behaviour.

4. Fit the physical model to the model fitted data.

5. Pinpoint important characteristics of the jet system, for example the period of jet precession.

References

Burke, B. and Graham-Smith, F.: 2002, *An Introduction to Radio Astronomy*, Cambridge University Press, second edition

Cohen, M.: 2009, *Active Galaxies And Quasistellar Objects, Superluminal Motion*, Part of "A Knowledgebase for Extragalactic Astronomy and Cosmology" (http://nedwww.ipac.caltech.edu/level5/)

D'Arcangelo, F. D., Marscher, A. P., Jorstad, S. G., Smith, P. S., Larionov, V. M., Hagen-Thorn, V. A., Williams, G. G., Gear, W. K., Clemens, D. P., Sarcia, D., Grabau, A., Tollestrup, E. V., Buie, M. W., Taylor, B., and Dunham, E.: 2009, *The Astrophysical Journal* **697(2)**, 985

Freedman, R. and Kaufmann III, W.: 2002, *Universe*, Freeman, sixth edition

Garcia, R.: 1995, Phd thesis, University of Edinburgh

Hardcastle, M.: 2007, in T. Rector and D. De Young (eds.), *Extragalactic Jets: Theory and Observation from Radio to Gamma ray*, Vol. 386 of *Astronomical Society of the Pacific Conference Series*, pp 46–55, Astronomical Society of the Pacific

Högbom, J.: 1974, *Astronomy and Astrophysics Supplement* **15**, 417

Hovatta, T., Nieppola, E., Tornikoski, M., Valtaoja, E., Aller, M. F., and Aller, H. D.: 2008, *Astronomy & Astrophysics* **485**, 51

Jennison, R.: 1958, *Monthly Notices of the Royal Astronomical Society* **118**, 276

Jorstad, S., Marscher, A., Lister, M., Stirling, A., Cawthorne, T., Gear, W., Gómez, J., Stevens, J., Smith, P., Forster, J., and Robson, E.: 2005, *The Astronomical Journal* **130**, 1418

Jorstad, S. G., Marscher, A. P., Mattox, J. R., Wehrle, A. E., Bloom, S. D., and Yurchenko, A. V.: 2001, *The Astrophysical Journal Supplement Series* **134**, 181

Kaastra, J. and Roos, N.: 1992, *Astronomy & Astrophysics* **254(Feb (I))**, 96

Kembhavi, A. and Narlikar, J.: 1999, *Quasars and Active Galactic Nuclei: An Introduction*, Cambridge University Press, first edition

Kitchin, C.: 2003, *Astrophysical Techniques*, Institute of Physics Publishing, fourth edition

Krolik, J.: 1999, *Active Galactic Nuclei*, Princeton Series in Astrophysics, Princeton University Press

Larionov, V. M., Jorstad, S. G., Marscher, A. P., Raiteri, C. M., Villata, M., Agudo, I., Aller, M. F., Arkharov, A. A., Asfandiyarov, I. M., Bach, U., Bachev, R., Berdyugin, A., Böttcher, M., Buemi, C. S., Calcidese, P., Carosati, D., Charlot, P., Chen, W.-P., Di Paola, A., Dolci, M., Dogru, S., Doroshenko, V. T., Efimov, Y. S., Erdem, A., Frasca, A., Fuhrmann, L., Giommi, P., Glowienka, L., Gupta, A. C., Gurwell, M. A., Hagen-Thorn, V. A., Hsiao, W.-S., Ibrahimov, M. A., Jordan, B., Kamada, M., Konstantinova, T. S., Kopatskaya, E. N., Kovalev, Y. Y., Kovalev, Y. A., Kurtanidze, O. M., Lähteenmäki, A., Lanteri, L., Larionova, L. V., Leto, P., Le Campion, P., Lee, C.-U., Lindfors, E., Marilli, E., McHardy, I., Mingaliev, M. G., Nazarov, S. V., Nieppola, E., Nilsson, K., Ohlert, J., Pasanen, M., Porter, D., Pursimo, T., Ros, J. A., Sadakane, K., Sadun, A. C., Sergeev, S. G., Smith, N., Strigachev, A., Sumitomo, N., Takalo, L. O., Tanaka, K., Trigilio, C., Umana, G., Ungerechts, H., Volvach, A., and Yuan, W.: 2008, *Astronomy & Astrophysics* **492**, 389

Levenberg, K.: 1944, *The Quarterly of Applied Mathematics* **2**, 164

Lister, M., Aller, H., Aller, M., Cohen, M., Homan, D., Kadler, M., Kellermann, K., Kovalev, Y., Ros, E., Savolainen, T., and Zensus, J. Vermeulen, R.: 2009, *The Astronomical Journal* **137**, 3718

Lobanov, A. and Roland, J.: 2005, *Astronomy & Astrophysics* **431**, 831

Marquardt, D.: 1963, *SIAM Journal on Applied Mathematics* **11**, 431

Marscher, A. and Gear, W.: 1985, *The Astrophysical Journal* **298**, 114

McKinney, J. and Blandford, R.: 2009, *Monthly Notices of the Royal Astronomical Society: Letters* **394**, 126

Meier, D. and Nakamura, M.: 2006, in H. Miller, K. Marshall, J. Webb, and M. Aller (eds.), *Blazar Variability Workshop II: Entering the GLAST Era*, Vol. 350 of *ASP Conference Series*, pp 195–204

Papageorgiou, A.: 2005, *Ph.D. thesis*, University of Central Lancashire

Reynolds, C.: 2002, *Ph.D. thesis*, Centre for Astrophysics University of Central Lancashire

Rieger, F., Bosch-Ramon, V., and Duffy, P.: 2007, *Astrophysics and Space Science* **309**, 119

Sparrow, G.: 2006, *Cosmos - A Field Guide*, Quercus Publishing

Thompson, A.: 1995, in J. Zensus, P. Diamond, and P. Napier (eds.), *Very Long Baseline Interferometry and the VLBA*, Vol. 82 of *ASP Conference Series*, pp 73–90

Walker, C.: 2004, *Very Long Baseline Interferometry*, Ninth Synthesis Imaging Summer School Talk

Zeilik, M. and Gregory, S.: 1998, *Introductory Astronomy and Astrophysics*, Brooks/Cole, fourth edition

Zensus, J. A., Krichbaum, T. P., and Britzen, S.: 2006, in J. Guirado, I. Marti-Vidal, and J. Marcaide (eds.), *Primer Encuentro de la Radioastronomía Española "Memorial Lucas Lara"*

CARDIFF UNIVERSITY ★ PRIFYSGOL CAERDYDD ★